Structures to Enhance

Light–Plasmonic Interactions

By

Alireza Maleki

A Thesis Submitted to Macquarie University for the

Degree of Doctor of Philosophy

Department of Physics and Astronomy

December 2015

MACQUARIE
University

Table of Contents

List of Figures

List of Boxes and Tables

Abstract

Remarkable data processing and transport capabilities provided by the development of chip scale electronics and photonic technology have affected almost every facet of our lives. The ever-increasing demand for faster data transfer and processing has driven electronic technology to smaller, faster and more efficient devices. Plasmonics exploits the unique properties of miniature metallic structures to control light at the nano-scale, integrating with micro-photonic devices. Among many circuitry elements, plasmonic-enhanced photodetectors are particularly promising, since the size of the active semiconductor absorber is constrained laterally by the diffraction limit, and in the longitudinal dimension by the finite absorption depth of the semiconductor.

In this thesis, we study three important plasmonic elements including plasmonic gratings and specifically the plasmonic focusing property of curved gratings, dielectric microspheres as the potential elements for replacing metallic nano-antennas, and plasmonic enhanced graphene photodetectors for amplifying photocurrent generation by graphene.

The ability of curved gratings to couple incident light into surface plasmons and to focus the surface plasmons is investigated. It is demonstrated by simulation and experiment that the focal spot of the curved gratings depends on the sector angle and can reach as low as 300 nm ($\sim \frac{\lambda_0}{2.3}$) at a wavelength of $\lambda_0 = 700$ nm for sector angles greater than 100°. The application of curved gratings in launching surface plasmons

onto micro-stripline waveguides is investigated and it is shown that curved gratings with small sector angles ~20° have 5% increased coupling efficiency in comparison to linear gratings. For larger sector angles the coupling efficiency of the curved grating decreases in comparison to linear gratings. In comparison to circular gratings that need to be illuminated with circularly polarized light and also do not give access to the focal spot because of the closed loop geometry, curved gratings can focus surface plasmons with linearly polarized light and also give access to the focal region for further process. In addition, the numerical aperture of curved gratings is defined for the first time based on the curvature of the gratings.

The ability of dielectric microspheres with a rather high refractive index to couple out propagating surface plasmons and radiate directionally is also investigated by simulation and experiment. It is shown that TiO_2 microspheres can scatter and radiate propagating surface plasmons. It is also shown by simulation that such radiation can be directional suggesting the dielectric microsphere as an antenna.

Finally, the photocurrent amplification of graphene photodetectors using electromagnetic near-field enhancement of surface plasmons is investigated. We use the novel idea of tunnelling light photons into surface plasmons at the graphene-metal contact to enhance the photocurrent generation in a graphene gap-photodetector consisting of two gold strips separated with a gap and covered with a graphene sheet. Maximum photocurrent amplification of 8 was achieved at 730 nm wavelength of incident light. The enhancement by tunnelling light photons through the evanescent field of the incident light is valuable for photodetection and sensing. Such a

photodetector can be used as a plasmonic detector for plasmonic waveguides in a plasmonic circuit.

Statement of Candidate

This project “Structures to enhance light-plasmonic interactions” is established by Macquarie University and funded by Macquarie University and the Australian Research Council Centres of Excellence program CUDOS.

The metallic structures were fabricated in steps. The gold deposition was performed at MQ photonics research centre with Dr. James Downes and the focused ion beam (FIB) fabrication was operated by Steven Moody using CSIRO facilities (Lindfield node).

The plasmonic enhancement graphene photodetectors (Chapter 7) is the result of collaboration between Macquarie University CUDOS node and Swinburne University CUDOS node. The graphene deposition and wire bonding of the photodetectors was performed at Swinburne University with the help and support from Dr. Benjamin Cumming, using equipment in the Swinburne University micro-photonic labs.

Scanning electron microscopy was performed at Macquarie University microscopy unit with the help and support from Ms. Debra Birch. The laser ablation of some of the samples was also done at Macquarie University ANFF node by Dr. Benjamin Johnson. COMSOL software access and use was provided by Macquarie University.

This thesis is submitted in fulfilments of the requirements of the degree of Doctor of Philosophy at Macquarie University and has not previously been submitted for a degree nor has it been submitted as part of requirements for a degree to any other

university or institution other than Macquarie university. I also certify that the thesis is an original piece of research and it has been written by me. Any help and assistance that I have received in my research work and the preparation of the thesis itself have been appreciably acknowledged. In addition, I certify that all information sources and literature used are indicated in the thesis.

Alireza Maleki

Acknowledgement

I sincerely thank my supervisor; Judith Dawes. Your encouragement, support and guidance educated me in doing research in science and set me up completing this PhD project.

I also thank Dayong Jin for his support, and guidance for doing this PhD project, and Thanh Phong Vo for helping me to develop the necessary practical knowledge and lab skills specially training me operating NSOM system.

David Coutts generously spent time to guide me in the scientific and technical problems and I always benefited his comments and support. Thank you David.

James Downes always kindly agreed to deposit gold films for our sample fabrication. Thank you very much James.

I thank Ben Cumming from Swinburne university for his help and support and collaboration in working on the plasmonic-enhanced graphene photodetectors, Steven Moody for fabricating the plasmonic structures by focused ion beam, Krystyna Drozdowicz-Tomsia for the training and support she provided me to do Raman spectroscopy, Debra Birch for scanning electron microscope training and support, Susan Law for doing cleanroom induction and safety support, and Regina Dunford for wet lab safety induction and preparation.

I would also like to thank Mick Withford for his support as the MQ Photonic Research Centre Director and MQ CUDOS node director, Mike Steel for supporting and guiding me doing my simulations, and Ben Johnson for doing laser ablation for my sample fabrications.

I also acknowledge CSIRO for giving access to FIB facility operated with Steven Moody for fabricating the structures.

There are a lot of people in the Department of Physics and Astronomy whose effort and support has a significant effect on the performance of each member of the department from students to academics. I appreciate their support and specially thank the administrative staff; Carol, Liz, Lisa Chanel, Lisa Pesavento and Amit.

At the end I would like to thank Macquarie University for the scholarship and the chance they gave me to found my future on this great academic experience.

Alireza

Chapter 1: Motivation and Background

1.1 Motivation

Controlling the interaction of light with matter is of fundamental importance to a wide range of applications in science and technology. Interest in the applications of light has increased dramatically over the past century as mysteries concerning black body radiation and line spectra led to the birth of quantum mechanics and consequent developments such as the laser. Although metals are usually considered as mirrors, we can also observe a fascinating physical phenomenon when light is absorbed by the metal. Surface plasmons, (SPs) are oscillations of free charges (conduction electrons) bound to the metal-dielectric interface. Surface plasmons enable us to couple light to a metal-dielectric interface, manipulating coupled light in two dimensions and even decoupling it from the interface, all on a nanometer scale. Surface plasmons have greater momentum than the incident light, so that the associated electromagnetic fields cannot propagate away from the metal-dielectric interface and the corresponding normal component of their field decays exponentially in strength away from the interface. Fig. 1-1 shows a schematic of surface plasmon oscillations confined at the metal-dielectric interface to dimensions significantly smaller than the wavelength of the light.

The history of surface plasmons dates to the 1950's when Ritchie presented his pioneering work [1], but it has recently attracted renewed interest due to advances in nano-scale fabrication technology. This in turn has enabled the nano-scale control of surface plasmons for specific applications [2]. For instance surface plasmons are being explored for their potential applications to integrate electronic and photonic devices on the same chip [3].

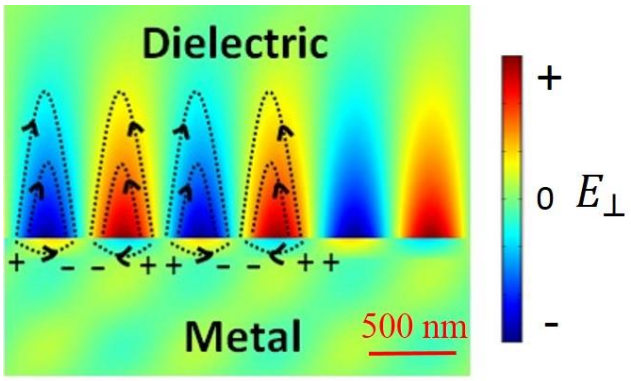

Fig. 1-1 Electromagnetic field of surface plasmons bound to the metal-dielectric interface as longitudinal oscillations of free charges on the nanometre scale. The image is from my simulation of a glass-gold-air interface with surface plasmons, using COMSOL

The use of surface plasmons also facilitates the concentration of light in subwavelength structures resulting in significant enhancement of the local electric field. This has propelled the use of SPs in a range of nano-photonics technologies and applications such as surface enhanced Raman spectroscopy (SERS) for detecting single molecules [4, 5], biosensors [6], photovoltaics [7,8], and nonlinear optics [9].

The demand for faster information transfer has driven the silicon-based electronics industry towards smaller, faster, and more efficient electronic devices over the past five decades. Optical connectors may offer interesting new solutions for increased

bandwidth and processing speeds, due to their huge data-carrying capacity. Optical approaches may also be a key element for fast electronic computing systems, linking high-speed computing cores.

Box1.1: Diffraction Limit

Large diameter dielectric waveguides support many modes, and as the core diameter or thickness of the waveguide decreases, higher order modes are eliminated until just the fundamental mode remains. The mode size decreases until the lateral size of the waveguide (d), is approximately the wavelength of the guided mode ($d \approx \lambda_{\circ}$). On further decrease of the waveguide lateral size, the fundamental mode expands and penetrates into the surrounding medium of the waveguide core. Finally, it evolves to become a plane wave in the surrounding medium when the size of the waveguide is zero ($d \approx 0$), approaching the diffraction limit for a dielectric waveguide.

The situation for surface plasmon waveguides and interconnects is quite different. As the lateral size of a plasmonic waveguide decreases, the fundamental surface plasmon mode experiences a strong monotonic increase in localization.

However, there is a large size mismatch between electronic and dielectric photonic components since dielectric photonic device sizes are limited to scales of the order of a wavelength. In other words, dielectric photonic components are restricted to the

micro-scale by the diffraction limit (see Box 1.1 for more details), but this does not fit well with nanoscale electronic technology. Surface plasmon-based technology (plasmonics) can use the unique properties of nanoscale metallic structures to route and manipulate light at the nanoscale. Plasmonics has been discussed as a candidate technology to integrate electronic and conventional photonic devices on the same chip [10, 11]. Several plasmonic circuitry elements have been investigated and demonstrated practically, including plasmonic waveguides with different configurations; micro-stripline waveguides [12], slot waveguides [13], nanowires [14], Bragg mirrors [15], integrated surface plasmon multiplexers [16], plasmonic modulators [17], interconnects [18], plasmonic lenses [19, 20], plasmonic nano-antennas [21], and photodetectors[22-24]. In this thesis we have focused on the last three components, discussing the related challenges for the ideal performance of each component and also introducing new ideas and design to improve their performance.

In-plane focusing and concentration of surface plasmons can improve the field enhancement effect with applications in plasmonic circuitry, sensing, and nonlinear surface plasmons. Among many interesting plasmonic focusing elements, circular gratings had been attracted a great deal of interest [19]. However, they need to be illuminated by circularly polarized light to provide a single focusing spot and also because of their closed loop nature are not able to integrate with other plasmonic elements. In Chapter 4 of this thesis we introduce and investigate the ability of curved gratings, as a sector cut of circular gratings, to focus surface plasmons in-plane, by illuminating them with linearly polarized light. Of particular advantages of curved gratings as plasmonic lenses are the ability to change the lateral distribution of

concentrated surface plasmons and also access to the focal spot. The focusing properties of curved gratings, such as the lateral focal spot size and intensity dependence, are investigated in this thesis and the numerical aperture is defined and proved by theory, simulation and experimental results. The application of curved gratings for coupling surface plasmons into micro-stripline waveguides is also investigated in Chapter 5. Prior to the study of the curved gratings the important parameters of plasmonics gratings (groove depth and groove width) are investigated and optimized for the design and fabrication of curved gratings, in chapter 3.

In another aspect, the interaction of light with metal nano-particles results in the collective oscillation of the conduction electrons, known as localized surface plasmons, leading to phenomena such as the subwavelength localization of electromagnetic energy, creation of hot spots at the surface of metal nano-particles, or the directional scattering of light from the structure [25]. Metallic nano-particles operate as nano-antennas since localized surface plasmons enable efficient transfer of localized electromagnetic energy from the near field to the far field and vice versa [21]. Plasmonic resonances in nano-antennas allow unprecedented control of light-matter interactions within subwavelength volumes, leading to many interesting applications such as surface-enhanced fluorescence [26] and surface-enhanced Raman spectroscopy (SERS) [27], single molecule detection [4], destruction of cancer cells using resistive heating of resonant nano-particles [28], and even nano-photonic circuitry [29].

However, some important issues of the use of nanoscale metallic structures as nano-antennas have recently been addressed [30-32]. First, the non-radiative relaxation rates of metallic nano-structures can become dominant when an emitter is placed in their vicinity, which destroys the advantages of localized surface plasmon excitation [33]. Second, the angular distribution of the radiated power from the metallic nano-antennas, that is, the directionality of the emitted radiation, depends on the number of nanoparticles. In fact, the directionality of the metallic nano-antennas requires coupling between the emitted light and the surface plasmon modes, which demands a large number of metallic nanoparticles and translates to higher ohmic loss. Although the metallic nano-antennas can be reduced to two nano-particles, this decreases the directionality of their radiation [34]. To solve this problem TiO_2 microspheres have been proposed and investigated as an alternative for metallic nano-antennas since they have lower loss in comparison to metallic nano-antennas and can emit directionally when positioned in the vicinity of a dipole emitter [30]. However, the fabrication of TiO_2 –dipole emitters is a challenge in practice, because of the micro and nano size scale of particles and the requirement for their precise positioning. In this thesis we present our idea of using TiO_2 microspheres as single dielectric emitters to scatter and emit propagating surface plasmons in Chapter 6.

Finally, plasmonic-enhanced photodetectors are discussed and investigated. Plasmonic-enhanced photodetectors are promising [35] as they offer the ability to shrink the lateral dimensions of conventional photodetectors below the diffraction limit to improve the signal to noise ratio rate, and also reduce the limitation on the longitudinal dimension due to the finite absorption depth of the semiconductor. Several

plasmonic nano-structures have been proposed and demonstrated to concentrate light laterally and increase absorption within semiconductor materials to increase the speed of photodetectors and decrease the required illumination power. In pioneering work [22], Ishi *et al.* used a 10 μm-diameter concentric grating coupler to funnel surface plasmons towards a central silicon photodetector. This coupler improved the detector photo-response time by more than a factor of 20. However, here we focus on graphene photodetectors and introduce novel ideas to enhance photocurrent generation in such detectors in Chapter 7.

The unique optical and electronic properties of graphene, such as high conductivity, light transmission and broad band response, suggests it as an appealing material for photonics and optoelectronic applications, in particular, photodetectors [36]. In graphene photodetectors based on photovoltaic effects one needs to separate photo-generated electron-hole (e-h) pairs by built-in fields between separately doped sections of graphene or at junctions where graphene is in contact with metals. However, extraction of photo-electrons is normally inefficient as only a small area of the p-n junction (the graphene to metal contact points) contributes to photocurrent generation. In addition, although 2.3% absorption of incident light by graphene is very high for a monolayer of atoms, it is very small in absolute terms[37]. Surface plasmon field enhancement can increase the photoresponse of graphene-based photodetectors. In this research we use the ability of curved gratings to focus surface plasmons in-plane to enhance the photocurrent generation in graphene photodetectors, presented in Chapter 7. The photocurrent enhancement of graphene photodetectors has previously been based on the diffraction of light by nano-plasmonic structures, such as gratings,

and nano-antennas [37-39]. However, our investigation led us to the novel idea of using photon tunneling of light into surface plasmons to enhance the photocurrent of simple graphene gap-photodetectors. Such a graphene gap-photodetector consists of two gold strips with graphene overlaying the gap between them. This idea offers a new range of graphene photodetectors in which the photocurrent is enhanced by coupling the evanescent field of the electromagnetic waves into surface plasmons. For instance, graphene gap-photodetectors on waveguides could use the evanescent field of the waveguides for coupling surface plasmons onto graphene gap-photodetectors for photodetection, plasmonic detection and sensing.

In the remained of this chapter further background on surface plasmons and on the properties of graphene is provided.

1.2 Surface plasmons at a metal-dielectric interface

For the simplest case, consisting of an interface of a metal and a dielectric, the surface plasmon dispersion relation, as a relationship between the surface plasmon wave vector k_{sp} and the related frequency ω, can be derived by solving Maxwell's equations (Box 2.1 in Chapter two) and finding surface mode solutions under appropriate boundary conditions [40-42]. For the metal-dielectric interface illustrated in Fig. 1-2, the electric field at the interface is described by [41];

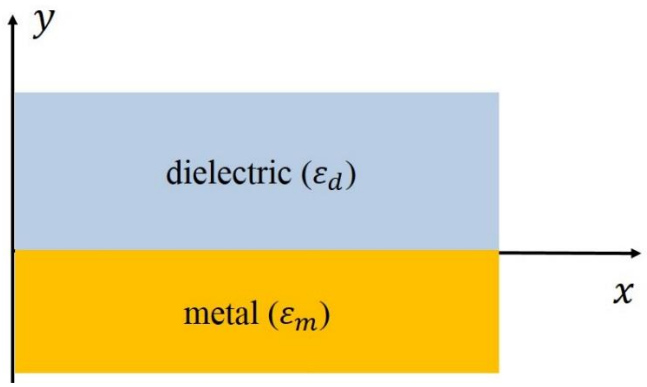

Fig. 1-2 Metal-dielectric interface with related dielectric constants

$$E = E_0{}^{\pm} \exp\left[+i\left(k_x x \pm k_y y - \omega t\right)\right] \qquad \text{Eq. 1-1}$$

in which $\pm$ stand for $y \geq 0$ and $y \leq 0$, respectively. The damping of surface plasmons in the normal direction to the interface (y axis) implies an imaginary k_y. The wave-vector (k_x) lies parallel to the interface of the metal-dielectric (x direction) and can be derived as;

$$k_x = \frac{\omega}{c} \sqrt{\frac{\varepsilon_m \varepsilon_d}{\varepsilon_m + \varepsilon_d}} \qquad \text{Eq. 1-2}$$

The dielectric constant of the metal is complex, with $\varepsilon_m = \varepsilon_m{}' + i\varepsilon_m{}''$. By assuming $\varepsilon_m{}'' < |\varepsilon_m{}'|$ we obtain a complex k_x, as $k_x = k_x{}' + ik_x{}''$with;

$$k_x{}' = \frac{\omega}{c} \left(\frac{\varepsilon_m{}' \varepsilon_d}{\varepsilon_m{}' + \varepsilon_d}\right)^{1/2} \qquad \text{Eq. 1-3}$$

$$k_x{}'' = \frac{\omega}{c} \left(\frac{\varepsilon_m{}' \varepsilon_d}{\varepsilon_m{}' + \varepsilon_d}\right)^{3/2} \frac{\varepsilon_m{}''}{2(\varepsilon_m{}')^2} \qquad \text{Eq. 1-4}$$

For a real $k_x{}'$ one needs $\varepsilon_d < |\varepsilon_m{}'|$ and $\varepsilon_m < 0$, which can be satisfied for a metal. The imaginary part of k_x ($k_x{}''$) is also related to internal absorption (ohmic loss) of the surface plasmons at the metal-dielectric interface. The propagation length (L_{sp}) of the surface plasmons along the metal-dielectric interface is defined as the length after which the intensity decreases to $1/e$ of its maximum value and it can be calculated as;

$$L_{SP} = (2k_x{}'')^{-1} \qquad \text{Eq.1-5}$$

The graph in Fig. 1-3 is plotted in MATLAB by numerical calculation of the dispersion relation [Eq. 1-2] for surface plasmons at a gold-air interface. The dielectric constant of gold is calculated according to the Drude model with a plasma frequency of $\omega_p = 8.9$ eV, and inverse of relaxation time of $\gamma = \frac{1}{\tau} = 0.07$ eV [43] (see Box 1.2 for more details). The dispersion relation shows two main features of surface plasmons. First, it shows that the momentum of the surface plasmon modes is greater than that of free-space photons with the same frequency, $\hbar k_{sp} > \hbar k_0$, in which $k_0 = {}^{\omega}/_{c}$ is the free-space wavevector. As a result, the dispersion curve of the excited surface plasmons lies to the right of the respective light-line of the dielectric and air (see Fig. 1-3). Second, the field perpendicular to the surface decays exponentially, indicating the binding of electromagnetic waves at the metal-dielectric interface. As a result, light illuminating the metal-dielectric interface cannot be directly coupled into surface plasmons. Special methods must be used to provide the extra required momentum for light photons to match the wave-vector of surface plasmons using either photon tunneling in a total reflection geometry, or diffraction effects.

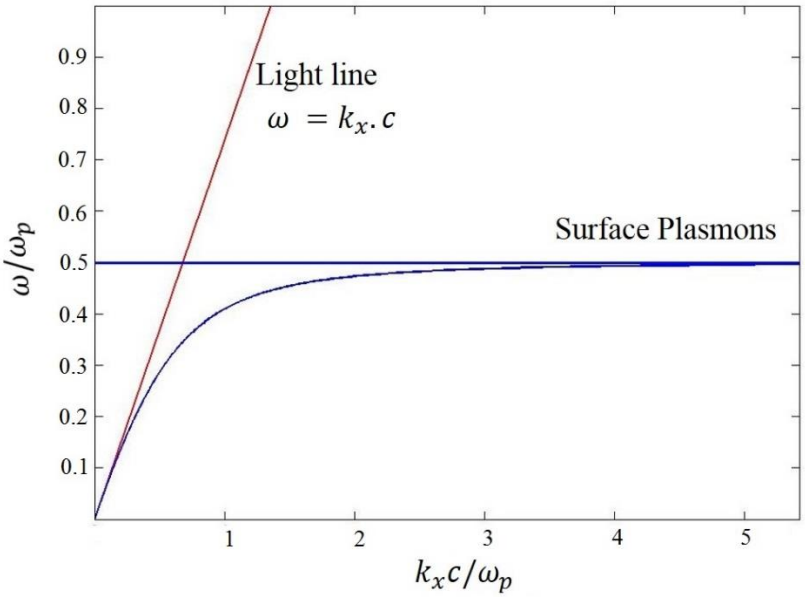

Fig. 1-3 Dispersion relation of surface plasmons for a gold-glass interface. The graph is plotted from a numerical calculation of the dispersion relation (Eq. 1-2). The dielectric constant of gold is calculated according to the Drude model

1.2.1 Total internal reflection

The Kretschmann-Raether configuration, as shown in Fig. 1-4 (a), consists of a dielectric prism in contact with a metal layer, and the metal-prism interface is illuminated through the prism. Here, the projection of the wave-vector of the incident light at the metal-dielectric interface ($\frac{\omega}{c}\sqrt{\varepsilon_{prism}}\,sin\theta$) apporaches the plasmon wave-vector for angles greater than the total internal reflection angle. At this coupling angle, the penetrating evanescent field through the metal layer can excite plasmon resonances at the air-metal interface [41, 42];

$$k_{sp} = \frac{\omega}{c}\sqrt{\frac{\varepsilon_m}{\varepsilon_m+1}} = \frac{\omega}{c}\sqrt{\varepsilon_{prism}}\, sin\theta \qquad \text{Eq. 1-6}$$

The coupling angle manifests as a sharp dip in the reflection at the prism-metal interface, just above the critical angle, see Fig. 1-6 (b) and Fig. 1-8. However, the coupling efficiency by the Kretschmann technique depends also on the thickness of the metal layer. As the metal thickness increases, the tunneling width increases, and fewer photons can tunnel through the metal-prism interface. For thicker metal layers, surface plasmons can be excited in another configuration (Otto configuration [44]), in which the prism is placed close to the metal surface, but not in contact with it, and photon tunneling occurs through the air gap between the prism and metal surface, as in Fig. 1-4 (b) .

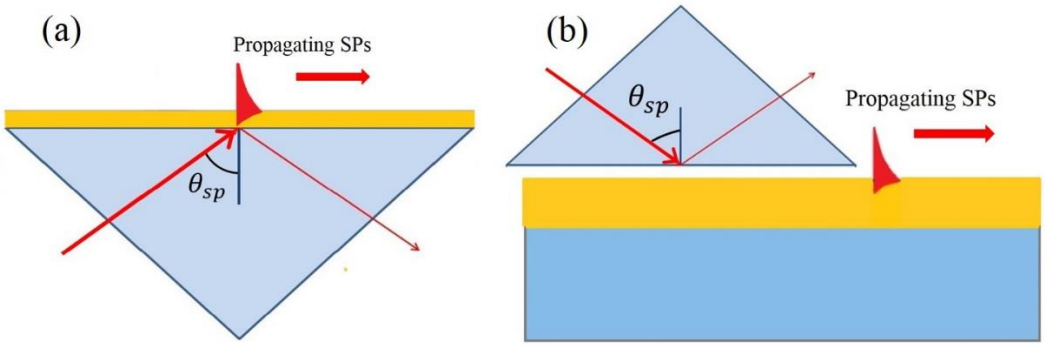

Fig. 1-4 Coupling surface plasmons by photon tunnelling (a) Kretschmann configuration and (b) Otto configuration

To illustrate this technique, I present some typical measurements and simulations. The dip in the reflection of the incident light due to coupling of surface plasmons at the metal film on the prism was measured for a 30 nm-thick gold film (with a

protective layer of 10 nm Zirconia (ZrO_2)) deposited on glass, as illustrated in Fig. 1-5. The result was compared with a simulation of the same structure using COMSOL software. Fig. 1-6 (a) shows the Kretschmann experiment setup and the measured dip in the reflection is illustrated in Fig. 1-6 (b). The structure was illuminated at $\lambda_0 = 642$ nm and the graph shows that the dip (coupling angle) for this structure occurs at $\theta = 52^{\circ} \pm 1^{\circ}$.

Box 1.2; Drude Model

The Drude model is a simple but nevertheless very useful model that describes the response of metals when exposed to an electromagnetic field. The model was first proposed by Paul Drude [45]. In the Drude model, the optical properties of metals over a wide range of frequencies can be explained by a plasma model, assuming a free electron gas. The model assumes a damped oscillation of the gas of free electrons between heavier, relatively immobile, positive ion cores;

$$m_e\ddot{r} + m_e\gamma\dot{r} = -eE \qquad \text{(B.1.2.1)}$$

where $\gamma = 1/\tau$ describes a phenomenological damping term with τ as the free electron relaxation time, m_e as the effective mass of the free electrons, e as the free electron charge, r as displacement, E and ω as the applied field and the frequency of applied field, respectively.

Consider a harmonic time dependence of the driving field, $E = E_0 e^{-i\omega t}$. Solving equation (B.1.2.1) with this field, and calculating the macroscopic polarization, to determine the plasma frequency of the free electron gas, ω_p, we obtain the desired model for the free electron gas dielectric function; (see reference [40] for more details);

$$\varepsilon(\omega) = 1 - \frac{{\omega_p}^2}{\omega^2 + i\gamma\omega} \quad , \quad \omega_p = \sqrt{\frac{n_e e^2}{\varepsilon_0 m}} \qquad \text{(B.1.2.2)}$$

where n_e is the electron density.

Fig. 1-5 Gold slab consisting of 30 nm gold (with a 10 nm protective layer of Zirconia) deposited on glass

(a) (b)

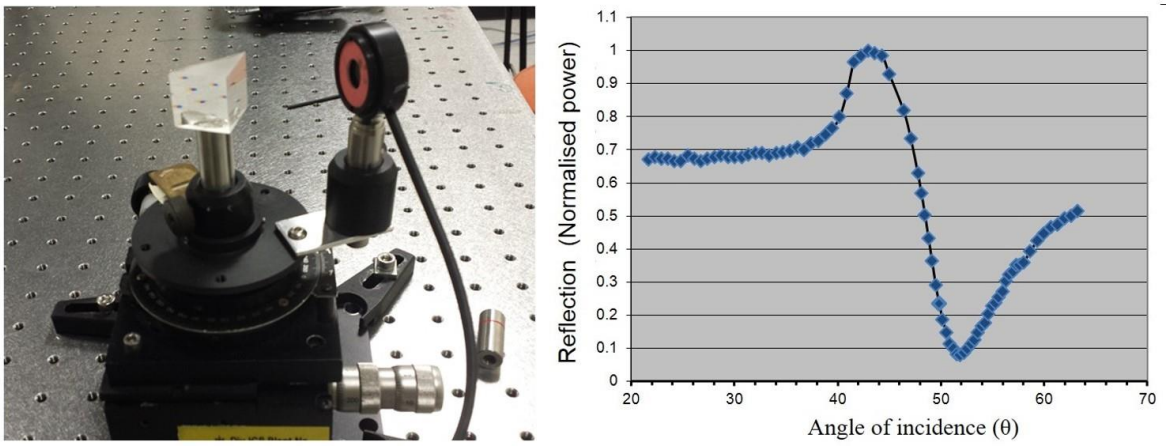

Fig. 1-6 (a) Kretschmann measurement setup, (b) angle of incidence versus the intensity of the reflected light shows the dip corresponding to the coupling of surface plasmons

By defining a real physical model, COMSOL Multiphysics internally compiles a set of equations representing the entire model (see Chapter two, Methodology, for more details). The software uses the finite element method (FEM) together with adaptive meshing and error control to analyze the defined physical model. The simulated structure is a 30 nm-thick gold film, with a protective layer of 10 nm Zirconia, deposited on glass with a refractive index of $n = 1.52$ illuminated at $\lambda_0 = 642$ nm, identical to the fabricated structure. The gold dielectric constant for this wavelength is taken as $\varepsilon = \varepsilon_m{}' + i\varepsilon_m{}'' = -12.28 + i(1.12)$ from [46] (see Box 1.3

for discussion on the dielectric constant of metals). The geometry and illumination of the structure are illustrated in Fig. 1-7. In the simulation, the left and right sides of the geometry have periodic boundary conditions. However, the top and bottom sides of the geometry are active ports, operating as both the input (illumination) and output ports.

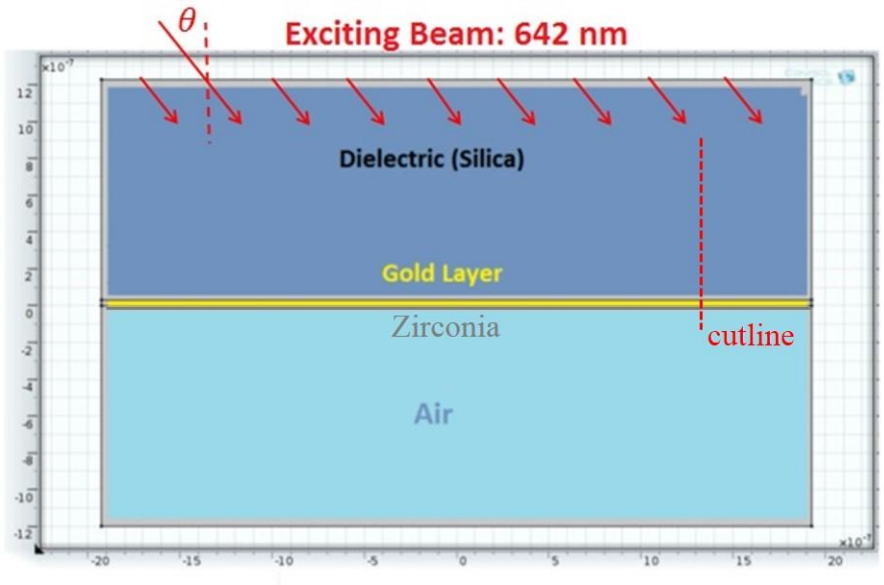

Fig. 1-7 Geometry of COMSOL simulation representing the Kretschmann configuration

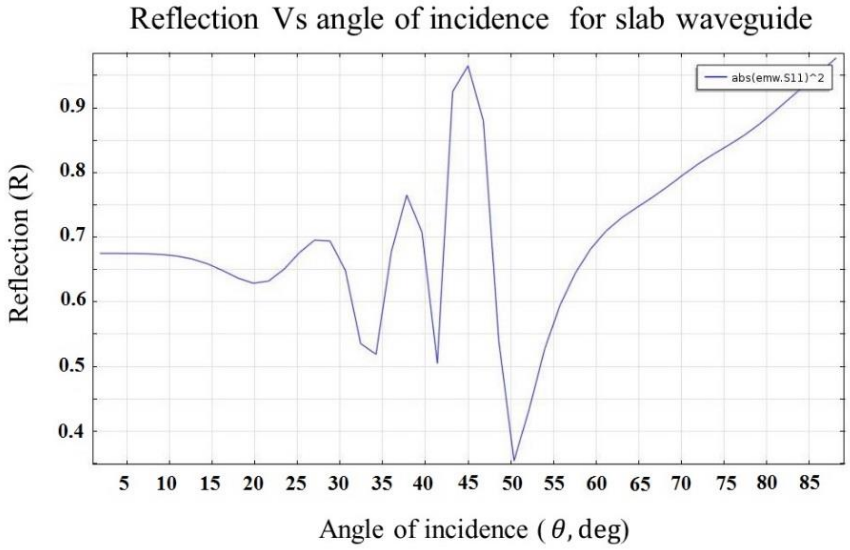

Fig. 1-8 Plot of calculated reflection of light through the output port against the angle of incidence shows the surface plasmon coupling angle as a dip just above the critical angle, which is at $\theta \cong 45^{\circ}$

In Fig. 1-8, the calculated reflection through the active ports is plotted against the illumination angle and it shows a dip at $\theta \cong 51^{\circ}$ in good agreement with the experimental result. In addition, to demonstrate the coupling of incident light into surface plasmons at this angle, the behavior of the near field at the gold-glass interface was also investigated. The multiple dips in the calculated reflection against the incidence angle before the plasmonic resonance dip can be attributed to planar guided waves through the substrate [41].

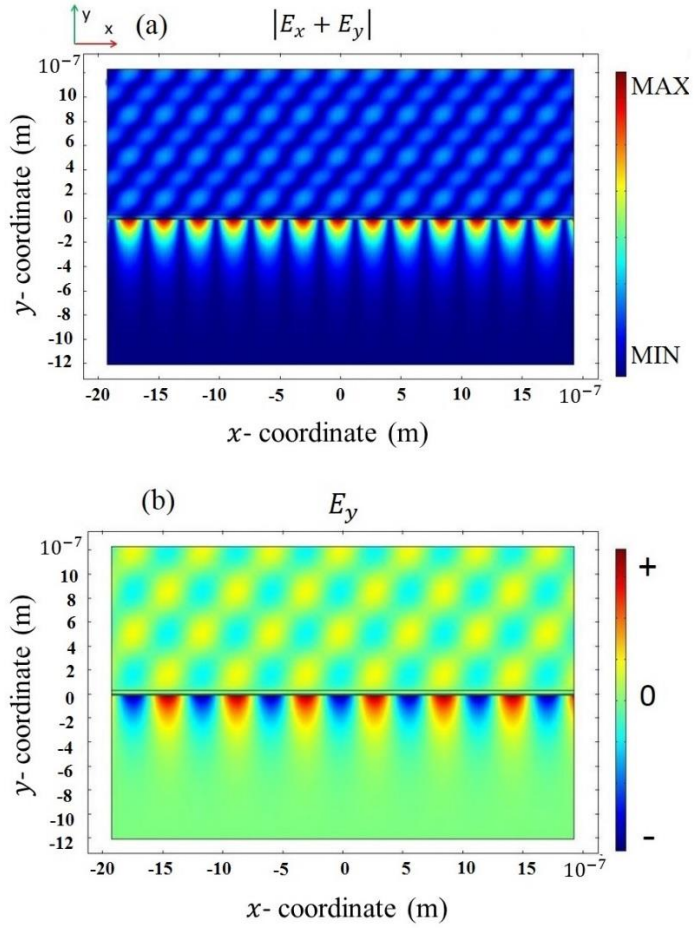

Fig. 1-9 Map of magnitude of the electric field, (b) the normal component ($\boldsymbol{E_y}$) of electric field.

Fig. 1-9 (a) illustrates the magnitude of the near-field intensity while Fig. 1-9 (b) shows the normal component of the near-field (E_y). Both these plots show the enhanced electric field bound at the gold-glass interface. This field enhancement is an important characteristic of surface plasmons at a metal-dielectric interface. The field enhancement is also shown in Fig. 1-10, where the normal component of the field along a cutline (shown in Fig. 1-7) normal to the gold-glass interface is plotted. The electric field shows an oscillatory behavior in the glass, but at the metal layer it is

coupled to the metal dielectric interface with significant field enhancement at the interface and exponential damping away from the interface.

Another method to couple light into surface plasmons is by diffraction of the incident light. The main technique is using plasmonic gratings, which is one of the major subjects of this thesis.

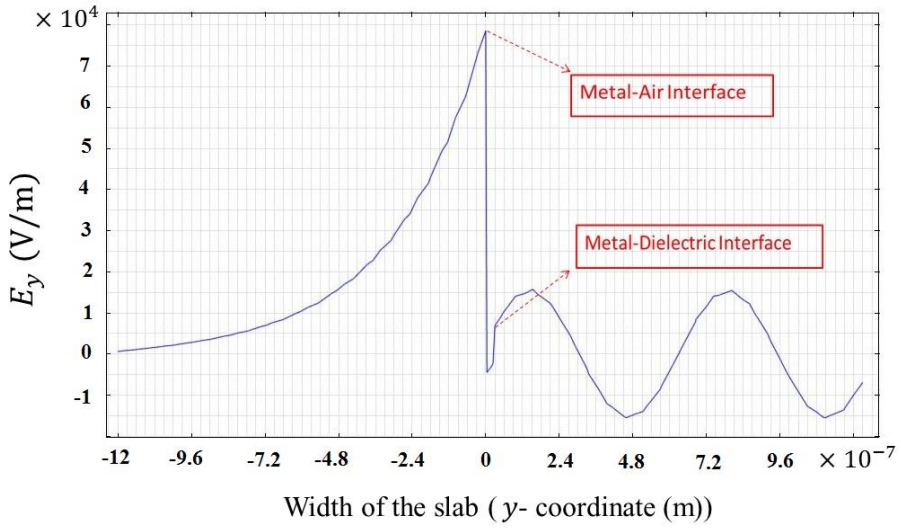

Fig. 1-10 The normal component of the electric field ($\boldsymbol{E_y}$) along the illustrated cutline in Fig. 1-7 (normal to the interface of gold-glass)

Box 1.3; Dielectric Constants for Metals

For frequencies smaller than ω_p ($\omega < \omega_p$) the dielectric constant of metals derived by the Drude model has a negative real part, as well as an imaginary part, which means metals retain their metallic properties. However, for frequencies greater than ω_p, the dielectric constant is positive. The treatment of the optical properties of metals assuming the free electron gas model (Drude model) gives accurate results for the optical properties of metals in the infrared wavelength region. For noble metals, interband transitions occur at visible frequencies, which limits the validity of the model in the visible. In our simulations, we use dielectric data obtained by experiment by Johnson and Christy [46].

1.2.2 Plasmonic Gratings

Photon tunnelling methods require out-of-plane elements (prisms for instance) which can be incompatible with desired lab-on-a-chip platforms and optoelectronic technologies. Nano-metallic antennas can also couple light into surface plasmons, but the antennas can suffer from high ohmic losses and low directivity of the radiation pattern [30, 31]. Hence, plasmonic gratings appear to be a practical technique to efficiently couple photons into surface plasmon modes on 2D platforms.

In optics, diffraction gratings are a set of regularly-spaced parallel variations in the refractive index, or periodic surface corrugations on an optical device. Metallic gratings (see Fig. 1-11) scatter the incident light and provide the extra required momentum for coupling light photons into surface plasmons. The wave-vector of the incident light, k_{in}, on a metallic grating couples into the crystal wave-vector of the grating, G, whose modulus is given by;

$$G = \frac{2\pi}{\Lambda_{gr}} \qquad \text{Eq. 1-7}$$

with Λ_{gr} depicting the grating period, as illustrated in Fig. 1-11.

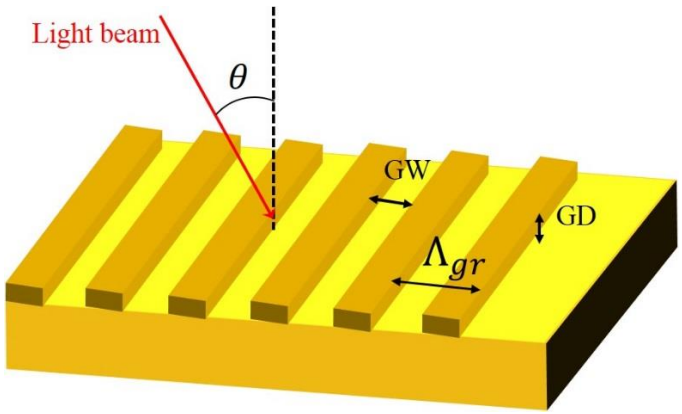

Fig. 1-11 Diffraction grating where Λ_{gr} is the grating period, *GW* is the groove width of grating, *GD* is the groove depth of the grating and θ is the angle of incidence for the light incident on the grating

Each diffracted order is associated with a wave-vector ($k_{(m)}$) given by;

$$k_{(m)} = k_{in} + m.G \qquad \text{Eq. 1-8}$$

where m is the diffraction order. The incident light couples into surface plasmons when the wave-vector of surface plasmons equals the in-plane wave-vector component

of a particular diffracted order. With the plane of linearly polarized (in-plane polarization) incident light parallel to the grating vector (G) equations 1-7 and 1-8 imply the following resonance condition;

$$k_{sp} = \frac{2\pi}{\lambda} n_i \sin(\theta) + \frac{2\pi}{\Lambda_{gr}} \qquad \text{Eq. 1-9}$$

in which λ is the wavelength of incident light and θ and n_i depict the incident light polar angle and the refractive index of the dielectric medium facing the grating surface, respectively.

It is also possible to couple incident light into surface plasmons by dielectric materials. Surface plasmon excitation and propagation in structures made of a photoactive polymer layer deposited over a metal surface has been studied by numerical methods (FDTD) by Karpinski *et al.* [47]. The coupling through a sinusoidal surface relief grating formed on top of a polymer layer (deposited over a flat gold layer) was compared with the coupling via the rectangular ridges of a grating etched directly into the metal layer. Their optimized geometrical parameters for the polymer relief grating suggest that the efficiency of the dielectric grating is comparable with similar gratings made in metals.

Surface plasmons are tightly bound to the metal-dielectric interface and extend only nanometer distances into the dielectric medium. Therefore, the geometrical parameters of the plasmonic gratings affect both the efficiency and quality of incident light coupling to surface plasmons. Coupling efficiencies in excess of 60% have been predicted by theory and simulation, however, they require the use of elaborate

geometries, such as slanted [48], sinusoidal [49], and variable-width grooves [50], that are difficult to fabricate in practice. For instance, in reference [50] numerical simulation by COMSOL was used to show 50% coupling of an incident light beam with a free space wavelength of $\lambda = 476$ nm and beam spot size of 1 μm to surface plasmons using an optimized geometry of a variable-width groove plasmonic grating. Koev et al. [51] optimized two important geometrical parameters of surface relief plasmonic gratings, the groove width (GW) and the groove depth (GD), to improve the coupling efficiency of the gratings. Koev et al. assumed that the scattering of incident light at the grooves increases monotonically with groove width and depth. Based on this assumption they conclude that an optimized value of groove width and depth needs to be selected so that the radiative surface plasmon propagation loss in the grating is equal to the non-radiative absorption loss. After fabricating several gratings with different groove characteristics to optimize the structures, they report their best coupling efficiency of 45% for surface relief gratings. They also conclude that increasing the groove width and depth improves scattering and increases efficiency. However, very deep grooves would partly scatter out the coupled surface plasmons and thus would decrease the coupling efficiency. In fact, they achieve the best results for rather shallow grooves of 35 to 70 nm depth. They also show that choosing an unsuitable groove size for surface relief gratings leads to a drop in the coupling efficiency of an order of magnitude in comparison to the best achieved value.

In Chapter three we also study the impact of grating groove width and depth on the coupling efficiency for different kinds of plasmonic gratings (surface relief and trench gratings) using COMSOL simulations. The results show that the optimum value of the

groove width is half of the grating period, or equivalently, half the surface plasmon wavelength (according to Eq. 1-2 and Eq. 1-9). This groove width satisfies the phase-matching condition for constructive interference of the propagating surface plasmons excited from different grooves when passing across other grooves. The groove depth shows less sensitivity to phase and can be treated in terms of the scattering strength of the incident light.

Bending the grooves of plasmonic gratings into a curve also changes their performance. In references [19, 52] circular gratings are used to focus surface plasmons into a focal spot at the center. The authors showed that to focus surface plasmons using circular gratings, (see Fig. 1-12), the grating must be illuminated with circularly polarized light in order to provide constructive interference between the counter-propagating surface plasmons from all around the circular grooves. Linearly-polarized light results in two hot spots along the direction of the light polarization and the resulting surface plasmons are not focused at the center of the circular gratings.

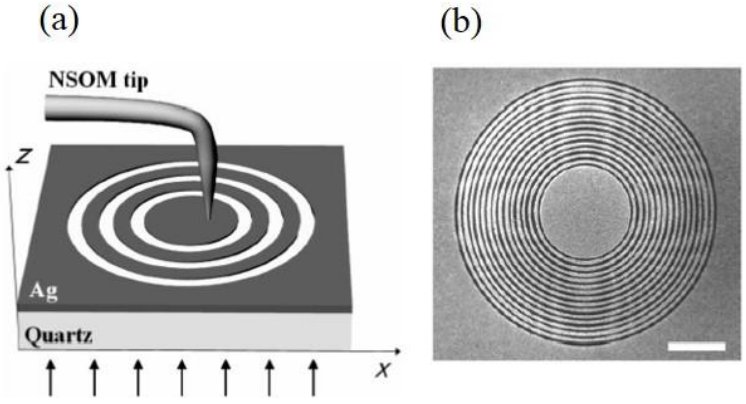

Fig. 1-12 (a) Schematic of a circular grating and the experimental method to detect the near-field intensity of surface plasmons (by NSOM), (b) scanning electron micrograph from the circular grating [19]. The scale bar is 5 μm.

Aligning the center of a circularly-polarized light beam with the center of the circular gratings is a challenging process in practice. In addition, full circular gratings are closed loops, and do not allow integration of coupled plasmons with other in-plane plasmonic components. In Chapter four, we investigate the use of curved gratings as a sector cut of complete circular gratings for coupling and focusing surface plasmons with linearly-polarized light. We show coupling and focusing of surface plasmons by curved gratings depending on their sector angle.

In reference [53] the application of semi-circular gratings for launching surface plasmons into nano-stripline dielectric-loaded-surface plasmon waveguides was investigated theoretically. Li *et al.* [53] showed that semi-circular gratings can focus and couple the excited surface plasmon polaritons into a $500\ \text{nm}$ wide dielectric-loaded plasmonic waveguide with a spatial field distribution which is well-matched with the waveguide mode. We also investigate the efficiency of launching surface plasmons onto micro-stripline waveguides with curved gratings in Chapter five of this thesis.

1.3 Graphene

Single or multilayer graphene is a two-dimensional (2D) form of sp^2 carbon atoms arranged in a hexagonal honeycomb lattice. Graphene is the strongest material known, with a Young's modulus (stiffness) of 1 Terapascal and breaking strength of $42\ \text{Nm}^{-1}$and it is a hundred times stronger than steel [54].

Graphene has also unique electronic and optical properties. It is a zero-gap semiconductor. The hexagonal honeycomb lattice of single atom thickness of graphene is formed by the overlap of π state (valence band) and π^*state (conduction band) at six points, which are termed Dirac points [55]. At low energies the bands have a linear dispersion expressed as $E_{n,k} = nv_f\hbar|k|$, with Fermi velocity $v_f = 10^6\, m/s$, n=1 conduction band and $n = -1$ valence band. The band structure can be considered as two cones touching (see Fig. 1-13) at the Dirac points (E_{Dirac}), indicating the zero band gap[56].

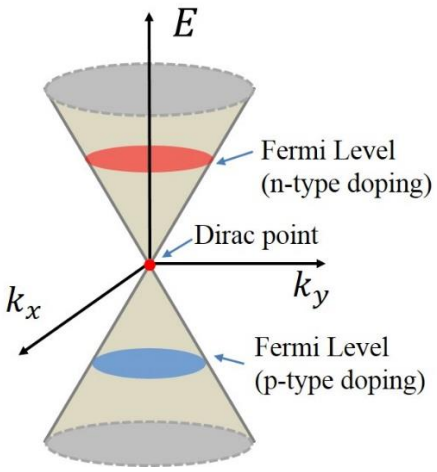

Fig. `1-13schematic of the band structure of graphene.

Graphene has also exceptional transport properties. The linear dispersion of electrons in graphene implies that the charge carriers in graphene have zero rest-mass and are treated as relativistic Dirac Fermions [57]. The charge carrier density significantly affects the mobility. Charge carrier mobilities higher than 1,000,000 $cm^2\, V^{-1}s^{-1}$ for suspended, exfoliated graphene with no substrate interactions [58],

and 100,000 $cm^2\,V^{-1}s^{-1}$ for ultraflat graphene on boron nitride have been reached [59, 60]. The latter is $10\times$ higher than that of InP HEMPT and $100\times$ higher than that for Si. Depending on the nature and purity of insulators, such as amorphous SiO_2, the charges on insulator graphene have a significantly lower mobility in the range of a few thousand $cm^2\,V^{-1}s^{-1}$. However, besides this exceptional charge mobility in graphene, the charge carriers have to be injected into and collected from graphene through chemical doping or electrical gating (metal contacts). The resulting free carriers arising from the doping (electrical gating or chemical doping) can reach around $0.001-0.01$ per atom, consistent with a doping concentration of 1×10^{12} to $1\times10^{13}\ cm^{-1}$ [61]. A higher free carrier concentration of 0.1 per atom, which translates to a chemical potential of $E_f=1$ eV, is achievable by solid electrolyte gating [62]. However, these values are significantly smaller than that of 1 per atom for noble metals. In the case of metal contacts, the charge carriers are transferred by generating potential energy barriers due to different work functions of graphene and metal.

At a finite doping, graphene has a characteristic absorption spectrum with its different optical transition process (optical conductivity). At terahertz frequencies (below $2E_F$) the optical transition is mostly attenuated to inter-band absorption of free carriers (Drude peak response). At near-infrared to visible frequencies the linear dispersion of the band results in direct inter-band transitions and light transmission through free-standing single mono-layer graphene can be calculated by using Fresnel equations. Assuming that only inter-band (vertical) transitions are allowed, the transmission can be calculated as [63,64];

$$T = (1 + \pi\alpha/2)^{-2} \approx 1 - \pi\alpha = 0.977 \qquad \text{Eq. 1-10}$$

where α is the fine structure constant. This transmission is independent of the illumination wavelength and shows that single mono-layer graphene absorbs 2.3% of illuminated light. This is relatively large for a single atomic layer, but small in terms of interaction of light with matter. This absorption can be modulated by an external gate field, or in other words, by changing the doping of graphene [65]. In fact, the electric field shifts the Fermi level from the Dirac point (ΔE_F) and inter-band absorptions within the range of $2\Delta E_F$ are blocked. Finally, in the mid-infrared regime the optical conductivity is dominated by Pauli blocking. However, some residual absorption which is detected in experiments is attributed to disorder. The characteristic schematic of graphene absorption is illustrated in Fig. 1-14.

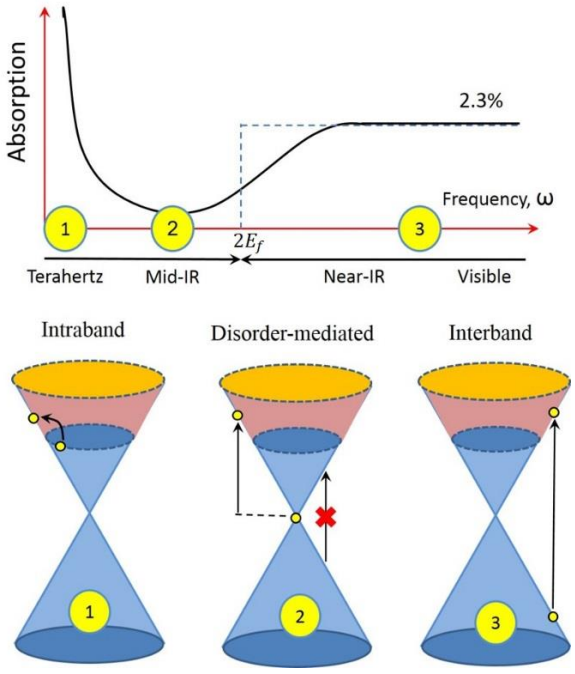

Fig. 1-14 Characteristics of light absorption by graphene. The illustration is replicated from reference [66]

1.3.1 Characterizing graphene by Raman spectroscopy

Raman spectroscopy is an ideal tool for characterizing graphene since it is fast, non-destructive, and has high resolution that can provide structural and electronic information of graphene samples [67-69]. The Raman spectra of graphene layers shows common features in the $800 - 2000\ \text{cm}^{-1}$ range with characteristic G and D peaks around 1560 and $1360\ \text{cm}^{-1}$, respectively. The G peak is related to high speed E_{2g} phonons at the Brillouin zone centre while the D peak corresponds to the breathing modes of sp^2 atoms (six atom rings) activated with defects. However, the most informative Raman spectroscopic feature is the second order D peak; 2D, which lies at around $2700\ \text{cm}^{-1}$. The 2D peak is always present in the Raman spectrum of graphene samples since it originates from a process where momentum conservation is satisfied by two phonons with opposite wave vectors and does not require defects for activation. The Raman spectrum can be used to calculate the number of layers, doping concentration, charge carrier mobility and edge effects.

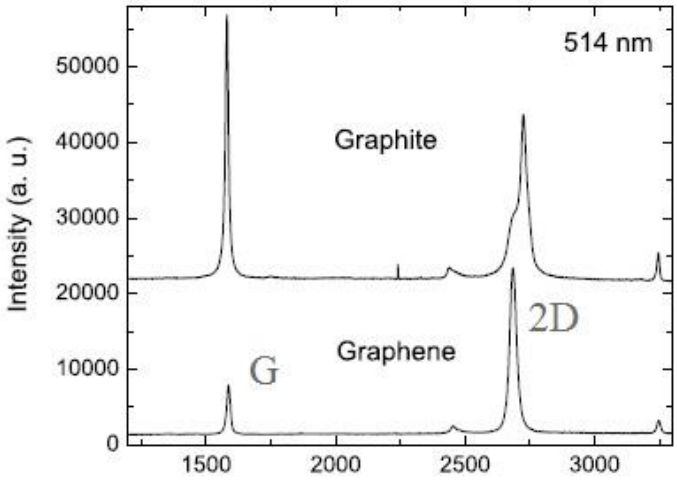

Fig. 1-15 Raman spectra of graphene and bulk graphite from reference [68]

Fig. 1-15 compares the 514 nm G peak and 2D peak of the measured Raman spectra of graphene and bulk graphite taken from reference [68]. The D peak is not present in this spectrum, as for a defect-free sample, the D peak can be observed only at the sample edges. The G peaks in graphene and graphite have comparable intensity, however, the position of the G peak is $3-5\ \mathrm{cm}^{-1}$ upshifted in comparison to that of bulk graphite. Note that in Fig. 1-15 the intensities of the peaks are rescaled to show identical peak intensities for the 2D peaks of graphene and graphite. The 2D peak of the graphene sample is four times more intense than the G peak while the 2D peak of graphite is lower in intensity in comparison to the G peak. In addition, the 2D line in single or multilayer graphite is broader and is up-shifted.

Doping single layer graphene sheets also has a significant effect on their Raman spectra. For both electron- and hole- doping, the G peak blueshifts with doping, However, the position of the 2D peak can be redshifted or blueshifted, corresponding to electron (n) or hole (p) doping [70, 71]. In addition, the full width at half maximum (FWHM) of the peaks and also the ratio of the peak maxima of the 2D and G peaks I(2D)/I(G) is a maximum for zero doping and decreases by increasing the doping level. Therefore the ratio of the area (A) of 2D and G peaks (A(2D)/A(G)) is a good representation of the doping level as it incorporates trends in the ratio of intensities and FWHM of the 2D and G peaks. That is, a decrease in the ratio of A(2D)/A(G) translates to an increase in the doping level of the graphene sheet [71-73].

1.3.2 Graphene plasmonics

Graphene supports plasmons with unusual properties. Plasmons in graphene are tunable by chemical doping or electrical gating. A sufficiently increased level of doping pushes the inter-band threshold frequency (ω_{inter}) towards higher values and consequently blocks the plasmon decay channel through inter-band losses which occur via emission of electron-hole pairs (first order process). To deactivate the second order process (the plasmon decay channel via emission of an optical phonon together with an electron-hole pair), the photon frequency must be smaller than the optical phonon frequency, $\hbar\omega_{Oph} \approx 0.2$ eV [56]. This can result in plasmons with low loss and significant wave localization. As a result, the optical loss can be suppressed at mid-infrared wavelengths for suitably doped graphene. The Drude model can be applied, by assuming zero temperature ($T \approx 0$) as a good approximation for highly doped graphene with $E_f \gg k_B T$, to derive the dispersion relation of single graphene for the transverse magnetic (TM) mode [56,74];

$$\beta(\omega) \approx \frac{\pi\hbar^2\varepsilon_\circ(\varepsilon_{d1}+\varepsilon_{d2})}{e^2E_f}\left(1+\frac{i}{\tau\omega}\right)\omega^2 \qquad \text{Eq. 1-11}$$

where β is the in-plane wave-vector of plasmons in graphene, $\varepsilon_{d1}$and ε_{d2} are the dielectric constants of the material below and above the graphene, τ is the carrier relaxation time and E_f is the absolute value of Fermi energy level. The carrier relaxation time is proportional to the carrier mobility μ from $\tau = \mu E_f/eV_f{}^2$. The loss of the propagating surface plasmons is proportional to the relaxation time, and is

shown as the ratio of the real part of the surface plasmon wave-vector to the imaginary part;

$$\frac{\mathcal{R}_\beta}{\mathcal{I}_\beta} = \omega\tau = \frac{2\pi c\tau}{\lambda_{air}} \qquad \text{Eq. 1-12}$$

This implies that the relaxation time must be quantified to estimate the loss of the surface plasmons in graphene.

1.3.3 Graphene photodetectors

The unique optical and electronic properties of graphene, such as field control of the graphene layers, high conductivity, light transmission and broad-band response suggest that it is an appealing material for photonics and optoelectronics applications such as solar cells [75,76], touch screens [77], and light emitting diodes [78]. In particular, significant effort has been devoted to investigate the application of graphene-based photodetectors. Graphene has a zero bandgap which enables photo-excitation of charge carriers over a very wide energy spectrum from the ultraviolet (UV) to terahertz (THz) spectral regimes. Graphene also exhibits low decay rates and high mobility of charge carriers which results in ultrafast conversion of photons or plasmons to electrical current or voltage [79,80]. Moreover, electrostatic doping can control the optical properties of graphene [81,82].

Photo-detectors measure optical power by changing the energy of absorbed photons into electrical energy. The dominant mechanism in most photodetectors is based on the absorption of light photons to excite charge carriers from the valence band to the conduction band, resulting in the flow of electric current. Several different

mechanisms have been proposed and demonstrated to convert absorbed photons to electrical signals. These include the photovoltaic effect, photo-thermoelectric effect, bolometric effect, and photo-gating effect.

Graphene-based photocurrent generated by the photovoltaic effect is the result of the separation of photo-generated electron-hole (e-h) pairs by the built-in electric field between differently doped (p-type and n-type) sections of graphene or at junctions [83-85, 36]. It is also possible to separate the e-h pairs by applying an external electric field as a source-drain bias voltage (V_{bias}). However, this can result in a large dark current since graphene is a semimetal.

Different ways of introducing a built-in field include local chemical doping [86], the use of split gates (with the ability to switch the doping between p or n) [83], or by work-function differences between graphene and metals at their contacts (with fixed doping at the contacts) [85,87]. For metals with a work-function higher than graphene (4.4 eV) the doping at the contacts is typically p-type while the graphene channel can be either p-type or n-type.

Graphene photodetectors based on any of the above-mentioned photo-detection mechanisms suffer from several problems. The first is the low light absorption of graphene monolayers. The 2.3% absorption is very high for a single layer of graphene but very small in absolute terms. Furthermore, in the case of a built-in field caused by the different work-functions of the metal-graphene contacts, extraction of the photo-electrons is very inefficient since only a small area of the p-n junction contributes to the current generation [37, 88-90].

One method to increase the efficiency of the photo-response of graphene photodetectors is to use the field enhancement resulting from the excitation of surface plasmons via plasmonic structures. The combination of graphene with nano-structures was first used to achieve surface-enhanced Raman scattering [91] and also to realize strong field enhancement within sub-nanometre gaps [92].

Strong plasmonic enhancement of the photo-voltage by combining graphene with plasmonic nano-structures (see Fig. 1-16) has been reported by Echtermeyer et al. [37]. Though these authors fabricated several different plasmonic nano-structures of titanium and gold (3 nm Ti , 80 nm Au), they report the best performance using a grating with 110 nm finger width, and 300 nm pitch.

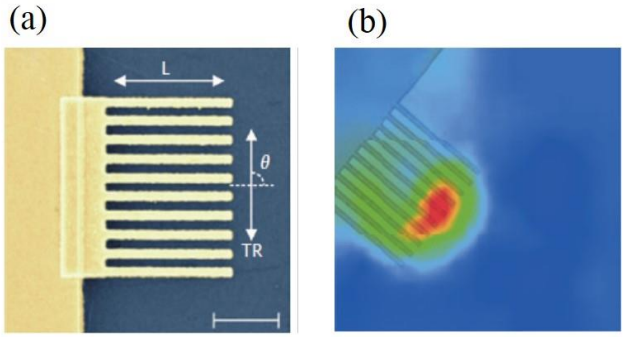

Fig. 1-16 (a) Graphene contact with a finger structure (plasmonic grating), longitudinal and transverse light polarizations are shown with L and TR, respectively [37]. The scale bar is 1 micron, (b) photo-voltage map of the structure

There was an observable enhancement of the photo-voltage at $457, 488, 514, 633,$ and 785 nm wavelengths. However, the maximum enhancement of up to 20 times occurs at the resonant wavelength of the nano-plasmonic structure. The wavelength dependence of the enhancement is attributed to efficient field concentration in the area

of the p-n junction by plasmonic resonances, and not just the geometric enlargement of the junction for nano-structured contacts. The observed enhancement also shows a strong dependence on the polarization of the incident light, proportional to $\cos^2(\theta)$, which also confirms the plasmonic enhancement of the photo-voltage.

Oligomer plasmonic nano-antennas (a nanomer consisting of eight disks surrounding a central larger disk, see Fig. 1-17) fabricated on graphene have been used to dope graphene by hot electrons from the excited surface plasmons [93]. A larger doping efficiency is reported for n-type graphene in comparison to p-type graphene for this configuration of nano-antennas. In addition, the doped carrier relaxation time scale is of the order of microseconds, which enables its application as an active optoelectronic material for photodetectors.

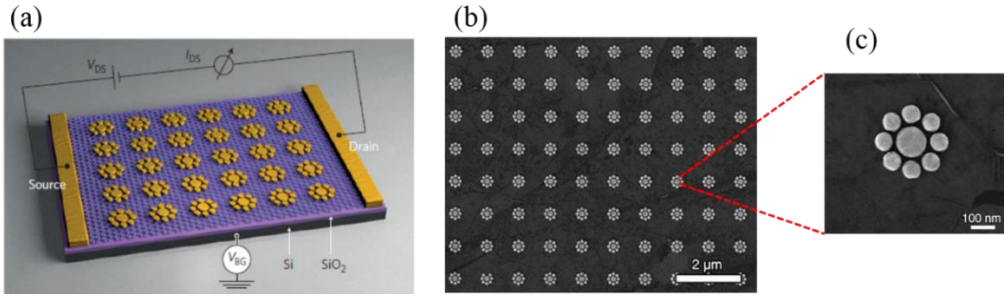

Fig. 1-17 (a)schematic of plasmonic oligomer nano-antenna on single layer graphene, (b) scanning electron micrograph of array of antennas and (c) a magnified scanning electron micrograph of one of the oligomer antennas [80]

Later the same research group [38] also demonstrated the use of the above-mentioned oligomer antennas, sandwiched between two graphene monolayers as illustrated in Fig. 1-18, as a graphene-based photodetector for converting visible and near infra-red photons into electrons with an 800% enhancement of the photocurrent

in comparison to a similar photodetector with graphene layers but without the antennas.

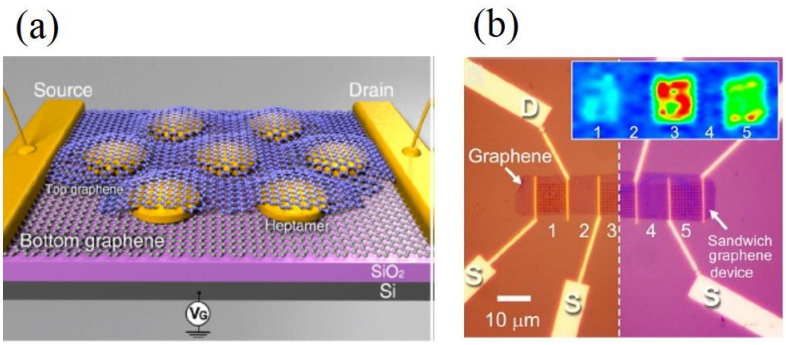

Fig. 1-18 schematic illustration of nano-antenna sandwiched between two graphene layer, (b) optical microscopy image of the fabricated structure [38]

In a very recent research report [94] a planar graphene-based plasmonic photodetector has been investigated, Fig. 1-19. In this device, a long narrow graphene strip extended along the device structure to serve as a plasmonic waveguide. The horizontally-coupled light into the graphene strip waveguides propagated as graphene surface plasmon waves which excite electron-hole pairs at the junction with the graphene photodetector. The Schotky-like barrier effect at the interface of the metal and graphene photodetector resulted in the separation of electron-hole pairs by the external electric field. At 1550 nm wavelength with 38 mW optical input power an average of 3.16 μA photocurrent was recorded. This configuration is proposed for the application of photonic integrated circuits.

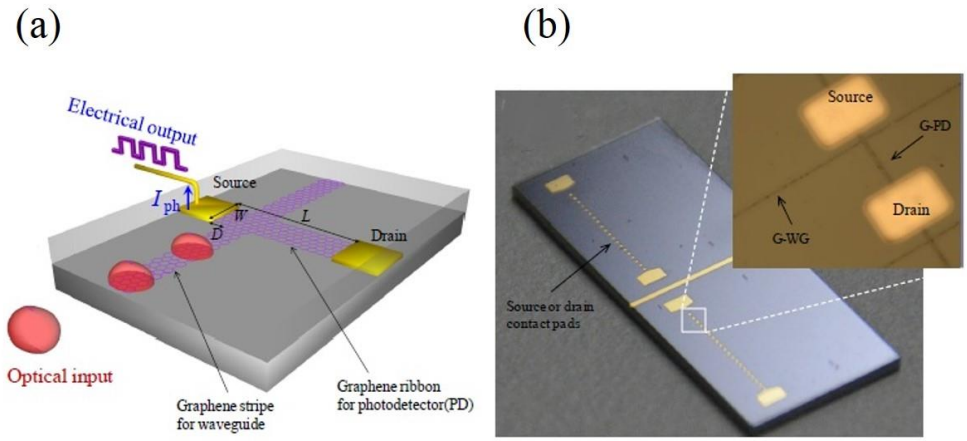

Fig. 1-19 schematic view of the planar graphene-based photodetector, (b) fabricated device, the images are taken from reference [94]

In Chapter seven we propose the use of single layer graphene integrated with curved gratings to enhance photocurrent detection in such a device.

1.4 Light scattering by passive spherical particles

The near- and far-field description of scattering of light by very small particles was developed historically in electrodynamics. However, until recently the near-field description was not accessible experimentally. Advances in nano-photonics and plasmonics have resulted in fascinating developments in the field of scattering of light by small particles, including metal particles and surfaces, where the excitation of localized surface plasmons leads to optical resonance phenomena [2, 95, 96].

Interaction of light with metallic nano-particles can result in subwavelength localized surface plasmons as collective oscillations of the conduction electrons at the interface of the metal nano-particles and the dielectric. Metallic nano-particles can

operate as nano-antennas and transfer the localized electromagnetic energy (surface plasmons) from the near field to the far field and vice versa [25]. However, due to high non-radiative relaxation rates of metallic nano-structures in vicinity of emitters and also the dependence of the directionality of radiated power from the metallic nano-antennas on the large number of nanoparticles, which increases the ohmic losses, dielectric nano-antennas have been proposed and investigated as an alternative for nano-metallic antennas [30, 33, 34].

Dielectric nano-antennas have been proposed and investigated as an alternative for metallic nano-antennas [30]. Dielectric particles have lower loss in comparison to metallic particles. It has been suggested that high permittivity dielectric nano-antennas may support both electric and magnetic resonance modes. Furthermore, a judicious combination of dipole emitters with high refractive index dielectric spheres has been investigated to generate highly directional emission with negligible backward scattering and no polarization dependence [31, 32-34, 97], and to efficiently collect light without spoiling the emitter quantum efficiency [30].

Devilez et al. [30] demonstrated (with numerical calculations) directional radiation by TiO_2 microspheres in the vicinity of a dipole emitter. They showed that a TiO_2 microsphere of 500 nm diameter can perform as an optical antenna and redirect the dipolar radiated power into a narrow beam with an angular radiation distribution of 25° full width at half maximum over a large frequency bandwidth. In addition, they demonstrated the presence of whispering gallery modes (WGM) as electromagnetic resonances, resulting from the high refractive index of the microsphere. They also

concluded that the WGM resonance does not reduce the strong directional properties of the microspheres illuminated by the dipole. However, WGMs can slightly enhance the radiative decay rates of the antennas.

In this research thesis, we investigate the interaction of TiO_2 dielectric microspheres with the evanescent field of propagating surface plasmons. The majority of this study was performed as simulation of the physical configuration, however, experiments were also performed to show the radiation of the microspheres when interacting with propagating surface plasmons.

Chapter 2: Methodology

2.1 Simulations using COMSOL

Many reports on plasmonic phenomena rest on the results of simulations. Since fabrication and characterization setups are quite challenging for nano-plasmonics, simulating the performance of structures to optimize their characteristics, or even investigating the underlying physical phenomena, can save time and money. Furthermore, experimental results may be more easily interpreted using simulations of near-field and far-field radiation from plasmonic structures.

This chapter concerns simulations of a variety of proposed plasmonic structures, and these are also compared with experimental measurements in subsequent chapters. The simulations have been done with the finite element method using COMSOL software. Discretisation of domains of the structures is a critical aspect of the finite element method simulations to increase the accuracy of the simulations and observe appropriate plasmonic effects. Since the size of plasmonic structures is in the range of several micrometres, it is important to make efficient models in order to decrease the required time and memory. The first sections of this chapter discuss methods to improve the efficiency and accuracy of models of plasmonic devices using COMSOL software. In addition, it is also important to analyse the results of the models to confirm the plasmonic effects and to optimize the characteristics of the structures.

2.1.1 The Finite Element Method

To investigate the physical properties of surface plasmons for a simple configuration we need to apply the Maxwell equations to the boundaries of a metal and a dielectric appropriately. This requires us to obtain the propagating electromagnetic wave equations from the fundamental Maxwell equations. By manipulating the Maxwell equations, we obtain the Helmholtz equation [98];

$$\nabla^2 E + {k_0}^2 \varepsilon E = 0 \qquad \text{Eq. 2-1}$$

The Helmholtz equation is the starting point for analysing the electromagnetic modes of surface plasmons in different configurations. For simple structures, such as the flat interface of a metal and a dielectric, it is possible to obtain analytical descriptions for the propagating electromagnetic waves bound to the interface. However, an analytical solution can be achieved only for a few simple problems, and more complex geometries require numerical approaches to solve the corresponding boundary-value problems.

The finite element method is a numerical technique to solve boundary-value problems of mathematical physics with good accuracy [99]. The method was proposed in the 1940's and was first used in the 1950's for structural design. It has been developed and increasingly applied to engineering and mathematical problems from that time.

On a physical boundary Γ (Fig. 2-1 is an appropriate example of a physical boundary, including all possible geometries such as straight line, curves and corners

and loops enclosing a domain Ω) a typical boundary-value problem can be defined by the related governing differential equations as;

$$\hat{O}u = f \qquad \text{Eq. 2-2}$$

in which $\hat{O}$ is a differential operator, u is the unknown quantity, and f is the excitation or forcing function. On each boundary one must specify either:

1) The values that a solution (u) needs to take along the boundary of the domain or Dirichlet boundary condition,
2) The value that the derivative of the solution (du/dn, with n normal to the boundary) is to take on the boundary of domain, or Neumann boundary condition,
3) The relationship between the solution and its normal derivative

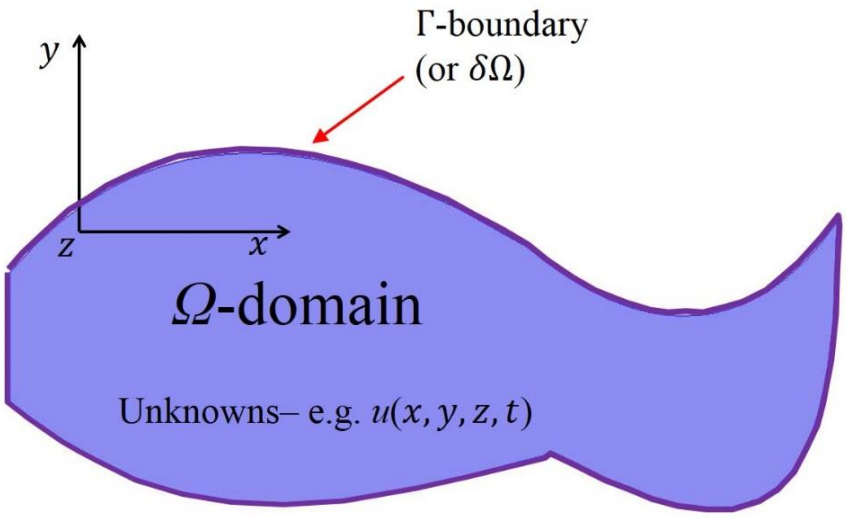

Fig. 2-1 An example of a physical boundary

The principle of the finite element method is to replace the entire continuous domain Ω by a number of subdomains. In this way, the unknown differential function is characterized by simple interpolation functions with unknown coefficients. As a result, the solution is approximated with a finite number of unknown coefficients. At the next step, by applying an approximation method, such as the Galerkin method, a system of algebraic equations is obtained and the final solution is achieved by solving the system of equations. There are different methods of approximations, however, the Galerkin method is better suited for a general purpose program to deal with arbitrary boundaries and many different problems, (see Box 2.2 for more details on the Galerkin method and its related references).

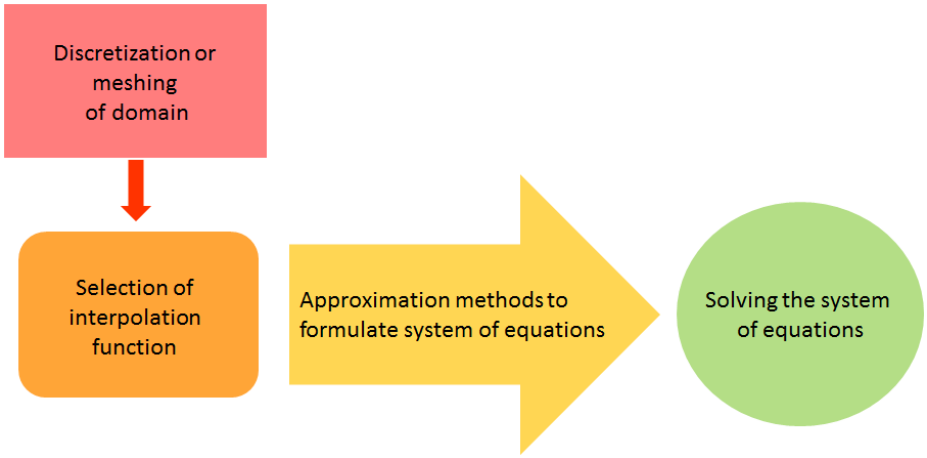

Domain discretisation of the boundary Ω is the first and perhaps the most important step, as the way the domain is discretised has an important impact on computer storage requirements, calculation time and the accuracy of the calculated results. Discretisation involves dividing the entire domain into small domains which are called elements. The elements of a one-dimensional domain (a straight or curved line) are short-line segments interconnected to form the original line. The line elements change to triangles or rectangles for a two-dimensional domain. Rectangular segments are best suited to rectangular sections and the triangular segments are best suited for irregular geometries. The main discretisation elements in a three-dimensional geometry are tetrahedral, triangular prisms, and rectangular bricks, all shown in Fig. 2-2. Among these, tetrahedral segments are the simplest and more adaptable for arbitrary volume domains.

Fig 2-3 shows how the arbitrary physical domain in Fig. 2-1 is properly discretised at corners, straight lines and curves with triangular elements.

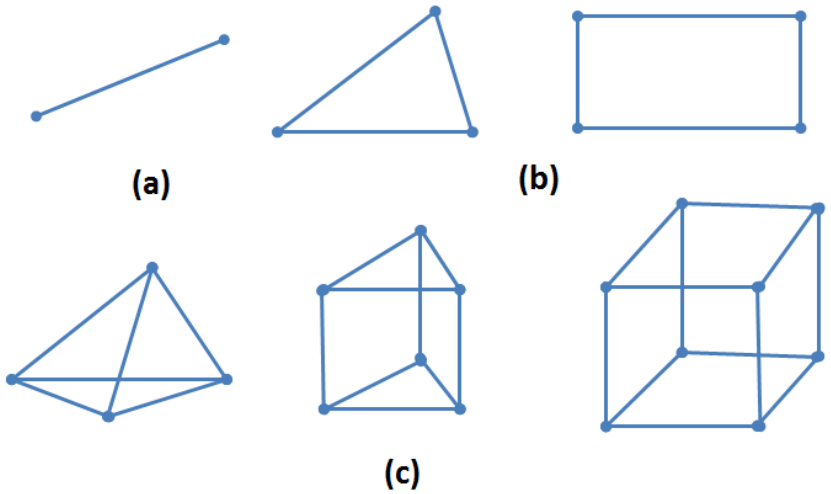

Fig. 2-2 Geometrical elements for discretising physical domains (a) straight line for one dimensional domains, (b) rectangles or squares for two dimensional problems, (c) tetrahedral, triangular prisms, and rectangular bricks for three dimensional domains.

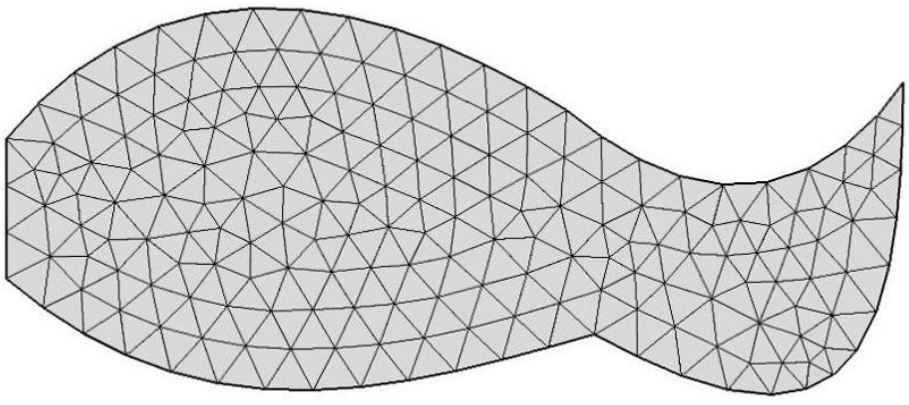

Fig. 2-3 Meshed arbitrary physical domain in Fig. 2-1 with triangular elements

Box 2.1: Galerkin method

The second step of the finite element method numerical calculation is to select an interpolation function to derive an approximation of the unknown solution within an element. Usually, a polynomial of first (linear), second (quadratic) or higher order is selected. By increasing the order of polynomials, the accuracy of the solution increases, but it can lead to a more complicated formulation. The third step is to formulate the system of equations by one of the approximation methods. Among these approximations, the Galerkin method is recognized to be suited for a range of problems.

The Galerkin method is a weighted residual method, which tries to find solutions by weighting the residual of the differential equations. According to equation 1-2, if we assume that $\tilde{u}$ is an approximate solution, then the residual r (defined below) would be nonzero:

$$\boldsymbol{r = O\tilde{u} - f \neq 0}$$

The best approximation of $\tilde{u}$ must minimize the residual r at all points of the domain, or in other words a weighted residual on the whole domain would be zero:

$$R_i = \int_{\Omega} \omega_i r d\Omega = 0$$

in which R_i denotes the weighted residual integral and ω_i are the weighting functions. In the Galerkin method, the weighting functions are selected to be the same as those used for the expansion of the approximate solution. The Galerkin method is presented in detail in reference [99].

2.1.2 COMSOL platform for modeling

COMSOL multiphysics uses finite element methods (FEM) to analyse and simulate various physics models, in particular, coupled physical phenomena [100]. The radio frequency (RF) and optics modules solve problems in the field of electromagnetic waves, optics and photonics. The physics interfaces cover in-plane, axi-symmetric and full 3D electromagnetic wave propagation, together with a full vector model analysis in 2D and 3D.

2.1.3 Frequency domain approach:

There are two main approaches to model time-varying electromagnetic waves. The simpler approach is to calculate the evolution of the system with time. However, in the case of very small time steps this method can be very time consuming, and demands high memory capacity. For transient time problems, such as turn-on and turn-off responses, it is necessary to calculate each time step.

However, by calculating the phasor form of the electromagnetic waves in the frequency domain, one can efficiently simplify the solution and assume that all variations in time occur as sinusoidal signals. The frequency domain computes the response of a linear or linearized model exposed to a harmonic excitation at a defined frequency. In electromagnetics, the frequency domain is used to compute the transmission and reflection versus the frequency. All the models in this research thesis are made in the frequency domain. The two crucial parts of any defined physical system in the frequency domain are the meshing of the physical domain and definition

of the domains of the physical system by ports, scattering boundary conditions and perfect matching layers (PML).

2.1.4 Meshing criteria

COMSOL applies the finite element method to compute simulations of the behaviour of a given device. In the finite element method, the accuracy of the solution depends on the mesh size. As the mesh size is decreased, a more precise solution of the physical equations is approached. However, any simulation is limited by finite computational resources and time, and one can obtain an approximation of the real solution by defining an optimized meshing size. In the frequency domain, acceptable results can be obtained with a mesh size of the physical system of less than one third of the applied free space electromagnetic wavelength. One needs to optimize the meshing of the physical system to balance the simulation accuracy against the memory and time available. In the simulations of this research thesis all the mesh sizes are less than one fifth of the applied wavelength, and in most cases the mesh size is even smaller.

2.1.4.1 Domains of a physical object and ports

In frequency domain simulations, the domains of a physical system need to be defined appropriately to allow electromagnetic waves to enter or pass through the domain. Different ports and boundary conditions are defined for electromagnetic waves in the frequency domain simulations for use in different situations. The main ports and boundary conditions used in the simulations of this research project are input or output ports, periodic boundary conditions, and scattering boundary conditions.

Ports are used where electromagnetic waves enter or exit the system, for example for excitation. The “periodic boundary condition” is used to make equal solutions for boundaries which are equally shaped. In this thesis, the Kretschmann configuration for coupling incident light into surface plasmons through a prism, and investigating the plasmonic resonance at the gold-air and gold-glass interfaces, is simulated using periodic boundary conditions for the right and left sides of the domains. One can use scattering boundary conditions as transparent boundaries to let scattered waves exit the domains with minimal reflections back into the unit cell. This boundary condition is perfectly transparent for scattered waves that are at normal incidence to the boundaries, and it partly reflects waves at oblique incidence angles. However, for most simulations, this is an acceptable boundary condition. An alternative for this boundary condition is to assume “perfect matching layers” which are absorbing layers that attenuate all waves that are incident on the layer, with no reflections. The “perfect matching layer” is a domain feature which allows the simulation of an infinite domain, in which any wave can propagate and disappear without reflecting back into the domain. Problems can arise in finite element simulations as one needs to limit the scale of the domain to save time and memory for the simulation. As a result, there is a trade-off between the use of scattering boundary conditions or perfect matching layers. For perfect matching layers one needs to make an extra unit cell for the model domains to cover the main unit cell. In this thesis, scattering boundary conditions are assumed for the simulations.

2.2 Near Field Scanning Optical Microscopy (NSOM)

The interaction of light with matter, such as a microscopy specimen, generates both far-field and near-field components of light. The far-field component propagates without restriction and is normally utilized in conventional optical microscopy, see Fig. 2-4.

According to Abbe's theory, the diffraction of light [101] at each point of the image ultimately limits the spatial resolution of an image, which is affected by the wavelength of the incident light, the numerical aperture of the condenser, and the objective lens. In theory, conventional optical microscopy has a limit of resolution of approximately half the wavelength of the illuminating light ($\frac{\lambda_\circ}{2}$ ~ 200 to 300 nm). The near-field component is bound to the surface of the sample within a distance of less than a wavelength and carries high spatial-frequency information about the object. However, the maximum amplitude of the near-field component occurs only a few nanometres from the surface of the object, and it cannot be detected by conventional microscopy techniques [102].

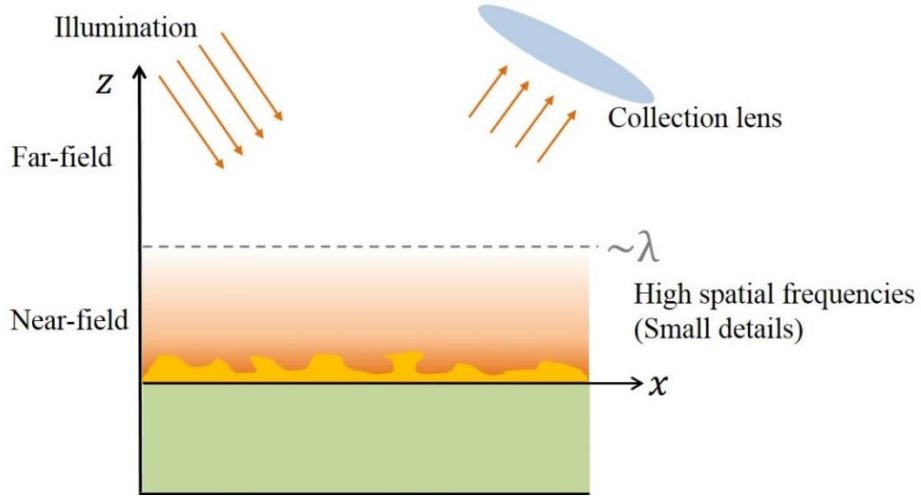

Fig. 2-4 Illumination of sample from the far-field and collection of the far-field radiation of the sample

In near field scanning optical microscopy, a subwavelength tip is placed very close to the surface of the nanostructure (much less than the light wavelength (λ), as illustrated in Fig. 2-5) to exploit the high spatial information from the non-diffracted evanescent field [103].

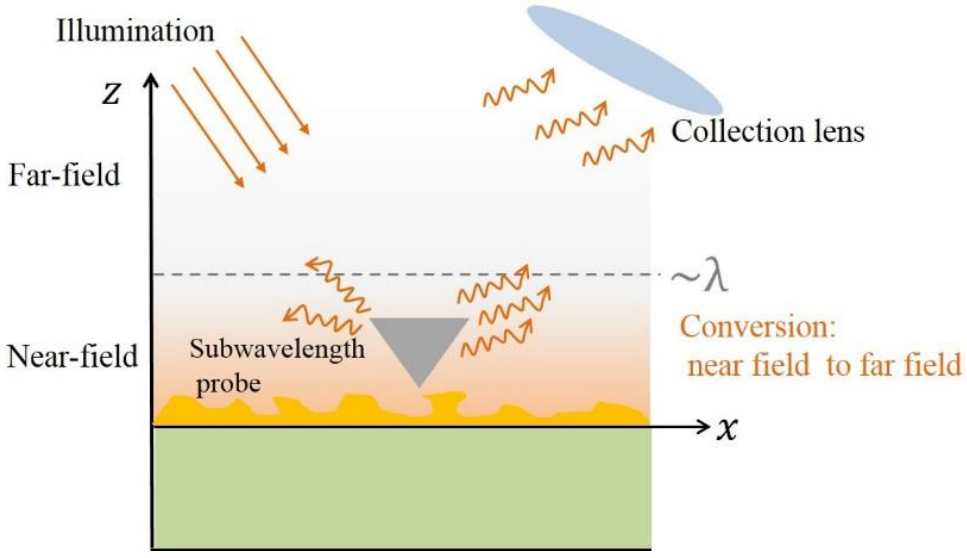

Fig. 2-5 The subwavelength tip scatters the near field radiation at the vicinity of the sample, to be detected in the far field

The concept of using near-field information for imaging was first introduced by Synge in 1928 [104]. Synge proposed the use of a sub-micrometre aperture in a plate to illuminate biological specimens at sub-micrometre distances above the aperture and then detecting the light from the specimen from the other side with a microscope objective. His idea was later implemented by different groups, Pohl et al. recorded subwavelength resolution optical images (detecting 25 nm details) of a test object using extremely fine apertures [105] followed by a report by Betzig *et al.* [106] achieving 12 nm surface resolution using near-field interaction of a sharp tip with the surface of a sample. The technique has been improving continuously and recently three-dimensional scanning near field optical microscopy has been reported [107].

Surface plasmons are electromagnetic fields bound to a metal- dielectric interface. Near field scanning optical microscopy (NSOM) exploits the high spatial frequency information of the surface plasmons in the near field, to provide high resolution scans of the nano-structure and field distribution at the structure. The NSOM technique has been used widely to characterise surface plasmons and a good review of the principles and applications of the technique can be found in reference [108].

2.2.1 NSOM instrumental configuration

Different techniques have been used for near field scanning optical microscopy [103]. In one technique, the sample is illuminated in the near field and the signal is collected in the far field. It is also possible to illuminate the sample in the far field and collect the signal in the near field, and in the third technique both illumination and signal collection occur in the near field.

The illumination or collection in the near field is through a near-field probe consisting of an optical fibre with a subwavelength aperture smaller than 100 nm. Far-field illumination and detection can be achieved using a microscope objective. Most NSOM instruments combine their near-field high resolution capabilities with conventional optical imaging modes by incorporating the NSOM into an inverted optical microscope. This arrangement delivers the capability to combine topographical data with the associated optical data, at sub-wavelength resolution. This is not achievable with conventional microscopy because of the limitations of diffraction of the focussed light.

2.2.2 NSOM instrumentation

The heart of a near field scanning optical microscope is the scanning system, which must have very small position fluctuations and precise positioning accuracy (within 1 nm) [102]. It is necessary to maintain the near-field probe at a constant distance from the sample surface so that first; any change in the optical response is attributable to the topography of the structure and not the structure-probe distance variations, and second; the probe is within the near-field domain, not contacting the surface. Such precise control necessitates the entire NSOM system to be placed on a vibration-isolated table to eliminate the transfer of vibrations into the NSOM system. In addition it is necessary to use low-noise electronics and large dynamic range amplifiers to drive the piezo-electric actuators of the probe.

An accurate tip-to-surface distance is achievable by using a controlled feedback mechanism. The two main feedback mechanisms for positioning NSOM tips are

optical methods which control the tip vibrations by interferometry, and the acoustic tuning fork method.

The acoustic tuning fork method is based on shear-force feedback, in which the probe is attached to a tuning fork, illustrated in Fig. 2-6 (a). The tuning fork oscillates laterally at its oscillation frequency with an amplitude of a few nanometres. When the probe approaches the surface of the structure, the interaction between the probe and the structure dampens the amplitude of the oscillations, which results in a phase shift of the resonance. The amplitude changes monotonically with distance within a range of 0-10 nm from the surface of the sample, and this amplitude can be used in a feedback loop to regulate the distance.

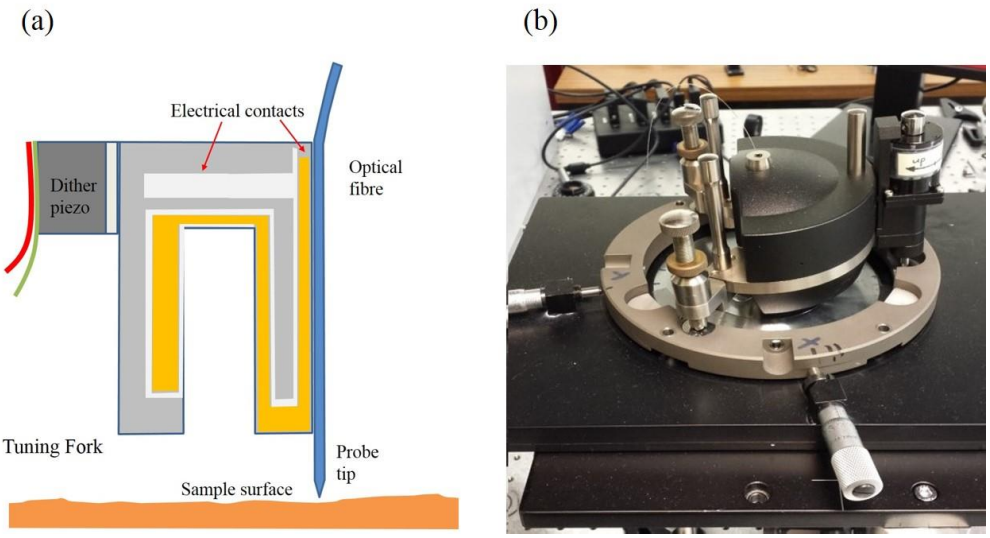

Fig. 2-6 (a) An illustration of the tuning fork [5], (b) NSOM head accommodated on microscope stage

The NSOM instrument (see Fig. 2-6 (b), NT-MDT NSOM head with controller model BL222RNTF) that was used in this research project works with the shear-force feedback mechanism, where the tip is maintained at a distance of 10 nm from the sample surface. The NSOM head is accommodated on the stage of an inverted microscope (Olympus IX81) and scans in collection mode, so that the optical fibre tip is above the sample and the illumination is through the microscope objective from below the sample.

Chapter 3: Optimizing Geometrical Parameters of Plasmonic Gratings

Plasmonic gratings scatter light at the grating grooves and couple the light into surface plasmons by providing the extra required momentum for the light photons. A more detailed discussion of the theory of coupling surface plasmons by plasmonic gratings is provided in Chapter one, and can also be found in the sources cited in that chapter. For an optimized design of curved gratings its important to optimize the grating parameters. This chapter concerns the optimisation of the grating geometrical parameters to design an efficient linear grating which can be extended to curved gratings.

The three important geometrical parameters of a plasmonic grating are the grating period (Λ_g), groove width (*GW*) and the groove depth (*GD*). Efficient coupling of surface plasmons by plasmonic gratings depends strongly on the choice of these parameters. We used simple theoretical guidelines for selecting the period of gratings, as discussed in Chapter one (Eq. 1-9). However, the role of groove width and depth has received less attention, in general. Therefore, we concentrate on the impact of these grating parameters on surface plasmon coupling.

Giannattasio et al. [109] experimentally investigated the role of the width of the grating grooves and they compared their results with theoretical calculations using Fourier analysis of the grating profile. They used the leakage radiation of the coupled surface plasmons to evaluate the coupling efficiency and concluded that the best coupling occurs for a groove width of half of the grating period ($\Lambda_g/2$). They also indicated that the depth of the grooves would influence the coupling efficiency. Koev et al. [51] have presented the impact of the characteristics of the grooves on coupling surface plasmons using experiment and theory. They used decoupling gratings at a distance from the coupling gratings to measure the coupling efficiency of the grating and determined the optimal groove dimensions experimentally by using the input grating intensity profile as an indicator of groove scattering strength. Moreover, they showed that the grating efficiency can be more than an order of magnitude lower if the groove dimensions are not chosen properly. Both of these reports concern surface relief gratings, in which the grooves are milled into the gold layer to a depth less than the metallic film thickness (Fig. 3-1 (b)). However, an alternative group of plasmonic gratings in which the depth of the milled grooves is equal to the thickness of the metal film on dielectric are termed trench gratings, (see Fig. 3-1 (a)). The selection of trench grating parameters has received less attention than surface relief gratings, and is presented in Section 3.1.1.

We assume that the coupling of surface plasmons to a curved grating obeys the same physics as the coupling of surface plasmons to linear gratings. However, the transverse magnetic component of linearly-polarized light drops proportional to the

cosine of the angle between the polarization direction and normal to the grating grooves at each point [110].

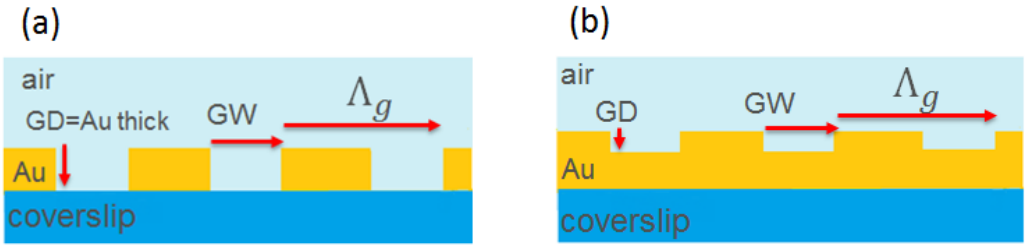

Fig. 3-1 (a) Trench grating: the groove depth is equal to the thickness of the gold layer, (b) surface relief grating: the grooves are partially milled into the gold layer and the groove depth is less than the thickness of the gold

Two different kinds of plasmonic gratings are investigated and compared in this chapter; surface relief gratings (Fig. 3-1 (a)) and trench gratings (Fig. 3-1 (b)). The incident, free-space light beam scatters at the grooves of the plasmonic grating, resulting in the local excitation of surface plasmons. For a specific wavelength of free space light at the correct angle of incidence and groove spacing, the excitations at different grooves interfere constructively, resulting in coupling of surface plasmons to the metal-dielectric interface [19]. At normal incidence the period of the grating is equal to the wavelength of surface plasmons; as a result, for $\lambda_0 = 810$ nm excitation, the grating period would be $\Lambda_g = 790$ nm. The simulations in this study are based on sweeping three parameters: groove width and groove depth and the excitation wavelength, to study the response of the grating at different wavelengths to the change in grating parameters; groove depth and width.

These simulations are calculated and run using COMSOL software in the frequency domain (Chapter 2). In order to simplify the calculations and also decrease

the required time and memory, the study of these parameters is done with two-dimensional models (2D) in which the third dimension, which is the length of the grooves (or width of the grating), would be considered infinite. The results of these optimizations provide the input parameters for the design of curved gratings.

3.1 Surface relief gratings

In a surface relief grating the grooves are partially milled into the gold film, Fig. 3-1 (b). Surface relief gratings are simulated in order to optimize their design parameters and compare their performance with trench gratings. The simulation is accomplished by illuminating a surface relief grating with six grooves from air (air-gold interface) with a plane wave at normal incidence, Fig. 3-2 (a), at wavelength $\lambda_0 = 810$ nm with dielectric constant; $\varepsilon = -24.9 + i\ 1.55$ [46]. The substrate material is glass with a refractive index $n = 1.52$ and the superstrate is air with $n = 1$. The geometry of the model is meshed with $\frac{\lambda_0}{2000}(4.0 \times 10^{-10}\ \text{m}) \leq$ element size $\leq \frac{\lambda_0}{50}(1.6 \times 10^{-8}\ \text{m})$ for the gold layer and the interface, and a coarser mesh $\frac{\lambda_0}{2000}(4.0 \times 10^{-10}\ \text{m}) \leq$ element size $\leq \frac{\lambda_0}{8}(1.0 \times 10^{-7}\ \text{m})$ for the remaining domains. We applied scattering boundary conditions for all boundaries. This means emission passing out of the cell is not reflected back into the cell (perfect absorption if the wave-vector of the incident light is normal to the boundaries of the cell and partial absorption for oblique incidence). The illumination port also extended over the grating length only, see Fig. 3-2 (a).

The intensity of electromagnetic waves is proportional to the square of amplitude of electric field ($I \propto |E|^2$). Since the various structures are made from the same materials with different geometries, we define the intensity of the surface plasmons as the square of the electric field amplitude of the confined electromagnetic waves at the metal-dielectric interface ($|E|^2$). In order to compare the results of different structures, the amplitude of the electric field of the illuminating light is selected to be the same for all structures.

The intensity of the coupled surface plasmons shows instability in the vicinity of the last grating groove, which can be attributed to the interference of the incident light with the surface plasmon waves. As a result, the coupling performance is assessed as the average of the intensity of the propagating surface plasmons at a position 11 μm from the last groove. This distance is less than the propagation length of surface plasmons at this wavelength ($L_{sp(\lambda=810nm)} = 48$ μm), but at the same time offers good stability for calculating the intensity of the surface plasmons. The average intensity of the surface plasmons is calculated by integrating the intensity of the norm of the near field along a cutline (with a length of twice the wavelength of the propagating surface plasmons, $2 \times \lambda_{sp} = 1.58$ μm, at 10 nm above the gold-air interface) and dividing it by the length of that cutline according to the following formula;

$$|E|^2_{avg} = \frac{1}{x_1 - x_2} \int_{x_2}^{x_1} |E|^2 dx \qquad \text{Eq. 1-1}$$

In which $x_1$and x_2 are the starting point (11 μm) and the end point of averaging process (11 μm + 1.58μm = 12.58μm).

Fig. 3-2 (b) shows the point (green arrow) in the model cell in which the average calculation starts in the simulation and the model cell. The cutline on which the average is calculated is also shown in a red colour in the schematic.

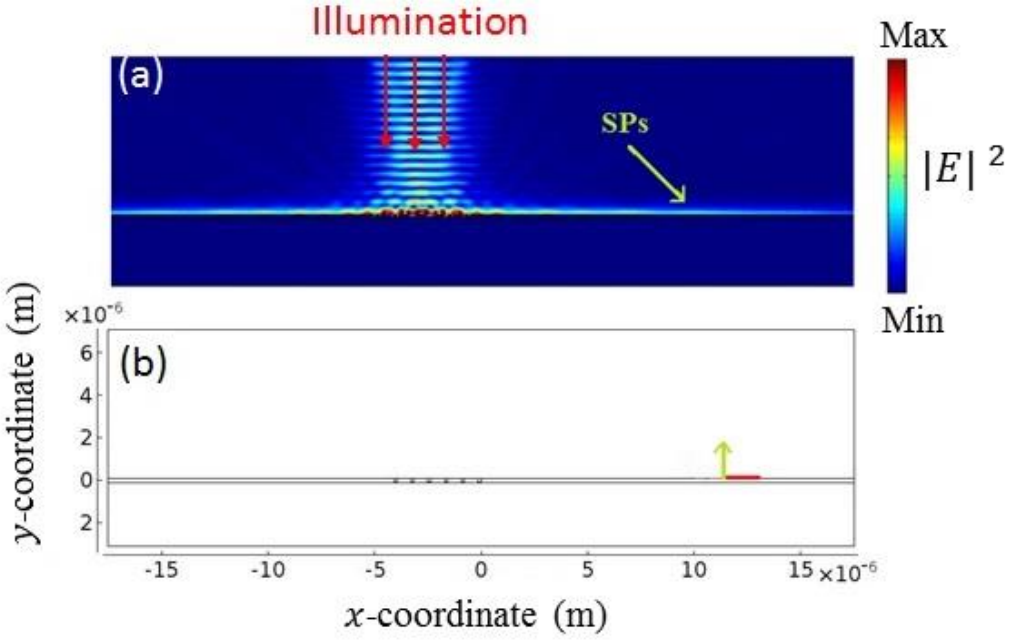

Fig. 3-2 (a) The intensity map shows propagating surface plasmons at the gold-air interface, (b) the structure geometry with the red line showing the cutline where the average surface plasmon intensity is calculated

The simulation was swept for different groove widths (*GW*) and groove depths (*GD*). The groove widths were calculated in terms of the period of the grating, as Λ_g/m, in which m takes the values; m=1.2, 1.4, 2, 4, 6. The groove depths were swept from 20 nm to 180 nm with 20 nm increments, Fig. 3-3.

The performance of the propagating surface plasmons coupled by the surface relief grating is shown in Fig. 3-3 as the intensity of surface plasmons along a cutline at 10 nm vertical distance from the gold-air interface for five different groove widths (as $GW=\Lambda_g/m$) with groove depth of 60 nm. The instability of the coupled surface plasmons at the beginning of their propagation along the gold-air interface is manifest as ripples. However, after propagating for a short distance, the surface plasmons become more stable.

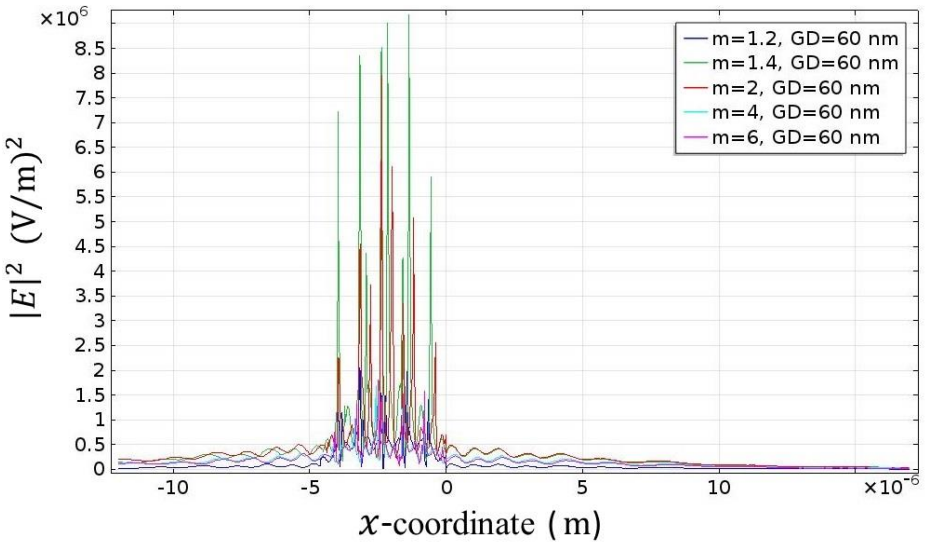

Fig. 3-3 Intensity profile along a cutline with 10 nm vertical distance from the interface

In Fig. 3-4 each symbol-colour shows the change in the average intensity of surface plasmons for a specific groove width versus the groove depth. The best coupling occurs at a groove width of half of the grating period ($GW = \Lambda_g/2$) at depths in the range of $40\ \text{nm} < GD \leq 60\ \text{nm}$ and drops sharply for groove depths outside this range. However, it again rises from $GD = 120\ \text{nm}$ and reaches another maximum at $GD = 180\ \text{nm}$. For other groove widths the coupling shows a monotonic increase in the average intensity as the depth of the grooves increases.

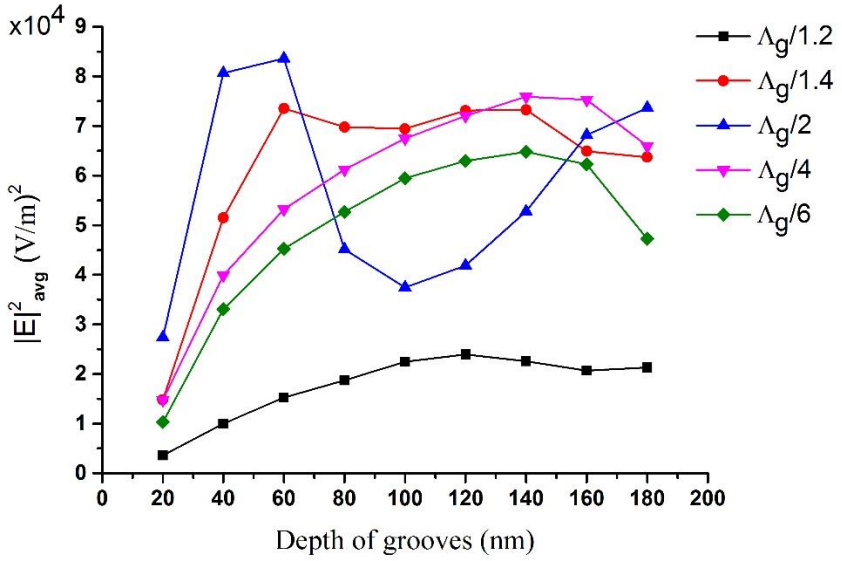

Fig. 3-4 Surface relief grating illuminated from the air, the graph shows the average intensity of coupled surface plasmons versus the groove depth (*GD*) for different groove widths (*GWs*). Each *GW* is presented with a different colour-symbol

The justification for this behaviour is that for a groove width of half the grating period, (half of the surface plasmon wavelength), the phase change of the surface plasmons when passing across the other grooves is zero, resulting in constructive interference of the coupled surface plasmons [19, 54]. However, the explanation of the

coupling efficiency in terms of groove depth becomes more complicated. The groove depth influences the coupling efficiency in two ways; by the scattering strength and by the phase of the surface plasmons when passing across other grooves. For a groove width of half the surface plasmon wavelength, the scattering is very weak at very shallow grooves and thus coupling light into surface plasmons is not efficient. The scattering increases dramatically with increasing groove depth (between 40 to 60 nm), while the impact of the depth of the grooves on the phase change is negligible. This gives the maximum value of the coupling efficiency. For deeper grooves, the scattering further increases, with an increase in the dephasing of the propagating surface plasmons passing over other grooves, and, consequently, the coupling drops sharply. For depths greater than $GD = 120$ nm, the total added path to the propagating surface plasmons by the groove depth ($2 \times GD = 2 \times 180$ nm $= 360$ nm) approaches half of the surface plasmon wavelength (395 nm), resulting in constructive interference of the surface plasmons. This manifests as another rise in the coupling of surface plasmons at a groove depth of $GD = 180$ nm.

For other groove widths the coupled surface plasmons are out of phase when passing over other grooves and the dominant effect in the surface plasmon coupling is that the scattering strength of the grooves is clearly related to the groove depth. As a result, by increasing the groove depth, the scattering of the incident light beam increases, resulting in a monotonic increase of the intensity of the coupled surface plasmons.

Fig. 3-5 shows snapshots of the normal component and the intensity of the electric field for different depths, but the same groove width. Fig. 3-5 (a) shows the weak scattering of the light beam at very shallow grooves ($GD = 20$ nm) with the resultant weak surface plasmons. In image (b) the scattering is increased and as the groove depth is still small in comparison to the surface plasmon wavelength, the change in the phase due to the depth is trivial and very strong coupling occurs. In (c) the scattering increases but the dephasing of the surface plasmons at different grooves is quite obvious. In (d) the scattering is still increasing and the increased depth approaches the surface plasmon wavelength which decreases dephasing, and finally in (e) with strongest scattering and better phase matching the plasmonic coupling improves again. Images (f) to (j) show the intensity of the fields demonstrating that, by increasing the depth of the grooves, the scattering improves despite the impact of the phase mismatch.

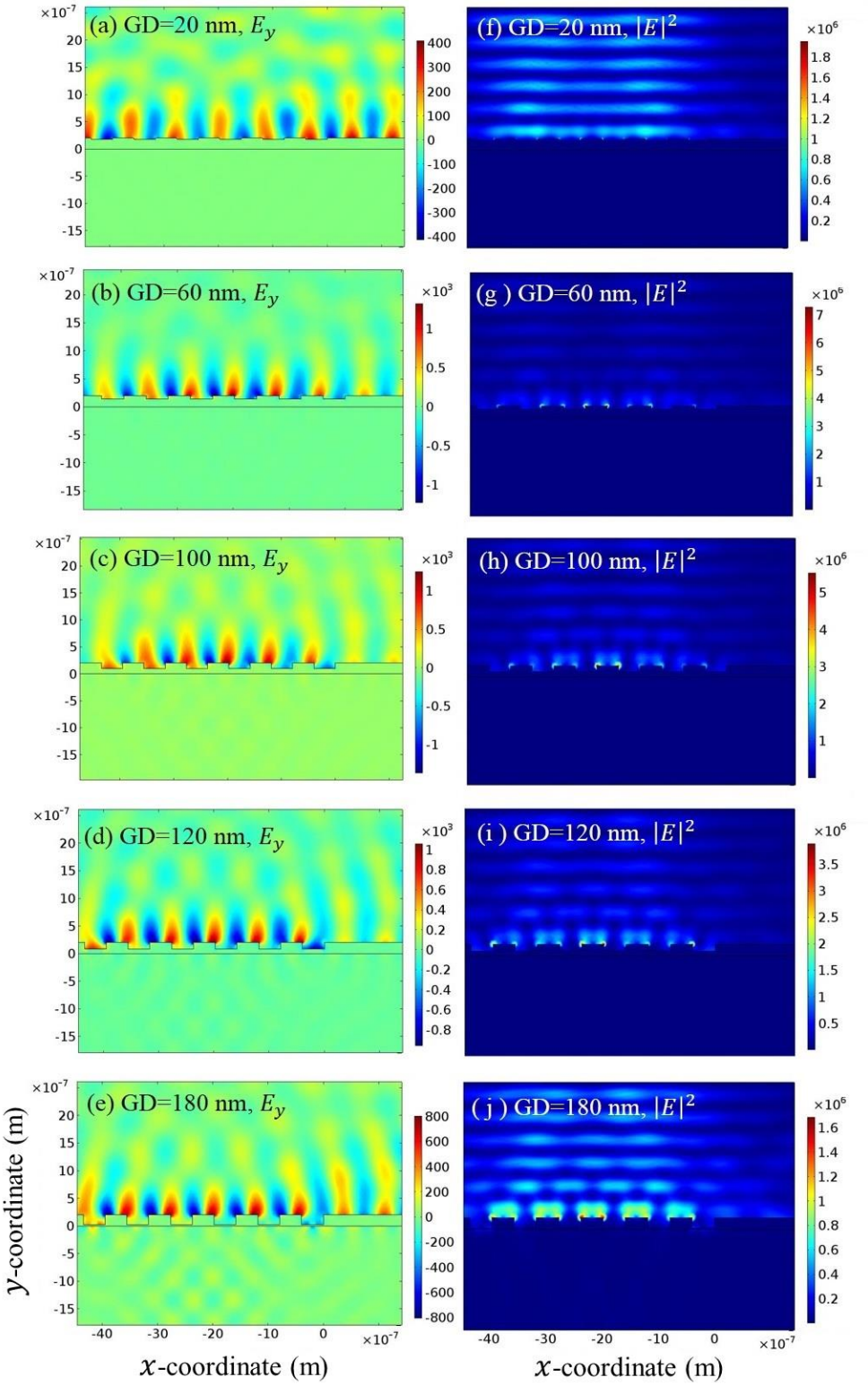

Fig. 3-5 Snapshots of scattered light and coupled surface plasmons at the edges of the grating grooves for $GW = \Lambda_g/2$ and for groove depths swept from 20 nm to 180 nm

Another aspect of grating characteristics is their response to different wavelengths, that is, the bandwidth of the grating. To investigate this, the average intensity was calculated for a range of wavelengths from 690 nm to 1050 nm, Fig. 3-6. All the simulation parameters are the same as the previous simulation in the current section, with optimized values for groove width and groove depth chosen according to the results in Fig. 3-4 ($GW = \Lambda_g/2$ and $GD = 60$ nm). Although these optimized values for the groove width and depth are a consequence of the grating period, which is also the result of the selection of the incident electromagnetic wavelength, choosing them as fixed parameters when sweeping the wavelength allows us to show the response of a grating, designed for the best performance at $\lambda_0 = 810$ nm, but under illumination with other wavelengths.

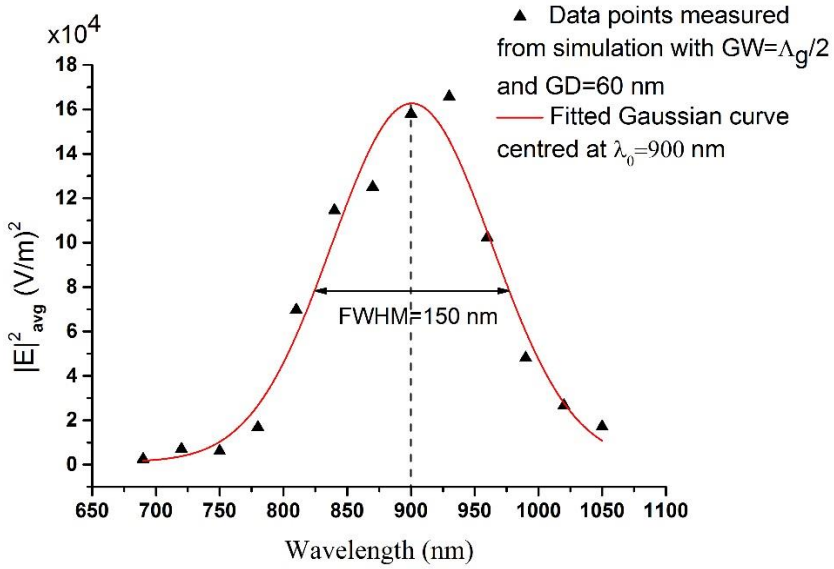

Fig. 3-6 Bandwidth of surface relief grating, FWHM is estimated as the wavelength response of the grating

In Fig. 3-6, the full width at half maximum (FWHM) of the Gaussian fitted curve is estimated as the bandwidth response of the grating (150 nm). The grating shows the maximum response at $\lambda_c = 900$ nm, not centred at the resonance wavelength of the designed structure (810 nm), and is shifted towards larger wavelengths. This behaviour may be explained because the increase in the wavelength increases the absolute value of the real part of the dielectric constant of gold (ε_r) enhancing the plasmon resonances at the gold-air interface and the propagation length of surface plasmons and consequently an increment in the measured average intensity. In other words, although by moving from $\lambda_0 = 810$ nm to $\lambda_0 = 900$ nm, the incident wavelength gradually becomes out of resonance with the grating periodicity, the increase of the real part of the dielectric constant compensates for this.

3.1.1 Trench gratings

The main difference between trench gratings and surface relief gratings is that in trench gratings, the depth of the grooves is equal to the thickness of the metal layer (gold in this case), and the base of the grooves is the dielectric substrate. As a result, there are two possibilities for illuminating trench gratings; from below the grating through the substrate (dielectric with higher refractive index) or from above the grating (through the dielectric with lower refractive index) and one may expect therefore a different performance as compared with surface relief gratings, illustrated in Fig. 3-7.

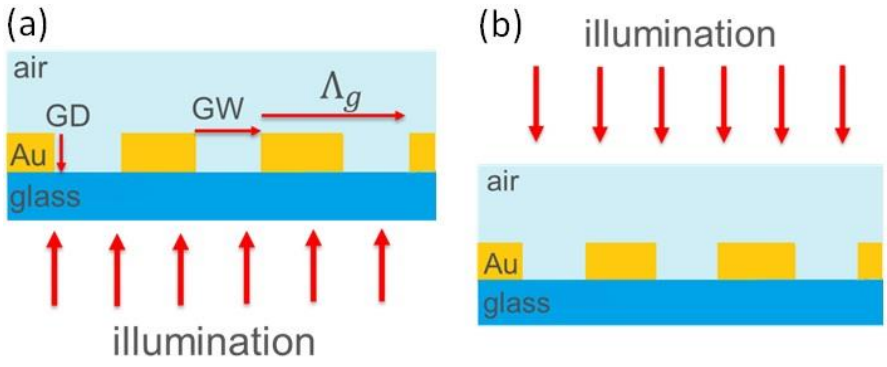

Fig. 3-7 Trench gratings illuminated from (a) below the sample through the substrate (dielectric with higher refractive index (glass)), and (b) from above the sample (dielectric with lower refractive index (air)).

In order to investigate and compare the performance of trench gratings in different illumination conditions with surface relief gratings, two simulations were run to compare the response to these different directions of illumination.

3.1.2 Trench grating illuminated from below the sample (through glass)

Here, the grating is illuminated from below the structure with normal incidence at a free space wavelength of $\lambda_0 = 810$ nm, and the grating period was chosen to be the same as the surface relief grating ($\Lambda_g = 790$ nm). The substrate material is glass with refractive index (n=1.52) and the superstrate material is air with n=1, the same as for the surface relief grating simulation. The width of the grooves depends on the grating period as Λ_g/m, where m takes the values: m=1.2, 1.4, 2, 4, 6. The depth of the grooves is the thickness of the gold layer, and to allow for different groove depths the model sweeps the thickness of the gold layer from 30 nm to 150 nm. The measurement of the coupling strength is the same as for surface relief gratings, calculated as the average intensity of the propagating surface plasmons along a cutline

with length of twice the surface plasmon wavelength, $2\lambda_{sp} = 2 \times 790$ nm, at a vertical distance (10 nm) above the gold-air interface. The cutline again begins at 11 μm distance from the grating, Fig. 3-2 (b).

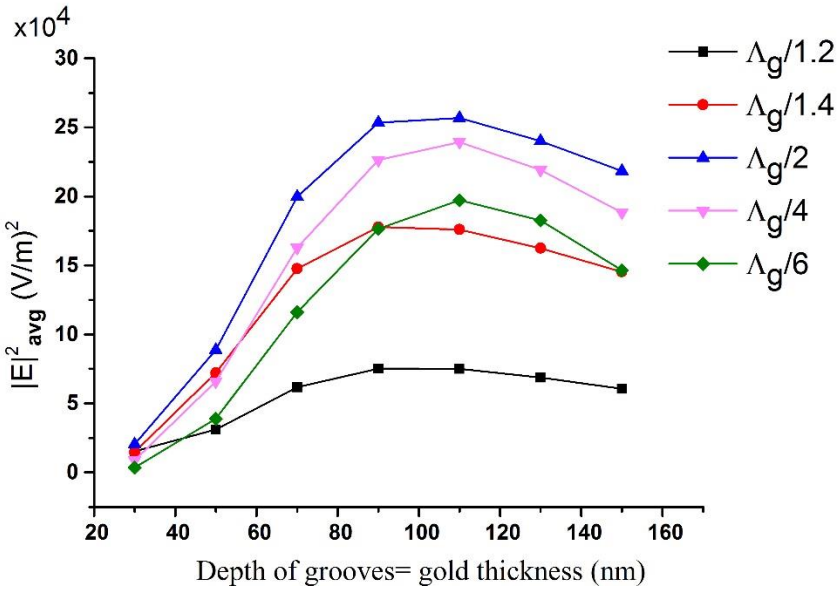

Fig. 3-8 Surface plasmon coupling as the average intensity versus the thickness of the gold layer (depth of grooves) for different groove widths (GW=Λ_g/m). The best coupling occurs for m=2 and for a gold thickness of 100 nm

The graph in Fig. 3-8 shows that the best coupling occurs for a groove width equal to half of the surface plasmon wavelength, that is half the period of the grating ($\Lambda_g/2$), and at a groove depth of around 100 nm. As a result, phase mismatch resulting from the width of the grooves is consistent with the phase mismatch occurring in surface relief gratings.

Fig. 3-9 shows that assuming a constant depth of grooves (GD=100 nm), increasing the width of the grooves from GW=395 nm (m=2) to GW=658 nm (m=1.2) changes

the amount of light that passes through the grooves with a resultant decrease in the strength of the surface plasmons coupled to the gold-air interface. The coupled surface plasmon intensity is represented as the bright light line along the interface labelled with an arrow.

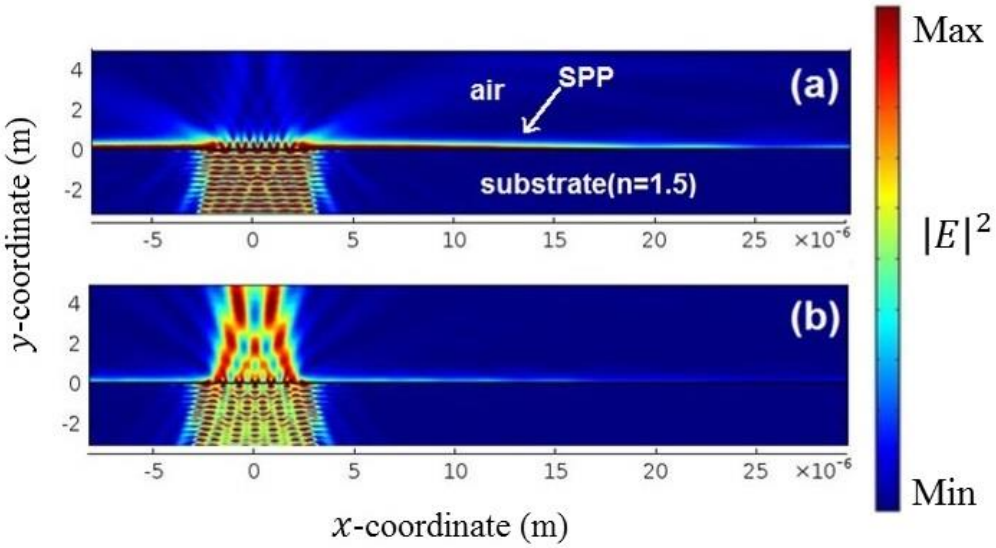

Fig. 3-9 Intensity map of surface plasmons excited at 810 nm free space wavelength (a) stronger surface plasmon coupling for a groove depth of 100 nm and groove width of 395 nm (m=2) in comparison to (b) the same groove depth but a groove width of 658 nm (m=1.2) in which most of the light passes through the grating to the air side. The bright line at the interface of gold-air shows the propagating surface plasmons

However, as seen in Fig. 3-8, the groove width is not as critical as for surface relief gratings. The average intensity of coupled surface plasmons is not strongly dependent on groove width between; $\frac{\Lambda_g}{4} = \frac{\lambda_{sp}}{4} \leq \text{GW} \leq \frac{\Lambda_g}{1.4} \propto \frac{3\lambda_{sp}}{4}$. In surface relief gratings, the base of the grooves is gold while for trench gratings the base is glass. The additional gold at the base of the grooves increases the phase delay across the grooves by increasing the effective path length of the surface plasmons. However, overall, the

coupling efficiency of trench gratings is approximately 2.5 times larger than for surface relief gratings.

The depth of the grooves also has a more significant influence on the scattering strength of the incident light beam than the phase of the coupled surface plasmons. Fig. 3-8 illustrates the reduced sensitivity of the grating to the groove depth. For a detailed illustration of the role of the groove depth, some snapshots of the simulations illustrating intensity ($|E|^2$), the normal component of the field (E_y), and the horizontal component of the field (E_x) for a fixed groove width (GW=$\Lambda_g/2$) but different groove depths are shown in Fig. 3-10.

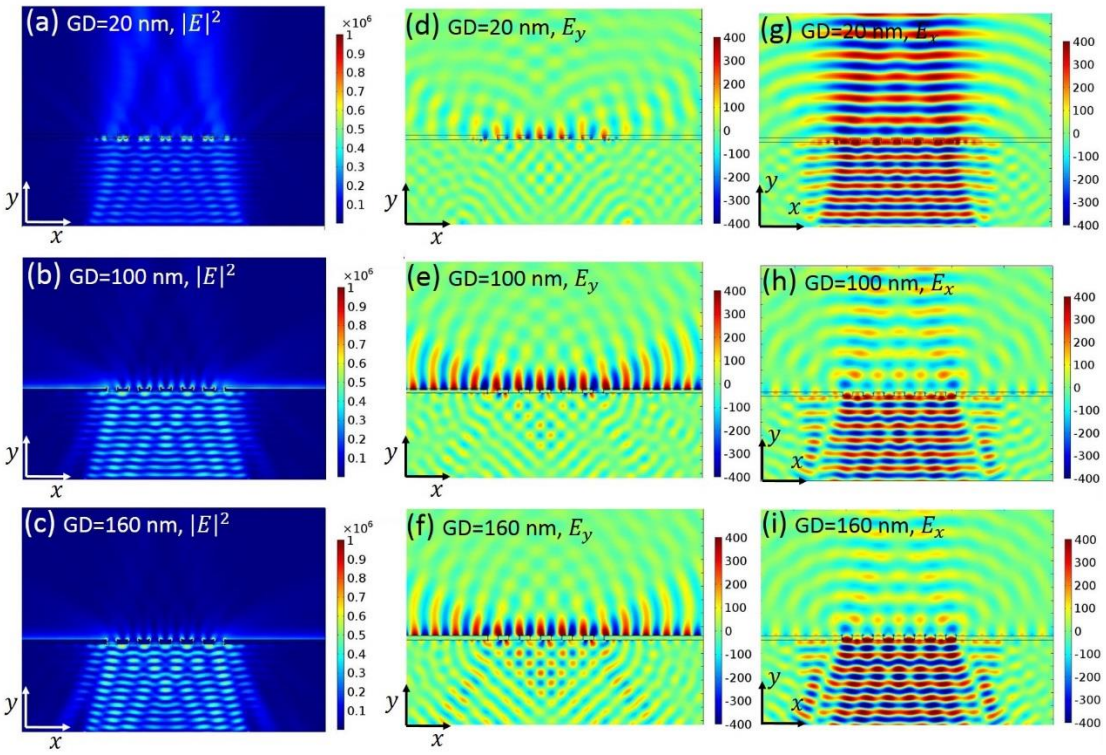

Fig. 3-10 Snapshots of the trench grating grooves illuminated from below for the same groove width (*GW*=395 nm, *m*=2) to compare the effect of depth of the trench grating grooves on coupling surface plasmons, (a) to (c) show the intensity of the electric field: for very shallow grooves scattering is not efficient; the best scattering happens at 100 nm but by going to deeper grooves the reflection of the incident light also increases from the high walls of the grating, (d) to (f) show the normal component of field (E_y) normal to the interface, and (g) to (i) show the horizontal component of field (E_x)

Fig. 3-10 (a), (d) and (g) show that for very shallow grooves, very weak scattering of the light beam at the grooves results in the passage of more light to the air and consequently less coupling into surface plasmons. Increasing the depth of the grooves improves the scattering, and more light is coupled into surface plasmons and consequently less light passes through the grooves to the air, Fig. 3-10 (b, e, h). However, for deeper grooves, the walls of the grooves become taller and the reflection

of the incident light into the glass (substrate) increases. Some of the incident light couples into surface plasmons at the glass-gold interface, decreasing the coupling of the light beam into surface plasmons, Fig. 3-10 (c, f, i).

The bandwidth of the trench grating response when illuminated from below, through the glass substrate, was also studied for a range of wavelengths from 600 nm to 1050 nm.

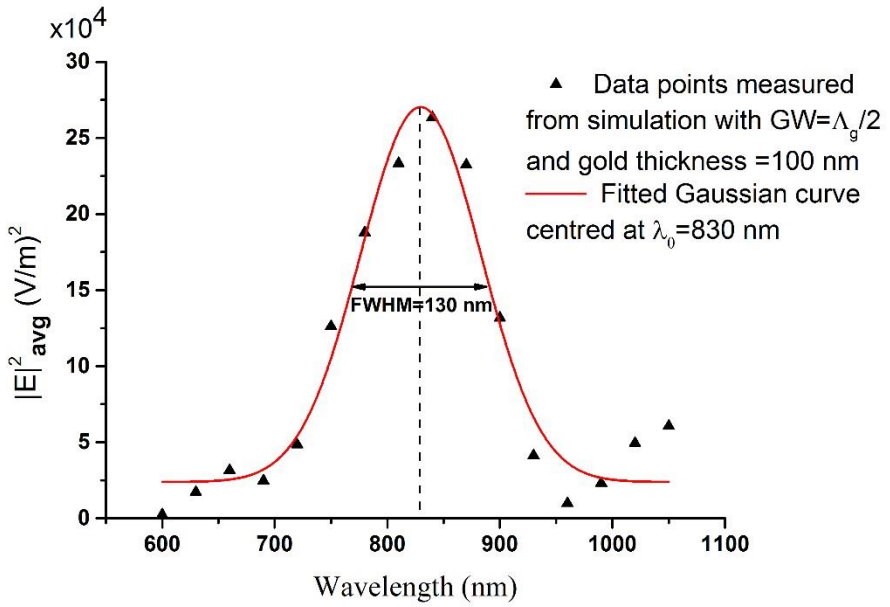

Fig. 3-11 Bandwidth of the trench grating when illuminated from below the grating through the substrate with higher refractive index. The peak wavelength is $\lambda_0 = 830$ nm

The effective bandwidth of the trench grating is 50 nm smaller than the bandwidth of surface relief gratings. The central wavelength is also shifted to $\lambda_c = 830$ nm, a smaller wavelength than for surface relief gratings. This may be related to the full gold

coverage of the grooves in the surface relief gratings which results in a broader wavelength response and stronger scattering by the grooves.

3.1.3 Trench grating illuminated from above the sample (through air)

Simulations of the illumination of a trench grating with the same grating characteristics at $\lambda_0 = 810$ nm from above the sample through air show that the best width for the grooves is still half the period of the grating, which gives the phase matching condition for the coupled surface plasmons, Fig. 3-12.

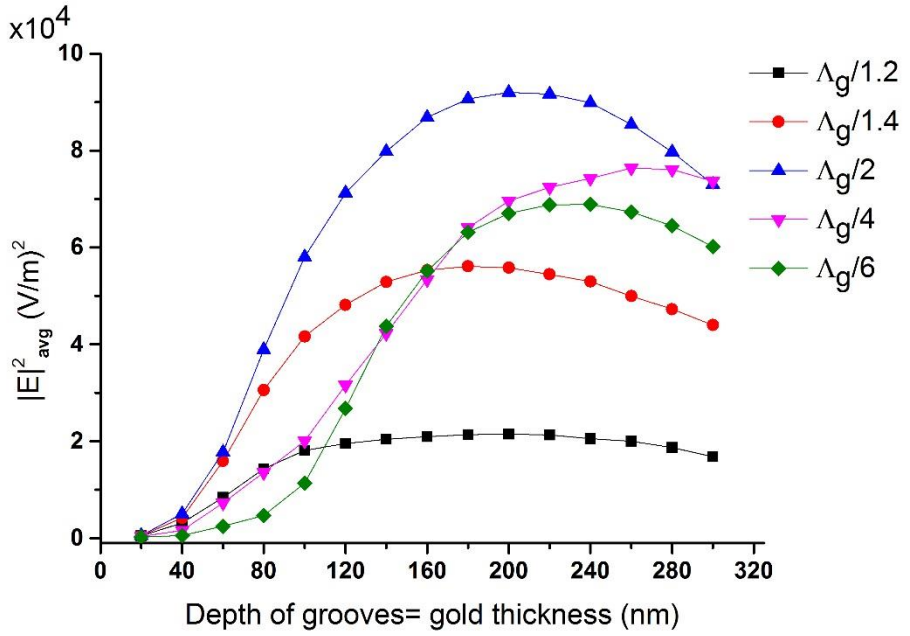

Fig. 3-12 Average intensity of surface plasmons coupled by trench gratings versus the groove depth, for different groove widths. The grating is illuminated from above at its resonance wavelength $\lambda_0 = 810\,nm$ for a grating period of $\Lambda_g = 790$ nm. The graph shows that the best coupling happens for GW=Λ_g/m=395 nm for a groove depth of around 200 nm

The groove depth is swept from 20 nm up to 300 nm. The best coupling occurs for a groove depth (gold thickness) of 200 nm, which is different from the results for the trench grating when illuminated from below the glass substrate. The scattering increases with increasing depth of the grooves, resulting in increased coupling. However, unlike the case of illumination from below the glass substrate, for depths greater than 100 nm, the coupling is a maximum for a groove depth of 200 nm.

Overall, the coupling when the grating is illuminated from air is 2.5 times less than the identical grating illuminated from below the glass substrate (the medium with higher refractive index) but similar to the coupling efficiency of surface relief gratings. This change in the coupling efficiency is due to the difference in refractive index of the illumination medium.

The bandwidth of the grating in this case is the same as the bandwidth of the trench grating illuminated from below the structure through the glass substrate. The response of the grating is calculated for wavelengths from 600 nm to 1050 nm for groove widths of $\Lambda_g/2$ and a groove depth of 200 nm. The centre wavelength is 830 nm, however, the response for the wavelengths above and below the peak wavelength is slightly asymmetric, which is different from the case of illumination from below the glass substrate, as shown in Fig. 3-11.

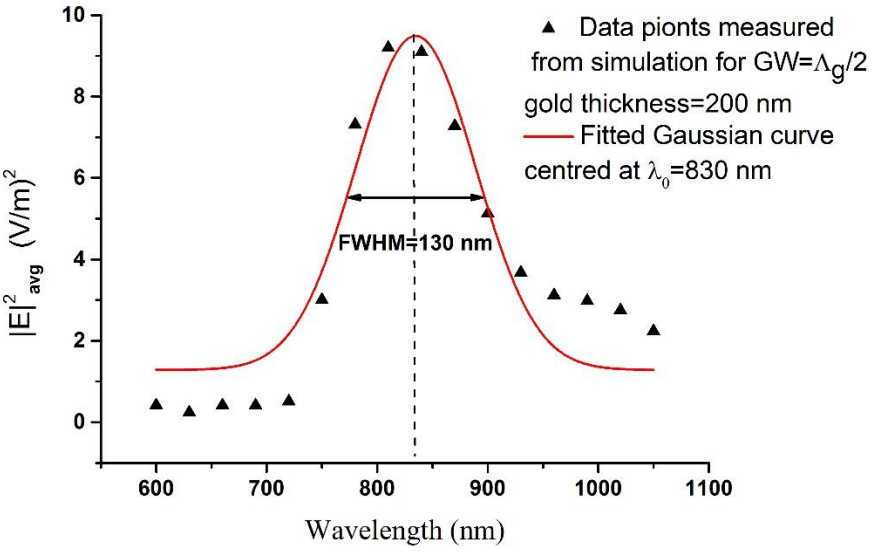

Fig. 3-13 Bandwidth of the trench grating coupling response when illuminated from the air. The bandwidth, as the full width of half maximum (FWHM) of the fitted Gaussian, is 130 nm and the central wavelength is shifted to $\lambda_c = 830$ nm, as in the case of the trench grating illuminated from below the glass substrate

3.2 Conclusions

This investigation of the coupling efficiency of surface relief gratings and trench gratings illuminated from the different dielectric media reveals that the strongest surface plasmon coupling occurs for the trench grating illuminated from below, through the substrate (higher refractive index), with a groove width equal to half of the grating period, (that is, half the surface plasmon wavelength) at the gold-air interface, with a groove depth of around 100 nm. The coupling efficiency of the trench grating illuminated through the air is in the range of that for the surface relief grating and the maximum coupling efficiency of the surface plasmons for both these cases is 2.5 times smaller than the maximum surface

plasmon coupling efficiency in the case of a trench grating illuminated through the substrate (higher refractive index).

Although all the gratings considered in this chapter are linear gratings, for curved gratings, the coupled surface plasmons at each point of the curved gratings propagating across other grooves are expected to behave in the same way as plasmons propagating across linear grooves. However, in the case of curved gratings, the polarization of incident light with the grooves at each point makes different angles with respect to the normal to that point, thus is investigated in Chapter 4 in detail. The results of this chapter were used to determine the best parameters for design and fabrication of curved gratings, as discussed in Chapter 5.

Chapter 4: Curved Gratings for Coupling and Focusing Surface Plasmons

Plasmonic focusing concentrates surface plasmons in 2D at a metal-dielectric interface. Various plasmonic focusing structures have been demonstrated experimentally, including engineered arrays of metallic nano-slits [111], an arc of nano-holes [112], parabolic nanoparticle chains [113], diffraction gratings [114], and an elliptical corral [115] with particular applications in wavelength division multiplexing, spectral filtering, waveguide coupling, correction of divergent surface plasmon beams and angular interferometry, respectively. Elliptically curved gratings [116] and periodically corrugated wires have been proposed and investigated for terahertz frequencies [117]. Single circular slits can also act as surface plasmon focusing elements [118-120]. However, illumination with linearly polarized light results in two high intensity spots along the polarization direction of the beam due to destructive interference of counter-propagating surface plasmons at the centre of the circle. In order to create a single spot at the centre of a circular slit, one needs to illuminate the structure with radially polarized light to achieve constructive interference of the surface plasmons at the centre of the circular slit. Building on this result, it has been shown that circular gratings, consisting of several circular slits and

illuminated with circularly polarized light, focus surface plasmons at the centre of the concentric circles with a higher intensity due to the increased number of diffracting slits [19, 52, 121]. In an alternative approach using linearly polarized light, focussed surface plasmons may be created by placing two half-circular slits or corrals facing each other and centred at the same point. However, the radius of the opposing circular slits needs to be shifted by half of the surface plasmon wavelength, in order to provide constructive interference of counter-propagating surface plasmons at the centre [122, 123].

The circular gratings need to be illuminated with circularly polarized light. Although this problem can be solved in asymmetric circular grating structures, both the circular gratings and asymmetric gratings make a closed loop which does not give access to the focal spot for in-plane applications to use the benefits of the focused surface plasmons. In this chapter, we study the use of curved gratings as sectors of full concentric circular gratings, to focus surface plasmons, see Fig. 4-1. We show the theory, simulation and experimental results that demonstrate the effect of the sector angle of the curved gratings on the width of the focussed surface plasmons. The "numerical aperture" of these plasmonic lenses is defined and it is shown that the definition is in very good agreement with simulation and experimental results.

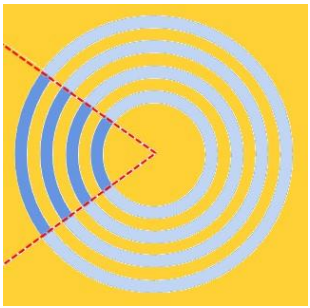

Fig. 4-1 Trench curved grating (dark blue) as a sector cut (red dashed line) of full circular gratings, the curved grooves are milled into a gold film on glass substrate

All these simulations are performed under illumination of the curved gratings with linearly polarized light (p-polarized). This offers advantages in comparison to the earlier results for full circular gratings, as efficient focusing of surface plasmons at the centre of the full circular gratings is only achieved in practice if the centre of the radially polarized beam is aligned with the centre of the circular slits. Furthermore, curved gratings are positioned to one side of the focal spot and the region beyond the focal point allows access to concentrated surface plasmons for further processes. However, the depth of focus for such a plasmonic lens is larger in comparison to its almost subwavelength width.

An alternative approach uses two curved gratings facing each other in a concentric asymmetric configuration. The radius of each groove of the curved gratings is shifted by half of the surface plasmon wavelength, relative to the opposite grating groove. This structure leads to focussing of the surface plasmons with a significant decrease in the length of the focal spot. The peak intensity at the hot spot is also enhanced significantly in comparison to the single curved gratings, and to the asymmetric configuration of single slits.

The specific design of the curved gratings suggests their application for coupling light into surface plasmons and launching the coupled surface plasmons onto plasmonic strip-line waveguides. One would expect that a larger sector angle curved grating, keeping constant aperture size, would collect more incident light and efficiently launch surface plasmons onto plasmonic waveguides. The efficiency of coupling surface plasmons by curved gratings in comparison to linear gratings is discussed in Chapter 5.

Considering the above-mentioned advantages these structures can facilitate the use of focused surface plasmons for applications in sensing, plasmonic photo-detectors, nonlinear plasmonics, and even integrated nano-photonic circuits.

In this chapter, the performance of curved gratings to couple and focus surface plasmons is investigated by simulations which are then compared with experimental results. The numerical aperture of these plasmonic lenses is defined and compared with the simulations and measurements. Finally, a design with two curved gratings facing each other in an asymmetric configuration is investigated by simulation.

4.1 Investigating the performance of curved gratings

Curved gratings are taken as sectors of full circular gratings. At each point of the grooves of the curved gratings, linearly polarized light (p-polarized) makes an angle (α) with the normal to the grooves at that point, which is illustrated in Fig. 4-2.

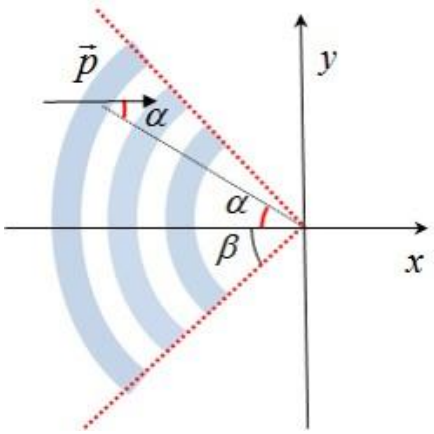

Fig. 4-2 Curved grating illuminated with linearly polarized light (p-polarization). At each point of the grating the direction of polarization of the incident light would couple surface plasmons in the direction of the grating vector at that point proportional to the angle between them (α). β is half the grating sector angle

The electric field of the coupled surface plasmons along the direction of the normal unit vector to the grooves of the grating (the grating vector) is proportional to the component of the polarization direction along the grating vector, that is, the $cosine$ of the angle between the grating vector and the polarization direction [124];

$$E_{\substack{sp(at\ each\ point \\ of\ the\ grooves)}} \propto \cos(\alpha) \qquad \text{Eq. 4-1}$$

These electric fields interfere with each other in their path towards the centre of the curved grooves, and, depending on the sector angle, they result in different surface plasmon concentrations at different distances. As the sector angle is increased, the focal point approaches the centre of the curved gratings. These sector-angle-dependent distributions are very complicated to calculate analytically; therefore, COMSOL software is used to simulate the structure and the resulting surface plasmon distribution.

4.1.1 Simulation

As the curved gratings are assumed to perform as plasmonic lenses, an identical aperture size was chosen for each curved grating to facilitate comparisons, (see Appendix A). In Chapter five, we investigate the efficiency of coupling surface plasmons onto 3 μm wide plasmonic stripline waveguides. Thus, the design aperture of all the curved gratings was chosen to be 3 μm.

Full circular gratings and curved gratings with different sector angles were simulated assuming design parameters based on the results of the previous chapter. Thus, trench gratings were selected as the best option for simulation and fabrication. Near-infrared illumination with light at $\lambda_0 = 810$ nm was selected, as near-infrared light sources were available, and the corresponding near-infrared surface plasmons have reasonable propagation lengths. For normal incidence, the period of the grating should be equal to the wavelength of the coupled surface plasmons, namely, $\Lambda_g = \lambda_{sp} = 790$ nm.

The width of the grooves is selected to be half of the grating period ($\Lambda_g/2$), from the results of Chapter 3, with a groove depth, $GD = 100$ nm equal to the thickness of the gold layer (curved trench gratings). The structures are illuminated from below the sample through the glass substrate ($n = 1.5$), with illumination by a plane wave at normal incidence confined to the area of the grating, Fig. 4-3, with identical power per unit area for all the simulations. This is to minimise spurious effects on the near-field of the coupled surface plasmons due to the incident light beam.

The superstrate is air (n=1). All the boundaries are defined as scattering boundary conditions which means the incident electromagnetic waves, with wave vectors normal to the boundary, pass through the boundary with minimal reflection back into the simulation cell. The simulated structure is meshed in two steps. The thin 100 nm gold layer is meshed with an element size given by; $\frac{\lambda}{7} \leq \text{element size} \leq \frac{\lambda}{5}$, and the substrate and superstrate element size is given by; $\frac{\lambda}{5} \leq \text{element size} \leq \frac{\lambda}{4}$, in order to achieve convergent results.

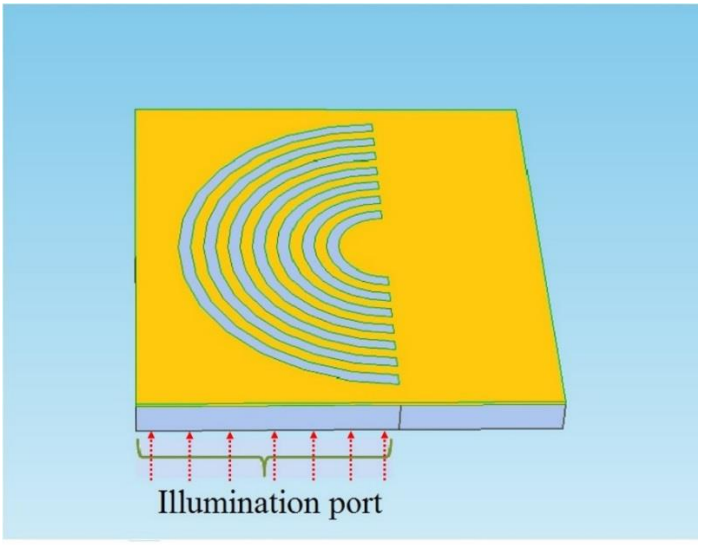

Fig. 4-3 The simulation cell for a curved trench grating with sector angle of 180°. The illumination by the plane wave is only on the area of the grooves, the rectangular port is distinguished in the image with red arrows lines showing the direction of illumination (upward, from below the sample through the substrate)

The number of grooves also influences the intensity of the coupled surface plasmons. All gratings were simulated with seven grooves. Assuming the phase matching condition is met, increasing the number of grooves of the circular gratings

increases the intensity of the coupled surface plasmons. However, as the radius of the largest grooves exceeds the surface plasmon propagation length, the advantage of adding more grooves to the grating decreases [19, 52]. Additional grooves would enhance the intensity of the coupled surface plasmons. However, this enhancement also depends on the propagation length of the surface plasmons together with other geometrical parameters such as the period, groove width and depth. These geometrical parameters affect the phase and transmission of excited surface plasmons when crossing other grooves leading to constructive or destructive interference of surface plasmons at the focal spot. The impact of the number of grooves is discussed in Section 4.2, where it is shown that increasing up to seven grooves increases the surface plasmon intensity at the focal spot. This also affects the required fabrication time and the illumination area for coupling surface plasmons with the grating.

4.1.2 Simulation results

The simulation results show that when the sector angle of the curved gratings increases, the coupled surface plasmons are concentrated in the front of the grating (see intensity maps in Fig. 4-4).

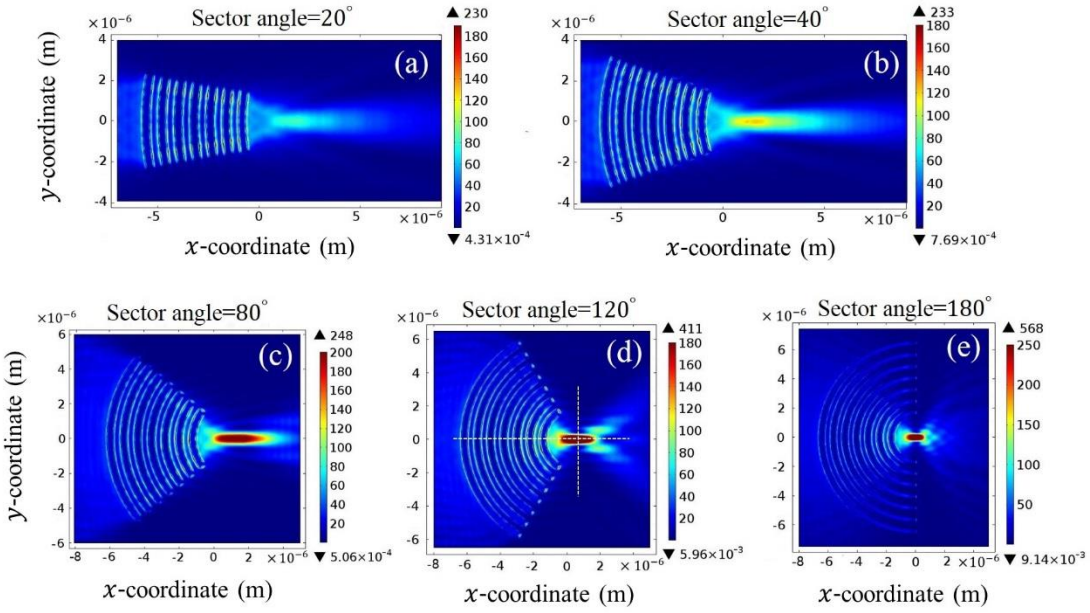

Fig. 4-4 (a) to (e) show the $|E|^2$map and compare the distribution of coupled surface plasmons due to the curved grating. With increasing sector angle, the coupled surface plasmons are more concentrated and are focussed in front of the curved grating. The white crossed dashed lines show the cutlines for the intensity profiles shown in Fig. 4-5

The intensity profile calculated at a height of 10 nm above the gold-air interface, and taken on a horizontal cutline along the bisector of the gratings (horizontal white dashed line in Fig. 4-4 (d)) is shown in Fig. 4-5 for each scheme in Fig. 4-4.

The frequent sharp peaks in the negative x-coordinate (before the larger peaks) illustrate the scattering of the incident light and the resulting surface plasmons at the grating grooves. The larger peaks at the positive and zero x-coordinate positions correspond to the focussed surface plasmons. The sequence of the images for different sector angles shows the decreasing horizontal dimension and increasing intensity of the focussed surface plasmon spotsize with increasing sector angle. The variation of the focal spot with increasing sector angle, was studied by measuring the intensity profiles of the concentrated surface plasmons along a vertical cutline normal to the

bisector of the gratings. These profiles are plotted for all the sector angles in Fig. 4-6, to compare their evolution by sector angle.

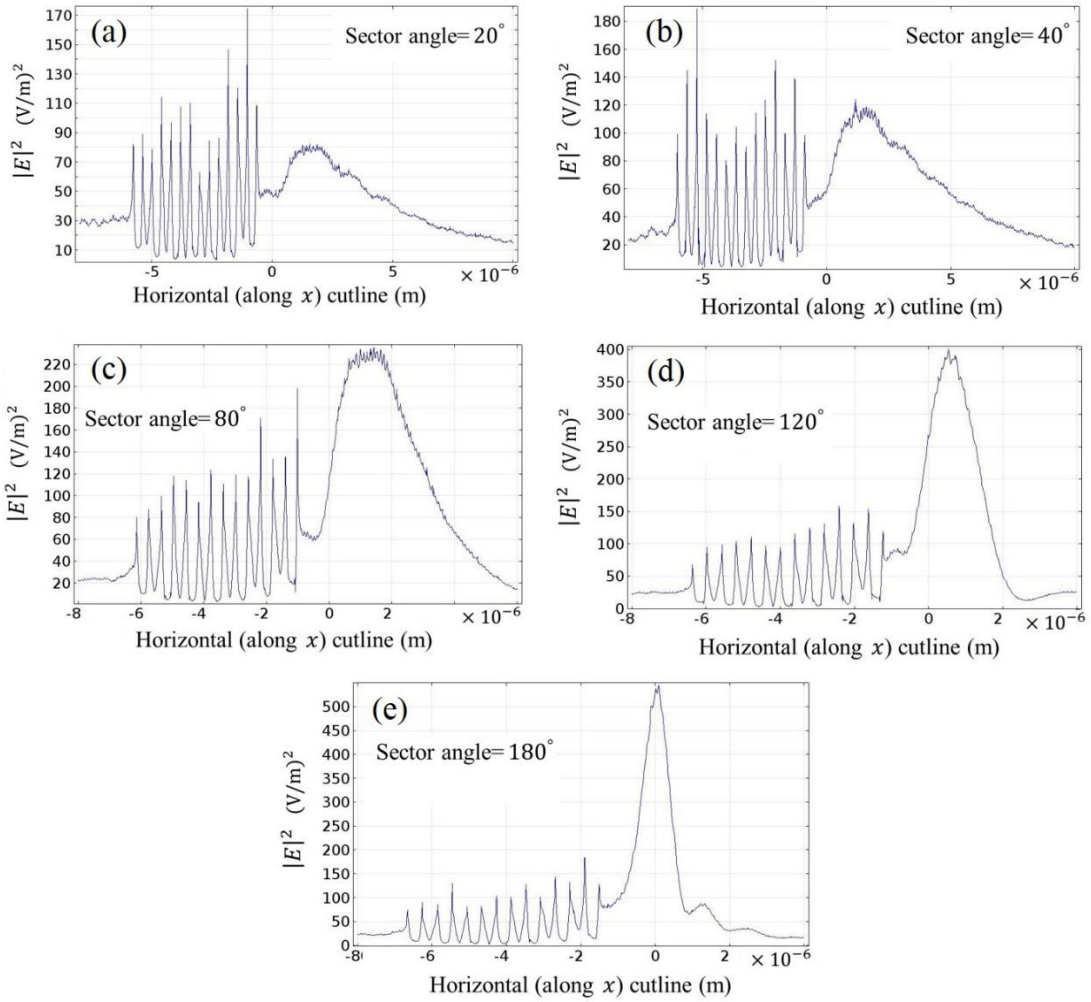

Fig. 4-5 (a) to (e) Intensity profile taken at 10 nm vertical height above the gold-air interface, along the bisector of the curved gratings for different sector angles

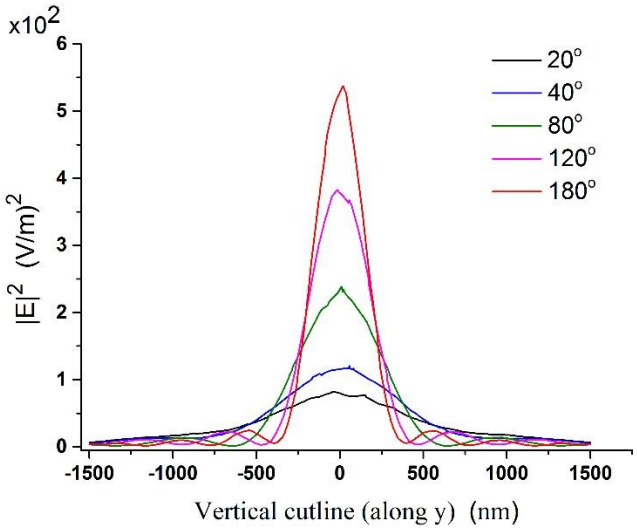

Fig. 4-6 Intensity profiles showing the evolution of the width of the focused surface plasmon spot-size coupled by curved gratings with different sector angles

The graph shows that by increasing the sector angle of the curved gratings the width of the concentrated surface plasmons decreases while the intensity of the hot spot increases. This is similar to the performance of optical classical lenses.

4.1.3 Fabrication of curved gratings

Experiments with curved gratings to demonstrate coupling and focusing surface plasmons were made with devices fabricated with four different sector angles ($20^{\circ}, 40^{\circ}, 120^{\circ}, 180^{\circ}$). Identical aperture sizes (3 μm) were selected for all of the fabricated curved gratings. The period of the gratings was calculated assuming the illumination wavelength $\lambda_0 = 810$ nm at normal incidence, which results in $\Lambda_g = 790$ nm. The width of the grooves was selected according to the results of Chapter three, as half of the surface plasmon wavelength; $GW = \frac{\lambda_0}{2} = \frac{\Lambda_g}{2} = 395$ nm. Although the simulation shows that the best depth of the grooves and consequently the thickness

of gold film is around 100 nm (for the case of a trench grating illuminated from below the sample through the glass substrate), because of the availability of good quality gold films (roughness $\leq$ 5 nm) the gratings were fabricated into 30 nm gold films. This thickness doesn't change the performance of the curved gratings as plasmonic lenses but would decrease the coupling efficiency. These 30 nm gold films were deposited by ion-assisted deposition using an oxygen plasma-assisted thermal deposition system [125], to ensure good adhesion, flatness and uniformity of the gold film on glass substrate (refractive index, $n = 1.5$). All the gratings were fabricated with seven grooves.

Focused ion beam (FIB), using a Zeiss Auriga 60 cross beam SEM with an Orsay Canion FIB column, Fig. 4-7 (a), was used to mill seven grooves to 30 nm depth in the gold layer, (see Fig 4-7 (b)). Characterization of the fabricated structures by SEM shows the final grating period to be 770 nm, (revealing a 2.5% tolerance in fabrication) and 30 nm groove depth ($GD = 30$ nm).

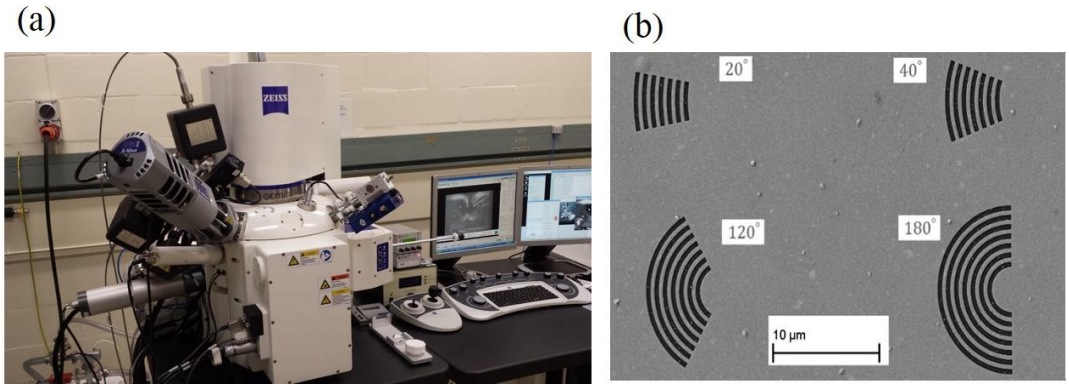

Fig. 4-7 (a) shows the scanning electron microscope (SEM) with the focussed ion beam (FIB) column, (b) shows the scanning electron micrographs of the fabricated curved gratings

Using 3D COMSOL simulations, we calculated the wavelength response of the fabricated structures (assuming the exact fabricated structural parameters) by sweeping the simulation for a range of wavelengths from 600 nm to 930 nm.

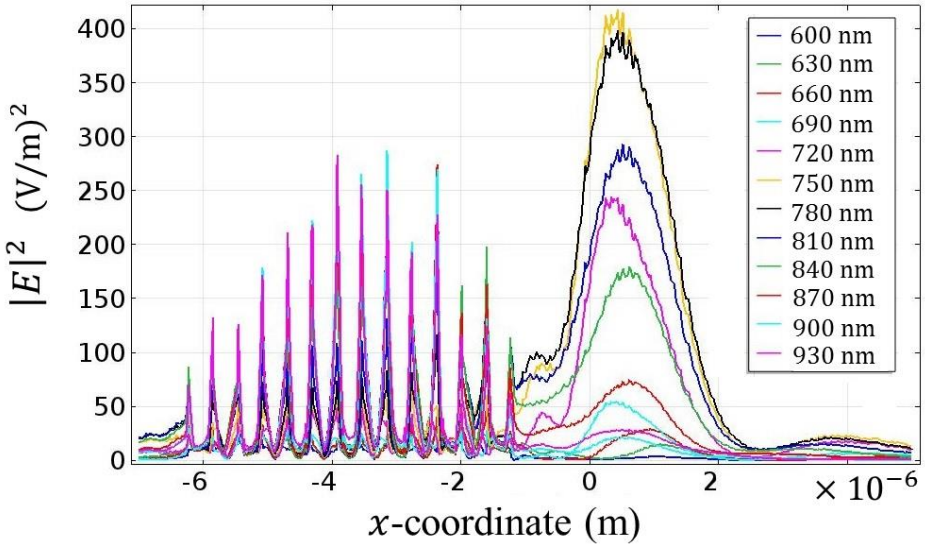

Fig. 4-8 intensity profile along the bisector of a 120° curved grating illuminated with a range of wavelengths showing the change of intensiy of surface plasmons at the focal spot according to simulation results

The bandwidth of the grating is measured according to the conventional full width at half maximum (FWHM) of the fitted Gaussian curve to the response of the structure to different wavelengths. Simulation results (see Fig. 4-8, and Fig. 4-9) reveal that the bandwidth is centred at $\lambda_0 = 780$ nm with FWHM=100 nm ($\lambda_0 = 780 \pm 50$ nm). According to Eq. 1-9 and Eq. 1-2, for normal illumination ($\theta = 0$) of surface plasmon gratings the resonance wavelength of surface plasmons for a grating with period of $\Lambda_g = 770$ nm is at $\lambda_0 = 790$ nm which is very close to the simulation result of $\lambda_0 = 780$ nm in Fig. 4-9. However, during the conduct of the experiment we observed better

signal collection by the NSOM tip at $\lambda_0 = 700$ nm and decided to illuminate the structures at this wavelength.

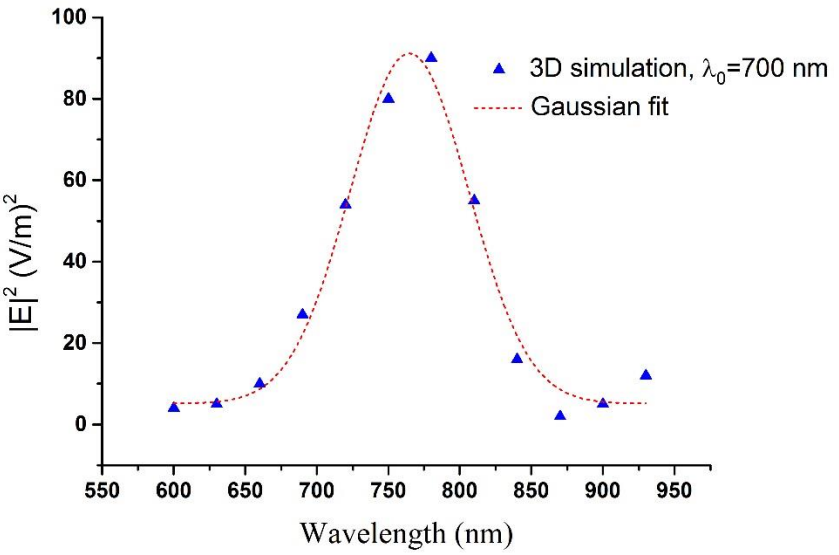

Fig. 4-9 Bandwidth of the curved grating (full width of half maximum (FWHM)) for a grating period of $\Lambda_g = 770$ nm according to simulation resutls. The fitted Gaussian curve is centred at $\lambda_0 = 780$ nm

4.1.4 Experiments

The performance of the fabricated curved gratings was studied by near-field scanning optical microscopy (NSOM) with an appropriate optical coupling system as shown schematically in Fig. 4-10. A laser source provided the excitation light at a wavelength of 700 nm at approximately 1 mW, with 5 nm bandwidth, illuminating the grating by a $10\times$ microscope objective from below the sample through the glass substrate. The NSOM tip was positioned at $\sim$10 nm height from the gold surface to collect the evanescent field of the surface plasmons coupled by the gratings.

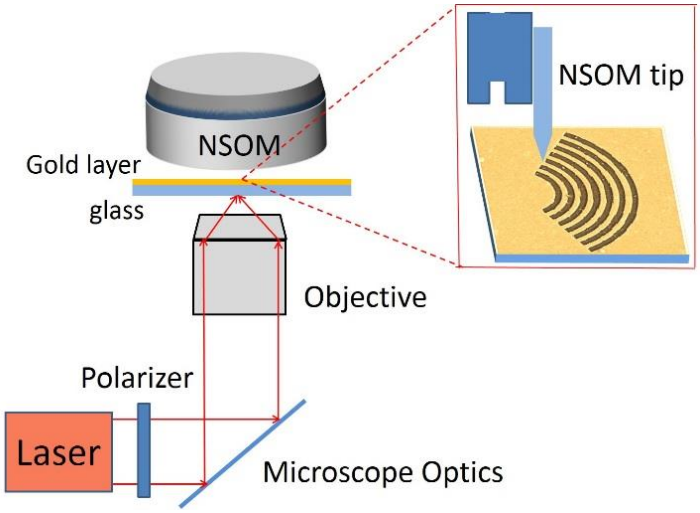

Fig. 4-10 experimental setup for illuminating the fabricated curved gratings from below (through the substrate) and scanning the near field of the coupled surface plasmons to study their intensity distribution

Some NSOM scans for different sector angles are presented in Fig. 4-11. The focusing is clearly evident for 120° sector angle. For the 180° sector angle, the focusing is less clear, possibly due to the bright scattering from the grating area. However, the focusing is clearly shown in the intensity profiles.

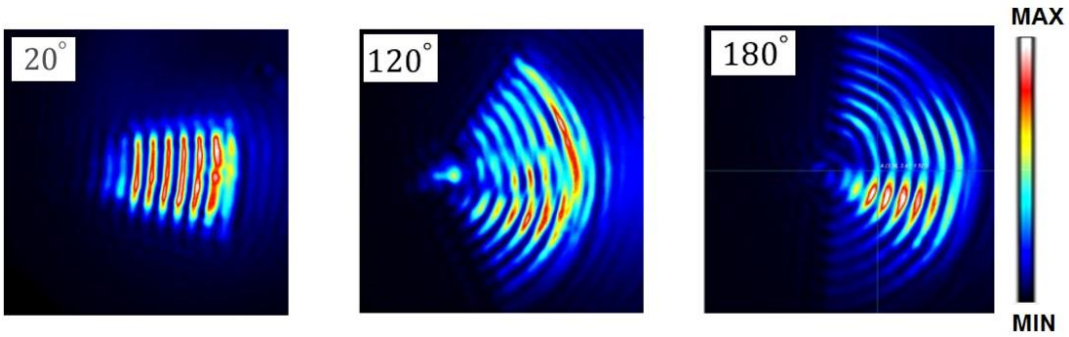

Fig. 4-11 NSOM scans for different sector angles of curved gratings taken with tip distance of 10 nm from surface

In Fig. 4-12 (a), the NSOM image (256×256 pixels) for a 120° sector angle grating shows the concentration of surface plasmons at the focal spot. There is a phase

change in the image, which is attributed to irregularities of the hand-made NSOM probe. 3D simulations with identical structural characteristics, Fig. 4-12 (b), shows the near-field intensity map at a height of 10 nm above the gold-air interface, which demonstrates the focusing of surface plasmons in good agreement with the NSOM scan.

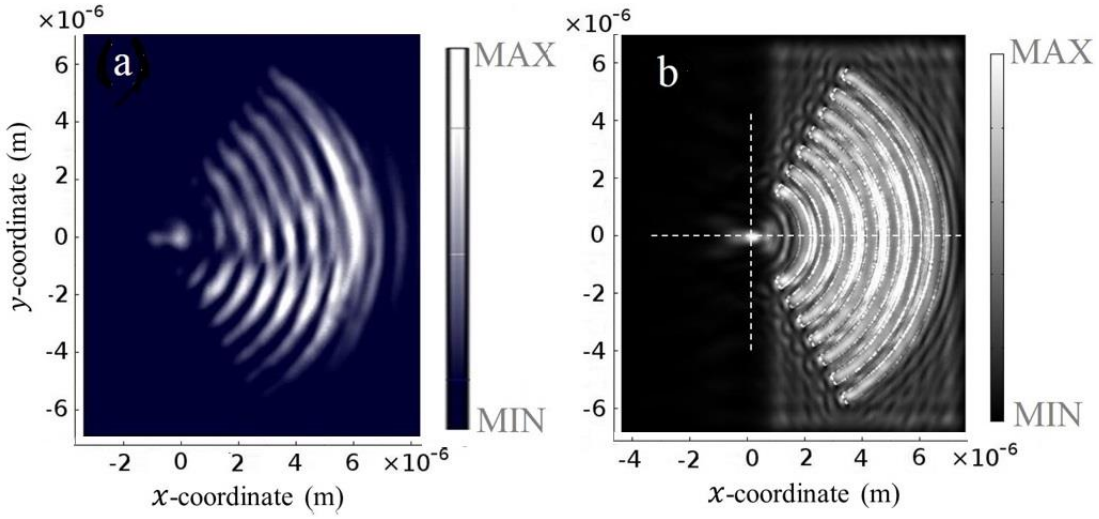

Fig. 4-12 (a) intensity map of NSOM scan for 120° sector angle curved grating illuminated at $\lambda_0 = 700$ nm illustrating the focusing of surface plasmons in front of the grating, (b) 3D simulation of the near field intensity map for the same grating structure illustrating the focusing of surface plasmons in front of the grating

In order to demonstrate the surface plasmon focusing, intensity profiles along a horizontal cutline matched on the bisector of the grating (horizontal white dashed cutline in Fig. 4-12 (b)) and at 10 nm vertical distance from the interface were extracted and plotted for both the simulation (red dashed line) and experiment (black solid line) in Fig. 4-13.

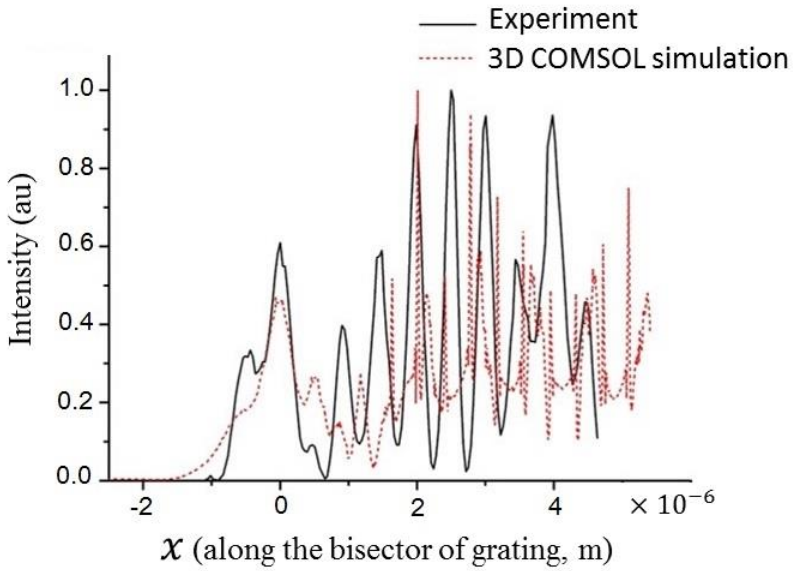

Fig. 4-13 comparison of intensity profiles between the experimental NSOM scan data and the 3D COMSOL simulation for the 120° sector angle curved grating. The intensity profiles are individually normalised to the maximum intensity value of each profile.

In Fig. 4-13 the scattering of the light at the grooves contributes to observed oscillations in the positive x-coordinate and the focal spot occurs at the zero position. The results show the concentration of surface plasmons at the focal spot, although the field enhancement is relatively weak. This weak field enhancement is due to the off-resonance of the illumination wavelength and the 30-nm groove depth. According to the simulation result of Chapter 3 (Fig. 3-8) and wavelength response of the curved gratings (Eq. 1-2, Eq. 1-9, and Fig. 4-9) a new simulation was performed and showed that the most efficient coupling, and consequently the best field enhancement at the focal spot, would occur for 100-nm gold thickness (groove depth) when illuminated at the peak resonance wavelength ($\lambda_0 = 790$ nm) for the grating period of $\Lambda_{gr} = 770$ nm, see Fig. 4-14.

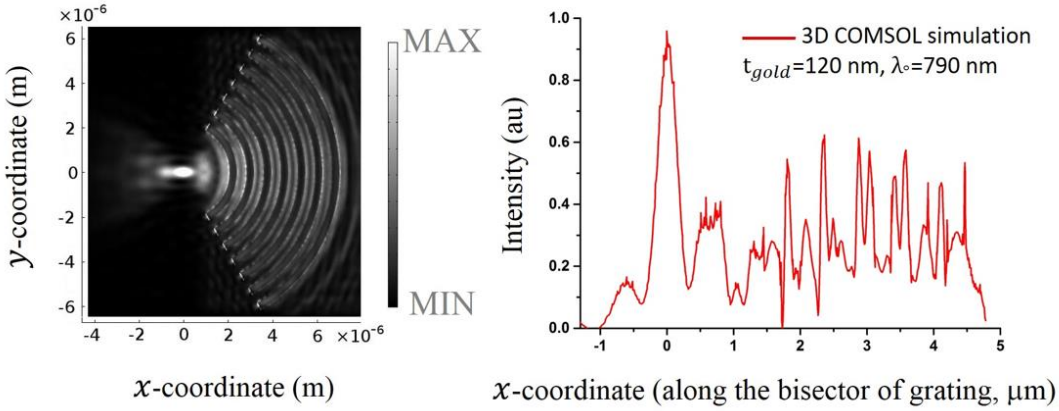

Fig. 4-14 (a) 3D simulation of near-field intensity map of 120° sector angle curved grating with optimized structural parameters, (b) the intensity profile along the bisector of grating

The full width at half maximum (FWHM) of the intensity profile along a vertical cutline (horizontal cutline in Fig. 4-12) passing through the focal spot is defined as the width of the focal spot. Fig. 4-15 compares the simulation calculations and NSOM measurement of the width of the focal spot for seven different sector angles and four sector angles, respectively. It shows that by increasing sector angle, the width of the coupled surface plasmons decreases and for sector angles of more than 100°, the coupled surface plasmons are well focused at the focal spot of the curved gratings. This decreasing width of the focal spot with increasing sector angle is analogous to the performance of classical optical lenses.

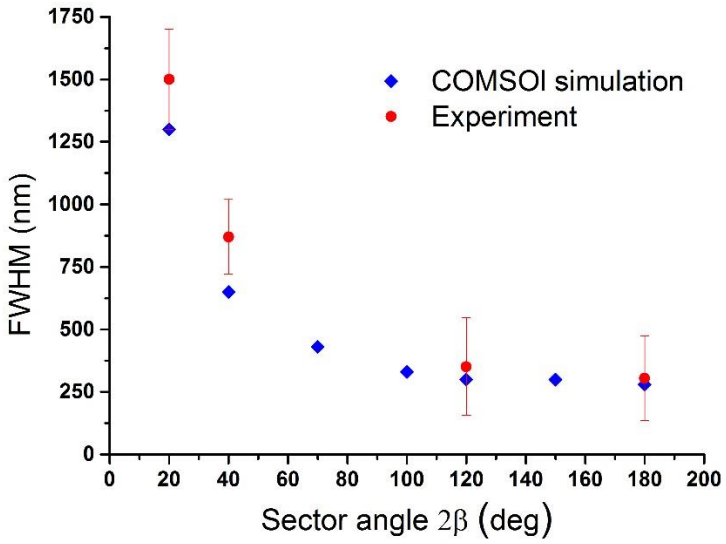

Fig. 4-15 The width (FWHM). of the curved grating focal spot is measured using simulation and experimental data

In another experiment, a 120° sector angle curved grating is illuminated at three different positions, (see Fig. 4-16). The NSOM scans show that the coupled surface plasmons are directed along the grating vector (normal to the grooves at the spot). This is also again analogous to the performance of classical optical lenses which bend the light beams towards the focal spot.

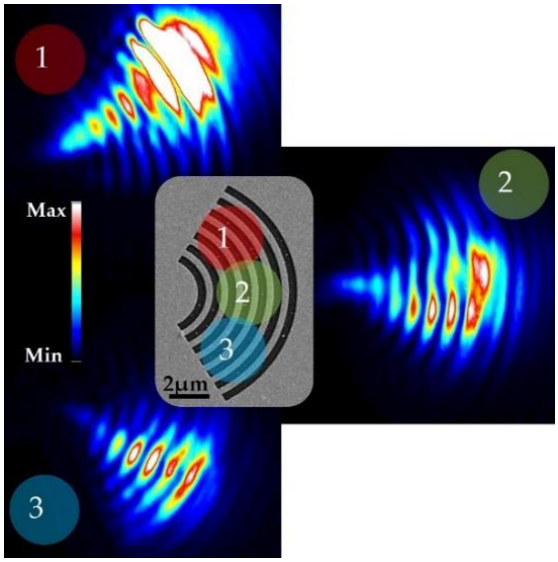

Fig. 4-16 illuminating the 120° sector angle curved grating on three different spots illustrates the coupling of the surface plasmons along the grating vector at each spot. The coupled surface plasmon intensity is proportional to the cosine of the angle between the polarization direction and the grating vector ($cos\alpha^2$)

It was assumed in Eq. 4-1 that the electric field of the coupled surface plasmons at each point of the grating grooves is proportional to the cosine of the angle between the grating vector and the polarization direction at that point (α, in Fig. 4-2). As a result, the intensity of the coupled surface plasmons along the grating vector at each point (P) of the grooves would be proportional to;

$$I_P \propto cos^2\alpha \qquad \text{Eq. 4-2}$$

On integrating over each groove section, the total intensity of the surface plasmons coupled by the grating through a given aperture is given by;

$$I_{total} \propto \int_{-\beta}^{\beta} cos^2\alpha \; d\alpha \qquad \text{Eq. 4-3}$$

with β as half of the sector angle (as defined in Fig. 4-2).

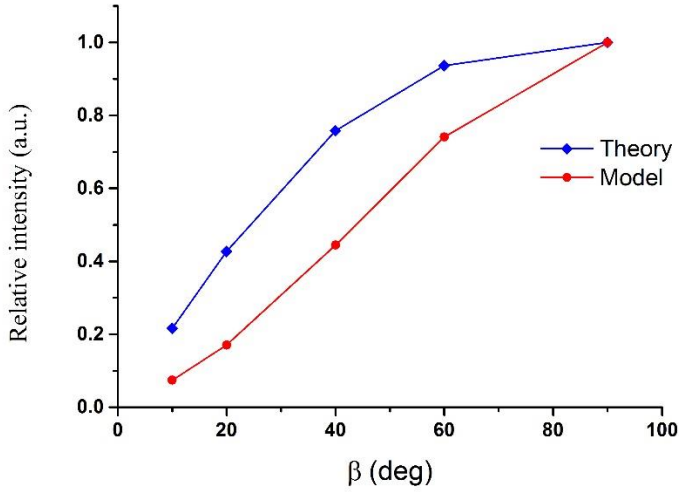

Fig. 4-17 Intensity of surface plasmons at the radial centre of the curved grooves calculated by theory and COMSOL simulation

Fig. 4-17 compares the result of numerical calculation of Eq. 4-3 with simulation results by COMSOL. The intensity for different angles are normalised to the intensity of maximum intensity which occurs for the maximum angle $\beta = 90^{\circ}$. Both graphs for the numerical calculations and COMSOL simulations show that by increasing the sector angle the intensity of the surface plasmons at the centre of curved gratings increases. However, for angles smaller than $\beta = 90^{\circ}$ there is an offset for different angles. It can be due to the fact that here it is assumed that while the surface plasmons are concentrated in the radial centre of the curves, for smaller angles than $\beta = 90^{\circ}$, or in other words half-circular gratings, the surface plasmon distribution expands around the focal spot.

In addition, as the sector angle of surface plasmons is increased, the coupling of the surface plasmons increases. As a result, we define the numerical aperture (NA) of these plasmonic lenses as;

$$NA = \int_0^{\beta} cos^2\alpha \; d\alpha = \frac{sin2\beta}{4} + \frac{\beta}{2} \qquad \text{Eq. 4-4}$$

In order to demonstrate the appropriateness of the defined NA, we plot the reciprocal of the NA against sector angles in Fig. 4-18 (solid black line). The fitted line closely agrees with the simulation and experiment results for the focal width, analogous to the inverse of NA for classical optical lenses.

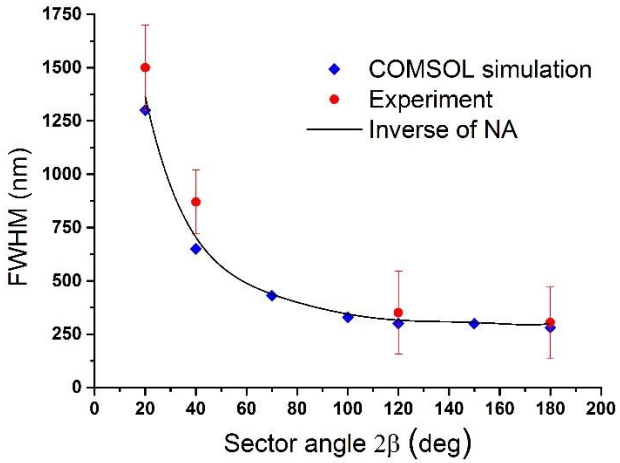

Fig. 4-18 The black line is the reciprocal of the analytically defined numerical aperture (NA) from Eq. 4-4, and it fits closely with the data from the simulations and experiments

Plasmonic lenses can couple and direct surface plasmons into the focal spot while also allowing access to the focal spot for further processes. In addition, according to Eq. 4-3, adjustment of the curved grating sector angle changes both the quantity and quality (focusing) of the coupled surface plasmons.

4.2 Impact of the number of grooves on the performance of curved gratings

As the theoretical definition and results shows (Eq. 4-4) the distribution of the concentration of surface plasmons depends on the sector angle of the curved grooves [19, 52, 118-123]. The simulation results also show that the change of the number of the grooves does not affect the distribution of the concentration of surface plasmons. However, increasing the number of grooves of a grating generates additional surface plasmons and affects the intensity of the surface plasmons at the focal spot.

The propagating surface plasmons gain a phase change when passing across other single grooves. Constructive interference of the coupled surface plasmons when passing across other grooves depends on the period of the grating and the other geometrical parameters, particularly, the width of the grooves. It is shown in Chapter 3 that for a multi-groove linear grating, the best coupling for normal-incidence light occurs when the period of the grating exactly matches the surface plasmon wavelength and the width of the grooves is half of the surface plasmon wavelength or half of the grating period. The wavelength response of the curved gratings (Fig. 4-9) illustrates that the curved grating period determines the constructive interference of the excited surface plasmons at each groove, analogous to the linear grating ones. As a result, in this discussion we neglect the role of phase changes for the propagating surface plasmons across other single grooves.

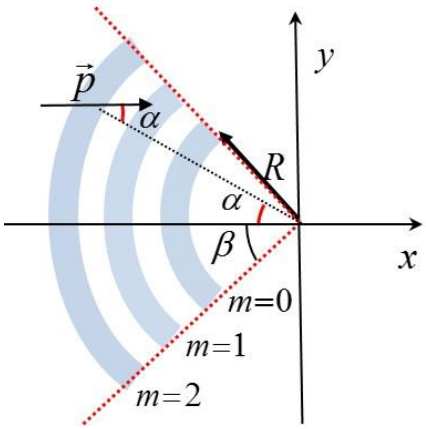

Fig. 4-19 curved grating illustrating the number of grooves and other geometrical parameters

With an increase in the number of grooves, the radius of the curves approaches the surface plasmon propagation length and the field enhancement at the focal spot of the curved gratings is reduced due to damping of the surface plasmons at the gold-air interface. In addition, the length of each groove is increased. This increase is proportional to the radius of the groove, and the sector angle of the curved gratings. The intensity enhancement does not rise linearly with increasing sector length. It is shown in Chapter four that the generation of surface plasmons at each point of the grooves is proportional to the square of the cosine of the angle between the light polarization and the groove vector at that point ($\cos(\alpha)$). However, since all the grooves have identical sector angle, by integrating over sector angle the cosine term results in the same multiplication factor. In addition, by normalising the length of the added grooves to the length of the first groove with the smallest radius the sector angle factor is omitted. First, we assume that the electromagnetic field is proportional to this ratio as $((R + m\Lambda_g)/R)$ and as a result the intensity enhancement is proportional to

the square of this ratio, see Fig. 4-19. The accuracy of this assumption is examined as the first step, and then is used to study the effect of increasing the number of grooves.

By considering the fact that for large sector angles ($2\beta > 100^{\circ}$) the coupled surface plasmons are focused at the centre of the curved gratings, the analytical expression for the intensity enhancement (I) of surface plasmons at the focal spot (centre of the curved gratings) is proportional to the following terms;

$$(I)_{sp}^{\boldsymbol{m}} \propto \left(\frac{R+\boldsymbol{m}\Lambda_g}{R}\right)^2 T^{2\boldsymbol{m}}\, e^{\frac{2(R+\boldsymbol{m}\Lambda_g)}{l}} \qquad \text{Eq. 4-5}$$

where m is the groove number, R is the radius of the first groove with smallest radius, Λ_g is the grating period, and l designates the propagation length of surface plasmons. When surface plasmons propagate across other grooves their intensity would be modified by a transmission coefficient (T). Therefore the total transmission coefficient when surface plasmons cross multiple grooves is accounted by T^m in which m designates the groove number.

In order to derive this analytical expression, we consider illumination of a curved grating at $\lambda_0 = 810$ nm. The propagation length of the surface plasmons at the gold-air interface is $l = 45$ μm at this wavelength. At the first step we consider the ideal situation of full transmission of surface plasmons across other grooves with $T = 1$. The graphs in Fig. 4-20 demonstrate the intensity enhancement versus the groove number for two different expressions of the function; when the ratio $(R + m\Lambda_g)/R$ is taken as the correct form of the expression (1) and when the square of the ratio of the radii is considered (2). In graph (1), at around the 25th ring the added intensity reaches its maximum value. However, in graph (2) this maximum value is reached at 57th

groove. In theory, one expects that for an ideal situation of complete transmission of propagating surface plasmons across other grooves, the enhancement of the surface plasmons continues to increase with additional grooves until the radius of the grooves reaches the propagation length of the surface plasmons. Beyond this radius the intensity enhancement reduces. Considering the propagation length of surface plasmons at this wavelength, this groove number is $l = 45\ \text{nm} = 0.790\ \text{nm} \times m$ which results in $m = 57$. This value is exactly the one that is achieved by the square of the ratio of radii ($\left(\frac{R+\boldsymbol{m}\Lambda_g}{R}\right)^2$) in graph (2). Thus the proposed form of the intensity enhancement in Eq. 4-5 is consistent with simulations.

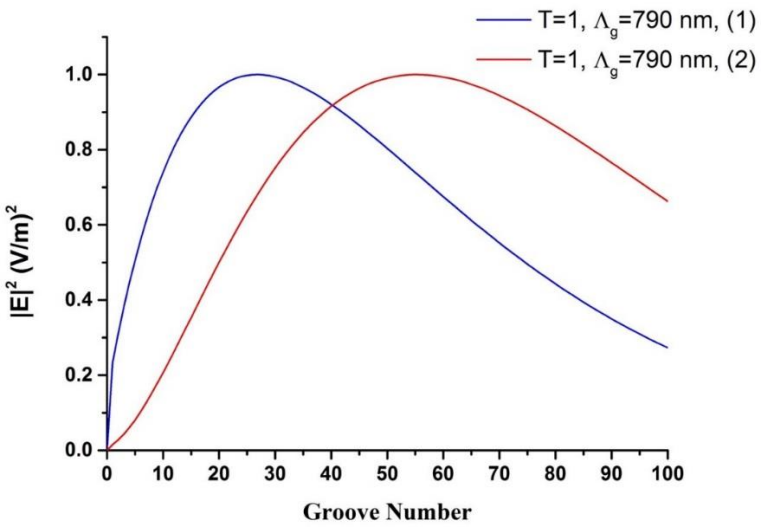

Fig. 4-20 The proportionality of the enhanced intensity versus the groove number is plotted for (1) $(R + m\Lambda_g)/R$ and (2) for $((R + m\Lambda_g)/R\ )^2$

Fig. 4-21 also shows the change in the groove number that creates the maximum intensity enhancement of surface plasmons at the focal spot for $T = 0.9$ & 0.8. With a

decrease in the transmission of the propagating surface plasmons, the groove number of the maximum enhancement decreases, as expected.

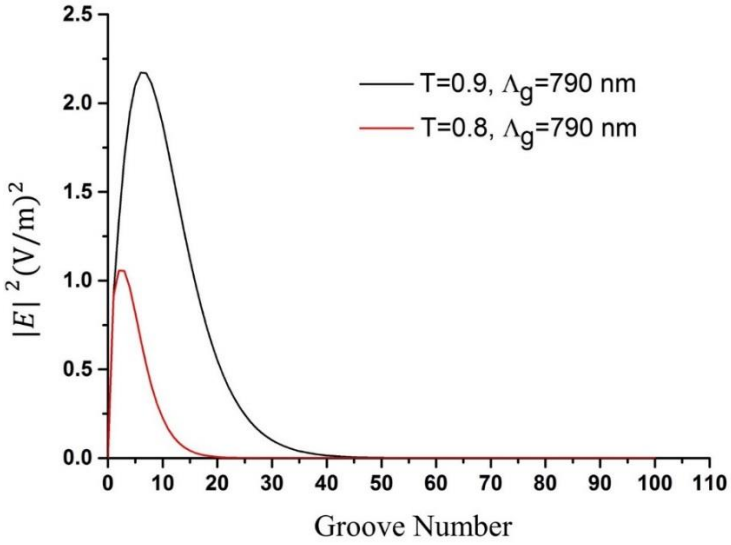

Fig. 4-21 Enhancement of the intensity for transmission factors less than 1: showing a very strong dependence on the transmission factor

In addition, calculation of the total intensity enhancement at the focal spot requires the sum of the intensity enhancement of all the grooves. As a result we have;

$$I \propto \sum_{m} \left(\frac{R+m\Lambda_g}{R}\right)^2 T^{2m}\, e^{\frac{2(R+m\Lambda_g)}{l}} \qquad \text{Eq. 4.6}$$

In Fig. 4-22 the behaviour of the total field enhancement for an ideal transmission of propagating surface plasmons ($T = 1$) is illustrated.

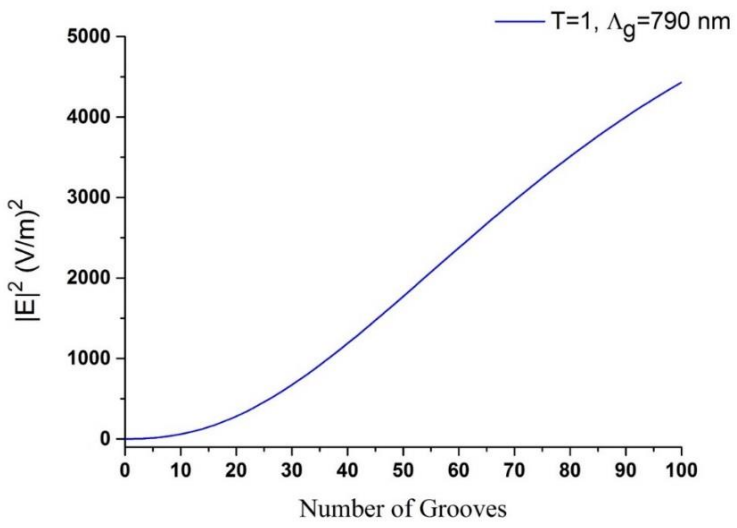

Fig. 4-22 Change in total intensity by groove number for an ideal transmission (T=1)

Fig 4-22 shows that even up to 100 grooves the field is enhanced, though the slope of enhancement changes somewhere between 50 to 70 grooves. Decreasing the transmission coefficient dramatically changes the effective number of grooves, illustrated in Fig. 4-23.

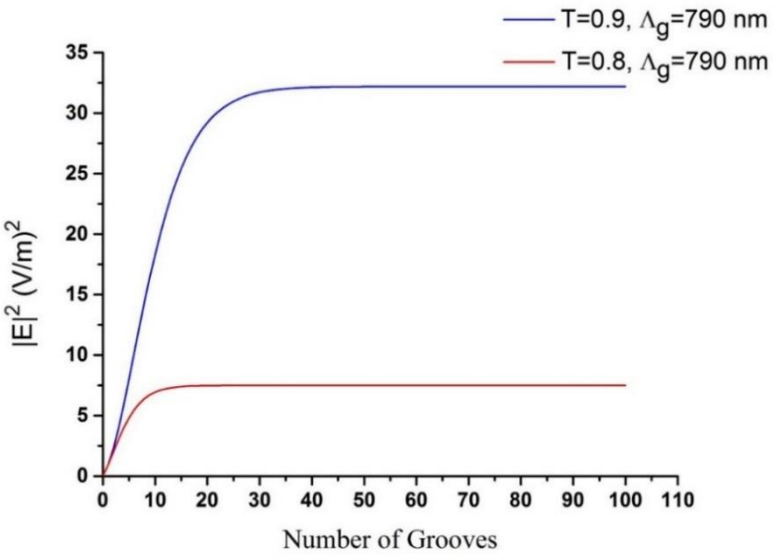

Fig. 4-23 Change in total intensity by groove number for transmission factors less than one (T=0.8, 0.9)

The COMSOL simulation is also used to investigate the effect of adding grooves to the curved gratings. The simulation is accomplished for a curved grating with sector angle of $2\beta = 120^{\circ}$. The grating period is chosen $\Lambda_g = 790$ nm (to be illuminated at $\lambda_0 = 810$ nm) with groove width of half of the grating period and depth of 100 nm according to the optimized values for grating coupling efficiency, in order to minimize the influence of the phase factor in the calculations. Due to the limits of memory and running time, up to seven grooves are considered for the grating. The simulation data show that by increasing the number of grooves up to seven, the intensity of the focal spot increases, see Fig. 4-24. Considering both the milling time of fabricating the curved gratings and also the beam spot size for an efficient grating illumination, this number of grooves was chosen to be fabricated.

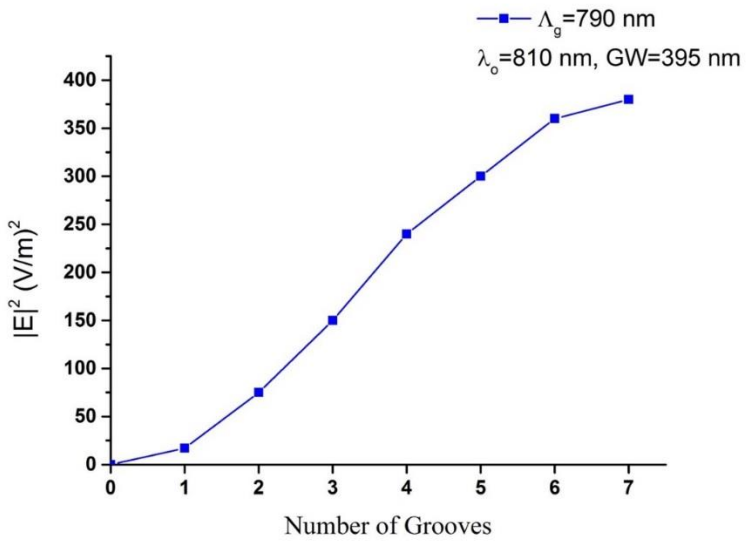

Fig. 4-24 Increase in intensity by increasing the number of grooves (3D) simulation

However, the images in Figs. 4-4, 4-5, 4-8, 4-11, 4-12, and 4-13, show that the length of the hot spot (depth of focus) is larger for smaller sector angles. Fang et al [122] showed that breaking the symmetry of the two faced slits results in focusing surface plasmons at the centre of the structure. Gjonaj et al [123] have also shown that the depth of the focused surface plasmons decreases dramatically. Now we apply the concept of breaking the symmetry of two faced curved gratings to decrease the spotsize of the focused surface plasmons and further enhance the intensity at the hot spot.

4.3 Curved gratings in a symmetry broken configuration

Circular slits and circular gratings have been proposed and investigated as plasmonic lenses to couple and focus surface plasmons at their centre [19, 52, 118-123]. However, the use of circular gratings to focus surface plasmons requires illumination with radially-polarized light. This setup is challenging in practice as one needs to align

the centre of the radially-polarized light beam to the centre of the circular slits. In this section, the performance of circular gratings under illumination by linearly-polarized light (p-polarized) is investigated and then the symmetry-broken configuration of curved gratings for focusing surface plasmons to a single spot is proposed. This investigation is performed by 3D simulations of the structures using COMSOL. The simulation details are identical to those used for investigating curved gratings, so the details of the simulation are omitted.

4.3.1 Circular gratings with a linearly polarized light beam

Illumination of a complete circular grating with linearly polarized light (p-polarized) results in two hot spots on the diameter of the curved gratings along the direction of the light polarization.

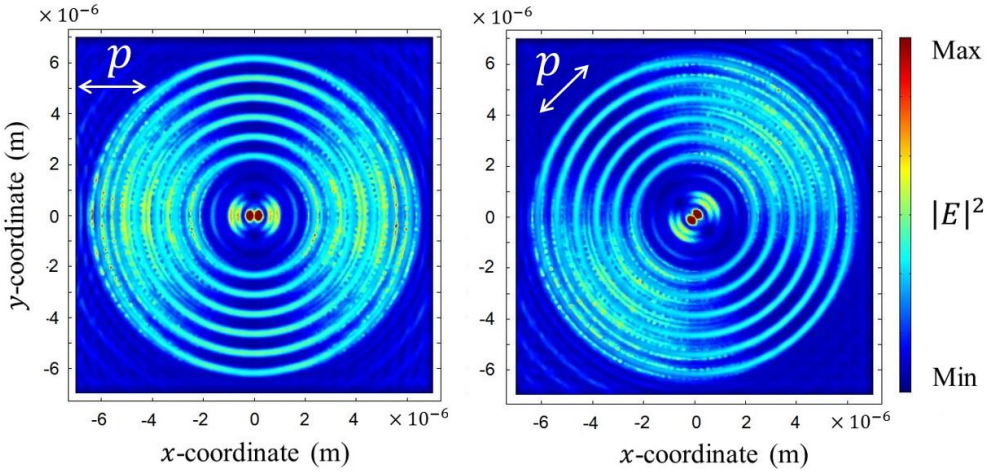

Fig. 4-25 Intensity map of surface plasmons coupled by complete circular gratings. Illumination by linearly polarized light (polarization direction indicated by the arrows on the figures) results in two hot spots along the direction of polarization on the diameter of the circles, $\Lambda_{gr} = 790$ nm, $\lambda_0 = 810$ nm

In Fig. 4-25, the intensity map of the near field of a normally-illuminated complete circular grating illustrates the double hot spot phenomenon along the polarization direction and its change when the polarization direction is rotated by $\frac{\pi}{4}$.

The linearly-polarized light (p-polarized or TM polarized) is scattered at the grooves of the grating, and excited surface plasmons are directed towards the centre of the circular grating. However, for each pair of oppositely placed points on the grooves, the coupled surface plasmons propagate in opposite directions and the normal components of their evanescent fields acquire a $\frac{\pi}{2}$ phase difference relative to each other that results in destructive interference. The in-plane components of the evanescent field of the surface plasmons are in phase and result in constructive interference [110]. Fig. 4-26 illustrates the map of the magnitude of the normal and in-plane components of the near field, E_z and E_x, respectively, and their related profiles along a cut line in the direction of polarization (x-axis) passing through the centre of the structure. The destructive interference of the normal components results in two intense lobes adjacent to the centre of the structure, while the constructive interference of the in-plane components is shown as the central peak with two smaller lobes on the sides.

In addition, a comparison of the magnitudes of E_z and E_x in Fig. 4-26 reveals that the normal component of the evanescent field of the surface plasmons is around four times stronger than the in-plane component. Consequently, E_z constitutes 97% of the total intensity ($|E|^2$) of the evanescent field of the surface plasmons. The illumination

of the circular grating by linearly-polarized light (p-polarized) results in two hot spots adjacent to the centre of the circular rings, as shown in Fig. 4-27.

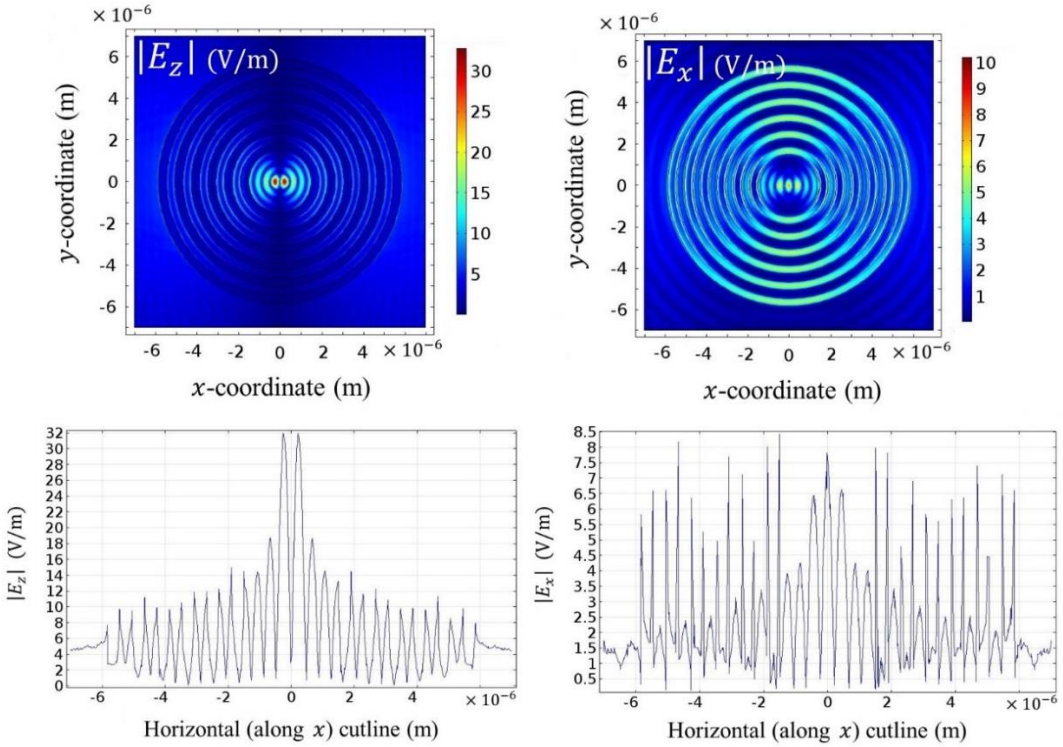

Fig. 4-26 Magnitude of the normal component (E_z) and the in-plane component (E_x) of the evanescent field of the surface plasmons, with their related intensity profile along a horizontal cutline in the direction of the light polarization (x-coordinate in this situation)

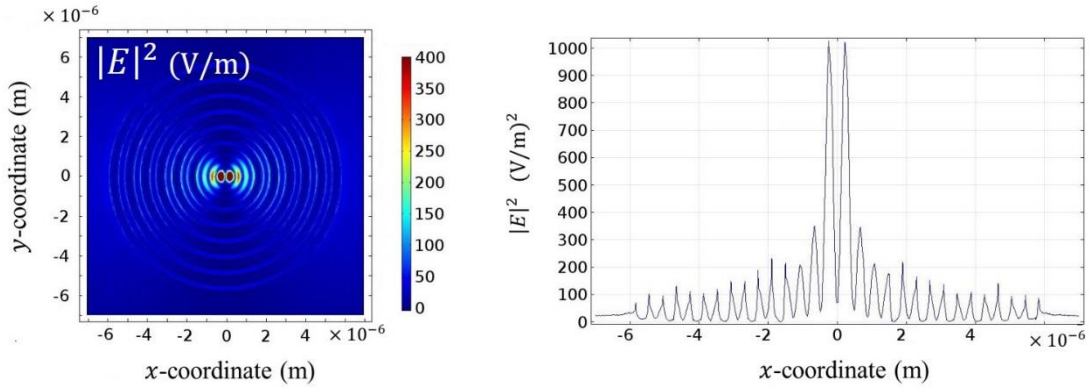

Fig. 4-27, Intensity map of the circular grating illuminated with linearly polarized light (p-polarization) along the x-coordinate with the related intensity profile along a cutline in the direction of the light polarization, $\Lambda_{gr} = 790$ nm, $\lambda_0 = 810$ nm

4.3.2 Symmetry broken curved grating configuration

Asymmetric curved gratings are designed with two facing curved gratings in a symmetry broken configuration in which the centre of each groove of the curved gratings is shifted half of the surface plasmon wavelength relative to the opposite groove, as shown in Fig. 4-28.

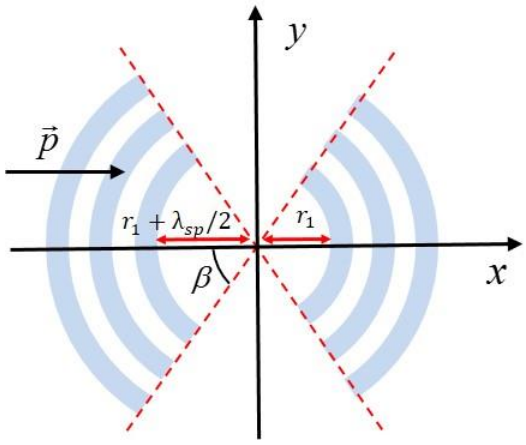

Fig. 4-28 Two facing curved gratings in a symmetry broken configuration; the radius of the concentric gratings are shifted half of the wavelength of the surface plasmons for providing the phase matching condition for the normal component of the evanescent field of surface plasmons (normal to the plane of the image)

Illumination of a symmetry broken configuration grating with linearly polarized light, results in the coupled surface plasmons being focused at the centre of the structure. Fig. 4-29 (a) shows the focused surface plasmons from a single curved grating illuminated with linearly polarized light, and (b) illustrates the performance of curved gratings in focusing surface plasmons when two curved gratings facing each other in the symmetry broken configuration are illuminated at $\lambda_0 = 810$ nm with linearly polarized light. The sector angle of each grating is 160° ($2\beta = 160^\circ$), which

results in highly focused surface plasmons with a small focal spot width. The other details of the gratings are identical to those used for the curved gratings in the previous sections.

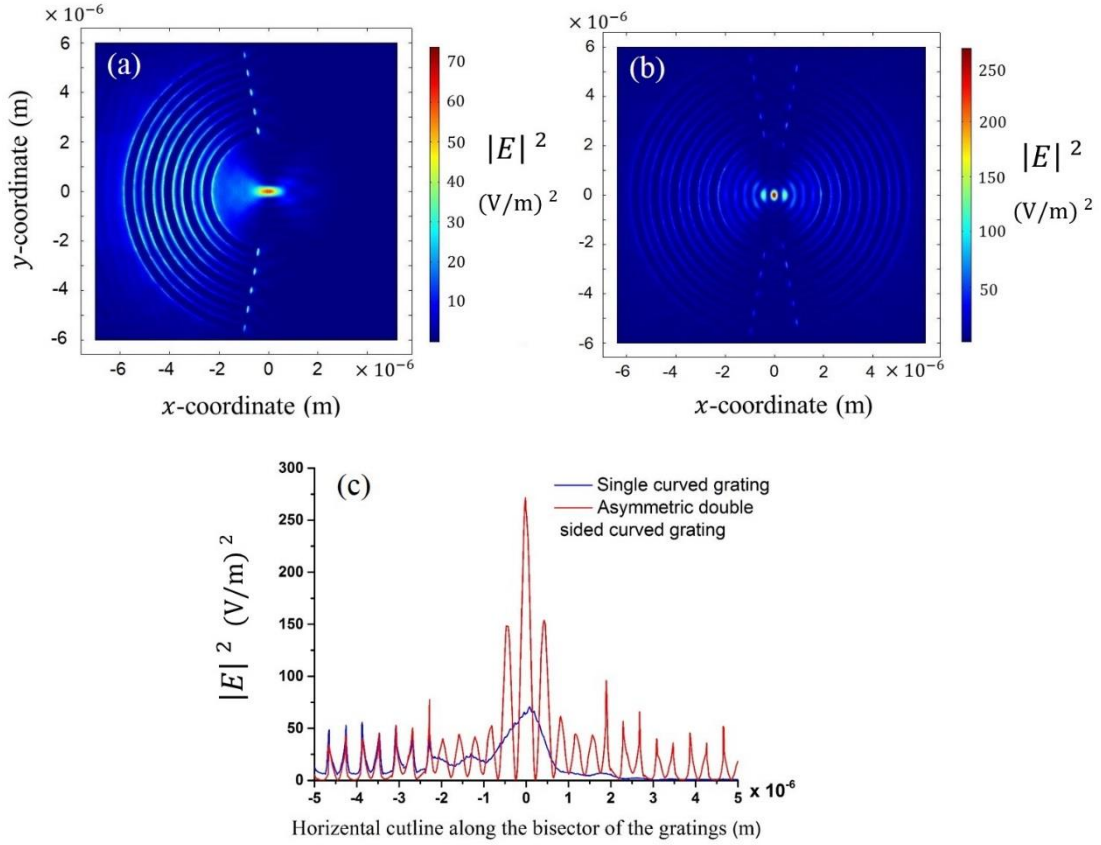

Fig. 4-29 (a) curved grating with sector angle of $2\beta = 160^{\circ}$ illuminated with linearly polarized light (along the x-coordiante) shows the focusing of surface plasmons. The two facing curved gratings in a symmetry broken configuration focus surface plasmons at the centre of the curved gratings, (c) shows the change in the intensity profile (along the x axis) for both the curved gratings and double sided curved grating in an asymmetric configuration

A comparison of the intensity profile of the hot spot on a horizontal cut line along the bisector of the curved gratings (the x-coordinate in Fig. 4-29 (c)), reveals that the length of the hot spot (depth of focus) decreases considerably from 800 nm for a

single curved grating to 240 ± 60 nm for the asymmetric double-sided configuration of the identical gratings. In addition, the intensity of the peak of the hot spot is enhanced for the asymmetric configuration, resulting in a very sharp focus of the surface plasmons.

Moreover, it is possible to control the intensity of the focal spot for the asymmetric configuration by changing the number of the grooves. Fig. 4-30 shows that by increasing the number of the grooves of the asymmetric curved gratings, the intensity of the peak of the sharp focal spot increases. This design offers another approach to manipulate the focused surface plasmons.

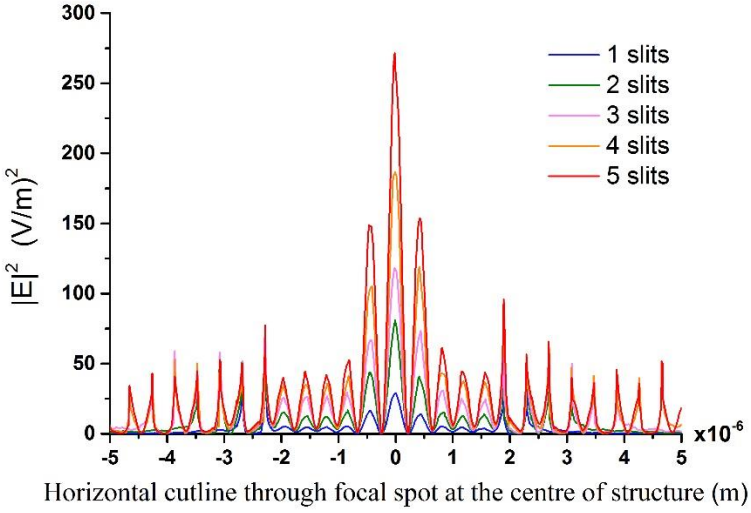

Fig. 4-30 Intensity profile along x-coordinate in Fig. 4-21(the bisector of the asymmetric curved grating configuration), for different number of grooves (slits) per each curved grating

4.3.3 Conclusion

We have shown that curved gratings (sectors from full circular gratings) focus coupled surface plasmons at their radial centre. The width of the focused spot changes with changing sector angle of the gratings. Based on this, the numerical aperture (NA) of these surface plasmon lenses is defined and the reciprocal of the defined NA versus the sector angle fits closely to the measured focal widths, demonstrating the accuracy of the definition of NA for these curved gratings.

The performance of the curved gratings under illumination with linearly polarized light (p-polarized), is in contrast to the focusing properties of full circular gratings which require illumination with radially-polarized light. Radial polarization illumination is challenging in practice as it needs alignment of the centre of the beam with the centre of the circular gratings. In addition, for curved gratings, the focal spot is positioned to one side of the curved grating, allowing access to it for further processes, while for full circular gratings, the focal spot is surrounded by the circular grooves. These properties facilitate the application of these structures in sensing, imaging and even nonlinear plasmonics. The use of these curved gratings for plasmonic waveguides may not be suitable as the results of the next chapter do not show any appreciable advantages for coupling surface plasmons onto plasmonic waveguides.

However, the length of the focused spot of the surface plasmons (depth of focus) from the curved gratings is larger than the width of the focus. It is shown that by placing two curved gratings in front of each other in a symmetry-broken configuration, it is possible to focus the surface plasmons at the centre of the structure with

significantly decreased depth of focus. Moreover, the intensity at the peak of the hot spot increases, depending on the number of the grooves.

The asymmetric configuration results in further enhancement of the performance of curved gratings as plasmonic lenses, particularly for detection and sensing.

Chapter 5: Integrating Curved Gratings with Plasmonic Micro-Stripline Waveguides

With many potentially useful applications in signal processing, there is a goal to develop efficient plasmonic waveguides with subwavelength confinement and long propagation lengths. However, efficient coupling of free-space light into the propagating plasmonic modes of plasmonic waveguides is a significant challenge for this area of nano-photonics. In fact, to couple light into surface plasmon modes of a surface plasmon waveguide, we must overcome the momentum mismatch between surface plasmon modes and free-space light at the same frequency. Plasmonic gratings can provide the additional momentum to couple the light into surface plasmons and plasmonic waveguides [51]. The main challenges for the design of plasmonic gratings are the efficiency of coupling light into surface plasmons and launching these surface plasmons in a single direction.

In this chapter, we investigate the coupling of surface plasmons by curved gratings and linear gratings onto micro-stripline waveguides, and compare the performance of the two kinds of gratings in terms of the propagation length, the efficiency of coupling, and the directionality of the launched surface plasmons. Micro-stripline waveguides are obtained by limiting the lateral width of metal-slab waveguides which leads to

lateral confinement of propagating surface plasmons and consequently, creates a more complex spectrum than for slab waveguides [126].

The specific curved grating design suggests they would be suitable to integrate as couplers for plasmonic waveguides. However, for large sector angles of curved gratings, they are not very efficient to couple surface plasmons onto micro-stripline waveguides for two reasons; first, for larger sector angles the coupling of the incident light into surface plasmons drops by the cosine ($\cos(\alpha)$) of the angle between the normal to the grooves and the tangent to the light polarization (p-polarization), and second, the focusing of the launched surface plasmons onto the strip-line waveguide results in shorter propagation lengths since the focused surface plasmons are not well mode matched to the waveguides, and are scattered out.

5.1 Simulations of the integration of curved gratings with plasmonic waveguides

To compare designs for the integrated configuration of curved gratings with micro-stripline waveguides, an identical aperture size was set to 3 μm for all sector angles. The aperture size of the linear grating was also 3 μm. These aperture sizes are selected for coupling surface launching surface plamsons onto 3 μm micro-stripline waveguides. The width of the stripline waveguide is selected according to the experimental results in reference [127]. Weeber *et al.* show that asymmetric gold stripline waveguides with 3 μm width, or even smaller, support micro-stripline surface plasmon modes at exciting wavelength around 800 nm, with strong lateral mode confinement within the width of micro-stripline waveguide. They also investigate the

effect of waveguide thickness and show that unlike the symmetric stripline waveguides, the gold thickness does not affect the mode configuration of the asymmetric stripline waveguides.

The curved gratings were designed to be illuminated at $\lambda_0 = 810$ nm. As a result, the period of the gratings was selected to be $\Lambda_g = 790$ nm (See Eq. 1-9) with groove width of half the grating period and 100 nm groove depth, equal to the thickness of the gold layer, for five periods. The selected parameters of the curved gratings are chosen according to the grating parameters calculated in Chapter three. The gold stripline waveguide was 3 μm in width and 100 nm in thickness. The boundaries of the simulation cell were scattering boundary conditions, with a meshing element size in the range of $\frac{\lambda}{8} \leq \text{element size} \leq \frac{\lambda}{3}$ for the grating, waveguide, and the surrounding medium.

Grating couplers facilitate experimental alignment for launching surface plasmons onto plasmonic waveguides. The performance of linear gratings for coupling surface plasmons onto plasmonic waveguides have been investigated widely [51, 128-130]. Here we investigate the efficiency of coupling surface plasmons onto micro-stripline plasmonic waveguides using curved gratings and comparing with the efficiency of linear gratings. Therefore, a linear grating with analogous parameters; period of $\Lambda_g = 790$ nm, illuminated at $\lambda_0 = 810$ nm with five periods, a groove width of half of the grating period, and depth of 100 nm, was also simulated. The resulting maps of intensity and out-of-plane field components for the linear grating integrated with a micro-stripline waveguide are presented in Fig. 5-1.

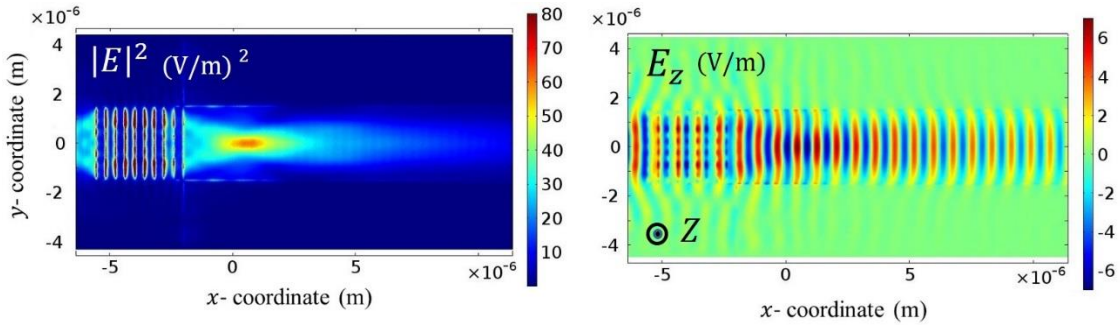

Fig. 5-1 Intensity map ($|E|^2$) and normal field component map (E_z) for a linear grating integrated with a 3 μm width and 100 nm height micro-stripline plasmonic waveguide

The simulation of the integrated configuration of the curved gratings with micro-stripline waveguides for very large sector angles showed that there is no appreciable propagation of focused surface plasmons by the waveguides as the coupled surface plasmons are highly focused at the focal spot inside the waveguide. However, the simulations for the smaller sector angles show propagating surface plasmons on the micro-stripline. As a result, four sector angles; $20^{\circ}, 40^{\circ}, 60^{\circ}, 80^{\circ}$, were selected to study the performance and efficiency of coupling incident light into propagating surface plasmons by curved gratings as shown in Fig. 5-2 (a)-(d). Each pair of images includes the intensity map ($|E|^2$) and the z component of the confined electromagnetic field (E_z) for various sector angles of the curved gratings.

Inspection of the images in Fig. 5-1 shows that even for the integrated linear grating, the coupled surface plasmons are concentrated near the beginning of their propagation on the waveguide. As the plasmons propagate along the waveguide, the wavefront of the propagating surface plasmons evolves to become a plane wave as the mode is established.

This effect also occurs in the case of curved gratings integrated to micro-stripline waveguides. In moving from the smallest (20°) to the largest angle (80°), the coupled surface plasmons become more concentrated when they are launched at the beginning of the waveguide, resulting in an increased curvature of the wavefront. However, as the plasmons propagate along the waveguide, the curvature of the wavefronts decreases and the surface plasmons evolve into plane waves. The figures show that, by increasing the sector angle and consequently the focusing of coupled surface plasmons, the apparent propagation length of the surface plasmons decreases.

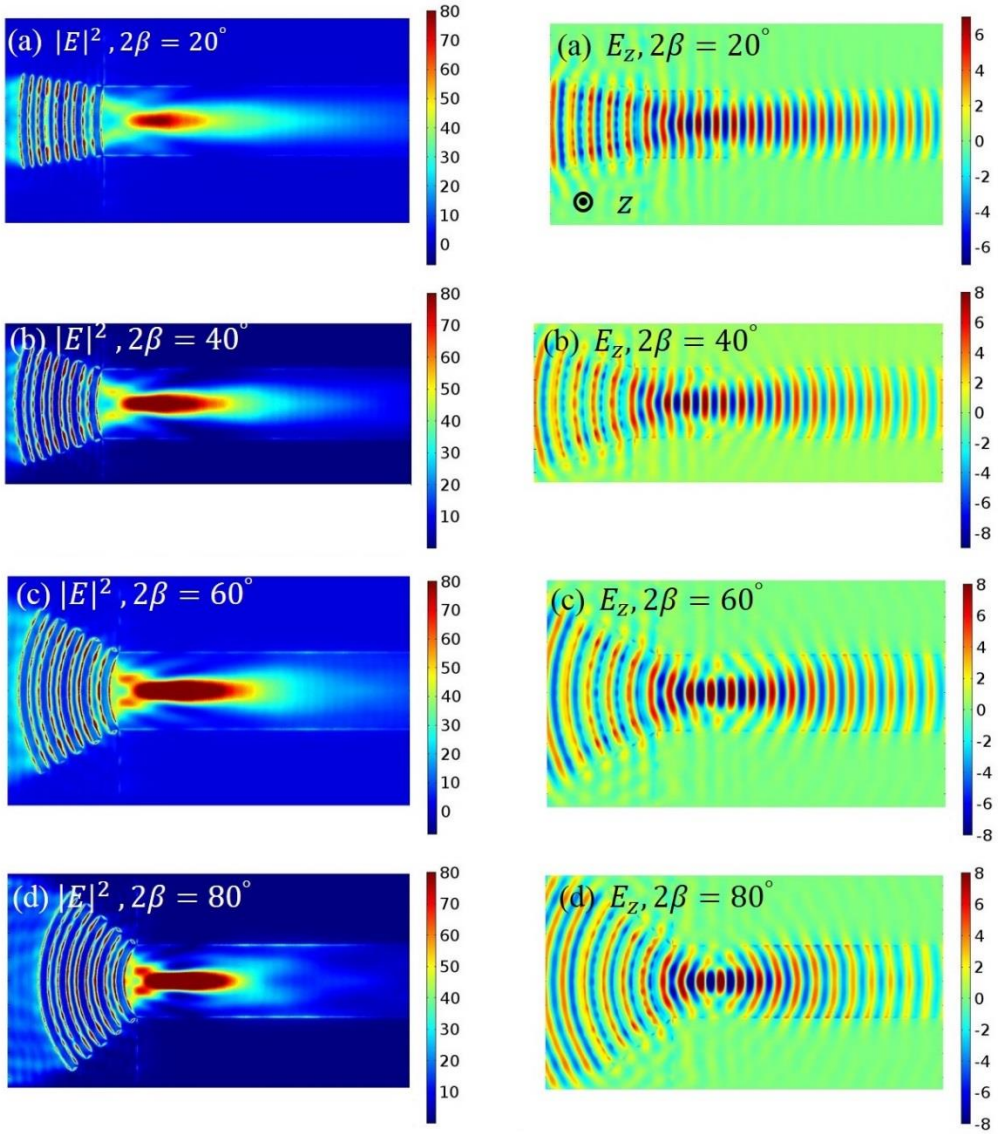

Fig. 5-2 (a)-(d) Intensity ($|E|^2$) map and normal field component (E_z) map for the integrated curved gratings with micro strip-line waveguides with four different sector angles.

The propagation of the surface plasmons launched by the curved gratings with different sector angles is compared in Fig. 5-3. This shows that with increasing sector angle, the surface plasmon propagation length decreases. The intensity profiles are

taken along the bisector of the gratings, where the symmetry axis of the waveguides is along the x axis, at a height of 10 nm above the waveguide surface.

5.1.1 Comparison of propagation length and coupling efficiency

Different approaches are followed to compare the propagation of coupled surface plasmons on micro-stripline waveguides launched by the linear and curved gratings with different sector angles.

Initially, the propagation lengths of the surface plasmons coupled onto the micro strip-line waveguides by the linear gratings and curved gratings with different sector angles were measured from the simulation data. The simulation results show that the effective propagation length of surface plasmons coupled by the linear grating is 4.8 μm. The propagation lengths of surface plasmons coupled by the curved gratings with different sector angles were measured. Fig. 5-3 shows that with increasing sector angle of the curved gratings the surface plasmon propagation length of decreases in comparison to the linear grating surface plasmon propagation length.

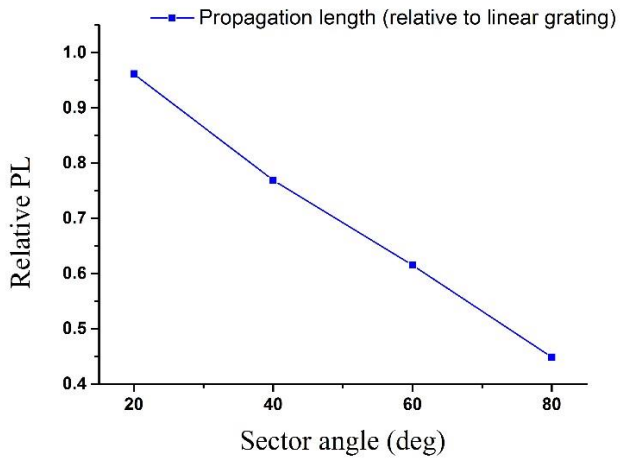

Fig. 5-3 Ratio of the propagation length of the curved grating surface plasmons to the linear grating surface plasmons

In addition, we measure the coupling of surface plasmons by the linear grating and compare it with the coupling of surface plasmons by the curved gratings with different sector angles. For the quantitative comparison of the coupling of surface plasmons by different gratings, the intensity of the surface plasmons was measured over an area with a width equal to the waveguide width and a length twice the surface plasmon wavelength, starting where the grating contacts the waveguide (red parametric surface in Fig. 5-4).

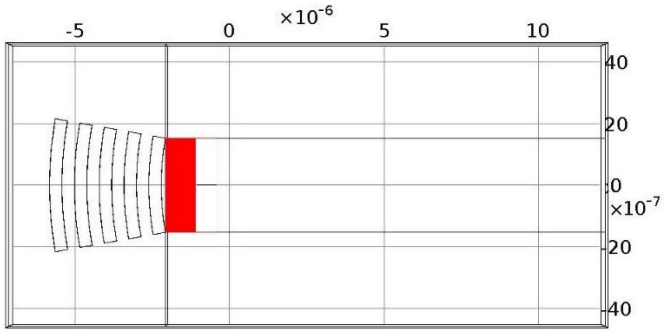

Fig. 5-4 A 20° sector angle curved grating integrated with a micro-stripline waveguide. The intensity was measured over a parametric surface (red rectangle) with a width equal to the width of waveguide and a length of twice of the surface plasmon wavelength

The ratio of the measured intensity of the coupled surface plasmons from the curved gratings with different sector angles to the intensity of the surface plasmons coupled by the linear grating was measured and is plotted in Fig. 5-5 (red squares). Fig. 5-5 shows that by increasing the sector angle of the curved gratings the intensity of the surface plasmons coupled into the waveguide increases compared with the intensity of the surface plasmons coupled into the waveguides by the linear gratings.

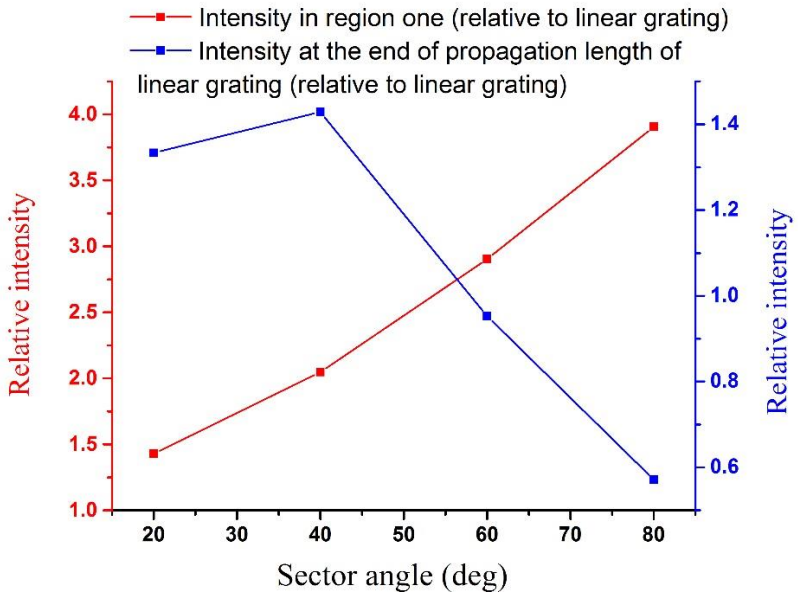

Fig. 5-5 Quantitative comparison of the intensity of the surface plasmons coupled onto the micro-stripline waveguides by the curved gratings with different sector angles

We attribute the decrease in propagation length and also the increase of the coupling of surface plasmons by the increase of curved grating sector angle to the focusing property of the curved gratings; as the sector angle increases, the coupled surface plasmons are more focused onto the waveguide, and this leads to the surface plasmons diverging as they propagate in the waveguide. This divergence results in the excitation of different modes of the propagating surface plasmons along the waveguides, with different propagation lengths. This effect is shown in the intensity and normal field component maps in Fig. 5-2. Fig. 5-6 also shows the distribution of the magnitude of the normal component of the fields ($|E_z|$) at 8 μm distance from the grating, on a cut plane normal to the waveguide, demonstrating the evolution of the launched surface plasmons to different modes by changing the sector angle of the curved gratings.

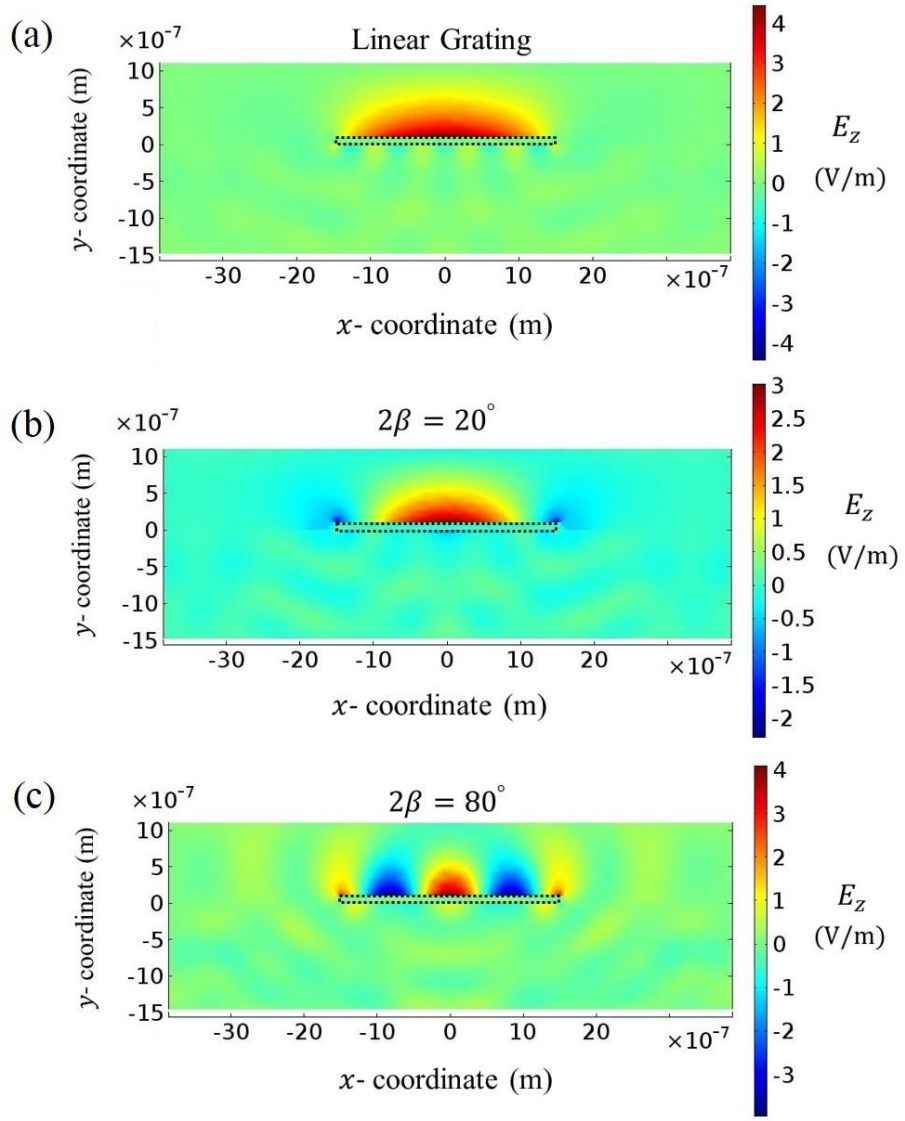

Fig. 5-6 Map of the normal field component of the surface plasmons on a cut plane normal to the micro-stripline waveguide. The waveguide cross section is distinguished with dotted black lines. (a) is for a linear grating coupled to a waveguide, (b) and (c) are for curved grating with sector angles of 20° and 80°, respectively

In addition it is also expected that the intense coupled surface plasmons at the beginning of the waveguide do not propagate efficiently along the waveguide. Because

of the greater NA and surface plasmon divergence with the larger sector angles, the propagating surface plasmons partly diverge and are scattered out at the edges of micro-stripline.

The intensity of the surface plasmons at a distance equal to the propagation length of the launched surface plasmons from the linear grating was measured for the integrated configuration of the linear grating and for the curved gratings with different sector angles. This was performed by measuring the intensity of the propagating surface plasmons over an area identical to the dimensions of the previous parametrized surface (red parametrized surface in Fig. 5-7).

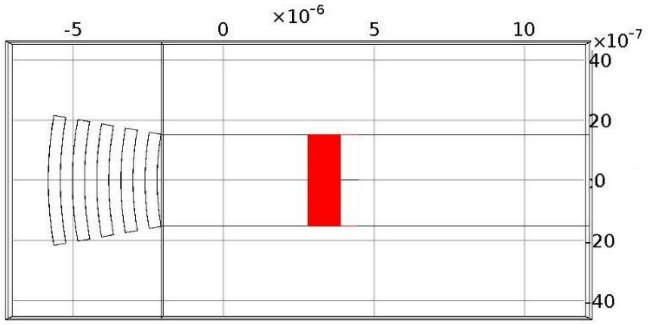

Fig. 5-7 The parametrized surface (red rectangle) at the end of the propagation length of propagating surface plasmons coupled by the linear grating

The intensity of the surface plasmons coupled from the curved gratings integrated to the waveguide relative to the surface plasmons coupled from the linear grating integrated to the waveguide is calculated and plotted (blue squares in Fig. 5-4). Fig. 5-4 shows that for the 20° and 40° sector angle curved gratings, the intensity of the coupled surface plasmons that propagate over a $4.8\,\mu m$ distance (the propagation length of the surface plasmons on the waveguide with the linear grating) is comparable

with the intensity of the surface plasmons coupled by the linear grating. While this appears contrary to the former calculated propagation length for these sector angles, consider that the propagation length was calculated according to its definition as the distance by which the intensity of surface plasmons drops to $\frac{1}{e}$ of its maximum value. Since a fraction of the surface plasmons are lost because of the focusing and increased divergence, the propagation length appears smaller. Consequently, for larger sector angles, as the focusing becomes more confined, losses due to the divergent surface plasmons increase.

To summarize the above comparisons, we note that by increasing the sector angle of the curved gratings an increased surface plasmon intensity can be launched onto the micro-stripline waveguides through a given acceptance aperture. However, for the small sector angles ($20^{\circ}$and 40°) the intensity of the coupled surface plasmons after one propagation length of the surface plasmons coupled by the linear grating was comparable to the intensity of the coupled surface plasmons on the waveguides from the linear grating. For larger sector angles, the launch efficiency of the surface plasmons increases but due to the surface plasmon focussing, a considerable fraction of the surface plasmon intensity is lost due to the increased divergence.

5.1.2 Energy efficiency

The energy efficiency of coupling light to surface plasmons is directly related to the efficiency of coupling surface plasmons compared with the light collecting area of the gratings. In effect, for gratings with identical surface plasmon coupling effectiveness

and identical illumination power density of the grating region, the gratings with smaller areas are more energy efficient.

The energy efficiency (the grating efficiency (γ)) of the various gratings was determined as the ratio of the coupled surface plasmon intensity in the waveguide for gratings integrated to stripline waveguides (C_g), assuming a definite aperture size, compared to the grating area (A_g);

$$\gamma = \frac{coupled\ surface\ plasmons\ onto\ the\ waveguide}{light\ collecting\ area\ of\ the\ grating} = \frac{C_g}{A_g} \qquad \text{Eq. 5-1}$$

Consequently, the relative coupling efficiency of the two kinds of gratings (γ_r) can be calculated as follows;

$$\gamma_r = \frac{\gamma_1}{\gamma_2} = \frac{C_{g1}}{C_{g2}} \times \frac{A_{g2}}{A_{g1}} \qquad \text{Eq. 5-2}$$

As a result, to calculate the coupling efficiency of the curved gratings relative to the linear gratings, the calculated intensity of the coupled surface plasmons from the curved gratings relative to the surface plasmon intensity from the linear grating, is multiplied by the ratio of the linear grating area to the area of the curved grating.

These values were calculated from the intensity of the coupled surface plasmons on a parametrized surface on the waveguide. The results of section (5.1.1) above concerning the propagation of the coupled surface plasmons due to the curved gratings suggest that it is appropriate to use a parametrised surface beyond the propagation length of the surface plasmons coupled by linear gratings as a reference for the measurement. As a result, the intensity was measured over the area of a parametrised

surface with dimensions identical to the previous ones positioned at a distance of 5.8 μm along the waveguide, beyond the propagation length of the coupled surface plasmons from the linear gratings onto the plasmonic waveguide. This calculated relative efficiency is plotted as a graph against the sector angle of the curved gratings in Fig. 5-8.

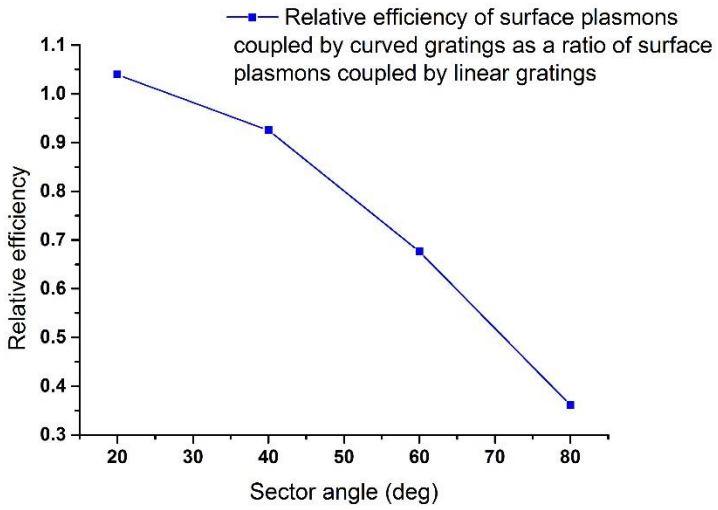

Fig. 5-8 Relative efficiency of the coupled surface plasmons from curved gratings integrated to micro-stripline plasmonic waveguides compared with the coupled surface plasmons from linear gratings integrated to an identical plasmonic waveguide (γ_r)

Fig. 5-8 shows that for curved gratings with sector angles equal to or smaller than 40° ($2\beta \leq 40^{\circ}$), the energy efficiency of the curved gratings is comparable to that of linear gratings. For larger sector angles, though the increase in sector angle results in increased grating area, the energy efficiency is smaller for two reasons;

- First, focusing of the surface plasmons by the grating results in loss of a fraction of the coupled surface plasmons scattered by the edges of the grating and,

- Second, in Chapter four it was shown that the coupling of surface plasmons at any point on the grooves of the curved gratings drops proportional to the square of the cosine of the angle between the light polarization at that point and the normal to the groove at that point (grating vector), $\cos\alpha^2$. However, for linear gratings, the coupling is proportional to the area of the grating.

In addition, for curved grating with sector angle of 20° the efficiency is slightly larger than that of linear grating. In fact, for very small sector angles the limit of $\cos\alpha$ is equal to 1 and the slight increase in the area of the grating results in the increase of the coupling efficiency of the small sector angle curved grating in comparison to the linear grating.

5.1.3 Directionality of surface plasmons coupled by curved and linear gratings

Inspection of the images of surface plasmons coupled by the curved gratings to the micro-stripline plasmonic waveguide in Fig. 5-2 reveals that the coupling of surface plasmons in the backward direction (Fig. 5-9) decreases with increasing sector angle of the curved gratings. However, the image in Fig. 5-1 also illustrates equal backward and forward coupling of surface plasmons by linear gratings.

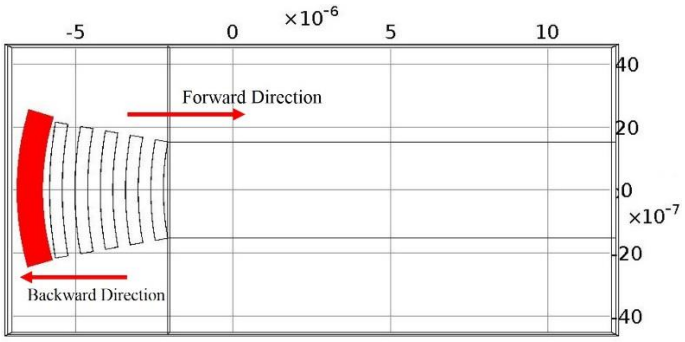

Fig. 5-9 The arrows illustrating backward and forward directions; the red curved parametrised surface illustrates the area over which the intensity of surface plasmons is measured, The width of the area is twice the wavelength of surface plasmons but with equal sector angle to the sector angle of the curved grating

For a quantitative comparison between the ratios of the forward to backward coupling of surface plasmons by curved gratings, the intensity of the coupled surface plasmons over the parametrised surface in Fig. 5-6 was measured and then the ratio of that average intensity to the intensity over the curved parametrised surface in Fig. 5-9 (the red surface) was calculated for different sector angles. This curved parametrised surface has a width equal to twice the wavelength of the surface plasmons and an equal sector angle to that of the curved grating.

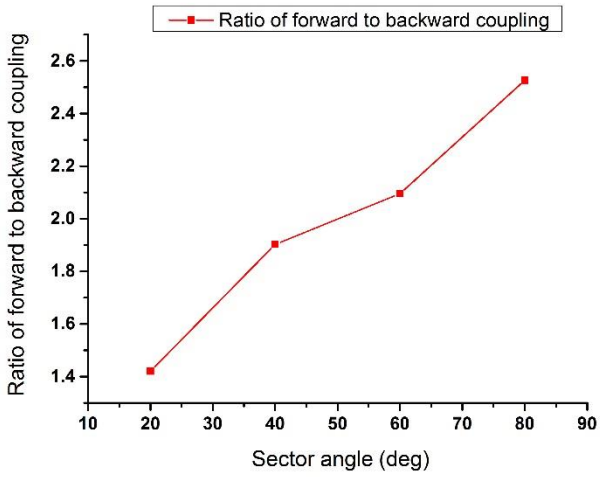

Fig. 5-10 Ratio of forward coupling to backward coupling by curved gratings as a function of sector angle

The calculated ratios for the different sector angles are plotted in Fig. 5-10. The graph shows that though the backwards area (red region in Fig. 5-9) is always larger than the forwards area (red region in Fig. 5-6), for increasing sector angle of the curved gratings, the ratio of the forward coupling to the backward coupling increases, so that the coupling becomes partially directional.

The forward coupling to backward coupling ratio is also measured for the linear grating by measuring the intensity over two identical parametrised surfaces (identical to the one in Fig. 5-6) but at both sides of the grating. This ratio is equal to one, which means for linear gratings the forward coupling is identical to the backward coupling.

To conclude, curved gratings couple surface plasmons more directionally in comparison to linear gratings. Comparing different sector angles of the curved gratings we note that the small sector angle curved gratings have slightly better coupling performance in comparison to that of the linear gratings. The 20° and 40° curved

gratings have improved coupling performance with a coupling efficiency comparable to that of the linear grating, and improved directionality.

5.2 Conclusion

The coupling of surface plasmons by curved gratings onto micro-stripline plasmonic waveguides was investigated, based on the effectiveness of coupling through the grating aperture, the propagation of coupled surface plasmons as a function of the sector angle of the curved gratings, the efficiency of coupling and the directionality of coupling. These parameters were compared to the same parameters for linear gratings when integrated to identical waveguides.

In conclusion, curved gratings with small sector angles 20° and 40° show comparable coupling efficiency to the linear gratings and suggest increased directionality. We determined that there is no significant advantage in using the curved gratings for launching surface plasmons onto micro-stripline waveguides.

Chapter 6: Interaction of Propagating Surface Plasmons with TiO2 Microspheres

The excitation of localized surface plasmons by metallic nano-particles leads to some interesting effects such as subwavelength localization of electromagnetic energy, creation of hot spots at the metal nano-particle surface, or directional scattering of light out of the structure [21, 25]. The latter effect results in the realization of nano-antennas which can transfer the localized near-field electromagnetic energy to the far field. However, the directional radiation of metallic nano-antennas requires an engineered configuration of a large number of nano-structures, which can result in a higher ohmic loss. Dielectric microspheres with high refractive index have been suggested as useful alternatives for metallic nano-antennas. Most previous studies have concentrated on the coupling of dipole emitters to high refractive index microspheres to generate highly directional emission. Reference [30] presents calculations showing TiO_2 microspheres can operate as dielectric antennas by redirecting and radiating the dipolar emission of a dipole in the vicinity of the microsphere.

The aim of this chapter is investigating the interaction of propagating surface plasmons with dielectric microspheres and the potential application of dielectric microspheres to

redirect the propagating surface plasmons as dielectric antennas. We first simulate the performance of TiO_2 microspheres, with a diameter of around one micron (≈ 1 μm) and a rather high refractive index of $n = 1.8$, in decoupling and radiating the evanescent field of propagating surface plasmons. We then show the experimental result of far-field detection of TiO_2 microspheres interacting with propagating surface plasmons.

6.1 Simulation of TiO_2 microspheres interacting with propagating surface plasmons

The interaction of propagating surface plasmons with a TiO_2 microsphere was investigated. We simulated propagating surface plasmons (excited by the Kretschmann configuration) on a 30 nm gold layer on glass, to interact with 950 nm diameter TiO_2 microspheres in their propagation path.

COMSOL multiphysics was used for 2D and 3D simulations of the interaction of TiO_2 microspheres with propagating surface plasmons. The 2D simulation considered a finite part of a 30 nm gold film on glass substrate (with several wavelength thickness) immersed in air, as illustrated in Fig. 6-1. In the simulation, the gold-glass interface was illuminated at the coupling angle, and measured by sweeping a range of angles for each wavelength. This is the same situation when the gold/glass sample is illuminated through a prism, as in the Kretschmann configuration. The TiO_2 microsphere was placed at 4 μm distance from the illumination port.

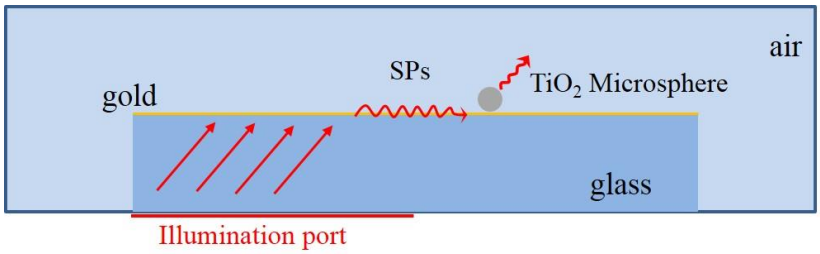

Fig. 6-1 An illustration of the simulation geometry. The gold film is illuminated through half of the glass substrate at the surface plasmon coupling angle

The far-field radiation pattern of the microsphere was measured as the time average of power flow, along a circular parametric line centred at the centre of the microsphere. The aperture size of the radiation was determined as the full width at half maximum (FWHM) of the far-field radiation time-average power distribution for a range of wavelengths from 530 nm to 830 nm. The radiation aperture is plotted against the illumination wavelength as shown in Fig. 6-2.

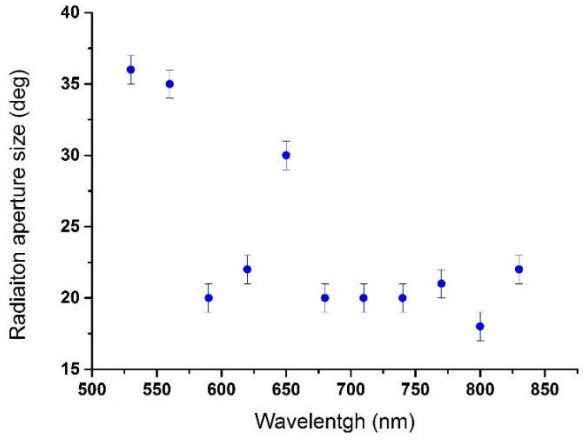

Fig. 6-2 Measured radiation aperture size (defined as full width at half maximum) versus a range of wavelengths

The plotted radiation aperture size indicates that the scattered radiation from surface plasmons exciting the TiO_2 microsphere is directional and depends on the illumination wavelength.

In addition to the radiation aperture size versus wavelength, the peak of the radiation power flow versus wavelength is also plotted in Fig. 6-3. This shows the peak power reaches its maximum at $\lambda_0 = 760$ nm.

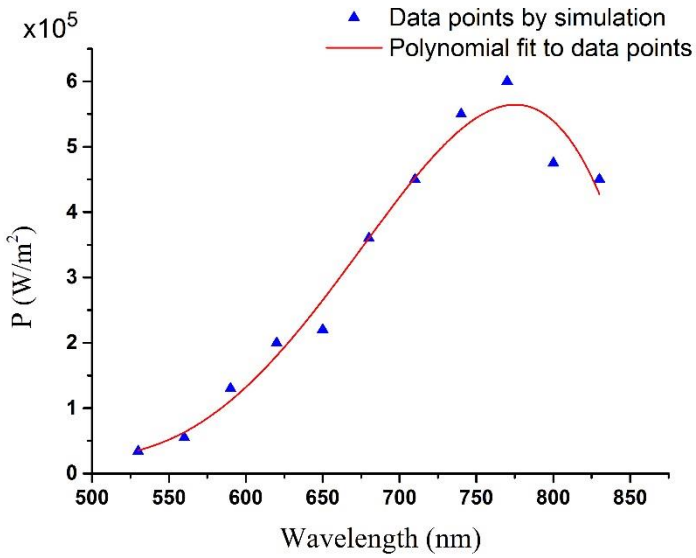

Fig. 6-3 Peak of power flow versus the incident light wavelength

The decrease in the radiation aperture size along with the increase in the peak of the radiation power towards longer wavelengths corresponds to increased directionality at longer wavelengths. In Fig. 6-4 (a and b) the angular distribution of the microsphere radiation for $\lambda_0 = 760$ nm is compared with the angular distribution of radiation for $\lambda_0 = 560$ nm. The comparison shows that radiation aperture at $\lambda_0 =$

760 nm is smaller than that at $\lambda_0 = 560$ nm. However, the peak radiation power is higher at the longer wavelength ($\lambda_0 = 760$ nm).

The TiO_2 microsphere effectively decouples the propagating surface plasmons, radiating the energy directionally. The increase in the peak of the radiated power can be attributed to the effect of the complex dielectric constant of gold at different wavelengths (depends on the dispersion relation of gold) and consequently the initial surface plasmons power decreases by wavelength.

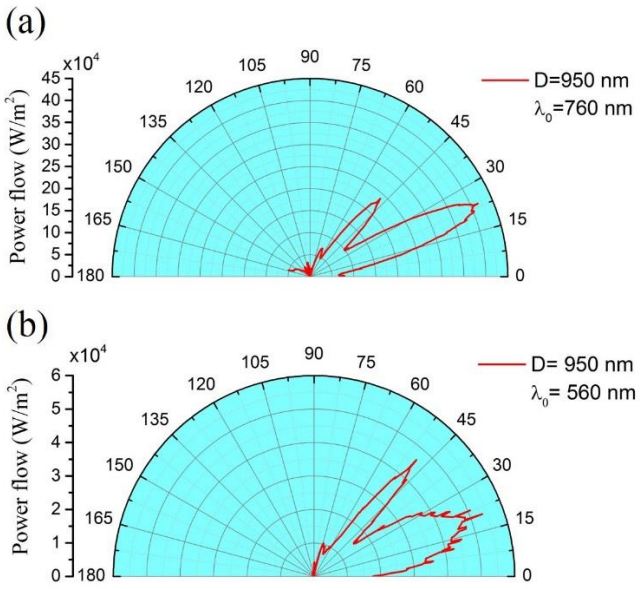

Fig. 6-4 Angular distribution of radiation by TiO2 microspheres at two different wavelengths (a) at $\lambda_0 = 760$ nm and (b) $\lambda_0 = 560$ nm

Incident light at the gold-air interface at $\lambda_0 = 760$ nm (with dielectric constant of $\varepsilon = -20.9 + i\ 1.29$) exhibits stronger surface plasmon coupling at the total internal reflection coupling angle and longer propagation length ($L_{sp} = 38$ μm) in comparison to the coupled surface plasmons at $\lambda_0 = 560$ nm, with a dielectric constant of $\varepsilon =$

$-6.7 + i\ 1.94$ and propagation length of $L_{sp} = 1.6$ μm. In Fig. 6-5 the difference of the coupling of surface plasmons at these two different wavelengths is illustrated by simulations of similar structures (gold / glass substrate immersed in air) in the absence of the TiO_2 microsphere. In order to compare the intensity of the evanescent field of the surface plasmons at the position of the microsphere, the average intensity of the evanescent field of the surface plasmons along a cut line with a length identical to the diameter of the microspheres is measured. This shows 36% decrease in the intensity of surface plasmons by moving from $\lambda_0 = 760$ nm to $\lambda_0 = 560$ nm.

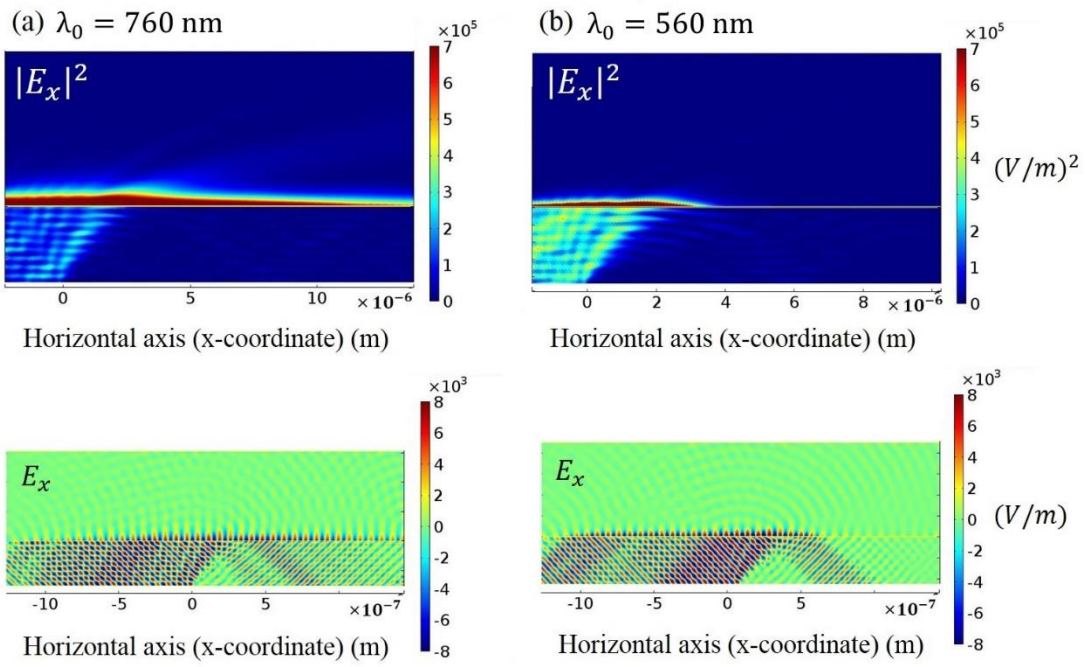

Fig. 6-5 Comparison of the intensity and propagation length of surface plasmons coupled at two different wavelengths (a) $\lambda_0 = 760$ nm and (b) $\lambda_0 = 560$ nm

However, the change in the radiation aperture size is related to the decoupling and redirecting of propagating surface plasmons out of the gold-air interface and can be

attributed to the dispersion of the microspheres at different wavelengths. The interaction of propagating surface plasmons with 2D dielectric optical components such as prisms has been demonstrated by Drezet *et al.* [131]. They show 2D dielectric components redirect the in-plane component (parallel or E_x) of the evanescent field of the propagating surface plasmons, though the exact mechanism of this kind of redirection may be very complicated.

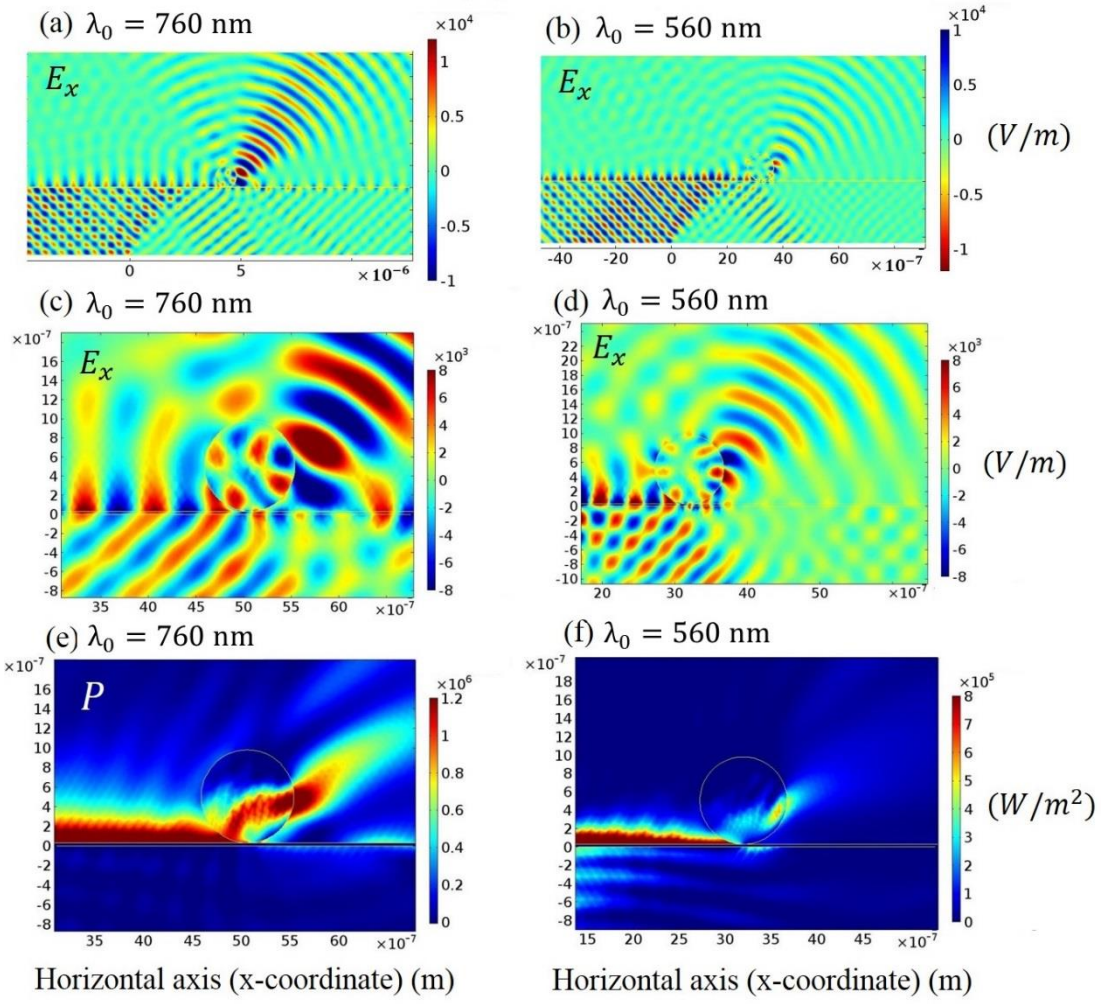

Fig. 6-6 Interaction of a TiO_2 microsphere with propagating surface plasmons coupled at two different wavelengths $\lambda_\circ = 760$ nm and $\lambda_\circ = 560$ nm; (a) and (b) show redirection and decoupling of the E_x field component of the propagating surface plasmons at $\lambda_0 = 760$ nm and $\lambda_0 = 560$ nm respectively, (c) and (d) show the corresponding zoom-in images, and (e) and (f) show the power flow from the TiO_2 microsphere at $\lambda_0 = 760$ nm and $\lambda_0 = 560$ nm wavelengths

The presence of a TiO_2 microsphere changes the direction and momentum of the in-plane component of the field (E_x) resulting in the out-coupling of propagating surface plasmons into air. In Fig. 6-6 the redirection and out-coupling of surface plasmons is illustrated at two different wavelengths ($\lambda_0 = 760$ nm and $\lambda_0 = 560$ nm).

Fig. 6-6 (a) and (b) show the change in direction of the E_x component of the propagating surface plasmons when decoupled and radiated by TiO_2 microspheres. The directionality of the out-coupled field is also obvious from the field map intensity contrast. Fig. 6-6 (c) and (d) show zoom-in images of the same field map to highlight the redirection of the E_x component of the field at the interaction point of the propagating surface plasmons with the TiO_2 microsphere for the two different wavelengths of incident light. In Fig. 6-6 (e) and (f) the time-average power flow of the field is illustrated. Fig. 6-6 (a) to (f) show qualitatively the broadening of the radiation aperture and decrease in the radiated power (along with the decrease in the coupling of the surface plasmons) for the smaller wavelength. In addition, the zoom-in image of the interaction of the propagating surface plasmons with the TiO_2 microsphere at the shorter wavelength ($\lambda_0 = 560$ nm in Fig.6-6 (d)) illustrates the E_x component along the circumference of the TiO_2 microsphere, which resembles the resonance modes of the evanescently coupled field into a microsphere.

In order to investigate the excitation of whispering gallery modes in TiO_2 microspheres, the interaction of microspheres with propagating surface plasmons was simulated with an incident light wavelength of $\lambda_0 = 760$ nm, and three different microsphere diameters; $D =$ 1.2 μm, 1.6 μm, and 2.0 μm.

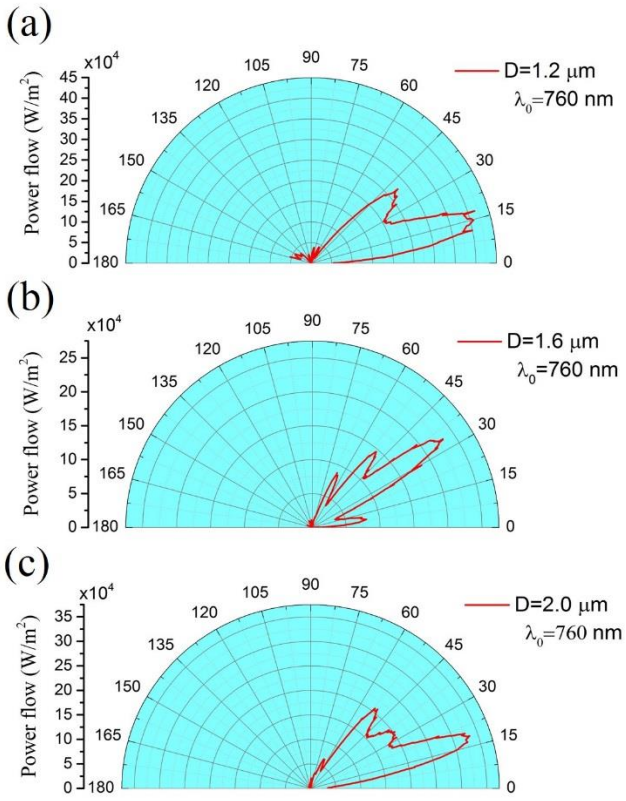

Fig. 6-7 Radiation pattern of TiO_2 microspheres at $\lambda_0 = 760$ nm for three different microsphere diameters; (a) $D = 1.2$ μm, (b) $D = 1.6$ μm, (c) $D = 2.0$ μm

In Fig. 6-7 (a), (b), and (c) the radiation pattern from TiO_2 microspheres with three different diameters shows that the diameter of the microspheres can influence the radiation pattern of the decoupled surface plasmons. For diameters of $D = 1.2$ μm and 2.0 μm, the radiation patterns change as follows; the side lobes become larger and the main peak becomes slightly wider, but the angle of the peak of the radiation power does not change in comparison to that for the microsphere with $D = 950$ nm. However, for the TiO_2 microsphere with $D = 1.6$ μm, the angle of the emitted radiation becomes twice that from the $D = 950$ nm microsphere but the radiation aperture size is slightly smaller than that for the case of $D = 950$ nm. Inspection of

the E_x field map in Fig. 6-8 (a), (b), and (c) reveals that the only difference between the TiO_2 microsphere with diameter of $D = 1.6$ μm and for the microspheres with $D = 1.2$ μm and $D = 2$ μm is the manifestation of cavity resonance modes inside the $D = 1.6$ μm microsphere, with increased radiation power peak angle and a slightly narrower radiation aperture size.

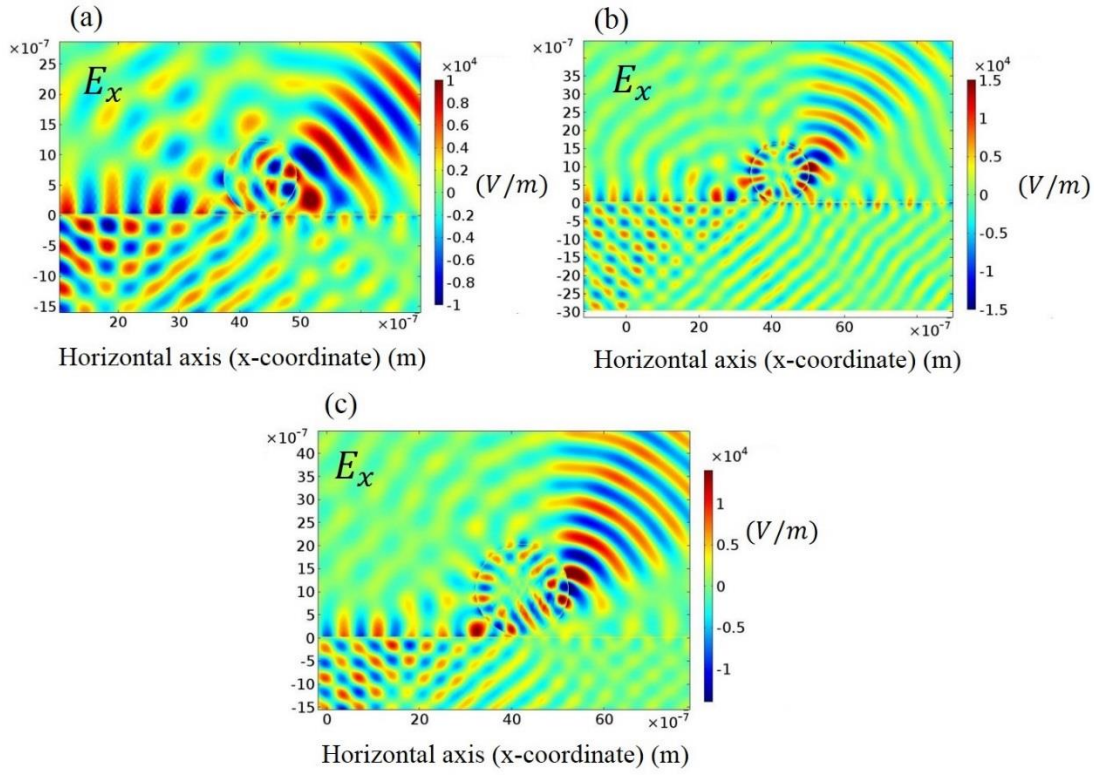

Fig. 6-8 Distribution of the $\boldsymbol{E_x}$ component of the field for TiO_2 microspheres with three different diameters (a) $D = 1.2$ μm (b) $D = 1.6$ μm (c) $D = 2.0$ μm. The incident light is at $\lambda_0 = 760$ nm

In addition to 2D simulations, 3D simulations of the interaction of the decoupling and radiation of propagating surface plasmons through the TiO_2 microsphere was also performed in order to observe the direction and distribution of the radiation. The

configuration of the 3D simulation is very similar to that for 2D simulation, and the illumination was from below the sample (through the left half of the glass substrate). The boundaries were selected as for the boundaries in the 2D simulation and the incident wavelength was $\lambda_0 = 760\,\text{nm}$. Fig. 6-9 (a) shows the map of the E_x component of the field. The propagating surface plasmons are decoupled by the TiO_2 microsphere and the radiation aperture is illustrated with the blue hot spot at the surface of the particle. The power flow is also presented in Fig. 6-9 (b) with the red hot spot as the radiation aperture on the surface of the particles. However, these images are surface field maps and do not show the propagation of the electromagnetic field through the air. In order to demonstrate the radiation of the electromagnetic field through the microspheres a parametrized surface was defined to surround the microsphere, at a far field distance ($\approx 2\lambda_0$), to map the far field E_x component and the average power flow through the microsphere. This is illustrated in Fig. 6-10 which (a) shows the directional emission as a red hot spot on the parametrized surface and (b) shows the corresponding power flow illustrated as a red hot spot on the parametrized surface.

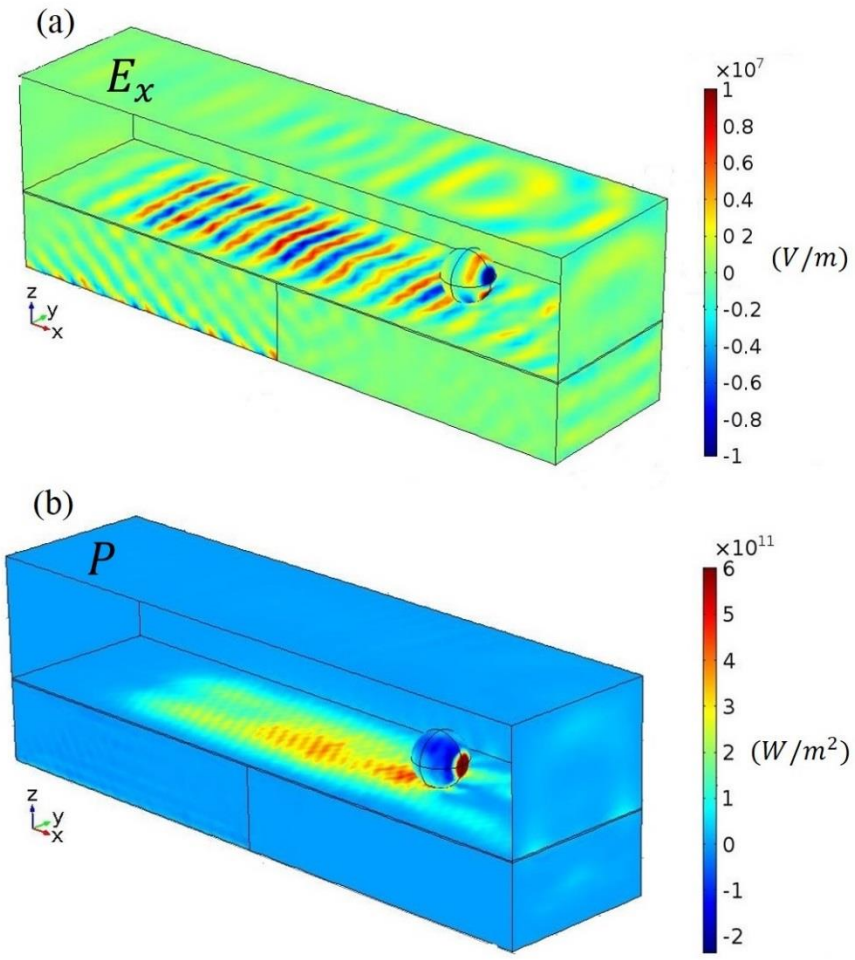

Fig. 6-9 3D simulation of TiO_2 microsphere on gold slab. The propagating surface plasmons are coupled by illumination through glass substrate at the correct coupling angle for $\lambda_0 = 760$ nm. (a) shows the E_x field map and with a blue hot spot as the radiation aperture and (b) shows the time average of the power flow map with a red hot spot as the radiation aperture on the surface of the microsphere

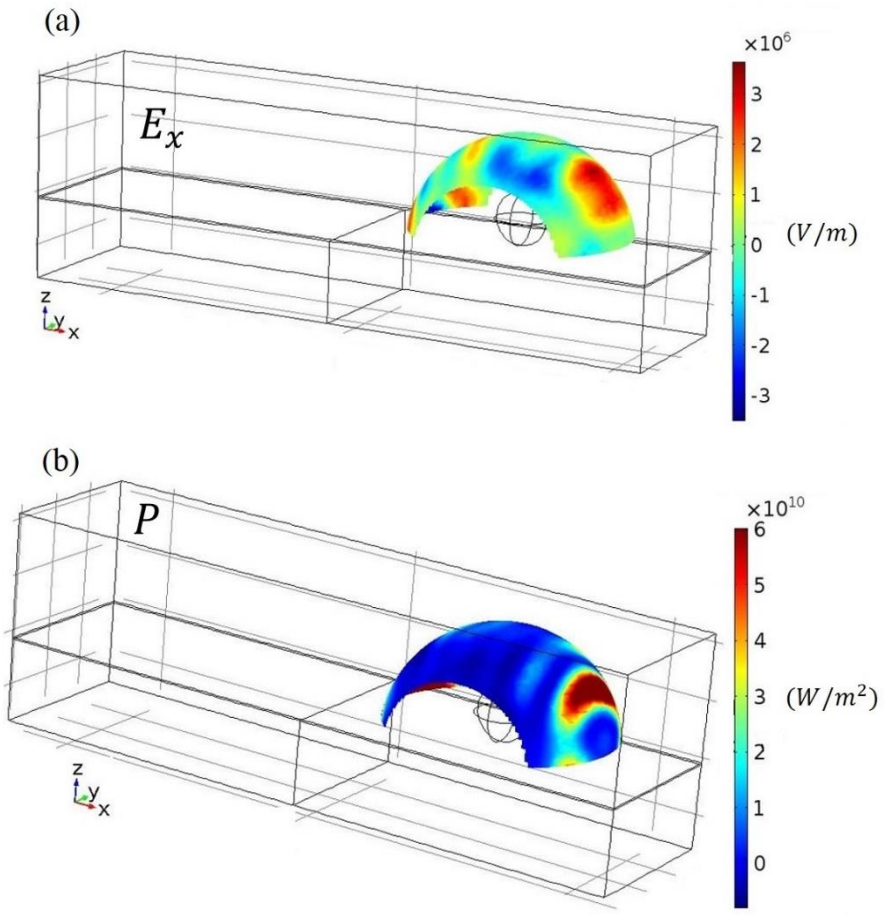

Fig. 6-10 The same simulation as Fig. 6-9; (a) the E_x field map on a parametrized surface at a radial distance of around $\approx 2\lambda_0$ demonstrating the radiation from the microsphere illustrated as a red hot spot on the surface, (b) the time-average power flow on the same parametrized surface demonstrating the radiation of the microsphere as a red hot spot on the surface

6.2 Experimental results

In order to demonstrate the decoupling and radiation of propagating surface plasmons into air through TiO_2 microspheres, amorphous TiO_2 microspheres[1] with refractive index of $n = 1.8$ and average diameter of $D = 950$ nm were deposited on 30 nm gold on glass cover slips. The scanning electron micrographs of the particles show uniform microspheres with average diameter of $D = 950$ nm, see Fig. 6-11.

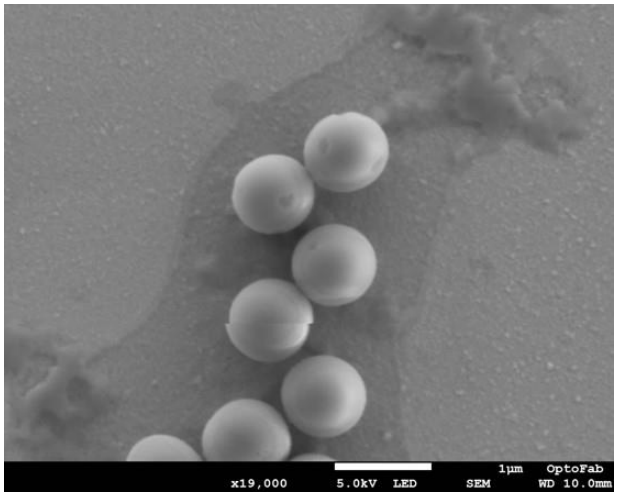

Fig. 6-11 Scanning electron micrograph of TiO_2 microspheres. The white scale bar is 1 µm

The sample of deposited microspheres on gold film was mounted on a microscope stage to couple surface plasmons onto the gold-air interface using a microscope

[1] Microspheres are purchased from MKnano (division of M K Impex Corp.)

objective (Kretschmann technique). The experimental set up was effectively a leakage radiation microscopy set up in which the microscope objective played the role of prism. The objective was contacted to the glass side with immersion oil and an off-axis light beam launched through it allowed the excitation of the propagating surface plasmons at the correct angle, see Fig. 6-12.

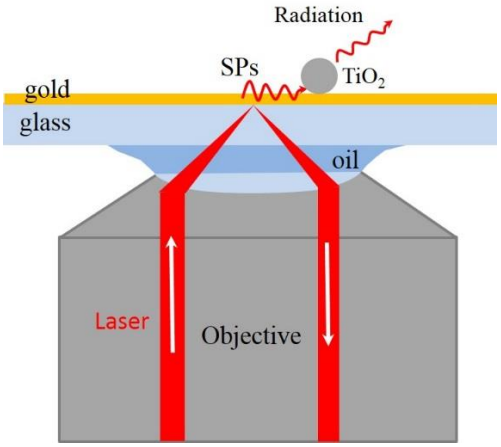

Fig. 6-12 Illustration of the experimental configuration using a microscope objective to support the coupling of surface plasmons. The propagating surface plasmons were brought close to TiO2 microspheres to facilitate their interaction

Light ($\lambda_0 = 760$ nm) was launched into the objective from the back aperture of the microscope and the leakage radiation and interaction of the propagating surface plasmons were imaged by the microscope camera. However, the radiation of the particles was also detected by the over-stage imaging system, as illustrated in Fig. 6-13 (a).

In order to detect the radiation from the TiO_2 microspheres, an imaging system, consisting of a $50\times$ microscope objective integrated with two plano-convex lenses and a compact CMOS camera (1280 x 1024 pixels), was mounted by a 3D

microcontroller over the microscope-sample stage. In Fig. 6-13 (b) an image of the imaging system mounted over the microscope stage is shown.

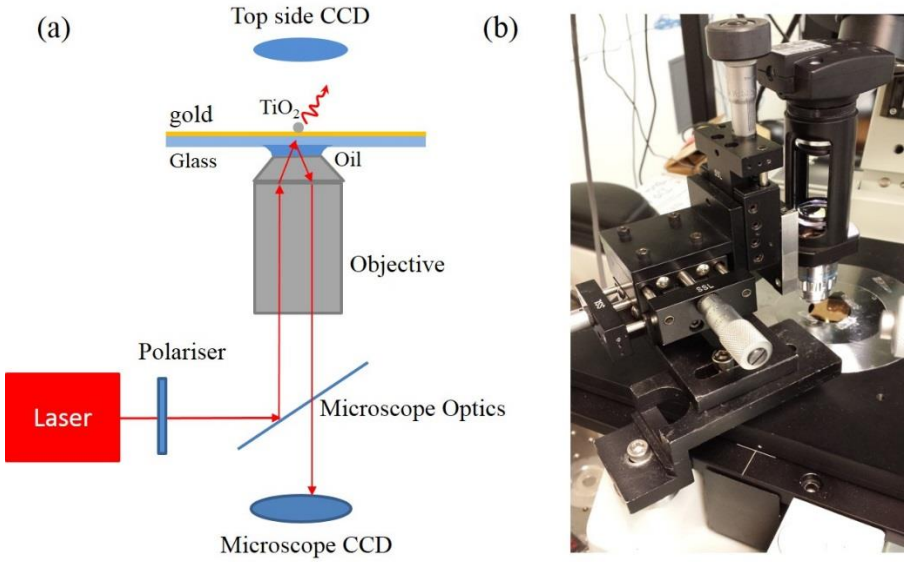

Fig. 6-13 (a) Experiment set up using the microscope and (b) photograph of the imaging system mounted over the microscope-sample stage

To obtain distinct single TiO_2 microspheres, the microspheres were suspended in water and small droplets of the solution were placed on the gold film. Although many of the microspheres aggregated on the gold surface, it was possible to find some single microspheres by scanning the surface of the gold with the microscope. The images taken by the microscope CCD camera (from below the sample) show that the

propagating surface plasmons, close enough to the single microspheres[2], were suppressed by the TiO_2 microspheres and the microspheres become very bright (the bright point distinguished by red arrow in Fig. 6-14 (a)). In Fig. 6-14(b) the intensity profile of the part (a) is illustrated which shows an appreciable enhancement of the intensity at the TiO_2 microsphere.

[2] The size of the microspheres is around one micron which means it is possible to observe them by optical microscope. However, there is still possibility of clumping some smaller size particles to make a particles around 1 microns. The SEM images show that majority of the particles have size around 1 micron and there are a lot of single particles on the sample. I have also repeated the experiment for several different samples, particles.

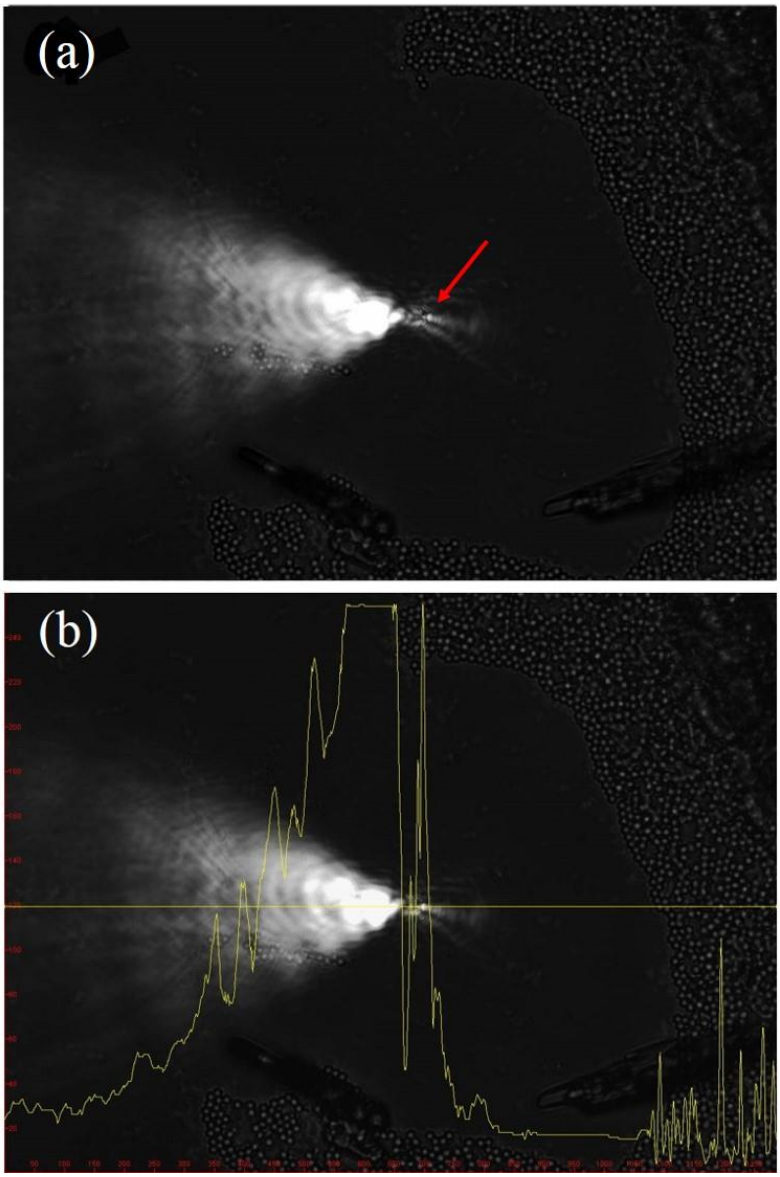

Fig. 6-14 (a) Interaction of single TiO2 microsphere with propagating surface plasmons observed through microscope objective, (b) the intensity profile of part (a)

The images taken by the CCD camera from above the sample also show the radiation of the decoupled surface plasmons into air from the TiO_2 microspheres excited by propagating surface plasmons, see Fig. 6-15. The white spot indicated by an arrow in Fig. 6-15 (a) shows the radiation from a single TiO_2 microsphere. The

large beam spot is the result of the transmission of part of the incident light through the very thin (30 nm) gold layer.

To test whether this radiation can be attributed to the interaction of the TiO_2 microsphere with propagating surface plasmons, the polarization of the incident light was rotated 90° (changed from p-polarization to s- polarization) while the position of the beam and the microsphere were unchanged. The image of this situation recorded by the CCD camera from above the sample, is presented in Fig. 6-15 (b). This shows that, by changing the polarization of the incident beam, the radiation from the microsphere extinguishes. In fact, by changing the polarization, the incident light does not couple into surface plasmons and consequently the TiO_2 microspheres cannot decouple and radiate surface plasmons.

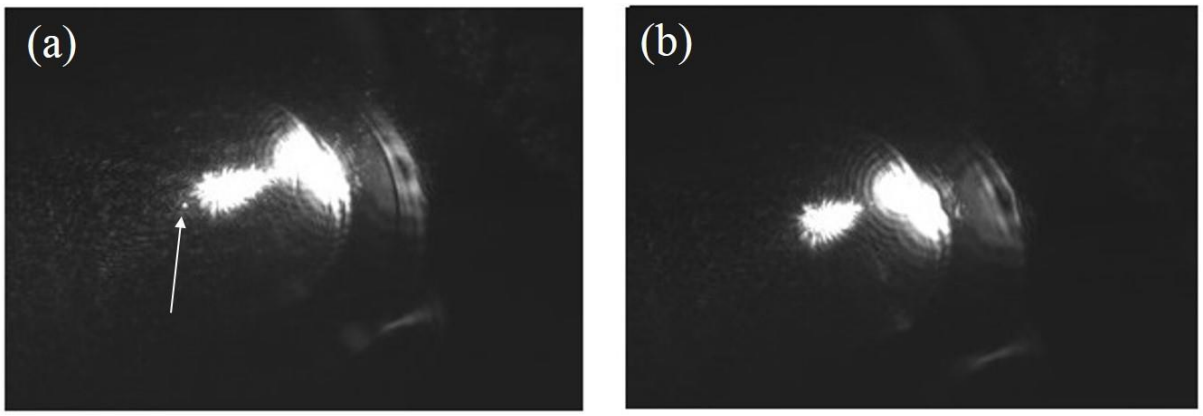

Fig. 6-15 The far field detection of the radiation of single TiO_2 microspheres by the imaging system above the microscope-sample stage (a) incident light with $\boldsymbol{p}$-polarization, (b) turning the polarization 90° ($\boldsymbol{s}$-polarization) no microsphere radiation is seen as the incident light cannot couple into propagating surface plasmons

6.3 Conclusions

Directional radiation of propagating surface plasmons by TiO_2 microspheres with refractive index of $n = 1.8$ and diameter of $D = 950$ nm was investigated by simulations. TiO_2 microspheres were shown to operate as dielectric antennae for decoupling the propagating surface plasmons to produce directional radiation. The radiation was investigated for a range of surface plasmon wavelengths (530 nm to 830 nm) and it was shown that for all the wavelengths the microspheres decouple and radiate the propagating surface plasmons directionally. The radiation aperture size decreases for larger wavelengths. The directionality and out-coupled power of the radiation also depends on the size of the microspheres. The simulation results also show that for fixed incident-light wavelength, microsphere diameters can influence the directionality and power of the radiation, because of the cavity resonance modes inside the microspheres.

The radiation from the microspheres adjacent to the propagating surface plasmons was confirmed experimentally. However, the experimental set up did not allow effective measurement of the directionality of the radiation, and this is proposed for future investigation. Though some configurations using dielectric microspheres as antennas with metallic dipoles in the vicinity of the microspheres, have been proposed, this configuration is challenging to fabricate. However, the use of TiO_2 microspheres on plasmonic platforms interacting with propagating surface plasmons is feasible with most plasmonic set ups, and the radiation from the microspheres could have applications in detection and sensing.

Chapter 7: Plasmonic Enhanced Graphene Photodetectors

Graphene is a promising material for photodetection due to its remarkable optical, electronic and mechanical properties, as mentioned in the Introduction. These include its gapless semiconductor band structure that provides exceptionally broadband photo-generation of charge carriers, the high optical absorption of 2.3%, relative to its monolayer thickness, and the record-breaking electron/hole mobility.

The aim of this project is to use the strongly enhanced electromagnetic near-field associated with surface plasmons to amplify the photocurrent generation of graphene-based photodetectors [37, 132].

There are two different ways of coupling light photons into surface plasmons, by diffracting the light beam through plasmonic structures and by tunnelling light photons into surface plasmons using evanescent field of light (Chapter 1). We apply two different structures to exploit both techniques to couple light photons into surface plasmons to detect.

The first set of structures using coupling based on diffraction, consisted of plasmonic gratings with different geometries to compare the role of grating geometry for photocurrent enhancement of graphene.

The second structure is a trench or a gap, between two gold strips to excite surface plasmons at the edges of the gap at the surface plasmon resonance angle in

which the light photons are coupled into surface plasmons by tunnelling photons through the evanescent field. These photodetectors on waveguides can employ the evanescent fields for photodetection, plasmonic detection, and sensing.

In both cases the existence of a junction is essential to spatially separate the excited electron-hole (e-h) pairs [133, 134]. In the case of the gratings the grating electrode is separated by a gap from the opposite gold electrode or the grating's interdigitated forks are connected to separate electrodes. For the case of the graphene gap-photodetector, the gap plays the role of the junction as well.

7.1 Graphene on plasmonic nano-structures

7.1.1 Design

The exact mechanism of photocurrent generation by graphene is still in debate, however, it is well known that a p-n junction is required to separate the photo-generated charge carriers. Such p-n junctions often occur close to the metal contacts, due to the difference in work function of metal and graphene [90, 135]. It has also been shown that plasmonic structures can enhance the photodetection charactristics of graphene by placing the plasmonic structures close to the contact boundary of metal and graphene [37]. We use the focusing property of the curved gratings (Chapter 4, [20]), to focus surface plasmons to a sharp edge which is also the border of the graphene-metal contact, structure (2) in Fig. 7-1. In order to compare the performance of the enhanced graphene photodetection by curved gratings with other possible structures, a linear trench grating is designed (structure (1) in Fig. 7-1) which sends the surface plasmons to two contact lines above and

below the grating. The third structure is also an inter-digitated grating (structure (3) in Fig. 7-1) which also increases the number of contact lines of the metal-graphene. A comparison between the performance of linear and inter-digitated gratings with the curved gratings enables a judgement on the advantages of focusing surface plasmons to a small detector area by the curved gratings. Positioned to the left and right of the three detectors, are large open spaces that should act as non-plasmonic graphene photodetectors. The top and bottom sectors of the detector were electrically isolated, with graphene to provide the electronic connection between the two electrodes.

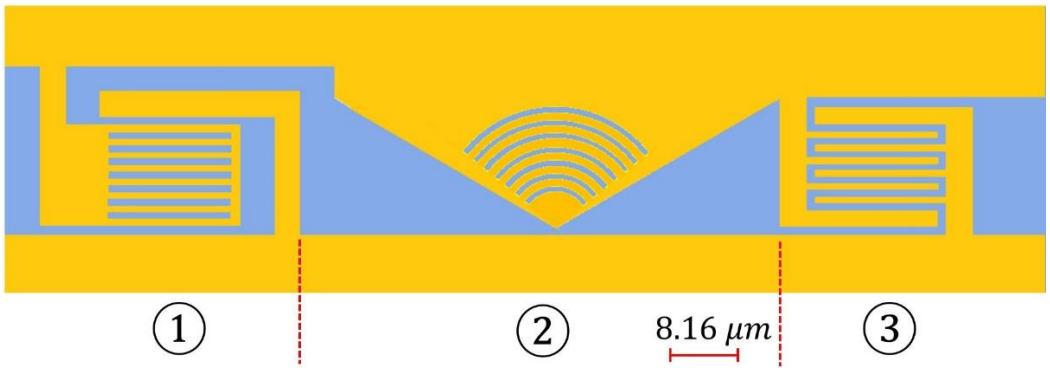

Fig. 7-1 Three designed plasmonic nano-structures for harvesting light and using the benefits of the energy confinement and field enhancement of plasmonic resonances to enhance the photo-detection performance of graphene sheets (1) linear grating with two collecting arms (2) curved grating, (3) inter-digitated linear grating, the gold colour shows the 100 nm gold layer and blue parts show the open spaces (air-glass)

All the gratings are designed to operate at $\lambda_0 = 1550$ nm for normal incidence light. The resulting grating period (according to Eq. 1-9) is $\Lambda_{gr} = 1540$ nm for all of the structures. The groove width of the structures is also considered half of the

grating period ($GW = \frac{\Lambda_{gr}}{2} = 0.77$ μm) as a result of optimizing the grating parameters in Chapter three (optimizing plasmonic grating geometrical parameters). It was shown in Chapter five (integrating curved gratings with plasmonic micro-stripline waveguides) that the linear gratings couple incident light in both backwards and forwards directions. As a result, two collecting arms are considered for the linear grating (structure (1) in Fig. 7-1) to collect the photo-carriers excited with surface plasmons in both sides of the grating while the interdigitated grating (structure (2) in Fig. 7-1) would collect the photocurrent at each period of the grating.

7.1.2 Fabrication

The structures were fabricated in 100 nm gold film as trench gratings, so that the depth of the grooves is the same as the thickness of the gold film (100 nm). The 100 nm gold films were deposited with ion-assisted deposition using an oxygen plasma-assisted thermal deposition system [125], to ensure good adhesion, flatness and uniformity of the gold film on the glass substrate (refractive index $n = 1.52$). The structures were fabricated into the 100 nm gold film with focused ion beam (FIB), using Zeiss Auriga 60 cross beam SEM with an Orsay Canion FIB column. The three different fabricated gratings have the same number of grooves (seven grooves each) with average 9% error in the fabrication, Fig. 7-2 shows the SEM images of the structures with scale bar.

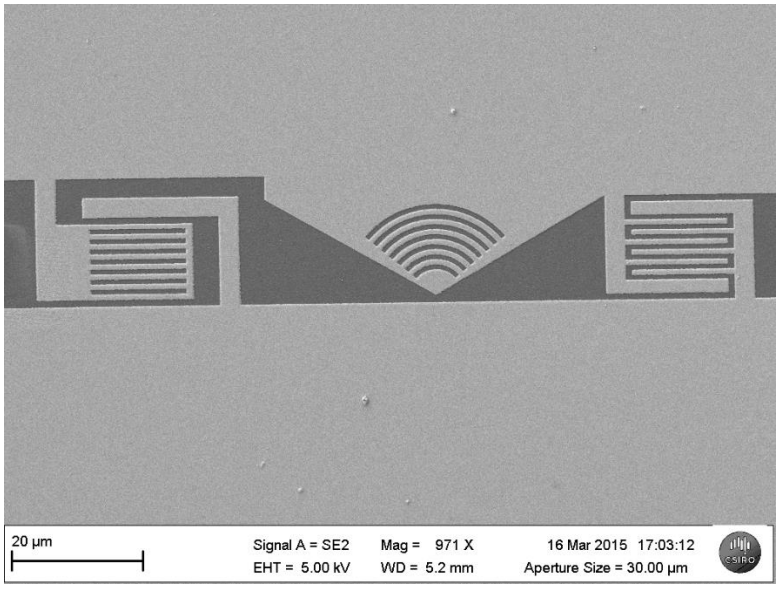

Fig. 7-2 Scanning electron micrograph of the fabricated structure. The bright parts show gold and the dark region shows glass substrate. The scale bar is 20 µm

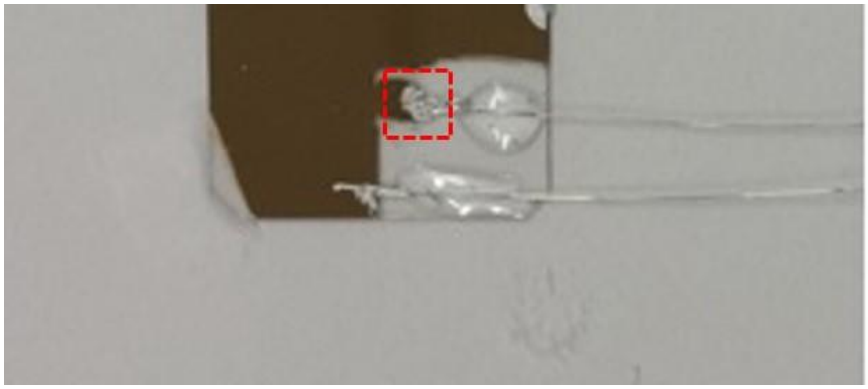

Fig. 7-3 The fabricated structure showing the isolated square gold film island (illustrated with the dashed red line) and the rest of gold film in which the structure is milled. The two separated regions are wire bonded by using silver glue

The plasmonic structures are at the edge of the gold film. An isolated square gold pad is also in front of the structures which can be connected to the opposite gold pad by the graphene layer deposited over the gold. The graphene layer connects the structured region to the square island electrically to enable transmission of the photocurrent excited by the plasmonic gratings. The two separated gold regions are wire bonded with silver glue to connect the structures to measuring instruments. Fig. 7-3 shows the sample with the isolated square gold film (illustrated with red dashed line) and the remaining gold film.

The 1×1 cm single layer graphene sheets were purchased. According to the manufacturer's production data sheet, the graphene layers are grown on copper foil[3].

[3] ACS Material (Advance Chemical Supplier), http://acsmaterial.com/product.asp?cid=96&id=118

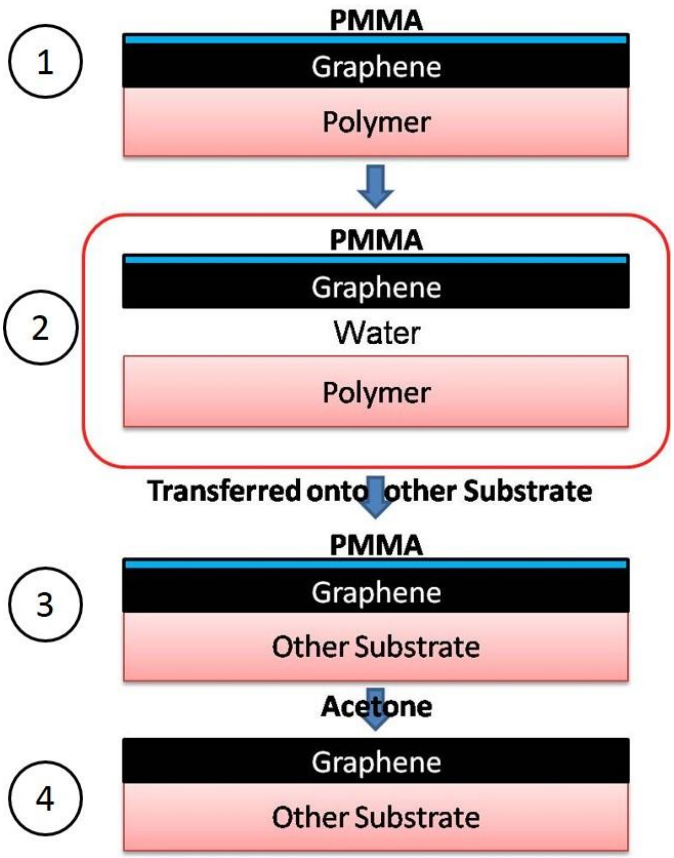

Fig. 7-4 Four steps graphene trivial transfer; (1) the graphene on polymer substrate is separated from the holder base, (2) immersion of the separated part into deionized water floats the graphene layer with PMMA coating on top of the water, (3) the floated part is deposited on the substrate and (4) the PMMA coating is washed out by acetone. Image taken from the manufacturer website[4]

[4] ACS Material (Advance Chemical Supplier), http://acsmaterial.com/product.asp?cid=96&id=118

The copper layer is etched and the graphene layer is coated with PMMA. The resulting graphene layer was deposited on the sample with the “four steps trivial transfer method” according to the illustrations in Fig. 7-4.

The existence of the graphene sheet on the structures was demonstrated in two different ways; by optical images and by the electrical properties. Fig. 7-5 shows the optical images of the graphene sheet on the sample. The horizontal white arrow in both Fig. 7-5 (a) and (b) indicates the borders of the graphene layer on the gold film, while the vertical white arrow in Fig. 7-5 (a) shows the structures and also the gap that separates the gold panels. The faint contrast between the regions with graphene and without graphene sheets demonstrates the presence of the graphene sheet at the desired position.

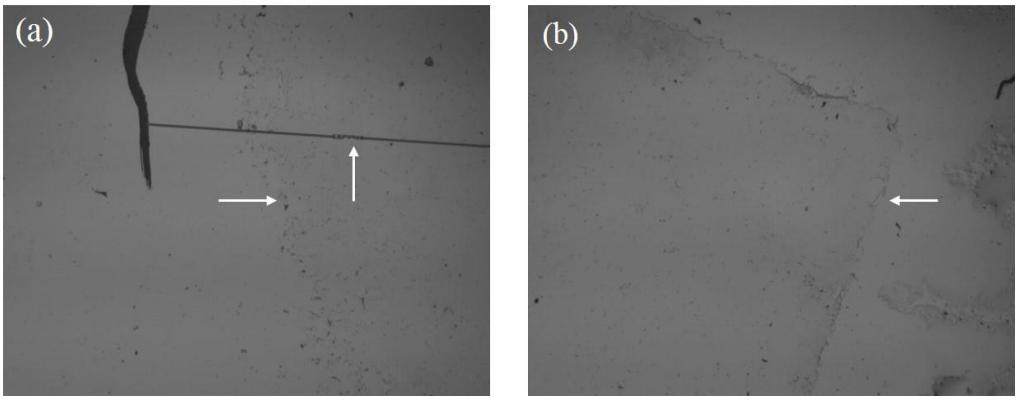

Fig. 7-5 Optical images of the graphene sheet on the sample (a) the horizontal white arrow indicates the border of the graphene sheet on gold, and the vertical white arrow shows the structure and the long groove milled to disconnect the gold pad from the structures milled into the rest of gold film, (b) the white arrow shows the borders of the graphene sheet on the gold film as a faint contrast between the gold film without graphene and graphene on the gold film.

According to the information provided by the manufacturer, the resistance of the graphene sheet is 600 $\Omega/_{sq}$. After depositing the graphene sheets across the grating structures and the opposite disconnected gold pad, the presence of the graphene sheet was tested by measuring the resistance of the graphene. Infinite resistance was measured before the graphene deposition showing the complete disconnection between the two separated regions. However, after deposition, there was 700 Ω resistance between the two gold regions showing the transfer of charges across the two separated regions. This charge transfer, together with the optical images, demonstrates the deposition of the graphene sheet across the fabricated plasmonic structures and the opposite gold pad.

7.1.3 Experiment

The sample was loaded into the microscope and illuminated through the 10 ×microscope objective. Fig. 7-6 shows a schematic of the experimental set up.

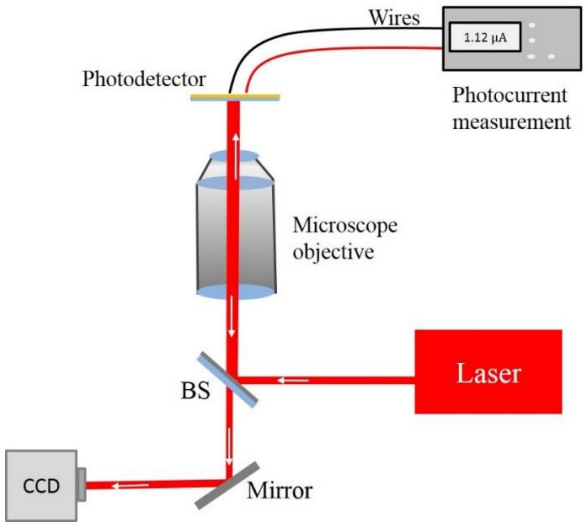

Fig. 7-6 Experimental set up for characterizing the enhanced plasmonic graphene photodetectors

The first measurement was performed by a photocurrent measurement instrument (Keithley programmable electrometer, model 617). In the absence of illumination, no photocurrent was observed in response to microscope or room light illumination. With a super-continuum laser source (Fianum) operating at both infrared and visible wavelength ranges, with a power of 1 mW at 1550 ± 100 nm, no photocurrent could be detected when the focused illumination light was scanned across each of the detectors and the gap between the electrodes.

The bias voltage was then swept from -10 V to 10 +V whilst the photocurrent was examined and dark current was recorded. The dark current was found to be quite large so that there was no detectable photocurrent by illuminating the structures. There was some hysteresis when varying the bias voltage. The graph of the measured current vs bias voltage in the absence of the illumination is shown in Fig. 7-7.

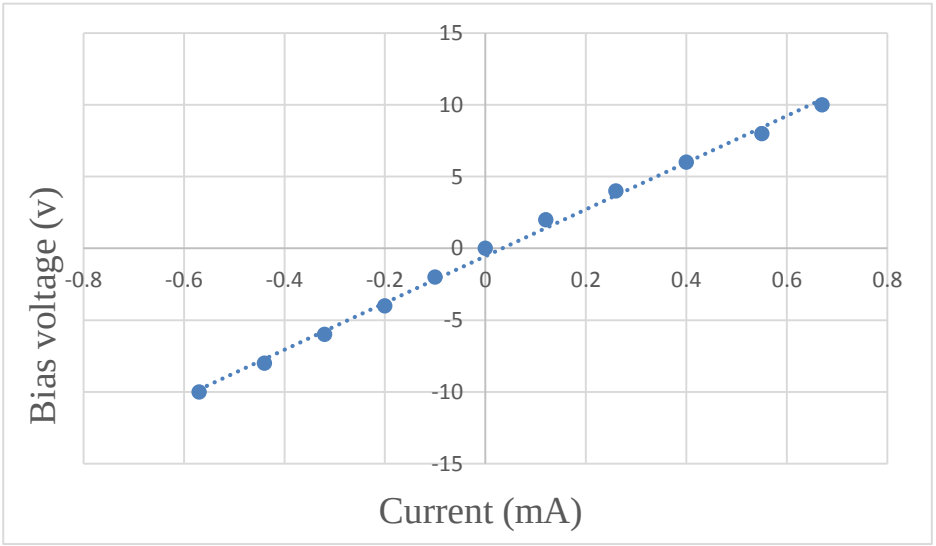

Fig. 7-7 measured current versus the bias voltage, with no illumination. The dashed line shows the linear fit to the data points

The graph in Fig. 7-7 gives 16.3 k Ω as the resistance of the graphene sheet bridging the two gold sections. However, besides some hysteresis when changing the bias voltage, there was no significant change in the measured current versus the bias voltage under illumination of any part of the structures.

The large dark current is unlikely to be from thermal sources and it is attributed to the relatively large area of the graphene sheet. The graphene sheet can be considered as a 2D layer, with length L and width w. Ohm's law relationship for a 2D sheet can be written as;

$$I = \frac{V}{R} = \frac{V}{\left(\frac{\rho L}{w}\right)} = \frac{V}{\left(\frac{\rho L}{w}\right)} = \frac{Vw}{\rho L} \qquad \text{Eq. 7-1}$$

where V is the applied electrical potential, ρ the resistivity of the graphene layer, L the length of the graphene sheet and w is the width of the graphene sheet across the gap. This relationship shows that by decreasing the width of the graphene sheet the dark current would be reduced.

A second sample was fabricated according to the fabrication process described for the previous sample. A 10×10 mm graphene sheet was deposited on the sample across the structure and the microscope images showed some folding and wrinkling of the graphene sheet.

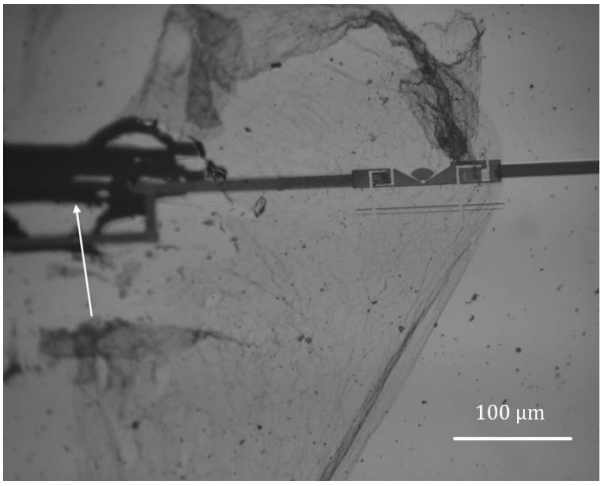

Fig. 7-8 The extended graphene sheet on the left hand side of the structure was scratched by a sharp needle to decrease the width of the graphene sheet that connects the two gold regions

In order to decrease the dark current, manual changes were made on the second sample, scratching a gap between the two gold pads by a sharp needle to eliminate the connection through the graphene sheet between the two gold regions. The scratched part is shown in Fig. 7-8. The resistance measurement between the two electrodes for the second sample also showed 700 Ω between the two gold pads.

The photocurrent measurement on the second sample also showed high dark current similar to the first sample, and no change when illuminating the structures and the gap between the structures. However, during the sample characterization when changing the bias voltage from 0 to 5 V the dark current dropped dramatically. Inspection of the sample with the microscope revealed voltage breakdown across the interdigitated structure because of high field concentration, as shown in Fig. 7-9.

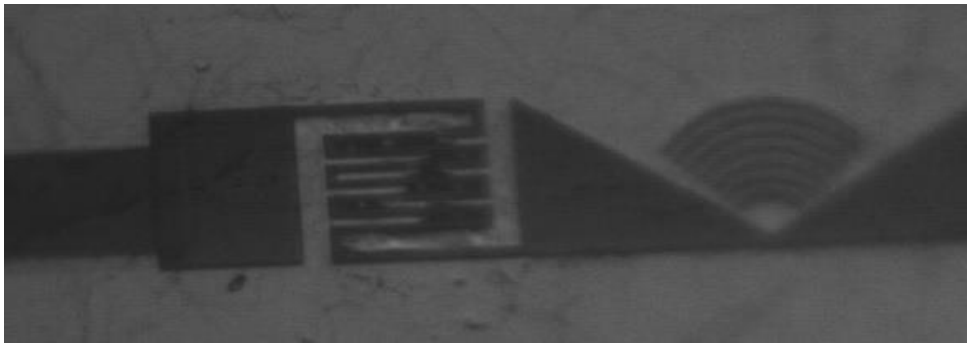

Fig. 7-9 The broken down inter-digitated structure due to the applied voltage

7.1.4 Characterization of sample by Raman spectroscopy

The fabricated sample was also characterized using Raman spectroscopy to demonstrate the existence of graphene on the sample and required regions. The spectroscopy was done using a Renishaw Ramascope 2000. The system is a compact Raman microscope that is used to collect Raman spectra with collection optics based on a Leica DMLM microscope. The samples were placed beneath a $50\times$ microscope objective and were excited by laser light at 785 nm, directed through the microscope. The backscattered light was collected along the same optical path as the incoming laser. Raman scattered light passed through a notch filter, and then to a grating with 2400 groove/mm which disperses the scattered light over a CCD array detector.

Fig. 7-10 Renishaw Ramascope 2000

The first Raman spectrum was taken from the gaps between the two gold pads. This was expected to be electrically connected via the deposited graphene on the sample, shown in Fig. 7-11.

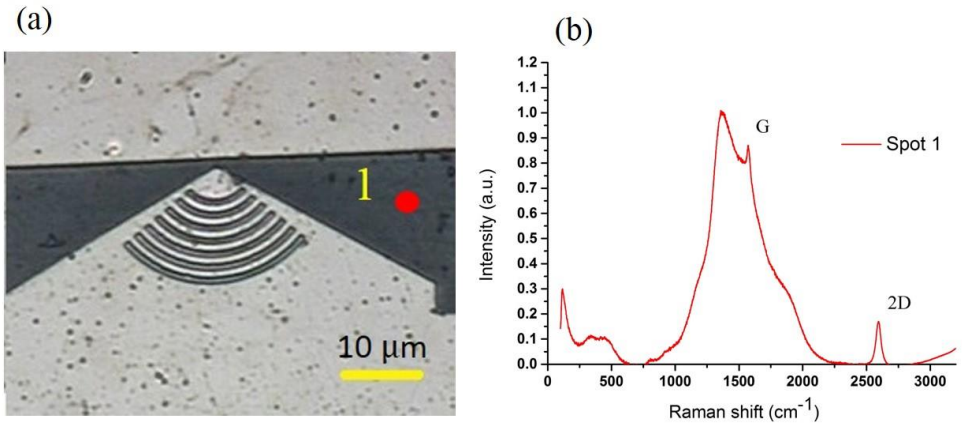

Fig. 7-11 (a) shows the exciting beam spot (marked in red) and position on the graphene on glass, (b) shows the Raman peaks of graphene on spot (1)

In Fig. 7-11 (a) the position of exciting laser beam spot is shown with a red dot on the optical image of the sample. Two Raman peaks were identified for graphene on spot (1); the G peak at 1577 cm-1 and the 2D peak at 2593 cm-1, shown in Fig. 7-11 (b).

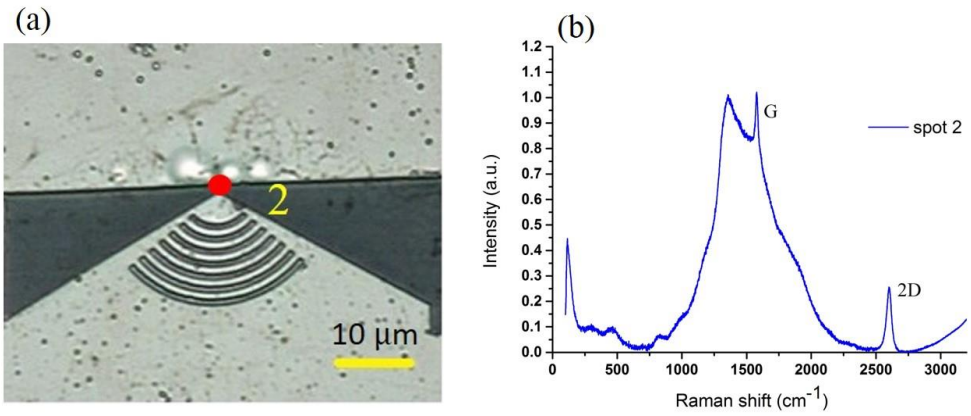

Fig. 7-12 (a) shows the laser beam spot position at the gap between the sharp corner of the structured gold region, and the opposite gold electrode

The second Raman spectrum was also taken from the glass side but in the gap between the structured gold region and its opposite gold electrode, shown with a red circle in Fig. 7-12 (a). The plot of the Raman signal for spot (2) reveals the G peak at 1578 cm-1 and the 2D peak at 2604 cm-1. This is good evidence of the presence of the graphene sheet on the glass. In each of the Raman spectra, the 2D peak is greater than the G peak, which is a signature of single layer graphene [68].

The broader peak at 1353 cm-1 is related to the emission spectrum of the glass when excited at $\lambda_{exc} = 785$ nm. The Raman spectrum for the same sample but in

a spot with no graphene sheet (far from the structure domain) is shown in Fig. 7-13, and shows the presence of the broad peak.

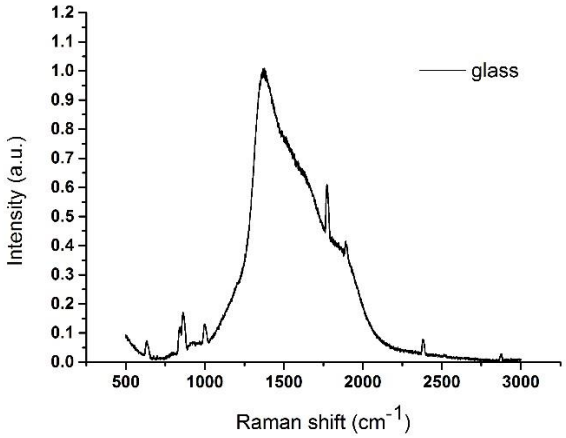

Fig. 7-13 Raman spectrum of glass excited at $\lambda_{exc} = 785$ nm

Besides the graphene on glass region, a large area of the graphene sheet is contacting the gold regions, including the structured domain. The Raman spectrum of the graphene on gold for a spot very close to the structures is shown in Fig. 7-14 (a) and this is compared with the Raman spectrum of the gold layer without the graphene sheet, Fig. 7-14 (b) .

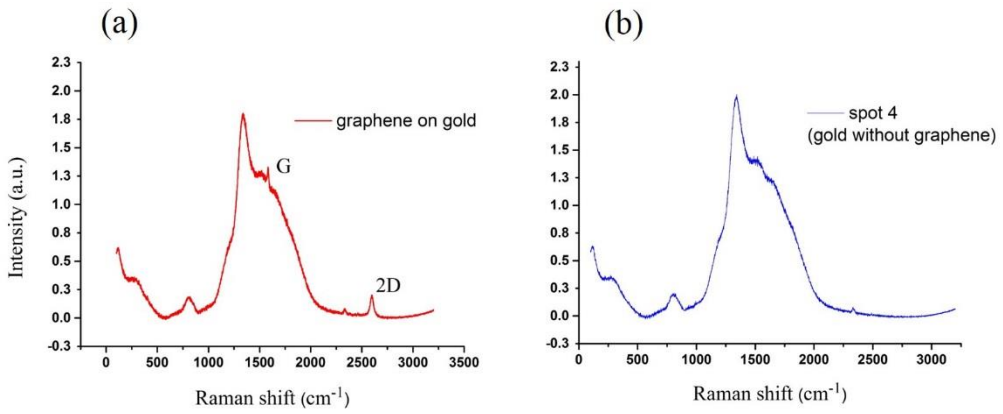

Fig. 7-14 (a) Raman spectrum of graphene on gold manifesting the G and 2D peaks, (b) the Raman spectrum of gold layer without graphene

A comparison of the Raman spectra in Fig. 7-14 (a) and (b) indicates that the peak at 1585 cm-1 is the graphene G peak and the peak at 2604 cm-1 is the graphene 2D peak. The ratio of the intensity of the 2D peak to G peak (I(2D)/I(G))and also the ratio of the areas of the 2D peak to G peak (A(2D)/A(G)) are smaller for the graphene on glass (spot 1, Fig. 7-14) in comparison to the graphene on gold (Fig. 7-14 (a)). This indicates that the graphene on gold has a higher doping level [69].

In order to investigate the photo-activity of the graphene layer deposited on the structures, the Raman spectrum for seven spots along the bisector of the curved grating with 4 μm steps were measured and plotted in Fig. 7-15 for excitation wavelength of $\lambda_{exc} = 785$ nm with a beam spot size of approximately 1.5 microns.

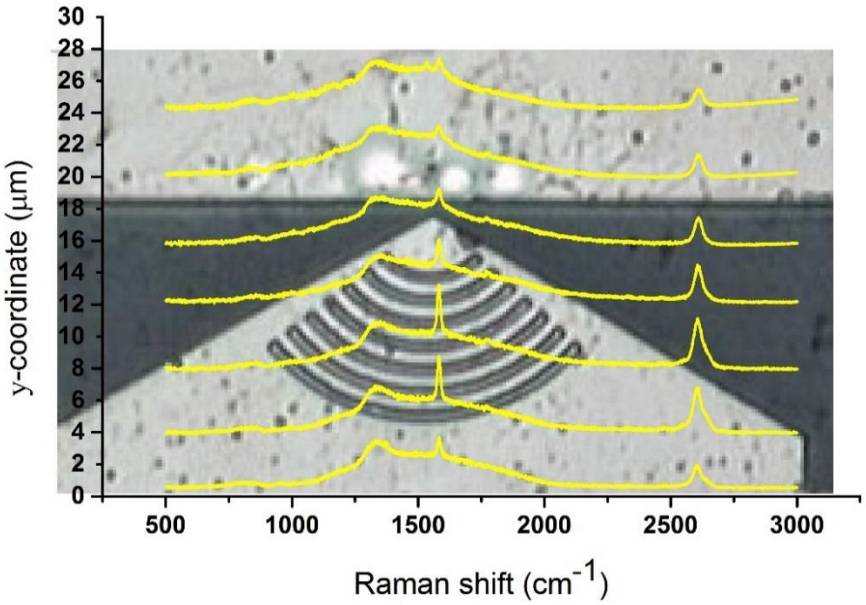

Fig. 7-15 Normalized Raman spectra at different spots along the bisector of the curved grating measured with excitation wavelength of $\lambda_{exc} = 785$ nm. The first spot is at the 0 y-coordinate and the excitation position moves with 4 μm step size along the y coordinate. The bisector of the grating is approximately at the position of G peaks

Inspection of the Raman spectra demonstrates the evolution of the G and 2D peaks as the excitation beam spots move. In particular, for the spectra taken at 4 μm and 8 μm, the graphene Raman G and 2D peaks become greater than the respective peaks in other positions, indicating the higher photo-activity of the deposited graphene at the curved grating grooves. In order to compare the activity of the deposited graphene quantitatively, the ratio of the area of 2D peak to G peak, and the ratio of the intensity of the 2D peak to G peak are measured by curve fitting to each peak and the results are presented in Fig. 7-16.

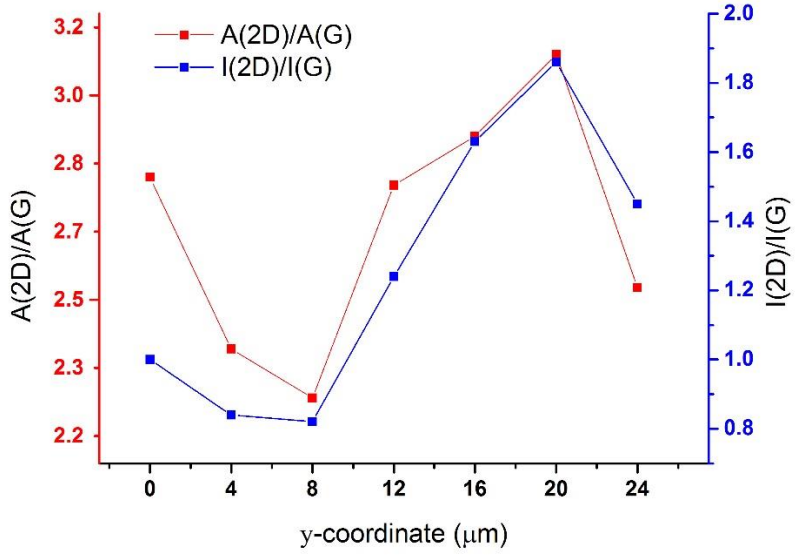

Fig. 7-16 The ratios of the area (left vertical axis) and intensity (right vertical axis) of the 2D peak and G peak of the Raman spectra in Fig. 7-15 for different excitation positions along the y coordinate of the curved grating bisector

The graphs in Fig. 7-16 show that the graphene on the grooves of the curved grating has the minimum ratio of the area and intensity of the 2D Raman peak to the G Raman peak, indicating a higher doping level on the grating grooves. This shows that the graphene sheet deposited on the structures is photo-active. Also the evanescent field of the surface plasmons at the grooves of the grating can enhance the photo-generation of charge carriers in the graphene consistent with previous results in [37].

7.2 Photocurrent enhancement of graphene gap-photodetectors by photon tunnelling of light into surface plasmons

As discussed in Chapter 1, the plasmonic field enhancement is the result of confinement of electromagnetic field of the incident light onto metal-dielectric interface. This is achieved by coupling light photons into oscillations of free charges (conduction electrons) bound at the metal-dielectric interface. One of the techniques for coupling light into surface plamsons is tunnelling of light photons into surface plasmons using a prism in the Kretschmann configuration [42].

In Kretschcmann configuration, illuminating the prism at angles greater than total internal reflection angle enables coupling of light photons into surface plasmons by photon tunnelling through the evanescent field. This can be used to enhance the photocurrent response of the graphene-gap photodetector attached on the prism, Fig. 7-23. The graphene-gap photodetector consists of two gold strips with a gap between. The graphene sheet is deposited across the gap and the gold strips, see figure 7-17.

7.2.1 Graphene gap-photodetector fabrication

The graphene gap-photodetector consists of two gold strips (30 nm thick gold film). The gold strips are 400 μm wide, deposited on glass (refractive index of glass $n_{glass} = 1.52$). The gold strips are separated from each other with a 40 μm gap

made by scratching the gold strips with a scalpel. This structure is shown in Fig. 7-17.

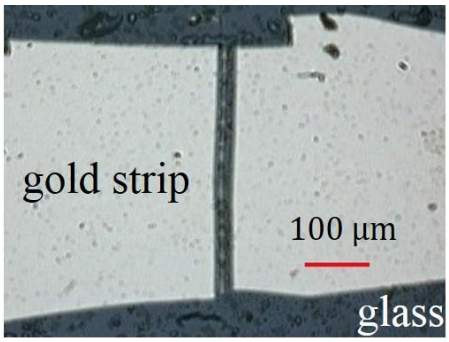

Fig. 7-17 Graphene gap-photodetector consists of two gold strips with a gap a 40 µm between

The graphene sheet is deposited on the gap using the "trivial transfer method" graphene sheets purchased from Advanced Chemical Supplier (http://acsmaterial.com/product.asp?). On immersing the structure in water below the floating PMMA-coated graphene sheet, the graphene adheres to the gap and gold strips, and cam be lifted out of the water, see Fig. 7-18.

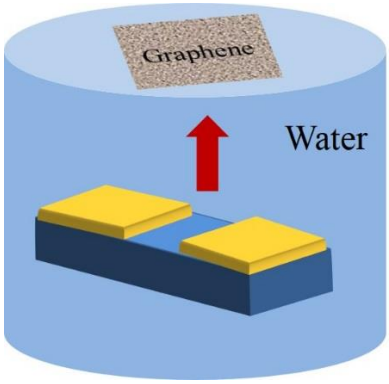

Fig. 7-18 Depositing PMMA coated graphene sheet on the gap and gold strip

After depositing the PMMA-coated graphene sheet on the structure, the sample is left for a few hours to dry and then the PMMA layer is dissolved by acetone. The wires are bonded by silver paste and fixed to the substrate with epoxy adhesive.

7.2.2 Raman spectroscopy characterization of the structure

Raman spectroscopy was used to prove the existence of the graphene on the structure and also characterizing the doping level of different parts of the graphene sheet, including the contact points with gold and the suspended parts on glass.

The spectra were taken using Renishaw Raman spectrometer 2000, by illuminating 5 different spots on the structure through a $50\times$ objective at $\lambda_0 = 532$ nm.

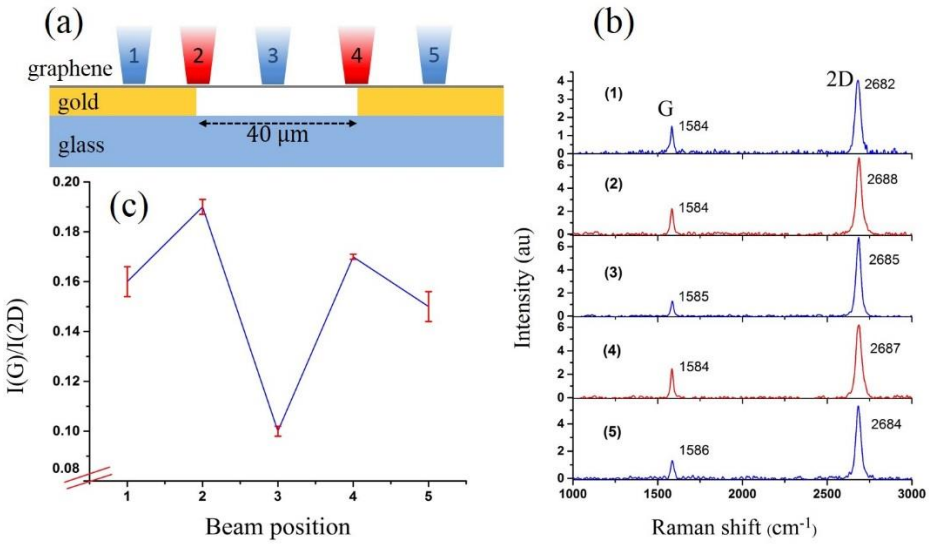

Fig. 7-19 (a) The beam position at 5 different spots, (b) Raman spectrum for each spot according to the beam position in (a), The ratio of the area (A) of G peak to 2D peak, representing the doping level at each spot

Fig. 7-19 (a) shows 5 spots in which the Raman spectrum of the graphene sheet on the structure is collected. Fig. 7-19 (b) shows the related spectrum of each point. The 2D peak at $\sim 2670\ \mathrm{cm}^{-1}$ is sensitive to the lattice constant of graphene and thus allows the use of the 2D peak shift direction to determine the electron or hole doping of graphene [70]. The redshift of the 2D peak corresponds to the electron doping of the graphene (n doped), and the blueshift corresponds to hole doping (p doped). Considering the position of the beam (Fig. 7-19) and the related 2D Raman shift in Fig. 7-19 (b) it is concluded that the graphene sheet at the contacts and over the gap make a unipolar $P^+ - P - P^+$condition as shown in Fig. 7-20.

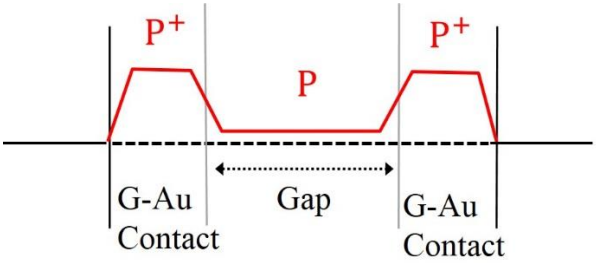

Fig. 7-20 Schematic of the doping type of graphene-gold junction (P^+) and graphene over the gap (P) according to the 2D Raman peak shift in Fig. 7-19

As discussed in Chapter 1(introduction) the decrease in the ratio of the area of 2D peak to the area of G peak shows the increase in doping level. Here, the inverse of the A(2D)/A(G) is shown in Fig. 7-19 (c) to demonstrate the increase in the doping level of the graphene sheet at the edges of the gold stirps.

7.2.3 Experiment and results

We use the Kretschmann configuration to couple light photons into surface plasmons. The fabricated photodetector is brought in contact with a prism (N-BK7, $n = 1.52$) with immersion oil, see Fig. 7-21.

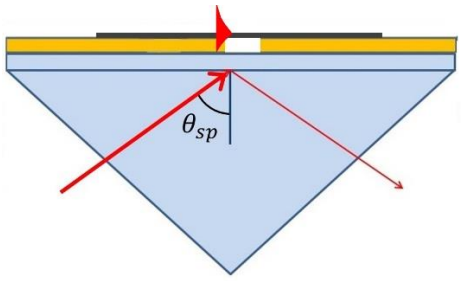

Fig. 7-21 Kretschmann configuration for coupling light into surface plasmons at the graphene gap-photodetector

The experiment is performed in three steps. In the first step the attenuated total internal reflection is measured for the 30 nm-thick gold film to measure the surface plasmon coupling angle of the gold film. The procedure for this measurement consists of illuminating the gold film (without graphene) through the prism at different angles and then measuring the reflection of the incident light through the prism. The surface plasmon resonance angle occurs just after the total internal reflection angle and manifests as a dip in the reflection, Fig. 7-22 (a). This measurement is performed for five different wavelengths including: $\lambda_0 = 730\ \text{nm}, 690\ \text{nm}, 650\ \text{nm}, 610\ \text{nm}, 570\ \text{nm}$. The measurements show that by increasing the wavelength of the incident light (p-polarization), the surface plasmon resonance angle increases and becomes wider, see Fig. 7-22 (a). The width of the surface plasmon dip is proportional to the loss of the surface plasmons and a wider

surface plasmon resonance dip means implies attenuation of the surface plasmons on the gold [136]. In addition, the calculated values for the wavelength of surface plasmons, from the measured surface plasmon resonance angles, according to Eq. 1-6, is in good agreement with the predicted surface plasmon wavelength using Eq. 1-3, see Table 1.

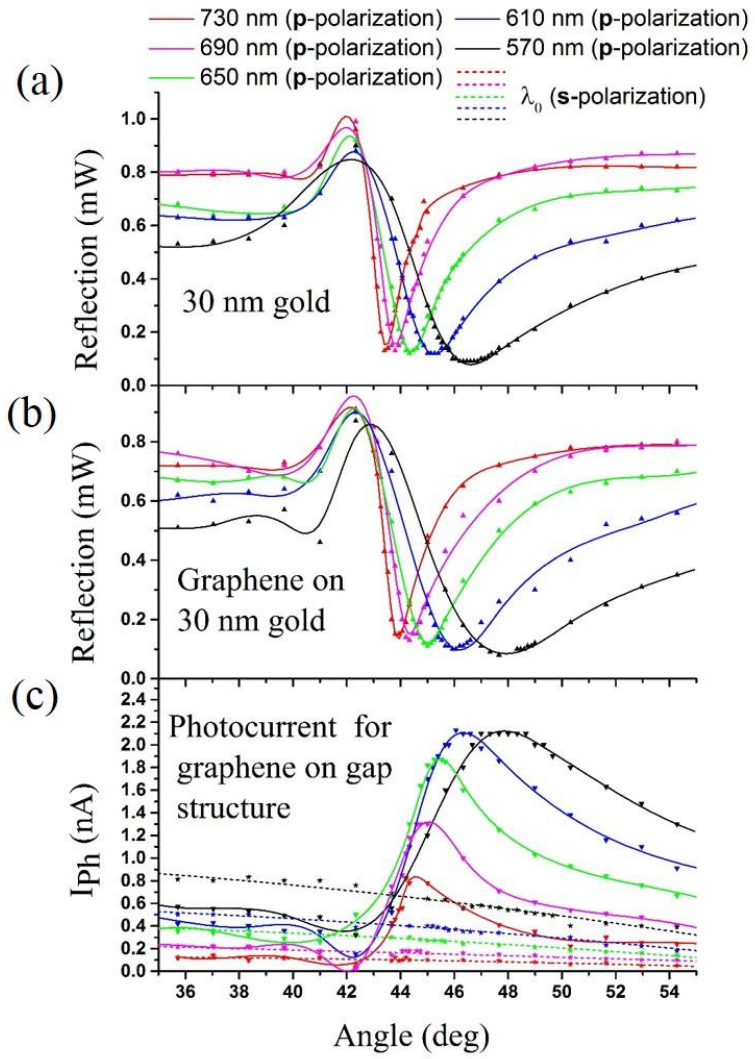

Fig. 7-22 (a) The reflection against angle of incidence for the godl film illuminated through prism, (b) shows the the reflection against the angle of incidence for graphene on gold film, and (c) shows the photocurrent versus the angle of incidnece

Table 1. Calculated (λ_{sp}) according to Eq. 1-3 and Eq. 1-6 (using gold dielectric constant from reference [46] and measured surface plasmon resonance angle from Fig. 7-22, respectively)

$\boldsymbol{\lambda_0}$ (nm)	$\boldsymbol{\lambda_{sp}}$ (Eq. 1-3) (nm)	$\boldsymbol{\theta^\circ_{sp}}$ (gold) Fig. 7-22 (a)	$\boldsymbol{\lambda_{sp}}$ (Eq. 1-6) (nm)	$\boldsymbol{\theta^\circ_{sp}}$ (graphene on gold) Fig. 7-22 (b)	$\boldsymbol{\lambda_{sp}}$ (Eq. 1-6) (nm)
730	710	43.4°	708	43.9°	702
690	668	43.8°	665	44.3°	659
650	625	44.3°	620	45.0°	613
610	579	45.3°	572	46.0°	565
570	530	46.5°	523	47.6°	514

Since the graphene sheet also covers the gold strips, the surface plasmons at the graphene-gold contact are expected to enhance the photocurrent generation. Consequently, the second experiment measures the shift of the surface plasmon resonance angle of the graphene on gold contact, Fig. 7-22 (b) and Table 1. The results show that introducing the graphene sheet on the gold layer shifts the surface plasmon resonance angles from $\Delta\theta^\circ = +0.5^\circ$ to $+1.1^\circ$ for $\lambda_0 = 730$ nm to $\lambda_0 = 570$ nm, respectively, which corresponds to 7 nm blue shift of the surface plasmon wavelengths on average, according to Eq. 1-6. `

Finally, to measure the photocurrent, a chopper at frequency of 400 Hz modulates the incident light beam and is locked-in to an amplifier (Stanford Research Systems SR510), see Fig. 7-23.

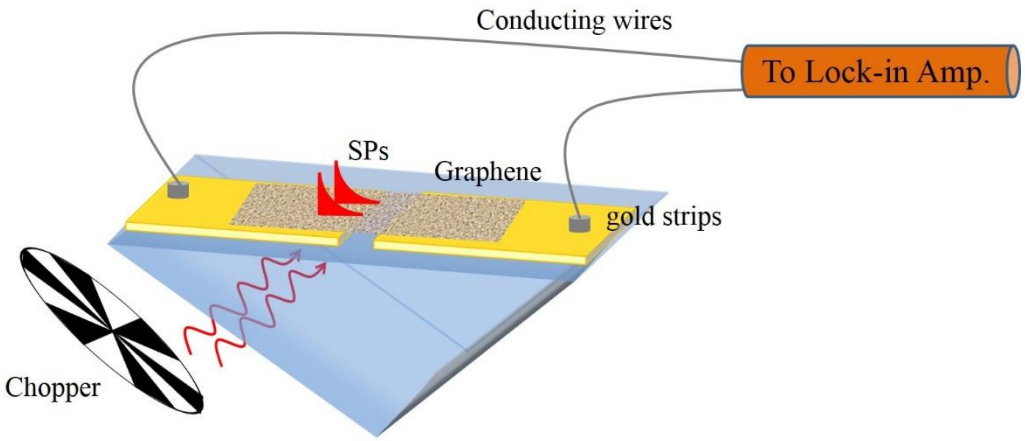

Fig. 7-23 Schematic of experimental configuration for measuring photocurrent

The results show that for p-polarized incident light, with incident angles greater than the total internal reflection angle, the photocurrent enhances and reaches its maximum value at around the plasmon resonance angles for each wavelength, Fig. 7-22 (c). At the same time by switching the polarization of the incident light to transverse electric (s-polarization), the photocurrent is not enhanced at the plasmonic resonance angles and it decreases monotonically with a small gradient. The maximum enhancement of the photocurrent occurs for $\lambda_0 = 730$ nm with an amplification factor of 8.

In addition, the results show that by moving to shorter wavelengths, the enhancement peak becomes wider. This is consistent with the increase of the width of the attenuated total internal reflection dip for the surface plasmon at shorter wavelengths. As mentioned above, the increased width of the surface plasmon resonance dip means a higher attenuation of the surface plasmons which also means that the surface plasmons are more confined to the gold-dielectric interface. As a

result, we attribute the increase of the photocurrent peak and width to the stronger interaction of the surface plasmons with the graphene sheet, resulting from the higher confinement of the surface plasmons to the gold-graphene-air interface. Moreover, photothermal effects also may play a role in this phenomenon. Higher attenuation means increased ohmic losses in the gold layer which may contribute to a thermoelectric current in the graphene. Structures with a graphene sheet deposited across the gold strips and the gap has more advantages for their thermoelectric effect coupled with the deposition of graphene on a Si substrate. Freitag. et al. [137] showed that photocurrent in suspended structures is one order of magnitude higher than the supporting structures, and they attributed this to the elimination of a dominant electron cooling channel via the surface phonons of the polar substrates.

The photocurrent response of the graphene gap-photodetector changes the sign as the incident beam position moves along the gap. When the incident beam is positioned close to the left edge of the gap, the photocurrent increases from zero to its maximum value and then gradually decreases as the beam is moved towards the right until it becomes zero when the beam illuminates the centre and both edges of the gap symmetrically, shown in Fig. 7-24.

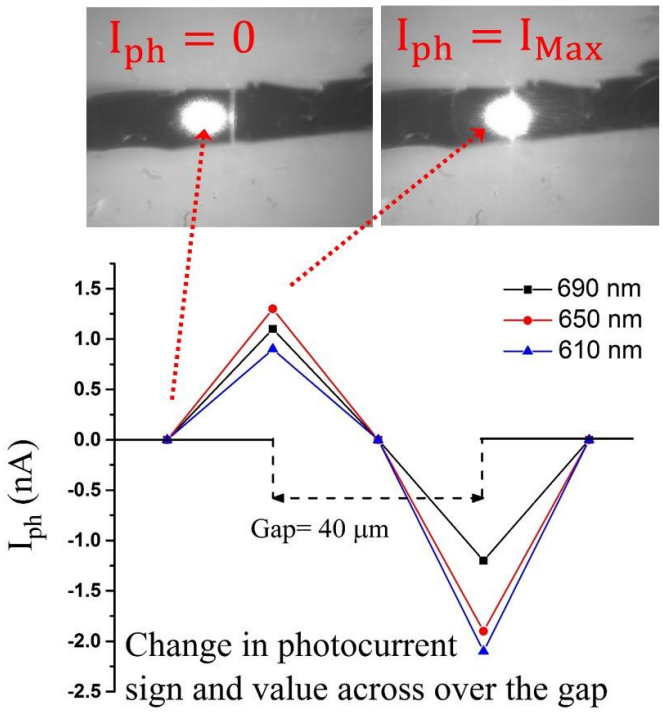

Fig. 7-24 Asymmetric photocurrent by moving the incident light along the gap

Moving the beam further to the right results in increased photocurrent, but with the opposite sign relative to the photocurrent generated at the left side. The photocurrent reaches its maximum (in absolute terms) when the beam illuminates the right edge of the gap. Moving the beam further to the right results in zero photocurrent. This asymmetric photocurrent response has been observed and discussed in graphene transistors with the applied gate bias [134, 138]. However, we are not using a gate voltage for the photocurrent measurement of our structure.

The dependence of the photocurrent on the intensity of the incident light is also measured for all the applied wavelength. The graphs in Fig. 7-25 shows the linear behaviour of the photodetector in response to the change of incident light intensity.

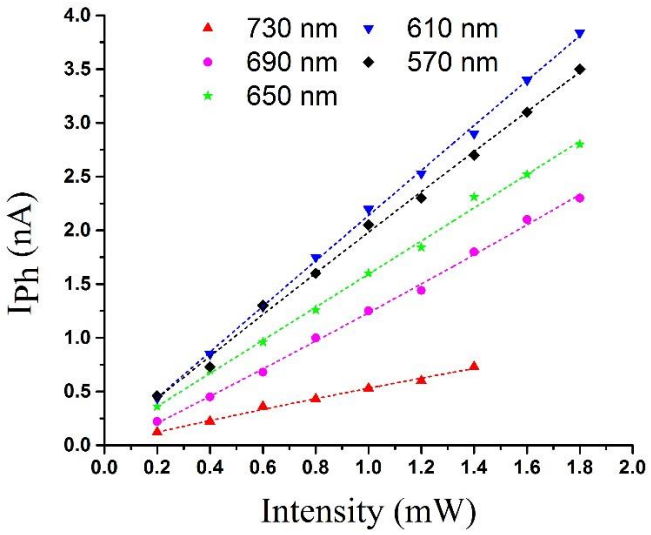

Fig. 7-25 Photocurrent dependence on the intensity of the incident light

In addition, the intensity change in shorter wavelength has a greater gradient in comparison to the longer wavelength.

7.3 Conclusions

The fabricated plasmonic structured graphene photodetectors including the curved grating and interdigitated gratings show a high level of dark current, which did not allow measurement of the plasmonic-enhanced photocurrent by the device. We attribute the dark current to the very large area of the graphene sheet in comparison to micro-scale plasmonic structures. However, Raman spectroscopy of the photodetectors shows the photo-activity of the deposited graphene layers and also the plasmonic enhancement of the graphene photo-excitation along the grooves of the plasmonic grating. The graphene gap-photodetector generates photocurrent when the gap of the photodetector is illuminated with light, and shows enhancement

of the photocurrent when the light photons are tunneled into surface plasmons by illuminating the gap at the surface plasmon resonance angle through a prism. Switching the polarization of light from transverse electric (s-polarized) to transverse magnetic (p-polarized) shows a comparative amplification of 8 at the illumination wavelength of 730 nm (for a 40 μm gap), which gives evidence for the role of surface plasmons in the enhancement of the photocurrent. Such a graphene gap-photodetector can be fabricated on waveguides to use the evanescent field for photodetection, plasmonic detection, and sensing.

Chapter 8: Conclusion

This project aimed to design and characterize three important plasmonic structures: plasmonic lenses, antennas, and photodetectors, due to their importance in plasmonic circuitry and also other applications, such as sensing. The first structures is gratings and curved gratings, for applications such as launching surface plasmons onto micro-stripline waveguides, enhancing the photodetection performance of graphene photodetectors and sensing. some important parameters of grating geometry are investigated in this thesis and the results are used to design curved gratings. Additionally, the capability of dielectric microspheres to decouple propagating surface plasmons and produce directional radiation is investigated. Finally, plasmonic-enhanced graphene photodetectors are investigated using two different approaches; the plasmonic coupling property of gratings with a diffracting light beam, and the use of evanescent electromagnetic fields. This chapter presents the conclusions of the work completed in this thesis and suggestions for possible future work and improvements.

The conclusions of this thesis can be divided in three main sections. The first section discusses the characteristics of plasmonic gratings and particularly curved gratings. The second section investigates the interaction of propagating surface plasmons with dielectric microspheres, and the third section is based on the application of plasmonic electromagnetic field enhancement for amplifying photogeneration by graphene photodetectors.

8.1.1 Characterizing plasmonic curved gratings

First, the parameters of surface relief gratings and trench gratings were optimized (based on FEM simulations) for the best coupling efficiency under normal incidence illumination. The results show that efficient coupling occurs for a trench grating illuminated through the substrate (higher refractive index), with a groove width equal to half the grating period that is half of the surface plasmon wavelength at the gold-air interface. In addition, it is shown that the depth of the grooves has a significant effect on the coupling efficiency of the gratings.

Based on some of the results of the optimization, the proposed curved gratings, as a sector of full circular gratings, were designed and fabricated. The results show the coupling of linearly polarized (p-polarized) light to focused surface plasmons at the radial centre of the grating. The focal width of the focused surface plasmons changes with the sector angle of the curved gratings and it is shown by experiment and simulation that for curved gratings with a sector angle larger than 100°, the focal width reaches 300 nm, or $\frac{\lambda_0}{2.3}$, with λ_0 as the free space wavelength of the incident light on the grating. Furthermore, the sector angle-dependent focusing property of the curved gratings motivates the definition of the numerical aperture (NA) for these plasmonic lenses. The numerical aperture for curved gratings is defined in this thesis, and its accuracy is demonstrated using simulation and experimental results.

It has been shown that circular gratings can also focus surface plasmons at the centre of the gratings [19]. However, circular gratings need to be illuminated with radially-polarized light to obtain a single focal spot, which is challenging to align in

practice, and they do not allow in-plane access to the focal spot. The two key advantages of the curved gratings in comparison to full circular gratings are: the ability to focus surface plasmons using linearly polarized light (p-polarization) and in-plane access to the focal spot for further processing. In addition, it is demonstrated in this thesis that using a symmetry-broken configuration of two curved gratings enhances the focusing of the surface plasmons to a single spot, with a smaller focal width and depth and increased focal spot intensity.

Finally, the use of curved gratings for launching surface plasmons into micro-stripline plasmonic waveguides is investigated. It is shown that for very small sector angles the coupling efficiency of curved gratings is comparable to linear gratings when integrated with micro-stripline waveguides (for 20°sector angle the coupling efficiency is 5% more than the coupling efficiency of linear gratings). However, due to the nonlinear relationship between the sector angle of the curved gratings and their focusing properties, for larger sector angles, the curved gratings show reduced coupling efficiency in comparison to linear gratings.

8.1.2 Interaction of surface plasmons with dielectric microspheres;

Plasmonic resonances or localised surface plasmons exciting metallic nano-particles give rise to some intriguing effects, such as the subwavelength localization of electromagnetic energy, creation of hot spots at the surface of metal nano-particles, or the directional scattering of light out of the structure [139], enabling the metallic nano-particles to operate as nano-antennas [21]. However, nano-metallic antennas have high ohmic loss and affect the quantum efficiency of the emitters in their vicinity [30].

In this thesis it is demonstrated that TiO_2 microspheres can scatter propagating surface plasmons and radiate them directionally, suggesting their application as an alternative for metallic nano-antennas. In addition, the effect of the diameter of the microspheres on their radiation is investigated and it is shown that for fixed incident-light wavelength, the microsphere diameter can influence the directionality and power of the radiation, because of the cavity resonance modes inside the microsphere (whispering gallery modes). Dielectric microspheres may find application in sensing and plasmonic-enhanced photodetection.

8.1.3 Plasmonic-enhanced graphene photodetectors

Surface plasmon-based technology has the potential to effectively integrate nano-electronic and micro-photonic devices [3]. Plasmonic enhanced photodetectors are particularly promising plasmonic elements, since the size of the semiconductor photodetector is constrained in the lateral dimension by the fundamental diffraction limit and in the longitudinal dimension by the finite absorption depth [35, 36].

In this thesis, plasmonic-enhanced graphene photodetectors are fabricated to use the electromagnetic near-field enhancement of surface plasmons to amplify the photocurrent generation by graphene photodetectors in two different approaches. The first approach is using the diffraction and focusing property of plasmonic curved gratings to enhance graphene photodetection performance. The large dark current measured in the device did not allow the detection of the plasmonic-enhanced photocurrent. However, Raman spectroscopic characterization of the fabricated samples shows the photo-activity of the deposited graphene and also shows the

enhancement of the photo-generation of charge carriers by plasmonic enhancement at the grooves of the grating.

The second approach uses the evanescent field at attenuated total internal reflection angle of the incident light to couple light photons onto the graphene-gold contacts to benefit the photocurrent enhancement of the surface plasmons. The results shows maximum photocurrent enhancement by a factor of 8 at a wavelength of 730 nm when the polarization of the incident light is switched to transverse magnetic (p) from transverse electric (s).

Appendix A

The aperture size of the curved gratings is the length of the chord of the first groove sector. As a result, having identical aperture size for different sector angles implies having a different radius for the first groove of the curved gratings. The schematic shows a curved grating with sector angle of 2β.

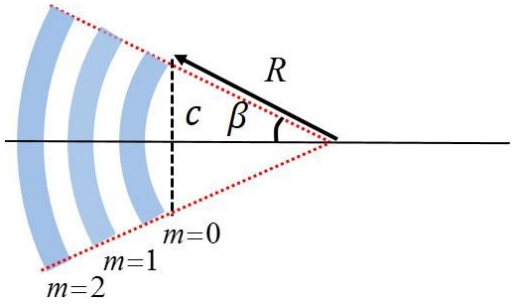

Fig. A-1 Schematic of a curved grating with aperture size of $\boldsymbol{c}$ (the chord of the first groove)

Here c shows the chord length of the first groove (the aperture size) and m designates the groove numbers in order.

The radius of the first groove (R) starts at;

$$R = \frac{c/2}{\sin(\beta)} \qquad \text{Eq. A-1}$$

Consequently the radius of the next groove can be calculated as;

$$r = R + m\Lambda_g \qquad \text{Eq. A-2}$$

References

1. R. H. Ritchie, "Plasma Losses by Fast Electrons in Thin Films," Physical Review **106(5)**, 874-881 (1957).

2. W. L. Barnes, A. Dereux, and T. W. Ebbesen, "Surface plasmon subwavelength optics," Nature **424(6950)**, 824-830 (2003).

3. R. Zia, J. A. Schuller, A. Chandran, and M. L. Brongersma, "Plasmonics: the next chip-scale technology," Materials Today **9(7-8)**, 20-27 (2006).

4. K. Kneipp, Y. Wang, H. Kneipp, L. T. Perelman, I. Itzkan, R. R. Dasari, and M. S. Feld, "Single Molecule Detection Using Surface-Enhanced Raman Scattering (SERS)," Physical Review Letters **78(9)**, 1667-1670 (1997).

5. K. Kneipp, H. Kneipp, I. Itzkan, R. R. Dasari, and M. S. Feld, "Surface-enhanced Raman scattering and biophysics," Journal of Physics: Condensed Matter **14(18)**, R597 (2002).

6. J. Homola, "Surface plasmon resonance sensors for detection of chemical and biological species," Chemical Reviews **108(2)**, 462-493 (2008).

7. Y. A. Akimov, W. Koh, and K. Ostrikov, "Enhancement of optical absorption in thin-film solar cells through the excitation of higher-order nanoparticle plasmon modes," Optics Express **17(12)**, 10195-10205 (2009).

8. H. A. Atwater and A. Polman, "Plasmonics for improved photovoltaic devices," Nature Materials **9(3)**, 205-213 (2010).

9. W. Fan, S. Zhang, K. J. Malloy, S. R. J. Brueck, N. C. Panoiu, and R. M. Osgood, "Second harmonic generation from patterned GaAs inside a subwavelength metallic hole array," Optics Express **14(21)**, 9570-9575 (2006).

10. J. Takahara and T. Kobayashi, "Low-Dimensional Optical Waves And Nano-Optical Circuits," Optics and Photonics News **15(10)**, 54-59 (2004).

11. M. L. Brongersma and V. M. Shalaev, "The Case for Plasmonics," Science **328(5977)**, 440-441 (2010).

12. R. Charbonneau, P. Berini, E. Berolo, and E. Lisicka-Shrzek, "Experimental observation of plasmon–polariton waves supported by a thin metal film of finite width," Optics Letters **25(11)**, 844-846 (2000).

13. J. A. Dionne, H. J. Lezec, and H. A. Atwater, "Highly Confined Photon Transport in Subwavelength Metallic Slot Waveguides," Nano Letters **6(9)**, 1928-1932 (2006).

14. H. Ditlbacher, A. Hohenau, D. Wagner, U. Kreibig, M. Rogers, F. Hofer, F. R. Aussenegg, and J. R. Krenn, "Silver Nanowires as Surface Plasmon Resonators," Physical Review Letters **95(25)**, 257403 (2005).

15. J.-C. Weeber, Y. Lacroute, A. Dereux, E. Devaux, T. Ebbesen, C. Girard, M. U. González, and A.-L. Baudrion, "Near-field characterization of Bragg mirrors engraved in surface plasmon waveguides," Physical Review B **70(23)**, 235406 (2004).

16. A. Drezet, D. Koller, A. Hohenau, A. Leitner, F. R. Aussenegg, and J. R. Krenn, "Plasmonic Crystal Demultiplexer and Multiports," Nano Letters **7(6)**, 1697-1700 (2007).

17. D. Pacifici, H. J. Lezec, and H. A. Atwater, "All-optical modulation by plasmonic excitation of CdSe quantum dots," Nature Photonics **1(7)**, 402-406 (2007).

18. J. T. Kim, J. J. Ju, S. Park, M.-s. Kim, S. K. Park, and M.-H. Lee, "Chip-to-chip optical interconnect using goldlong-range surface plasmon polaritonwaveguides," Optics Express **16(17)**, 13133-13138 (2008).

19. J. M. Steele, Z. W. Liu, Y. Wang, and X. Zhang, "Resonant and non-resonant generation and focusing of surface plasmons with circular gratings," Optics Express **14(12)**, 5664-5670 (2006).

20. A. Maleki, T. Vo, A. Hautin, J. Downes, D. Coutts, and J. Dawes, "Curved Gratings as Plasmonic Lenses for Linearly Polarized Light," Plasmonics, 1-8 (2015).

21. V. Giannini, A. I. Fernández-Domínguez, S. C. Heck, and S. A. Maier, "Plasmonic Nanoantennas: Fundamentals and Their Use in Controlling the Radiative Properties of Nanoemitters," Chemical Reviews **111(6)**, 3888-3912 (2011).

22. T. Ishi, J. Fujikata, K. Makita, T. Baba, and K. Ohashi, "Si nano-photodiode with a surface plasmon antenna," Japanese J. Applied Physics Part 2 44(12-15), L364-L366 (2005).

23. L. Tang, S. E. Kocabas, S. Latif, A. K. Okyay, D. S. Ly-Gagnon, K. C. Saraswat, and D. A. B. Miller, "Nanometre-scale germanium photodetector enhanced by a near-infrared dipole antenna," Nature Photonics **2(4)**, 226-229 (2008).

24. P. Neutens, P. Van Dorpe, I. De Vlaminck, L. Lagae, and G. Borghs, "Electrical detection of confined gap plasmons in metal-insulator-metal waveguides," Nature Photonics **3(5)**, 283-286 (2009).

25. X. Fan, W. Zheng, and D. J. Singh, "Light scattering and surface plasmons on small spherical particles," Light Science and Applications **3(**e179 (2014).

26. A. Kinkhabwala, Z. Yu, S. Fan, Y. Avlasevich, K. Mullen, and W. E. Moerner, "Large single-molecule fluorescence enhancements produced by a bowtie nanoantenna," Nature Photonics **3(11)**, 654-657 (2009).

27. A. McLeod, K. C. Vernon, A. E. Rider, and K. Ostrikov, "Optical coupling of gold nanoparticles on vertical graphenes to maximize SERS response," Optics Letters **39(8)**, 2334-2337 (2014).

28. P. Jain, X. Huang, I. El-Sayed, and M. El-Sayed, "Review of Some Interesting Surface Plasmon Resonance-enhanced Properties of Noble Metal Nanoparticles and Their Applications to Biosystems," Plasmonics **2(3)**, 107-118 (2007).

29. Z. Fang, L. Fan, C. Lin, D. Zhang, A. J. Meixner, and X. Zhu, "Plasmonic Coupling of Bow Tie Antennas with Ag Nanowire," Nano Letters **11(4)**, 1676-1680 (2011).

30. A. Devilez, B. Stout, and N. Bonod, "Compact Metallo-Dielectric Optical Antenna for Ultra Directional and Enhanced Radiative Emission," ACS Nano **4(6)**, 3390-3396 (2010).

31. A. E. Krasnok, A. E. Miroshnichenko, P. A. Belov, and Y. S. Kivshar, "All-dielectric optical nanoantennas," Optics Express **20(18)**, 20599-20604 (2012).

32. D. S. Filonov, A. E. Krasnok, A. P. Slobozhanyuk, P. V. Kapitanova, E. A. Nenasheva, Y. S. Kivshar, and P. A. Belov, "Experimental verification of the concept of all-dielectric nanoantennas," Applied Physics Letters **100(20)**, 201113 (2012).

33. P. Anger, P. Bharadwaj, and L. Novotny, "Enhancement and Quenching of Single-Molecule Fluorescence," Physical Review Letters **96(11)**, 113002 (2006).

34. T. Pakizeh and M. Käll, "Unidirectional Ultracompact Optical Nanoantennas," Nano Letters **9(6)**, 2343-2349 (2009).

35. J. A. Schuller, E. S. Barnard, W. Cai, Y. C. Jun, J. S. White, and M. L. Brongersma, "Plasmonics for extreme light concentration and manipulation," Nature Materials **9(3)**, 193-204 (2010).

36. F. Koppens, T. Mueller, P. Avouris, A. Ferrari, M. Vitiello, and M. Polini, "Photodetectors based on graphene, other two-dimensional materials and hybrid systems," Nature Nanotechnology **9(10)**, 780-793 (2014).

37. T. Echtermeyer, L. Britnell, P. Jasnos, A. Lombardo, R. Gorbachev, A. Grigorenko, A. Geim, A. Ferrari, and K. Novoselov, "Strong plasmonic enhancement of photovoltage in graphene," Nature Communications **2(**458 (2011).

38. Z. Fang, Z. Liu, Y. Wang, P. M. Ajayan, P. Nordlander, and N. J. Halas, "Graphene-antenna sandwich photodetector," Nano Letters **12(7)**, 3808-3813 (2012).

39. M. Freitag, T. Low, W. Zhu, H. Yan, F. Xia, and P. Avouris, "Photocurrent in graphene harnessed by tunable intrinsic plasmons," Nature Communications 4 (2013).

40. S. A. Maier, Plasmonics: Fundamentals and Applications (Springer, 2007).

41. H. Raether, "Surface-Plasmons on Smooth and Rough Surfaces and on Gratings," Springer Tr Mod Phys **111(**1-133 (1988).

42. A. V. Zayats, I. I. Smolyaninov, and A. A. Maradudin, "Nano-optics of surface plasmon polaritons," Physical Reviews **408(3)**, 131-314 (2005).

43. P. R. West, S. Ishii, G. V. Naik, N. K. Emani, V. M. Shalaev, and A. Boltasseva, "Searching for better plasmonic materials," Laser & Photonics Reviews **4(6)**, 795-808 (2010).

44. A. Otto, "Excitation of nonradiative surface plasma waves in silver by the method of frustrated total reflection," Z. Physik **216(4)**, 398-410 (1968).

45. P. Drude, "Zur Elektronentheorie der Metalle," Annalen Physik **306(3)**, 566-613 (1900).

46. P. B. Johnson and R. W. Christy, "Optical Constants of the Noble Metals," Physical Review B **6(12)**, 4370-4379 (1972).

47. P. Karpinski and A. Miniewicz, "Surface plasmon polariton excitation in metallic layer via surface relief gratings in photoactive polymer studied by the finite-difference time-domain method," Plasmonics **6(3)**, 541-546 (2011).

48. J. Andkjaer, S. Nishiwaki, T. Nomura, and O. Sigmund, "Topology optimization of grating couplers for the efficient excitation of surface plasmons," J. Optical Society America B **27(9)**, 1828-1832 (2010).

49. N. Rotenberg and J. E. Sipe, "Analytic model of plasmonic coupling: Surface relief gratings," Physical Review B **83(4)**(2011).

50. J. Lu, C. Petre, E. Yablonovitch, and J. Conway, "Numerical optimization of a grating coupler for the efficient excitation of surface plasmons at an Ag-SiO2 interface," J. Optical Society America B **24(9)**, 2268-2272 (2007).

51. S. T. Koev, A. Agrawal, H. J. Lezec, and V. A. Aksyuk, "An Efficient Large-Area Grating Coupler for Surface Plasmon Polaritons," Plasmonics **7(2)**, 269-277 (2012).

52. W. B. Chen, D. C. Abeysinghe, R. L. Nelson, and Q. W. Zhan, "Plasmonic Lens Made of Multiple Concentric Metallic Rings under Radially Polarized Illumination," Nano Letters **9(12)**, 4320-4325 (2009).

53. X. W. Li, L. L. Huang, Q. F. Tan, B. F. Bai, and G. F. Jin, "Integrated plasmonic semi-circular launcher for dielectric-loaded surface plasmon-polariton waveguide," Optics Express **19(7)**, 6541-6548 (2011).

54. C. Lee, X. D. Wei, J. W. Kysar, and J. Hone, "Measurement of the elastic properties and intrinsic strength of monolayer graphene," Science **321(5887)**, 385-388 (2008).

55. P. Avouris, "Graphene: Electronic and Photonic Properties and Devices," Nano Letters **10(11)**, 4285-4294 (2010).

56. M. Jablan, H. Buljan, and M. Soljačić, "Plasmonics in graphene at infrared frequencies," Physical Review B **80(24)**, 245435 (2009).

57. K. S. Novoselov, A. K. Geim, S. V. Morozov, D. Jiang, M. I. Katsnelson, I. V. Grigorieva, S. V. Dubonos, and A. A. Firsov, "Two-dimensional gas of massless Dirac fermions in graphene," Nature **438(7065)**, 197-200 (2005).

58. X. Du, I. Skachko, A. Barker, and E. Y. Andrei, "Approaching ballistic transport in suspended graphene," Nature Nanotechnology **3(8)**, 491-495 (2008).

59. C. R. Dean, A. F. Young, MericI, LeeC, WangL, SorgenfreiS, WatanabeK, TaniguchiT, KimP, K. L. Shepard, and HoneJ, "Boron nitride substrates for high-quality graphene electronics," Nature Nanotechnology **5(10)**, 722-726 (2010).

60. A. S. Mayorov, R. V. Gorbachev, S. V. Morozov, L. Britnell, R. Jalil, L. A. Ponomarenko, P. Blake, K. S. Novoselov, K. Watanabe, and T. Taniguchi, "Micrometer-scale ballistic transport in encapsulated graphene at room temperature," Nano Letters **11(6)**, 2396-2399 (2011).

61. T. Low and P. Avouris, "Graphene plasmonics for terahertz to mid-infrared applications," ACS Nano **8(2)**, 1086-1101 (2014).

62. D. K. Efetov and P. Kim, "Controlling electron-phonon interactions in graphene at ultrahigh carrier densities," Physical Review Letters **105(25)**, 256805 (2010).

63. T. Ando, Y. Zheng, and H. Suzuura, "Dynamical conductivity and zero-mode anomaly in honeycomb lattices," Journal of the Physical Society of Japan **71(5)**, 1318-1324 (2002).

64. A. Kuzmenko, E. Van Heumen, F. Carbone, and D. Van Der Marel, "Universal optical conductance of graphite," Physical Review Letters **100(11)**, 117401 (2008).

65. Z. Q. Li, E. A. Henriksen, Z. Jiang, Z. Hao, M. C. Martin, P. Kim, H. L. Stormer, and D. N. Basov, "Dirac charge dynamics in graphene by infrared spectroscopy," Nature Physics **4(7)**, 532-535 (2008).

66. S. Aksu, A. A. Yanik, R. Adato, A. Artar, M. Huang, and H. Altug, "High-Throughput Nanofabrication of Infrared Plasmonic Nanoantenna Arrays for Vibrational Nanospectroscopy," Nano Letters **10(7)**, 2511-2518 (2010).

67. A. C. Ferrari and D. M. Basko, "Raman spectroscopy as a versatile tool for studying the properties of graphene," Nature Nanotechnology **8(4)**, 235-246 (2013).

68. A. C. Ferrari, J. C. Meyer, V. Scardaci, C. Casiraghi, M. Lazzeri, F. Mauri, S. Piscanec, D. Jiang, K. S. Novoselov, S. Roth, and A. K. Geim, "Raman Spectrum of Graphene and Graphene Layers," Physical Review Letters **97(18)**, 187401 (2006).

69. C. Casiraghi, S. Pisana, K. Novoselov, A. Geim, and A. Ferrari, "Raman fingerprint of charged impurities in graphene," Applied Physics Letters **91(23)**, 233108 (2007).

70. W. X. Wang, S. H. Liang, T. Yu, D. H. Li, Y. B. Li, and X. F. Han, "The study of interaction between graphene and metals by Raman spectroscopy," Journal of Applied Physics **109(7)**, 07C501 (2011).

71. A. Das, S. Pisana, B. Chakraborty, S. Piscanec, S. K. Saha, U. V. Waghmare, K. S. Novoselov, H. R. Krishnamurthy, A. K. Geim, A. C. Ferrari, and A. K. Sood, "Monitoring dopants by Raman scattering in an electrochemically top-gated graphene transistor," Nature Nanotechnology **3(4)**, 210-215 (2008).

72. D. M. Basko, S. Piscanec, and A. C. Ferrari, "Electron-electron interactions and doping dependence of the two-phonon Raman intensity in graphene," Physical Review B **80(16)**, 165413 (2009).

73. A. Das, B. Chakraborty, S. Piscanec, S. Pisana, A. K. Sood, and A. C. Ferrari, "Phonon renormalization in doped bilayer graphene," Physical Review B **79(15)**, 155417 (2009).

74. W. Gao, J. Shu, C. Qiu, and Q. Xu, "Excitation of plasmonic waves in graphene by guided-mode resonances," ACS Nano **6(9)**, 7806-7813 (2012).

75. V. Yong and J. M. Tour, "Theoretical Efficiency of Nanostructured Graphene-Based Photovoltaics," Small **6(2)**, 313-318 (2010).

76. N. Yang, J. Zhai, D. Wang, Y. Chen, and L. Jiang, "Two-dimensional graphene bridges enhanced photoinduced charge transport in dye-sensitized solar cells," ACS Nano **4(2)**, 887-894 (2010).

77. S. Bae, H. Kim, Y. Lee, X. Xu, J.-S. Park, Y. Zheng, J. Balakrishnan, T. Lei, H. Ri Kim, Y. I. Song, Y.-J. Kim, K. S. Kim, B. Ozyilmaz, J.-H. Ahn, B. H. Hong, and S. Iijima, "Roll-to-roll production of 30-inch graphene films for transparent electrodes," Nature Nanotechnology **5(8)**, 574-578 (2010).

78. P. Matyba, H. Yamaguchi, G. Eda, M. Chhowalla, L. Edman, and N. D. Robinson, "Graphene and mobile ions: the key to all-plastic, solution-processed light-emitting devices," ACS Nano **4(2)**, 637-642 (2010).

79. T. Mueller, F. Xia, and P. Avouris, "Graphene photodetectors for high-speed optical communications," Nature Photonics **4(5)**, 297-301 (2010).

80. F. Xia, T. Mueller, Y. Lin, A. Valdes-Garcia, and P. Avouris, "Ultrafast graphene photodetector," Nature Nanotechnology **4(12)**, 839-843 (2009).

81. Z. Li, E. A. Henriksen, Z. Jiang, Z. Hao, M. C. Martin, P. Kim, H. Stormer, and D. N. Basov, "Dirac charge dynamics in graphene by infrared spectroscopy," Nature Physics **4(7)**, 532-535 (2008).

82. F. Wang, Y. Zhang, C. Tian, C. Girit, A. Zettl, M. Crommie, and Y. R. Shen, "Gate-Variable Optical Transitions in Graphene," Science **320(5873)**, 206-209 (2008).

83. E. C. Peters, E. J. Lee, M. Burghard, and K. Kern, "Gate dependent photocurrents at a graphene pn junction," Applied Physics Letters **97(19)**, 193102 (2010).

84. G. Rao, M. Freitag, H.-Y. Chiu, R. S. Sundaram, and P. Avouris, "Raman and photocurrent imaging of electrical stress-induced p–n junctions in graphene," ACS Nano **5(7)**, 5848-5854 (2011).

85. T. Mueller, F. Xia, M. Freitag, J. Tsang, and P. Avouris, "Role of contacts in graphene transistors: A scanning photocurrent study," Physical Review B **79(24)**, 245430 (2009).

86. D. B. Farmer, R. Golizadeh-Mojarad, V. Perebeinos, Y.-M. Lin, G. S. Tulevski, J. C. Tsang, and P. Avouris, "Chemical doping and electron− hole conduction asymmetry in graphene devices," Nano Letters **9(1)**, 388-392 (2008).

87. M. Freitag, T. Low, F. Xia, and P. Avouris, "Photoconductivity of biased graphene," Nature Photonics **7(1)**, 53-59 (2013).

88. J. H. LeeEduardo, K. Balasubramanian, R. T. Weitz, M. Burghard, and K. Kern, "Contact and edge effects in graphene devices," Nature Nanotechnology **3(8)**, 486-490 (2008).

89. T. Mueller, F. Xia, and P. Avouris, "Graphene photodetectors for high-speed optical communications," Nature Photonics **4(5)**, 297-301 (2010).

90. J. Park, Y. Ahn, and C. Ruiz-Vargas, "Imaging of photocurrent generation and collection in single-layer graphene," Nano Letters **9(5)**, 1742-1746 (2009).

91. F. Schedin, E. Lidorikis, A. Lombardo, V. G. Kravets, A. K. Geim, A. N. Grigorenko, K. S. Novoselov, and A. C. Ferrari, "Surface-enhanced Raman spectroscopy of graphene," ACS Nano **4(10)**, 5617-5626 (2010).

92. J. Mertens, A. L. Eiden, D. O. Sigle, F. Huang, A. Lombardo, Z. Sun, R. S. Sundaram, A. Colli, C. Tserkezis, and J. Aizpurua, "Controlling subnanometer gaps in plasmonic dimers using graphene," Nano Letters **13(11)**, 5033-5038 (2013).

93. Z. Fang, Y. Wang, Z. Liu, A. Schlather, P. M. Ajayan, F. H. Koppens, P. Nordlander, and N. J. Halas, "Plasmon-induced doping of graphene," ACS Nano **6(11)**, 10222-10228 (2012).

94. J. T. Kim, Y.-J. Yu, H. Choi, and C.-G. Choi, "Graphene-based plasmonic photodetector for photonic integrated circuits," Optics Express **22(1)**, 803-808 (2014).

95. C. F. Bohren and D. R. Huffman, Absorption and scattering of light by small particles (John Wiley & Sons, 2008).

96. E. Hutter and J. H. Fendler, "Exploitation of localized surface plasmon resonance," Advanced Materials **16(19)**, 1685-1706 (2004).

97. A. E. Krasnok, A. E. Miroshnichenko, P. A. Belov, and Y. S. Kivshar, "Huygens optical elements and Yagi—Uda nanoantennas based on dielectric nanoparticles," JETP Letters **94(8)**, 593-598 (2011).

98. J. Jackson, Classical Electrodynamics Third Edition (Wiley, 1998).

99. J. Jin, The finite element method in electromagnetics (John Wiley & Sons, 2014).

100. "RF Module," 2015 by COMSOL inc. www.comsol.com.

101. M. Born and E. Wolf, Principles of optics: electromagnetic theory of propagation, interference and diffraction of light (Cambridge university press, 1999).

102. "Introduction to Near Field Scanning Microscope," 2012 Olympus America Inc.http://www.olympusmicro.com/primer/techniques/nearfield/nearfieldhome.html.

103. P. N. Prasad, Nanophotonics (Wiley, 2004).

104. E. Synge, "XXXVIII. A suggested method for extending microscopic resolution into the ultra-microscopic region," The London, Edinburgh, and Dublin Philosophical Magazine and Journal of Science 6(35), 356-362 (1928).

105. D. W. Pohl, W. Denk, and M. Lanz, "Optical stethoscopy: Image recording with resolution λ/20," Applied Physics Letters 44(7), 651-653 (1984).

106. E. Betzig and J. K. Trautman, "Near-field optics: microscopy, spectroscopy, and surface modification beyond the diffraction limit," Science 257(5067), 189-195 (1992).

107. S. Ezugwu, H. Ye, and G. Fanchini, "Three-dimensional scanning near field optical microscopy (3D-SNOM) imaging of random arrays of copper nanoparticles: implications for plasmonic solar cell enhancement," Nanoscale 7(1), 252-260 (2015).

108. A. Bouhelier and L. Novotny, "Near-field optical excitation and detection of surface plasmons," in Surface Plasmon Nanophotonics (Springer, 2007), pp. 139-153.

109. A. Giannattasio, I. R. Hooper, and W. L. Barnes, "Dependence on surface profile in grating-assisted coupling of light to surface plasmon-polaritons," Optics Communications 261(2), 291-295 (2006).

110. G. M. Lerman, A. Yanai, and U. Levy, "Demonstration of Nanofocusing by the use of Plasmonic Lens Illuminated with Radially Polarized Light," Nano Letters 9(5), 2139-2143 (2009).

111. T. Tanemura, K. C. Balram, D. S. Ly-Gagnon, P. Wahl, J. S. White, M. L. Brongersma, and D. A. Miller, "Multiple-wavelength focusing of surface plasmons with a nonperiodic nanoslit coupler," Nano Letters 11(7), 2693-2698 (2011).

112. G. Gaborit, D. Armand, J.-L. Coutaz, M. Nazarov, and A. Shkurinov, "Excitation and focusing of terahertz surface plasmons using a grating coupler with elliptically curved grooves," Applied Physics Letters 94(23), 231108 (2009).

113. I. P. Radko, S. I. Bozhevolnyi, A. B. Evlyukhin, and A. Boltasseva, "Surface plasmon polariton beam focusing with parabolic nanoparticle chains," Optics Express 15(11), 6576-6582 (2007).

114. C. L. Zhao, J. Y. Wang, X. F. Wu, and J. S. Zhang, "Focusing surface plasmons to multiple focal spots with a launching diffraction grating," Applied Physics Letters 94(11)(2009).

115. A. Drezet, A. L. Stepanov, H. Ditlbacher, A. Hohenau, B. Steinberger, F. R. Aussenegg, A. Leitner, and J. R. Krenn, "Surface plasmon propagation in an elliptical corral," Applied Physics Letters 86(7)(2005).

116. G. Gaborit, D. Armand, J. L. Coutaz, M. Nazarov, and A. Shkurinov, "Excitation and focusing of terahertz surface plasmons using a grating coupler with elliptically curved grooves," Applied Physics Letters 94(23)(2009).

117. S. A. Maier, S. R. Andrews, L. Martín-Moreno, and F. J. García-Vidal, "Terahertz Surface Plasmon-Polariton Propagation and Focusing on Periodically Corrugated Metal Wires," Physics Review Letters 97(17), 176805 (2006).

118. Z. W. Liu, J. M. Steele, W. Srituravanich, Y. Pikus, C. Sun, and Z. X, "Focusing surface plasmons with a plasmonic lens," Nano Letters 5(9), 1726-1729 (2005).

119. F. López-Tejeira, S. G. Rodrigo, L. Martín-Moreno, F. J. García-Vidal, E. Devaux, T. W. Ebbesen, J. R. Krenn, I. P. Radko, S. I. Bozhevolnyi, M. U. González, J. C. Weeber, and A. Dereux, "Efficient unidirectional nanoslit couplers for surface plasmons," Nature Physics 3(5), 324-328 (2007).

120. E. H. Khoo, Z. Guo, I. Ahmed, and E. P. Li, "Near-Field Switching and Focusing using Plasmonic Nanostructures with Different Polarizations," Proc. SPIE 8457(1-8 (2012).

121. Y. Q. Fu, Y. Liu, X. L. Zhou, Z. W. Xu, and F. Z. Fang, "Experimental investigation of superfocusing of plasmonic lens with chirped circular nanoslits," Optics Express 18(4), 3438-3443 (2010).

122. Z. Y. Fang, Q. A. Peng, W. T. Song, F. H. Hao, J. Wang, P. Nordlander, and X. Zhu, "Plasmonic Focusing in Symmetry Broken Nanocorrals," Nano Letters 11(2), 893-897 (2011).

123. B. Gjonaj, A. David, Y. Blau, G. Spektor, M. Orenstein, S. Dolev, and G. Bartal, "Sub-100 nm Focusing of Short Wavelength Plasmons in Homogeneous 2D Space," Nano Letters 14(10), 5598-5602 (2014).

124. S. H. Chang, S. K. Gray, and G. C. Schatz, "Surface plasmon generation and light transmission by isolated nanoholes and arrays of nanoholes in thin metal films," Optics Express 13(8), 3150-3165 (2005).

125. P. J. Martin, W. G. Sainty, and R. P. Netterfield, "Enhanced Gold Film Bonding by Ion-Assisted Deposition," Applied Optics **23(16)**, 2668-2669 (1984).

126. P. Berini, "Long-range surface plasmon polaritons," Adv. Opt. Photon. **1(3)**, 484-588 (2009).

127. J.-C. Weeber, Y. Lacroute, and A. Dereux, "Optical near-field distributions of surface plasmon waveguide modes," Physical Review B **68(11)**, 115401 (2003).

128. C. Chengkun and P. Berini, "Broadside Excitation of Long-Range Surface Plasmons via Grating Coupling," Photonics Technology Letters, IEEE 21(24), 1831-1833 (2009).

129. C. S. Perera, K. C. Vernon, A. M. Funston, H. Cheng, F. Eftekhari, and T. J. Davis, "Excitation of bound plasmons along nanoscale stripe waveguides: a comparison of end and grating coupling techniques," Optics Express **23(8)**, 10188-10197 (2015).

130. C. Chen and P. Berini, "Grating couplers for broadside input and output coupling of long-range surface plasmons," Optics Express **18(8)**, 8006-8018 (2010).

131. A. Drezet, A. Hohenau, J. Krenn, M. Brun, and S. Huant, "Surface plasmon mediated near-field imaging and optical addressing in nanoscience," Micron 38(4), 427-437 (2007).

132. T. Echtermeyer, S. Milana, U. Sassi, A. Eiden, M. Wu, E. Lidorikis, and A. Ferrari, "Surface plasmon polariton graphene photodetectors," arXiv preprint arXiv:1505.06721 (2015).

133. J. H. LeeEduardo, K. Balasubramanian, R. T. Weitz, M. Burghard, and K. Kern, "Contact and edge effects in graphene devices," Nat Nano **3(8)**, 486-490 (2008).

134. T. Mueller, F. Xia, M. Freitag, J. Tsang, and P. Avouris, "Role of contacts in graphene transistors: A scanning photocurrent study," Physical Review B **79(24)**, 245430 (2009).

135. X. Xu, N. M. Gabor, J. S. Alden, A. M. van der Zande, and P. L. McEuen, "Photo-Thermoelectric Effect at a Graphene Interface Junction," Nano Letters **10(2)**, 562-566 (2010).

136. M. A. Noginov, V. A. Podolskiy, G. Zhu, M. Mayy, M. Bahoura, J. A. Adegoke, B. A. Ritzo, and K. Reynolds, "Compensation of loss in propagating surface plasmon polariton by gain in adjacent dielectric medium," Opt. Express **16(2)**, 1385-1392 (2008).

137. M. Freitag, T. Low, and P. Avouris, "Increased Responsivity of Suspended Graphene Photodetectors," Nano Lett. **13(4)**, 1644-1648 (2013).

138. F. Xia, T. Mueller, R. Golizadeh-Mojarad, M. Freitag, Y.-m. Lin, J. Tsang, V. Perebeinos, and P. Avouris, "Photocurrent imaging and efficient photon detection in a graphene transistor," Nano Lett. **9(3)**, 1039-1044 (2009).

139. X. Fan, W. Zheng, and D. J. Singh, "Light scattering and surface plasmons on small spherical particles," Light Science Applications **3(**e179 (2014).

Publications

Journal Publications

1. **A. Maleki**, B. Cumming, M. Gu, J. Downes, D. Coutts, and J. Dawes, “Photocurrent enhancment of graphene gap-photodetectors by tunneling light photons into surface plasmons” Manuscript in preparation (Dec 2015)
2. **A. Maleki**, T. Vo, A. Hautin, J. Downes, D. Coutts, and J. Dawes, “Dielectric nanoparticle antennas for plasmonic waveguides” Manuscript in preparation (Dec 2015),
3. **A. Maleki**, T. Vo, A. Hautin, J. Downes, D. Coutts, and J. Dawes, "Curved Gratings as Plasmonic Lenses for Linearly Polarized Light," Plasmonics, 1-8 (2015).

Conference Publications

1. **A Maleki**, B Cumming, M Gu, JE Downes, DW Coutts, JM Dawes, “Photocurrent enhancement of graphene gap-photodetectors by photon tunnelling of light into surface plamsons” Recent Progress of Graphene Research (RPGR) 2015, Melbourne, Lorne, Australi,
2. **A Maleki,** JE Downes, DW Coutts, JM Dawes, “Focusing surface plasmons with curved gratings” *Near Field Optics 13*, Salt Lake City, Utah USA (2014),
3. TP Vo, **A Maleki**, JE Downes, DW Coutts, JM Dawes “Focusing of surface plasmons with a plasmonic lens”, Proc SPIE 9163, 91633L1-4, *Plasmonics: Metallic Nanostructures and Their Optical Properties* XII, (2014).

4. **A Maleki,** A Hautin, TP Vo, JE Downes, JM Dawes. "Excitation of surface plasmon polaritons with half circular gratings" *Australian and New Zealand Conference on Optics and Photonics*, Fremantle, 2013.
5. TP Vo, **A Maleki,** JE Downes, DW Coutts, JM Dawes, "Investigation of surface plasmon amplification in finite-width gold stripline based on Nd:YVO_4 crystal" *CLEO USA* (2013)
6. **A Maleki,** TP Vo, D Jin, J Downes, JM Dawes, "Coupling light beams into surface plasmon structures" *AIP congress*, Sydney 2012

Plasmonics
DOI 10.1007/s11468-015-0031-2

Curved Gratings as Plasmonic Lenses for Linearly Polarised Light

Alireza Maleki[1,2] · **Thanh Phong Vo**[1,2] · **Antoine Hautin**[1,2,3] · **James E Downes**[2] · **David W Coutts**[1,2] · **Judith M Dawes**[1,2]

Received: 28 April 2015 / Accepted: 26 July 2015

Abstract The ability of curved gratings as sectors of concentric circular gratings to couple linearly polarised light into focused surface plasmons is investigated by theory, simulation, and experiment. The experimental and simulation results show that increasing the sector angle of the curved gratings decreases the width of the lateral distribution of surface plasmons resulting in focusing of surface plasmons, which is analogous to the behaviour of classical optical lenses. We also show that two faced curved gratings, with their groove radius mismatched by half of the plasmon wavelength (asymmetric configuration), can couple linearly polarised light into a single focal spot of concentrated surface plasmons with smaller depth of focus and higher intensity in comparison to single curved gratings. The major advantage of these structures is the coupling of linearly polarised light into focused surface plasmons with access to, and control of, the plasmon focal spot, which facilitate their potential applications in sensing, detection, and nonlinear plasmonics.

Keywords Plasmonics · Surface plasmons · Diffraction gratings

✉ Alireza Maleki
alireza.maleki@mq.edu.au

[1] ARC Centre of Excellence CUDOS, Macquarie University, Sydney NSW 2109, Australia

[2] MQ Photonics Research Centre, Department of Physics and Astronomy, Macquarie University, Sydney NSW 2109, Australia

[3] Ecole Centrale de Lyon, 36 Avenue Guy de Collongue, 69134 Ecully Cedex, France

Introduction

Engineered metallic nanostructures have the ability to confine and manipulate electromagnetic waves as collective oscillations of free electrons at a metal-dielectric interface at nanometre length scales, known as surface plasmons [1]. The capability of surface plasmons to concentrate electromagnetic fields with high local field intensities has attracted attention for novel nano-photonic technologies in sensing [2–4], photo-detection [5–7], nonlinear optics [8–10], and nano-photonic devices and circuitry [11–13]. Surface plasmons also show a larger effective propagation constant than light, necessitating specific techniques for coupling photons to surface plasmons. The coupling methods are in principal based on either photon tunnelling, for example, total internal reflection by prisms, or diffraction via tailored plasmonic structures, such as gratings and nano-antennas.

Plasmonic gratings have emerged as one of the best practical techniques to efficiently couple photons into surface plasmons on 2D platforms [14]. In addition, because of the highly confined electric field of plasmons to the metal-dielectric interface, tailoring the geometry of the gratings provides the opportunity to manipulate the surface plasmons. Here, we show the capability of curved gratings, as sectors of full circular gratings, to focus the coupled incident linearly polarised (*p*-polarised) light into surface plasmons.

Plasmonic focusing concentrates surface plasmons in 2D at a metal-dielectric interface. Various plasmonic focusing structures have been demonstrated experimentally, including engineered arrays of metallic nano-slits [15], an arc of nano-holes [16], parabolic nanoparticle chains [17], diffraction gratings [18], and an elliptical corral [19] with particular applications in wavelength division multiplexing, spectral filtering, waveguide coupling, correction of divergent surface plasmon beams, and angular interferometry, respectively. Elliptically

Published online: 25 August 2015

curved gratings [20] and periodically corrugated wires have been proposed and investigated for terahertz frequencies [21].

Single circular slits can also act as surface plasmon focusing elements [22–24]. However, using linearly polarised light results in two high-intensity spots along the diameter of the circular slits in the polarisation direction of the beam, due to destructive interference of counter-propagating surface plasmons at the centre of the circle. In order to have a single spot at the centre of a circular slit, one needs to illuminate the structure with radially polarised light for constructive interference of counter-propagating surface plasmons at the centre of the circular slit. Further, it has been shown that circular gratings, consisting of several circular slits, can focus surface plasmons to the centre of the concentric circles when illuminated with circularly polarised light [25–27]. Due to the increased number of circular concentric slits in circular gratings, the focused surface plasmons have a higher intensity in comparison to a single circular slit. Linearly polarised light may also be coupled to focus surface plasmons by placing two concentric half-circular slits or corrals facing each other. However, the slit radii need to be mismatched by half of the plasmon wavelength, to provide phase matching and enable constructive interference of the counter-propagating surface plasmons at the centre of the gratings [28, 29].

Curved gratings are sectors of full concentric circular gratings, as illustrated in Fig. 1. Here, we investigate the ability of curved gratings to focus surface plasmons. A key requirement of plasmonic focusing elements is the ability to control the width of the lateral distribution of the coupled surface plasmons. We present simulations and experimental results that demonstrate the effect of the sector angle of curved gratings on the width of the focussed surface plasmons, when they are illuminated with linearly polarised light (*p*-polarised). In comparison, full circular gratings offer efficient focusing of surface plasmons to the grating centre when radially polarised light beam is well-aligned with the radial centre of the circular slits, which can be challenging in practice. Furthermore, the curved gratings are positioned to one side of the focal spot and the region beyond the focal point allows access to concentrated surface plasmons for further processes. An alternative design uses two facing curved gratings with identical sector angles in an asymmetric concentric configuration (with the corresponding groove radii mismatched by half of the surface plasmon wavelength). This design can focus surface plasmons to a smaller longitudinal spot size, with higher intensity in comparison to the single-sector curved gratings. Considering these advantages, these asymmetric double curved grating structures have potential applications in sensing, detection, and nonlinear plasmonics.

Fabrication and Experimental Results

Four different sector angles, 20°, 40°, 120°, and 180°, each with seven grooves, were selected for the fabrication of the curved gratings. The inner groove radius was selected so as to maintain a constant effective aperture size of 3.0 μm for each structure. The 30-nm-thick gold films were deposited on a glass substrate (refractive index $n=1.5$) by ion-assisted deposition using an oxygen plasma-assisted thermal deposition system, to ensure good adhesion, flatness, and uniformity of the gold film on the glass [30]. The curved gratings were fabricated with grooves milled through the full thickness of the gold layer. Focused ion beam (FIB) etching, using a Zeiss Auriga 60 CrossBeam scanning electron microscope (SEM) with an Orsay Canion FIB column, was used to mill the grooves into the gold layer. Figure 1 shows SEM micrographs of the fabricated curved gratings.

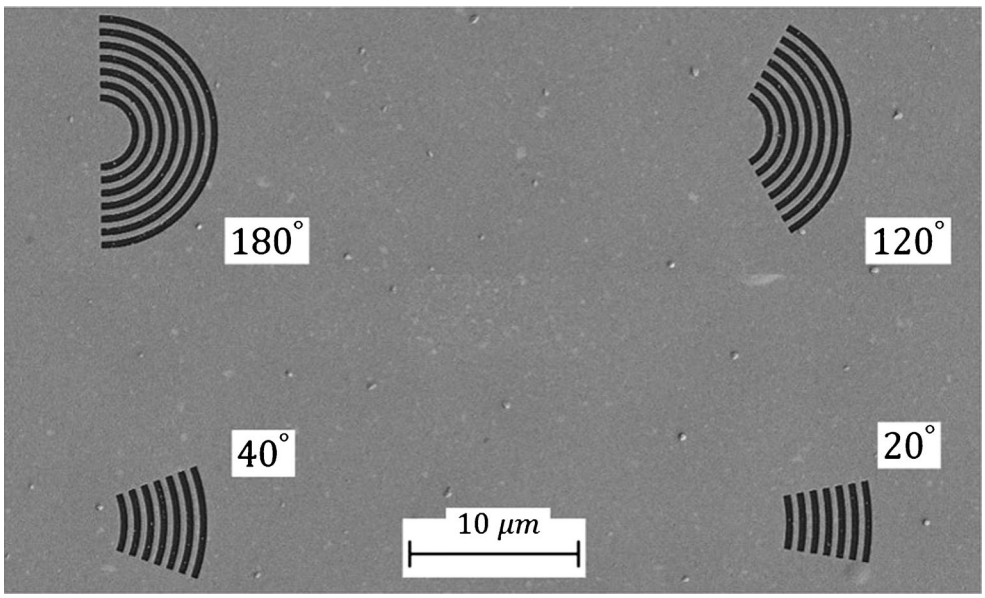

Fig. 1 SEM micrograph of fabricated curved gratings for four different sector angles

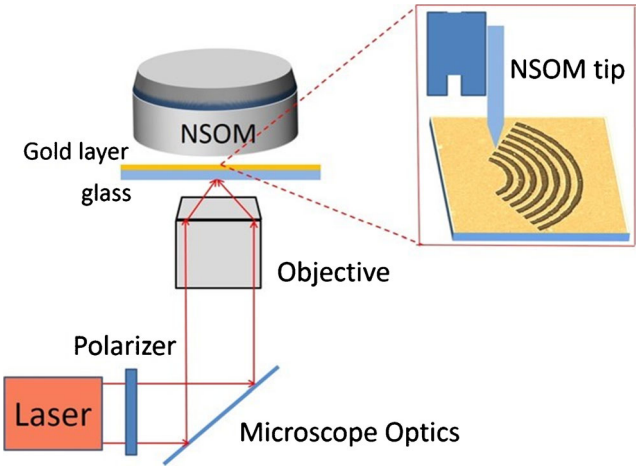

Fig. 2 Schematic of NSOM experimental setup

Characterization of the fabricated structures by SEM shows the final grating period Λ_{gr}=770±10 nm with groove width (GW) of half of the grating period ($GW = \frac{\Lambda_{gr}}{2} = 385$ nm).

The performance of the fabricated curved gratings is studied by near-field scanning optical microscopy (NSOM) with an appropriate optical coupling system as shown schematically in Fig. 2. The excitation light had a wavelength of 700 nm with ~5 nm bandwidth, illuminating the grating by a 10× microscope objective from below the sample through the glass substrate. The NSOM tip was positioned at a height of 10 nm from the gold surface to collect the evanescent field of the surface plasmons excited by the gratings.

In Fig. 3a, the NSOM image (256×256 pixels) for a 120° sector angle grating shows the focused surface plasmons. There is a phase change in the image, which is attributed to irregularities of the handmade NSOM probe. 3D simulations of the curved gratings were also performed using finite element methods (FEM) and adaptive meshing by COMSOL. The simulation parameters were identical to the fabricated structure and experiment parameters. Figure 3b shows the near-field intensity map at 10 nm vertical height above the gold-air interface, which demonstrates the focusing of surface plasmons in good agreement with NSOM scans. Focusing is also evident in the near-field intensity profiles along the bisector of the gratings (along the horizontal dashed cutline in Fig. 3b) for both the NSOM scan (black solid line) and the 3D simulation (red dashed line) as shown in Fig. 4. The intensity profiles are normalized to the maximum value of intensity of each line. In both cases, scattering of the light at the grooves contributes to observed oscillations in the positive x-coordinate and the focal spot occurs at the zero position. The results show the concentration of surface plasmons at the focal spot, although the field enhancement is relatively weak. This weak field enhancement is due to the off-resonance of the illumination wavelength and the 30-nm groove depth. Later optimization simulations showed that the most efficient coupling, and consequently the best field enhancement at the focal spot, would occur for 120-nm gold thickness (groove depth) when illuminated at the peak resonance wavelength ($\lambda_{\circ}$= 790 nm) for the grating period of Λ_{gr}=770 nm, see Fig. 9.

The width of the focal spot is defined by the full width at half maximum (FWHM) of the intensity profile along

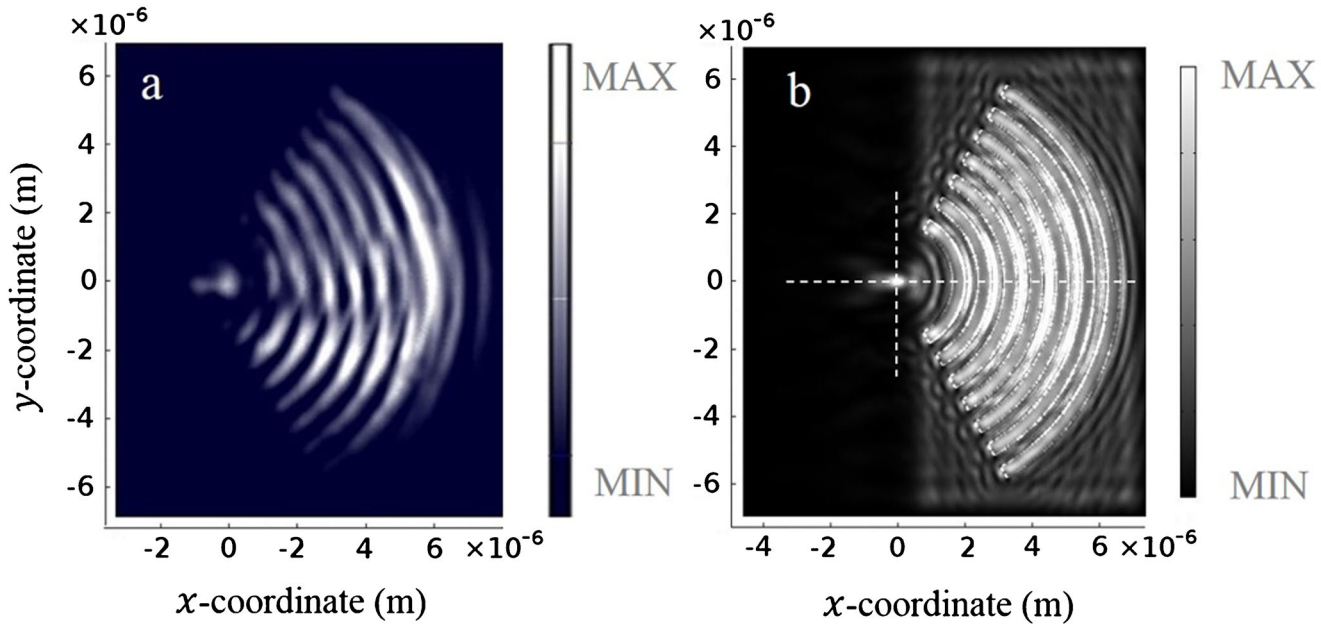

Fig. 3 NSOM scan **a** compared with simulation intensity map, **b** showing the focusing of coupled surface plasmons for 120° sector angle curved gratings

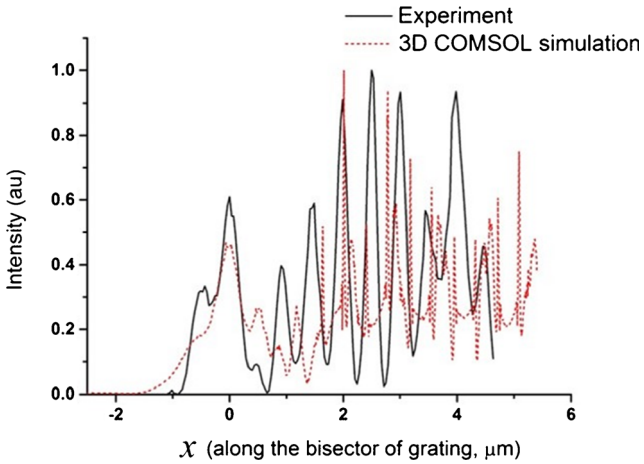

Fig. 4 Intensity profile along the bisector (*x*-axis in Fig. 6) of the simulated and experimental gratings (both with grating period of Λ_{gr}= 770 nm) determined at a 10-nm vertical height from the gold-air interface

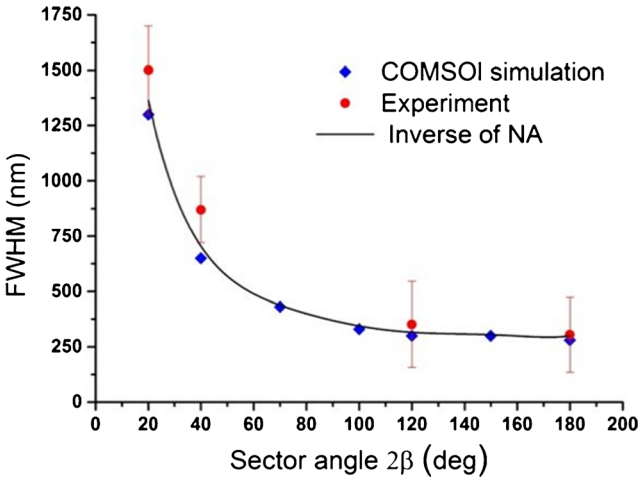

Fig. 5 Measurement and simulation for the vertical width of the focal spot from simulation (*blue diamonds*) and experimental measurement (*red circles*), and reciprocal of the effective NA (*black line*) which is consistent with the experimental and simulation results

the normal to the bisector of the gratings passing through the peak of the focal spot (along the vertical dashed cutline in Fig. 3b). Figure 5 compares the simulation calculations and NSOM measurement of the width of the focal spot for different sector angles. With increasing sector angle, the width of the coupled surface plasmons is decreased; for sector angles over 100°, the coupled surface plasmons are well focused at the focal spot with a minimum spot size of 300 nm, which is $\left(\frac{\lambda_\circ}{2.3}\right)$. The decreasing width of the focal spot with increasing sector angle is analogous to the performance of classical optical lenses. These plasmonic lenses can couple and direct surface plasmons into the focal spot allowing access to the focal spot for further processing.

In contrast to the excitation of linear gratings, for curved gratings, the *p* -polarised light makes different angles with the normal to the grooves at each point, as shown schematically in Fig. 6. As a result, the amplitude of the surface plasmons arising from each point of the grooves drops as the cosine of the angle between the light polarisation and the grating vector (cos(α)) [31]. Consequently, the total intensity of the coupled surface plasmons through the aperture of the grating is proportional to

$$I_{sp} \propto \int_{-\beta}^{\beta} \cos^2(\alpha)\, d\alpha \tag{1}$$

where β is half of the sector angle of the curved grating, and α is the angle between the plane of the linearly polarised beam (*p* -polarised) and the normal to the grooves at each point, as shown in Fig. 6.

Equation (1) shows that increasing the grating sector angle increases the coupling of the incident optical field to the surface plasmons by the curved gratings. In addition, the experimental and simulation results show that by increasing the sector angle the width of the focus of surface plasmons decreases. As a result, we define the effective numerical aperture (NA) of the curved gratings as

$$NA = \int_0^{\beta} \cos^2(\alpha)\, d\alpha = \frac{\sin(2\beta)}{4} + \frac{\beta}{2} \tag{2}$$

In order to show the appropriateness of the effective numerical aperture, its reciprocal versus sector angle is plotted in Fig. 5 (solid black line). The inverse matches closely to the simulation and experiment data points of the focal width, analogous to the inverse of the numerical aperture of classical optical lenses.

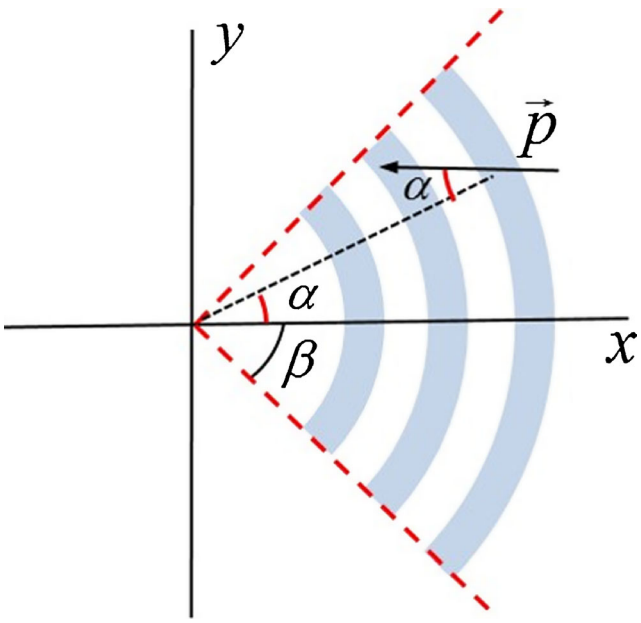

Fig. 6 Schematic of curved grating with sector angle of 120°. The linearly polarised light makes an angle of α at each point with the grating grooves

Investigating Plasmonic Grating Parameters by Simulation

Grooves of a plasmonic grating scatter linearly polarised light, (p -polarisation), to provide the required extra momentum for the photons to be coupled into surface plasmons. The efficiency of the scattering is mostly dependent on the groove characteristics—the period, width, and depth of the grooves (Λ_{gr}, GW, and GD). Detailed discussion of plasmonic gratings can be found elsewhere [32, 33], so here, we discuss the influence of the width and depth of the grating grooves to optimize curved gratings parameters. While the width of the grooves predominantly affects the phase delay between excited surface plasmons from different grooves, the groove depth influences the scattering [25, 32]. To save computer memory and time, we simulate linear gratings, with groove depth equal to the full thickness of the metal layer as shown in Fig. 7a, to optimize the grating parameters.

In order to optimize the effect of groove width and depth for efficient coupling of photons into surface plasmons, 2D simulations of linear trench gratings were calculated using the finite element method (FEM) and adaptive meshing by COMSOL. The selected grating period for the simulation was Λ_{gr}=770nm, and the grating was illuminated at normal incidence from below through the substrate (glass with refractive index n=1.5). The illumination wavelength was calculated according to the resonance wavelength of the plasmonic gratings under normal incidence (first order) [32]:

$$k_{sp} = \frac{2\pi}{\Lambda_{gr}} \tag{3}$$

in which k_{sp} is related to the illumination wavelength;

$$k_{sp} = \frac{2\pi}{\lambda_\circ}\left(\frac{\varepsilon_m \varepsilon_d}{\varepsilon_m + \varepsilon_d}\right) \tag{4}$$

with ε_m and ε_d as the dielectric constants of metal (gold) and dielectric (air), respectively.

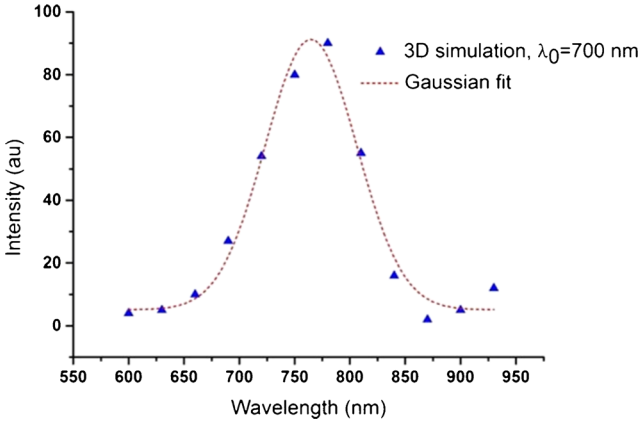

Fig. 8 Wavelength response of the curved grating from simulations 30-nm-thick gold film on glass with 120° sector angle

As a result, the grating was illuminated at $\lambda_\circ$=790 nm with the gold layer dielectric constants (ε_m) of ε_m=−23.3+i1.46 taken from Johnson and Christy [34]. The model geometry was meshed by a maximum element size smaller than $\lambda_\circ/8$ for the dielectric and smaller than $\lambda_\circ/50$ for the thin metal layer to ensure convergence. Figure 7b shows the average near-field intensity of surface plasmons calculated along a short cutline. Each coloured line and symbol relates to data for a specific groove width corresponding with a fraction of the grating period.

The selected groove widths for the fabricated structures were equal to half of the period of the gratings. The graph in Fig. 7b shows that the most efficient couplings for all the groove depths occur for a groove width of half of the grating period, or in other words, the surface plasmon wavelength ($GW = \frac{\Lambda_{gr}}{2} = \frac{\lambda_{sp}}{2} = 385$ nm). In fact, at this width, the phase change for the excited surface plasmons propagating across the other grooves would be zero, resulting in constructive interference of surface plasmons [25].

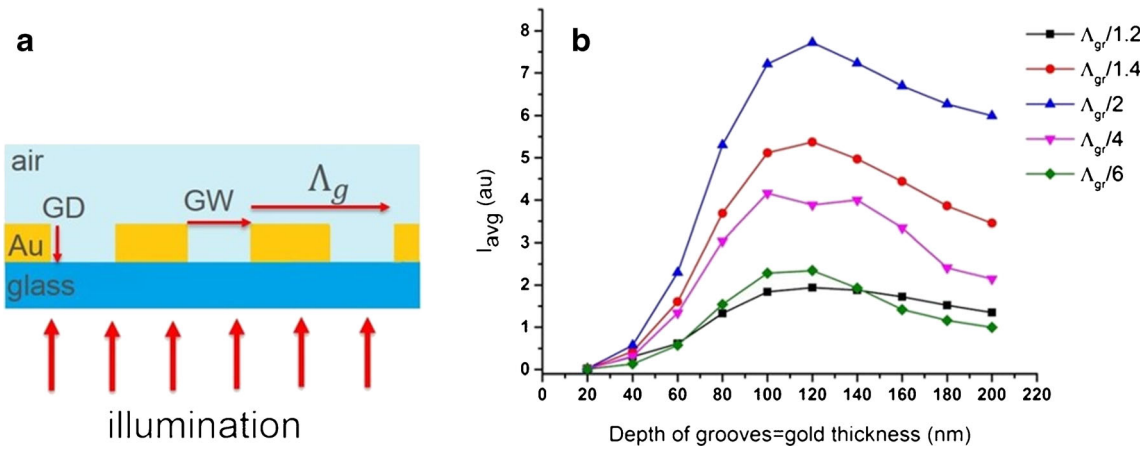

Fig. 7 **a** Trench grating illuminated through the gold substrate (material with higher refractive index); **b** average intensity of coupled incident light into surface plasmons versus the depth of grooves (GD). Each colour symbol shows a different groove width (GW) as a ration of the grating period (Λ_{gr}/m)

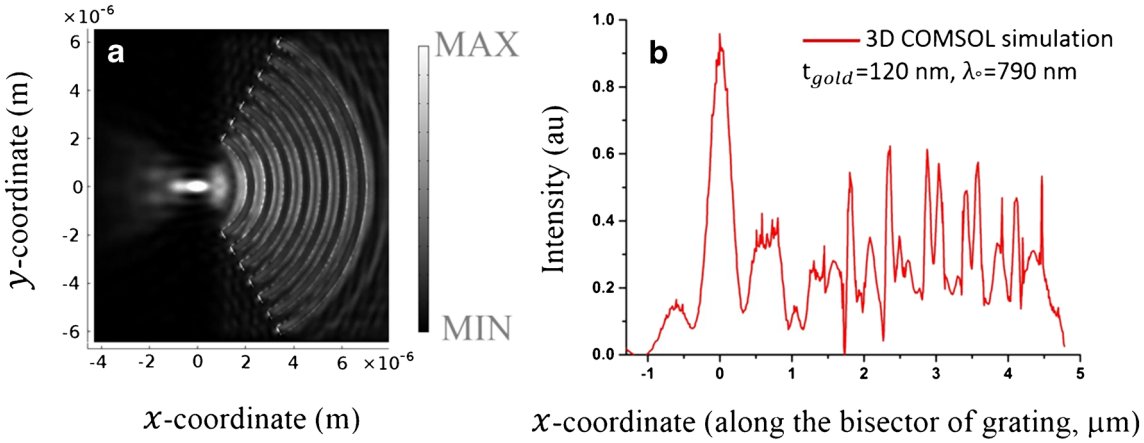

Fig. 9 **a** 3D simulation of near-field intensity map of 120° sector angle curved grating with optimized structural parameters (GW=385 nm and GD=120 nm) illuminated at $\lambda_{\circ}$=790 nm. **b** The intensity profile along the bisector of the grating (x-axis in Fig. 6)

In addition, Fig. 7b shows that maximum plasmonic coupling takes place at groove depths of 120 nm for all groove widths. The depth of the grooves in the case of trench gratings mostly influences the scattering of the incident light beam. For small depths, the scattering is not efficient, but for deeper grooves, scattering increases. However, very deep grooves would also scatter out the excited surface plasmons as radiation, reducing the coupling. Although the 30-nm groove depth of the fabricated trench curved gratings decreases the efficiency of coupling of the incident light into surface plasmons, it does not affect the performance of curved gratings as plasmonic lenses.

The number of grooves also influences the intensity of the coupled surface plasmons. Assuming the phase matching condition is met, increasing the number of grooves of circular gratings increases the coupled surface plasmon intensity. However, by increasing the radius of grooves beyond the propagation length of the surface plasmons, the influence of added grooves to the grating decreases and approaches to zero. A detailed discussion of the role of the number of grooves can be found elsewhere [25, 27]. Our simulation also shows that for the curved gratings with period equal to the surface plasmon wavelength and groove width of half of the grating period (consistent with phase matching when illuminated at normal incidence), increasing the number of grooves to seven increases the intensity of the focal spot.

Using 3D COMSOL simulations, we also tested the wavelength response of the curved gratings, in order to compare with the resonance wavelength of linear gratings through Eq. (3). The simulated curved grating period is identical to the period of the linear grating and fabricated structures (Λ_{gr}=770 nm). The groove width is equal to half of the period of the grating, and the thickness of the gold layer (groove depth) is also identical to the thickness of the fabricated curved grating (30 nm). The wavelength response of the grating is illustrated in Fig. 8 with maximum response of the grating at λ_{max}=780 nm, very close to the calculated value of resonance wavelength (λ_{max}= 790 nm) for linear gratings with identical grating period (Λ_{gr}= 770 nm), with an estimated bandwidth of 100 nm as the full width at half maximum (FWHM) of the fitted Gaussian curve. Additional simulations show that for a fixed resonance wavelength, 1 % change in the period of the curved gratings results in 5 % decrease in the intensity of the focal spot.

This simulation shows that the selected wavelength for the illumination of the structure in the experiment is not the resonance wavelength which results in less efficient coupling of incident light into surface plasmons. However, it does not affect the performance of the curved gratings as plasmonic lenses and only results in weaker NSOM signals through near-field scanning. The ideal situation of a 120° sector angle curved grating with optimized values of structural parameters for grating period of Λ_{gr}= 770 nm ($GW = \frac{\Lambda_{gr}}{2}$ = 385 nm, gold thickness=GD=120 nm), and illuminated at $\lambda_{\circ}$=790 nm was also simulated, see Fig. 9a, b. Figure 9a shows the intensity map of the near field and Fig. 9b exhibits the intensity profile along the bisector of the grating (along the horizontal dashed cutline). They show the focusing of surface plasmons with higher field enhancement at the focal spot in comparison to Fig. 3b, 4, due to the optimized parameters.

The focal spots from the curved gratings are not perfectly circular and are stretched to some extent. For the polarisation direction of the incident light along the bisector of the curved grating (x -direction), the depth of focus is along the x -axis. While we carefully aligned the direction of polarisation of the incident light along the bisector of the curved gratings, simulation shows that for misalignment of the polarisation angle relative to the curved grating bisector, the depth of the focus rotates slightly.

Asymmetric Faced Curved Gratings for a Tighter Focusing of Surface Plasmons

Although curved gratings focus surface plasmons, the depth of their focal spot is long in comparison to the width of the

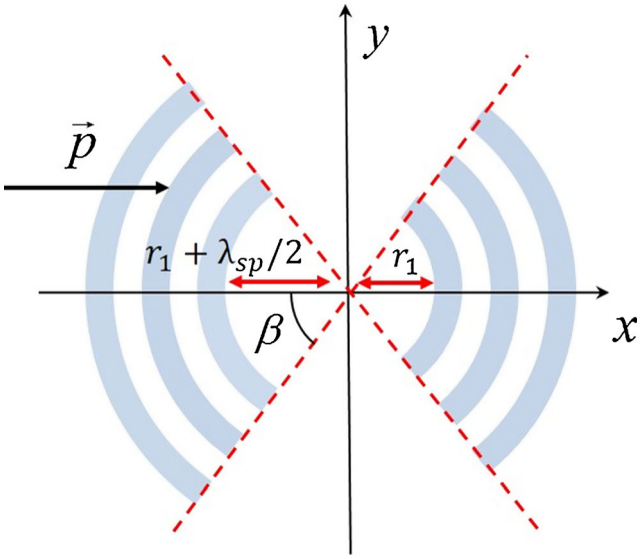

Fig. 10 Schematic for two faced curved gratings centred at the same point and in a symmetry-broken configuration

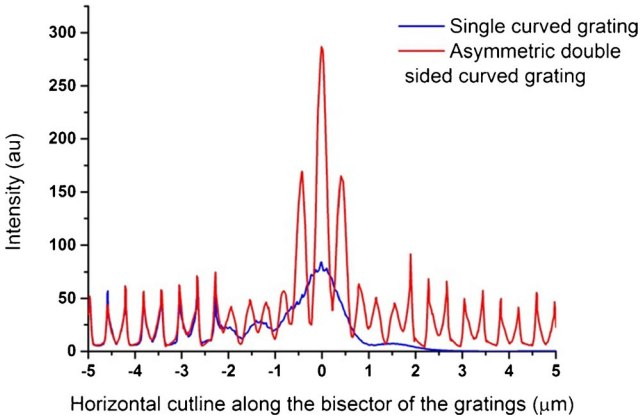

Fig. 12 Comparison of the longitudinal intensity profile along the bisector of the single curved grating and asymmetric double-sided curved gratings with six grooves

focal spot. This can be seen in Figs. 3 and 4. To address this problem, we studied arrangement of two curved gratings centred at the same point facing each other to focus surface plasmons using linearly polarised light, as shown in Fig. 10.

The radius of the grooves of each curved grating is mismatched half of the period of the surface plasmons relative to the opposite grating in order to provide the phase matching condition for counter-propagating surface plasmons to interfere constructively. Fig. 11a, b shows the 3D simulation of a single curved grating and an asymmetric double-sided curved grating for 160° sector angle with Λ_{gr}=770 nm, illuminated at $\lambda_{\circ}$=790 nm and with groove width of half of the grating period. The oval shape focal spot in single curved grating (Fig. 11a) changes to a small dot with higher intensity, demonstrating a significant decrease in the longitudinal distribution of plasmons at the focal spot (Fig. 11b). A detailed comparison is shown in Fig. 12 in which the intensity profile along the bisector of the gratings is plotted. It shows that the longitudinal width is changed from 800 nm for the single curved grating to 260 nm $\left(\approx\frac{\lambda_{\circ}}{3}\right)$ for the asymmetric double-sided curved grating with a significant enhancement in the intensity of the hot spot in comparison to the focused surface plasmons from the single curved gratings. However, the width of the focal spot does not change.

Conclusion

The capability of curved gratings to couple linearly polarised light to focused surface plasmons is investigated by theory and simulation and demonstrated experimentally. It is shown that controlling the sector angle of the curved gratings offers an additional tool to manipulate the width of the lateral distribution of surface plasmons. Moreover, curved gratings are positioned on one side of the focused surface plasmon spot, allowing the access to the concentrated surface plasmons for additional processes. Although illuminating a circular grating with radially polarised light provides a sharp high-intensity focal spot, it requires careful alignment of the beam with the structure, which is challenging in practice. In addition, the closed geometry of the circular gratings would limit their application.

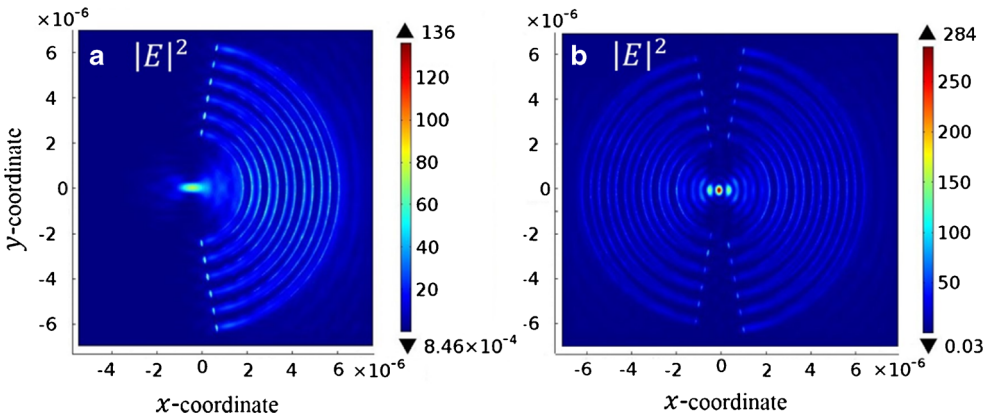

Fig. 11 Simulation of the performance of **a** single curved grating and **b** asymmetric double-sided curved gratings with six grooves

The focal spot of the curved gratings is not symmetric: consisting of a longer longitudinal focal depth compared with the width of the focal spot. However, it is shown that facing two curved gratings in an asymmetric configuration, and illuminating with linearly polarised light along the bisector of the curved gratings results in a very sharp focal point, similar to that obtained from the full circular gratings when they are illuminated with circularly polarised light. Curved gratings are amenable to planar architectures with potential applications in nonlinear plasmonics, plasmonic detectors, and sensing.

Acknowledgments This research was supported by the Australian Research Council Centre of Excellence for Ultra-high bandwidth Devices for Optical Systems (project number CE110001018) and Macquarie University. We also acknowledge CSIRO for the FIB facilities and thank Steven Moody for FIB operation.

References

1. Maier SA (2007) Plasmonics: fundamentals and applications: fundamentals and applications. Springer
2. Li XF, Yu SF (2010) Extremely high sensitive plasmonic refractive index sensors based on metallic grating. Plasmonics 5(4):389–394. doi:10.1007/s11468-010-9155-6
3. Dhawan A, Canva M, Vo-Dinh T (2011) Narrow groove plasmonic nano-gratings for surface plasmon resonance sensing. Opt Express 19(2):787–813. doi:10.1364/Oe.19.000787
4. Wong C, Olivo M (2014) Surface plasmon resonance imaging sensors: a review. Plasmonics 9(4):809–824. doi:10.1007/s11468-013-9662-3
5. Ishi T, Fujikata J, Makita K, Baba T, Ohashi K (2005) Si nano-photodiode with a surface plasmon antenna. Jpn J Appl Phys Part 2 44(12-15):L364–L366. doi:10.1143/Jjap.44.L364
6. Ren FF, Ang KW, Ye JD, Yu MB, Lo GQ, Kwong DL (2011) Split bull's eye shaped aluminum antenna for plasmon-enhanced nanometer scale germanium photodetector. Nano Lett 11(3):1289–1293. doi:10.1021/Nl104338z
7. Tang L, Kocabas SE, Latif S, Okyay AK, Ly-Gagnon DS, Saraswat KC, Miller DAB (2008) Nanometre-scale germanium photodetector enhanced by a near-infrared dipole antenna. Nat Photonics 2(4): 226–229. doi:10.1038/nphoton.2008.30
8. Xu T, Jiao X, Zhang G-P, Blair S (2007) Second-harmonic emission from sub-wavelength apertures: effects of aperture symmetry and lattice arrangement. Opt Express 15(21):13894–13906
9. Nahata A, Linke RA, Ishi T, Ohashi K (2003) Enhanced nonlinear optical conversion from a periodically nanostructured metal film. Opt Lett 28(6):423–425
10. Kauranen M, Zayats AV (2012) Nonlinear plasmonics. Nat Photonics 6(11):737–748
11. Bozhevolnyi SI, Volkov VS, Devaux E, Laluet JY, Ebbesen TW (2006) Channel plasmon subwavelength waveguide components including interferometers and ring resonators. Nature 440(7083): 508–511. doi:10.1038/Nature04594
12. Chen Z-x, Wu Z-j, Ming Y, Zhang X-j, Lu Y-q (2014) Hybrid plasmonic waveguide in a metal V-groove. Aip Adv 4 (1). doi: doi:http://dx.doi.org/10.1063/1.4861582
13. Kumar G, Li SS, Jadidi MM, Murphy TE (2013) Terahertz surface plasmon waveguide based on a one-dimensional array of silicon pillars. New J Phys 15. doi:Artn 085031 Doi 10.1088/1367-2630/15/8/085031
14. Lu J, Petre C, Yablonovitch E, Conway J (2007) Numerical optimization of a grating coupler for the efficient excitation of surface plasmons at an Ag-SiO2 interface. J Opt Soc Am B 24(9):2268–2272. doi:10.1364/Josab.24.002268
15. Tanemura T, Balram KC, Ly-Gagnon DS, Wahl P, White JS, Brongersma ML, Miller DA (2011) Multiple-wavelength focusing of surface plasmons with a nonperiodic nanoslit coupler. Nano Lett 11(7):2693–2698. doi:10.1021/nl200938h
16. Gaborit G, Armand D, Coutaz J-L, Nazarov M, Shkurinov A (2009) Excitation and focusing of terahertz surface plasmons using a grating coupler with elliptically curved grooves. Appl Phys Lett 94(23):231108. doi:10.1063/1.3153125
17. Radko IP, Bozhevolnyi SI, Evlyukhin AB, Boltasseva A (2007) Surface plasmon polariton beam focusing with parabolic nanoparticle chains. Opt Express 15(11):6576–6582. doi:10.1364/Oe.15.006576
18. Zhao CL, Wang JY, Wu XF, Zhang JS (2009) Focusing surface plasmons to multiple focal spots with a launching diffraction grating. Appl Phys Lett 94(11). doi:Artn 111105 Doi 10.1063/1.3100195
19. Drezet A, Stepanov AL, Ditlbacher H, Hohenau A, Steinberger B, Aussenegg FR, Leitner A, Krenn JR (2005) Surface plasmon propagation in an elliptical corral. Appl Phys Lett 86(7). doi:Artn 074104 Doi 10.1063/1.1870107
20. Gaborit G, Armand D, Coutaz JL, Nazarov M, Shkurinov A (2009) Excitation and focusing of terahertz surface plasmons using a grating coupler with elliptically curved grooves. Appl Phys Lett 94(23). doi:Artn 231108 Doi 10.1063/1.3153125
21. Maier SA, Andrews SR, Martín-Moreno L, García-Vidal FJ (2006) Terahertz surface plasmon-polariton propagation and focusing on periodically corrugated metal wires. Phys Rev Lett 97(17):176805
22. Liu ZW, Steele JM, Srituravanich W, Pikus Y, Sun CXZ (2005) Focusing surface plasmons with a plasmonic lens. Nano Lett 5(9): 1726–1729. doi:10.1021/Nl051013
23. López-Tejeira F, Rodrigo SG, Martín-Moreno L, García-Vidal FJ, Devaux E, Ebbesen TW, Krenn JR, Radko IP, Bozhevolnyi SI, González MU, Weeber JC, Dereux A (2007) Efficient unidirectional nanoslit couplers for surface plasmons. Nat Phys 3(5):324–328. doi:10.1038/nphys584
24. Khoo EH, Guo Z, Ahmed I, Li EP (2012) Near-field switching and focusing using plasmonic nanostructures with different polarizations. Proc SPIE 8457:1–8. doi:10.1117/12.929322
25. Steele JM, Liu ZW, Wang Y, Zhang X (2006) Resonant and non-resonant generation and focusing of surface plasmons with circular gratings. Opt Express 14(12):5664–5670. doi:10.1364/Oe.14.005664
26. Fu YQ, Liu Y, Zhou XL, Xu ZW, Fang FZ (2010) Experimental investigation of superfocusing of plasmonic lens with chirped circular nanoslits. Opt Express 18(4):3438–3443
27. Chen WB, Abeysinghe DC, Nelson RL, Zhan QW (2009) Plasmonic lens made of multiple concentric metallic rings under radially polarized illumination. Nano Lett 9(12):4320–4325. doi:10.1021/Nl903145p
28. Fang ZY, Peng QA, Song WT, Hao FH, Wang J, Nordlander P, Zhu X (2011) Plasmonic focusing in symmetry broken nanocorrals. Nano Lett 11(2):893–897. doi:10.1021/Nl104333n
29. Gjonaj B, David A, Blau Y, Spektor G, Orenstein M, Dolev S, Bartal G (2014) Sub-100 nm focusing of short wavelength plasmons in homogeneous 2D space. Nano Lett 14(10):5598–5602. doi:10.1021/Nl502080n
30. Martin PJ, Sainty WG, Netterfield RP (1984) Enhanced gold film bonding by ion-assisted deposition. Appl Opt 23(16):2668–2669
31. Lerman GM, Yanai A, Levy U (2009) Demonstration of nanofocusing by the use of plasmonic lens illuminated with radially polarized light. Nano Lett 9(5):2139–2143. doi:10.1021/Nl900694r
32. Koev ST, Agrawal A, Lezec HJ, Aksyuk VA (2012) An efficient large-area grating coupler for surface plasmon polaritons. Plasmonics 7(2):269–277. doi:10.1007/s11468-011-9303-7
33. Raether H (1988) Surface-plasmons on smooth and rough surfaces and on gratings. Springer Tr Mod Phys 111:1–133
34. Johnson PB, Christy RW (1972) Optical constants of the noble metals. Phys Rev B 6(12):4370–4379